Universität Hamburg
DER FORSCHUNG | DER LEHRE | DER BILDUNG

CHyN
Center for Hybrid Nanostructures

Nanoscale Engineering of Hybrid Graphene Architectures for Tailored Light-Matter Interactions Across the Microwave Spectrum

Dissertation
zur Erlangung des Doktorgrades
an der Fakultät für Mathematik, Informatik und Naturwissenschaften
Fachbereich Physik
der Universität Hamburg

Vorgelegt von

Vincent Kester Wunnibald Strenzke

Hamburg

2025

Gutachter der Dissertation:	Prof. Dr. Robert H. Blick Dr. Lars Tiemann
Zusammensetzung der Prüfungskommission:	Prof. Dr. Dorota Koziej Prof. Dr. Robert H. Blick Prof. Dr. Gabriel Bester Dr. Lars Tiemann Dr. Robert Zierold
Vorsitzende der Prüfungskommission:	Prof. Dr. Dorota Koziej
Datum der Disputation:	24.04.2025
Vorsitzender des Fach-Promotionsausschusses PHYSIK:	Prof. Dr. Wolfgang J. Parak
Leiter des Fachbereichs PHYSIK:	Prof. Dr. Markus Drescher
Dekan der Fakultät MIN:	Prof. Dr.-Ing. Norbert Ritter

Abstract

Graphene is an exceptionally versatile material, renowned for its robustness, strong light-matter interactions and high electrical conductivity. It can even acquire superconducting properties through proximity effects with superconducting electrodes or by stacking two layers of graphene with a relative twist angle of $1.1\,^{\circ}$. The incorporation of graphene into hybrid device architectures combining superconducting and high-frequency circuit elements enables parametric amplification, single-photon detection and innovative qubit designs. At the same time, these components open new pathways to investigate the fundamental properties of graphene.

In this thesis, various complex graphene devices are engineered by integrating van der Waals materials, superconductors, and high-frequency circuits into hybrid architectures to explore light-matter interactions. Lithographic techniques were optimized to create micro- and nanostructured samples comprised of exfoliated as well as large-area, polycrystalline graphene. Tailored for the investigation of light-matter interactions, these devices provide a versatile platform to study the charge carrier transport in graphene under electromagnetic radiation in the microwave spectrum. Radio-frequency and microwave signals used in low-temperature magnetotransport measurements revealed signatures of nuclear spin effects in isotopically purified ^{13}C graphene. To enhance the coupling efficiency of the radiation, hybrid circuits integrating large-area and exfoliated graphene with high-frequency waveguides were engineered for microwave spectroscopy experiments. However, the absence of resonant features in experiments suggests that an unknown mediator facilitating momentum transfer in electron spin resonance may be missing in pristine graphene.

Fabricating superconducting electrodes for graphene-based Josephson junctions (JJs) with sufficient electrical transparency to graphene proved technologically challenging and necessitated the substitution of niobium with titanium-aluminum. Under small magnetic fields, these aluminum-graphene junctions exhibited quantum interference effects that are attributed to Tomasch and McMillan-Rowell oscillations. These advancements in device performance pave the way for the integration of graphene JJs into superconducting microwave circuits, holding tremendous potential for quantum technologies, dark matter axion search and advanced photosensing applications.

In an alternative approach for light-matter interaction in a different spectral regime, asymmetric metallic grating gates on top of high-quality graphene structures enabled the rectification of sub-THz-radiation via plasmonic excitations. The photoresponse of these detectors is influenced by the incident frequency, temperature, and doping in the graphene channel, with their sensitivity estimated to be in the order of $\sim 10^{-12}$ W/Hz$^{1/2}$.

Zusammenfassung

Graphen ist ein äußerst vielseitiges Material, bekannt für seine Robustheit, starke Licht-Materie-Wechselwirkungen und hohe elektrische Leitfähigkeit. Es kann sogar supraleitende Eigenschaften erlangen, etwa mittels Proximity-Effekt mit supraleitenden Elektroden oder durch das Anordnen zweier Graphenschichten mit einem relativen Rotationswinkel von 1,1 °. Die Einbindung von Graphen in hybride Architekturen, die supraleitende und hochfrequente Schaltungselemente kombinieren, ermöglicht parametrische Verstärkung, Einzelphotonendetektion und innovative Qubit-Designs. Gleichzeitig stellen diese Komponenten neue Möglichkeiten zur Erforschung der grundlegenden Eigenschaften von Graphen dar.

In dieser Arbeit werden vielfältige Graphen-Devices durch die Integration von van der Waals-Materialien, Supraleitern und Hochfrequenzschaltungen in hybride Architekturen entwickelt, um Licht-Materie-Wechselwirkungen zu untersuchen. Lithografische Techniken wurden optimiert, um Mikro- und Nanostrukturen herzustellen, die sowohl aus exfoliertem als auch aus großflächigem, polykristallinen Graphen bestehen. Diese sind auf die Untersuchung von Licht-Materie-Wechselwirkungen zugeschnitten und bieten eine vielseitige Plattform zur Untersuchung des Ladungsträgertransports in Graphen unter elektromagnetischer Strahlung im Mikrowellenspektrum. Tieftemperaturmessungen mit Radiofrequenz- und Mikrowellensignalen bei hohen Magnetfeldern zeigten Anzeichen von Kernspineffekten in isotopenreinem ^{13}C Graphen. Um die Einkopplung der Strahlung zu verbessern, wurden hybride Schaltungen für Experimente der Mikrowellenspektroskopie entwickelt, die großflächiges und exfoliertes Graphen mit hochfrequenten Wellenleitern kombinieren. Das Fehlen von Resonanzen in den Experimenten deutet auf einen unbekannten Mechanismus hin, welcher den Impulsübertrag für Elektronenspinresonanz erleichtern könnte, jedoch in reinem Graphen fehlt.

Die Herstellung supraleitendender Elektroden für graphenbasierte Josephson Kontakte (engl. Josephson junctions, JJs) mit ausreichender Transparenz erwies sich als technologisch herausfordernd, weshalb Niob durch Titan-Aluminium ersetzt werden musste. Bei kleinen Magnetfeldern zeigten diese Aluminium-Graphen-Kontakte Quanteninterferenzeffekte, die auf Tomasch- und McMillan-Rowell-Oszillationen zurückzuführen sind. Die dargestellten Fortschritte in der Deviceperformance ebnen den Weg für die Integration von Graphen-JJs in supraleitende Mikrowellenschaltungen, welche ein enormes Potenzial sowohl für Quantentechnologien, der Suche nach dunkler Materie und für neuartige Photodetektoren bieten.

Asymmetrische metallische Gitterelektroden auf hochqualitativen Graphenstrukturen stellen einen alternativen Ansatz dar, um Licht-Materie-Wechselwirkungen in einem anderen Frequenzbereich mittels plasmonischer Anregungen zu erforschen. Das Detektorsignal wird von der einfallenden Frequenz, Temperatur und Dotierung im Graphen beeinflusst, wobei ihre Empfindlichkeit auf etwa $\sim 10^{-12}$ W/Hz$^{1/2}$ geschätzt wird.

Contents

List of abbreviations

1D	one-dimensional
2D	two-dimensional
3D	three-dimensional
ADGG	asymmetric dual-grating gate
AFM	atomic force microscopy
ALD	atomic layer deposition
CNP	charge neutrality point
CPW	coplanar waveguide
CVD	chemical vapor deposition
DNP	dynamic nuclear polarization
DUT	device under test
EBL	electron beam lithography
ESR	electron spin resonance
FP	Fabry-Pérot
FWHM	full width half maximum
GJJ	graphene Josephson junction
GSP	graphene surface plasmon-polaritons
GTeraFET	graphene terahertz field-effect-transistor
hBN	hexagonal boron nitride
IDT	interdigital transducer
JJ	Josephson junction
MAR	multiple Andreev reflections
MATBG	magic-angle twisted bilayer graphene
MBE	molecular beam epitaxy

MFC	mass flow controller
MEMS	micro-electromechanical systems
NEP	noise-equivalent power
NMR	nuclear magnetic resonance
PC	polycarbonate
PCB	printed circuit board
PDMS	polydimethylsiloxane
PPC	polypropylene carbonate
PPMS	physical property measurement system
PTE	photo-thermoelectric
PVD	physical vapor deposition
QED	quantum electrodynamics
RCSJ	resistively and capacitively shunted junction
RIE	reactive ion etching
RSM	resistive self mixing
SAW	surface acoustic wave
SdH	Shubnikov-de Haas
SEM	scanning electron microscopy
SPP	surface plasmon-polaritons
TBG	twisted bilayer graphene
TMDs	transition-metal dichalcogenides
vdW	van der Waals
VNA	vector network analyzer
WL	weak localization

1. Introduction

Materials science is at the heart of scientific progress and basic research. Novel material compositions can expand the frontiers of physics and inspire new technologies with a lasting impact on our everyday lives. Rarely a discovery had such an impact as the one by Novoselov *et al.* in 2004 of atomically thin carbon films, called graphene.[1,2] Layers of two-dimensional (2D) materials such as graphene are held together in the bulk crystal by weak van der Waals (vdW) forces that allow separation into individual monolayers by mechanical exfoliation. The ability to vertically arrange sheets of different exfoliated vdW materials into complex heterostructures revolutionized condensed-matter physics.[3–6] To this day, researchers rely on the same mechanical exfoliation method which Novoselov *et al.* employed over two decades ago to isolate a single layer of graphene. By repeated peeling with a simple adhesive tape, bulk graphite can be thinned down to atomically thin sheets and transferred onto a silicon substrate, as shown in figure 1.1.

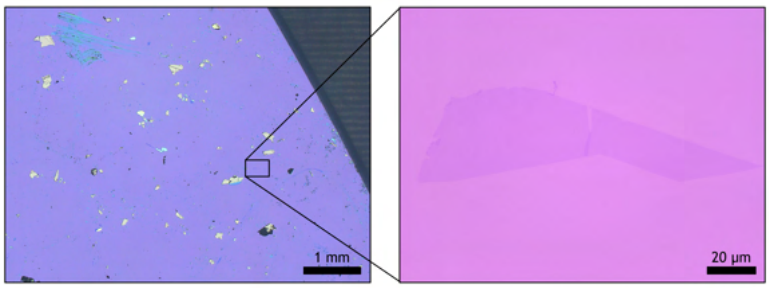

Figure 1.1.: Optical image of an exemplary silicon substrate after mechanical exfoliation of graphene. Among glue residues and thick graphite flakes, thin graphene can be found, as shown in the magnified view on the right.

Remarkably, using a simple optical microscope, this single layer of carbon atoms can be seen by the human eye. This observation is permitted by the surprisingly strong light-matter interactions in graphene. The distinctive optical properties, with an absorbance of $\sim 2.3\,\%$, arise from its unique electronic structure.[7–10] The gapless and linear bandstructure of graphene hosts quasi-relativistic charge carriers and leads to broadband light absorption.[10–12] Thus, electromagnetic radiation ranging from the ultraviolet to the microwave regime can be utilized to probe the intrinsic properties and charge carrier dynamics of graphene.[13,14]

One powerful technique to assess the low energy spectrum of graphene is electron spin resonance (ESR).[15–19] Analogous to nuclear magnetic resonance (NMR), ESR constitutes the *electron spin* counterpart of magnetic resonance spectroscopy, however, on a thousand times larger energy scale for graphene (tens of μeV). In ESR, microwave radiation activates transitions between discrete *electron spin*-split states.[20] Previous studies employed resistively-detected ESR at low temperatures with μeV accuracy to resolve effects of intrinsic spin-orbit coupling,[17,21] sublattice symmetry breaking[18] and nuclear spins[19] on the graphene band structure. However, the sensitivity of these ESR studies was limited by technological challenges such as the inefficient coupling of microwave radiation and their use of polycrystalline graphene with inferior electronic quality.[22,23]

The implementation of high-quality complex vdW heterostructures into tailored high-frequency circuits with precise coupling enables sensitive microwave spectroscopy of their physical phenomena. Interestingly, stacks of different vdW materials not just inherit the properties of their individual layers, but also new properties emerge, that can be controlled by carrier concentration or an interlayer twist angle. The most prominent example of such a structure is magic-angle twisted bilayer graphene (MATBG), which consists of two sheets of graphene rotated by $\sim 1.1\,^{\circ}$.[24] The rotational alignment of the two hexagonal graphene lattices gives rise to a moiré superlattice that drastically alters the bandstructure and leads to strong electron correlations with Mott insulating and superconducting states.[24,25] The nature of this unconventional superconductivity is still not fully understood and microwave studies may provide new insights, e.g., by probing the kinetic inductance.[26–28]

Apart from this unique kind of intrinsic superconductivity emerging in MATBG, superconductivity can also be induced in graphene via the proximity effect in the form of graphene Josephson junctions (GJJs).[29–31] Although the superconductivity originates from the superconducting electrodes, such as aluminum, the properties of the GJJ are determined by the graphene that acts as the weak link. The electrostatic control of graphene's charge carrier type and density allows precise tuning of the GJJ parameters. This significant advantage over conventional superconductor-insulator-superconductor junctions makes GJJs especially appealing for hybrid superconducting quantum technologies, providing gate tunable qubits,[32] parametric amplification with gate tunable working frequency[33,34] and microwave bolometers by coupling GJJs to high-frequency resonators.[35,36] These microwave bolometers and similar GJJ detectors harness the exceptional thermal properties of graphene to unlock single photon sensitivity from the near- to the far-infrared regime.[35–38]

The low energy of photons of this spectral domain ranging from megahertz (MHz) to terahertz (THz) is challenging for materials used in established technologies. Due to its exceptional properties, graphene has been identified as the ideal candidate material for photodetectors, bridging the gap between photonics and electronics. Based on either superconducting GJJs or on plas-

monic devices,[39–41] graphene provides high sensitivities with outstanding tunability, detection speed and bandwidth, which is useful for applications in telecommunication[37,42,43] and dark matter axion research.[44,45]

In this thesis, vdW materials, superconductors and high-frequency circuits are fused into hybrid architectures tailored for the investigation of light-matter interactions in graphene across the microwave spectrum. The unique properties of graphene will be described in chapter 2, along with superconducting effects in graphene. While this work mainly covers superconducting devices, it also briefly addresses plasmonic effects as both topics constitute essential theoretical concepts for the graphene-based photosensing approaches. Finally, the experimental technique of magnetic resonance spectroscopy will be introduced as well as the enabling technology of microwave transmission lines.

A significant part of this thesis is dedicated to the fabrication of hybrid graphene devices. The initial research of this group (and this thesis) was based on large-area, polycrystalline graphene. This work transitioned to high-quality exfoliated graphene devices that are essential for exploring novel emergent phenomena. Consequently, several key processes had to be developed from scratch, such as the assembly of vdW materials, the engineering of nanostructured superconducting electrodes, and the patterning of microwave circuits. The substantial technological advancements are presented along with a detailed description of the device fabrication, the measurement procedures and cryogenic setups in chapter 3.

The experimental results, the associated analysis and discussion are presented in chapter 4. It starts with the investigation of nuclear effects in isotopically purified ^{13}C graphene (section 4.1). While nuclear spin effects are typically neglected in natural graphene, nuclear spins in isotopically enriched graphene can provide an opportunity to store and retrieve quantum information.[46–48] Magnetotransport measurements were combined with radio-frequency and microwave radiation to search for signatures of nuclear effects. The next section 4.2 presents results obtained on hybrid circuits combining large-area or exfoliated graphene with high-frequency circuits for microwave spectroscopy.

Experimental findings on superconducting GJJ systems are discussed in section 4.3. Within a collaborative project including the group of Prof. Horns (University of Hamburg) and Prof. Fong (Raytheon BBN Technologies and Northeastern University), a graphene-based JJ bolometer was characterized that is intended for the use in dark matter axion search experiments. For our own in-house fabricated graphene junctions, the properties of the superconducting thin films forming the device electrodes are examined alongside superconducting microwave resonators. Additionally, their transport characteristics are systematically investigated to gain insight into the device performance.

Finally, the development of graphene-based THz-detectors is illustrated in section 4.4. The

asymmetric topgate structures of these devices results in plasmonic rectification effects that persist even at room temperature. Important advancements in the fabrication of these photodetectors led to the successful detection of THz-radiation with high sensitivity. However, a detailed analysis of the observed photoresponse is beyond the scope of this work.

The results of this work are summarized in chapter 5, which also provides ideas for improvements and outlines future research directions.

Some of the results presented in this thesis are part of peer-reviewed publications, such as the report on the deposition of superconducting niobium nanostructures[49] and experimental findings as well as a review on nuclear spin effects in ^{13}C graphene.[19,50] Additional publications addressing rectification mechanisms in graphene-based THz-detectors, interference effects in superconducting aluminum-graphene junctions and nuclear spin ordering effects in ^{13}C few-layer graphene are in preparation.

2. Theoretical Background

2.1. Van der Waals Materials and their Heterostructures

Graphene is an atomically thin and thereby truly two-dimensional material which was first experimentally discovered in 2004 by Novoselov and Geim *et al.* by mechanical exfoliation from bulk graphite.[1] Until then, it was generally thought of as a thermodynamically unstable and therefore elusive material, although the theoretical study of the graphene band structure dates back to 1947.[51] In a single layer of graphene, the carbon atoms are arranged in a honeycomb lattice. The unit cell consists of two inequivalent carbon atoms which form the triangular sublattices A and B as shown in figure 2.1 a). The atoms in graphene are sp^2 hybridized where the electrons from the $2s$, $2p_x$ and $2p_y$ orbitals form strong in-plane σ-bonds. The electron from the out-of-plane $2p_z$ orbital can move in the graphene lattice via π-bonds. Only electrons in this delocalized π-system contribute to conductivity and are considered in the single-particle band structure theory of graphene. The main results of the tight binding model employed by Castro Neto *et al.*[12] are presented in the following.

As shown in figure 2.1 a), the lattice of graphene is obtained by the lattice vectors $\vec{a}_1$ and $\vec{a}_2$ that construct the unit cell in real space and are given by

$$\vec{a}_1 = \frac{a}{2}(3, \sqrt{3}), \quad \vec{a}_2 = \frac{a}{2}(3, -\sqrt{3}), \tag{2.1}$$

where a corresponds to the distance between two carbon atoms, i.e., the lattice constant of graphene with $a = 1.42\,\text{Å}$. Two atoms in the same sublattice are separated by $|\vec{a}_{1,2}| = 2.46\,\text{Å}$.

With the approximation, that electrons can only hop from site A to the adjacent B site and *vice versa*, t is defined as the energy for nearest neighbor hopping and the tight-binding Hamiltonian in second quantization for graphene can be written as

$$\hat{H} = -t \sum_{\langle i,j \rangle, \sigma} \left(a^\dagger_{\sigma,i} b_{\sigma,j} + \text{h.c.} \right). \tag{2.2}$$

Here, $a_{\sigma,i}$, $a^\dagger_{\sigma,i}$ and $b_{\sigma,i}$, $b^\dagger_{\sigma,i}$ are defined as the annihilation and creation operators for an electron with the spin σ on site $\boldsymbol{R}_i$ in sublattice A and B, respectively. The units are defined so that $\hbar = 1$, while h.c. denotes the Hermitian conjugate.

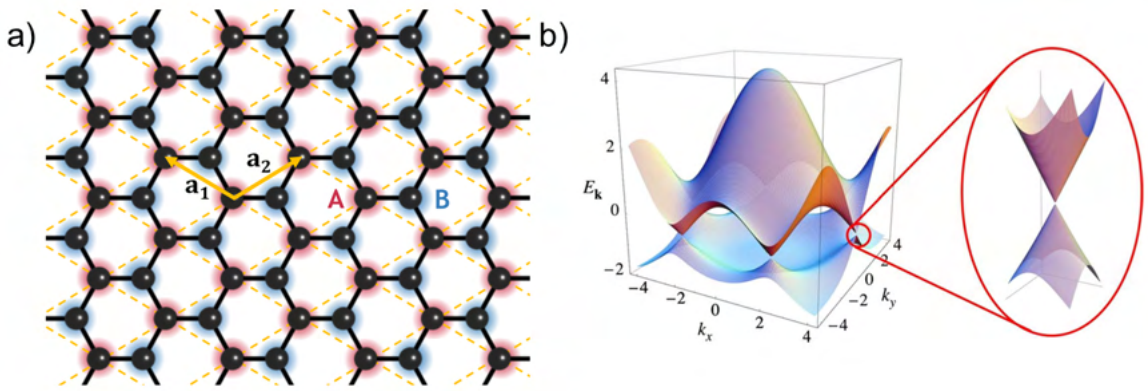

Figure 2.1.: a) The hexagonal lattice of graphene with the two triangular sublattices A and B. The lattice vectors $\vec{a}_1$ and $\vec{a}_2$ construct the unit cell, which is indicated by the yellow dashed line. b) Electronic bandstructure of graphene in the first Brillouin zone with a close-up of the low energy spectrum exhibiting a linear dispersion relation near one of the Dirac points. Figure b) is adapted with permission from A. H. Castro Neto, F. Guinea, N. M. R. Peres, K. S. Novoselov, and A. K. Geim. The electronic properties of graphene. Reviews of Modern Physics 81, 109162 (2009). Copyright 2009 by the American Physical Society.[12]

The eigenvalues of the Hamiltonian are given as

$$\begin{aligned} E_{\pm}(\boldsymbol{k}) &= \pm t\sqrt{3+f(\boldsymbol{k})}, \\ \text{with} \quad f(\boldsymbol{k}) &= 2\cos\left(\sqrt{3}k_y a\right) + 4\cos\left(\frac{\sqrt{3}}{2}k_y a\right)\cos\left(\frac{3}{2}k_x a\right), \end{aligned} \tag{2.3}$$

which describe the energy bands in momentum space with the components of the wave vector k_x and k_y. The energy dispersion of Eq. 2.3 can be seen in figure 2.1 b) and shows that the valence and conduction band of graphene touch at the *K* and *K'* points of the first Brillouin zone. The Hamiltonian can be expanded at small momentum q near these two valleys such that $\boldsymbol{k} = \boldsymbol{K} + \boldsymbol{q}$, with $|\boldsymbol{q}| \ll |\boldsymbol{K}|$. The result is a massless Dirac Hamiltonian that describes a two-level system with inversion symmetry

$$H_K(\boldsymbol{q}) = H(\boldsymbol{K}+\boldsymbol{q}) \approx \hbar v_F \begin{bmatrix} 0 & q_x - iq_y \\ q_x + iq_y & 0 \end{bmatrix} = \hbar v_F \boldsymbol{\sigma}\cdot\boldsymbol{q}, \tag{2.4}$$

with the effective Fermi velocity in graphene $v_\mathrm{F} = 3ta/2 \approx 10^6$ m/s and the vector Pauli matrices $\boldsymbol{\sigma} = (\sigma_x, \sigma_y)$.[12] Solving this Eq. 2.4, which describes massless Dirac fermions, yields the well-known linear dispersion of graphene close to the so-called Dirac points

$$E_{\pm}(\boldsymbol{q}) = \pm\hbar v_F |\boldsymbol{q}|. \tag{2.5}$$

Near the Dirac points in graphene, the presence of the two distinct sublattices A and B gives

rise to a valley degeneracy of $g_\nu = 2$. This valley degeneracy is also referred to as pseudospin, as it shares a similar formalism with real spin. Consequently, the combination of the pseudospin quantum number and the spin degeneracy of $g_s = 2$ results in a general four-fold degeneracy in graphene. While for other systems, helicity refers to the projection of real spin onto the direction of propagation, in graphene, chirality is defined by the projection of pseudospin.[11,21,52]

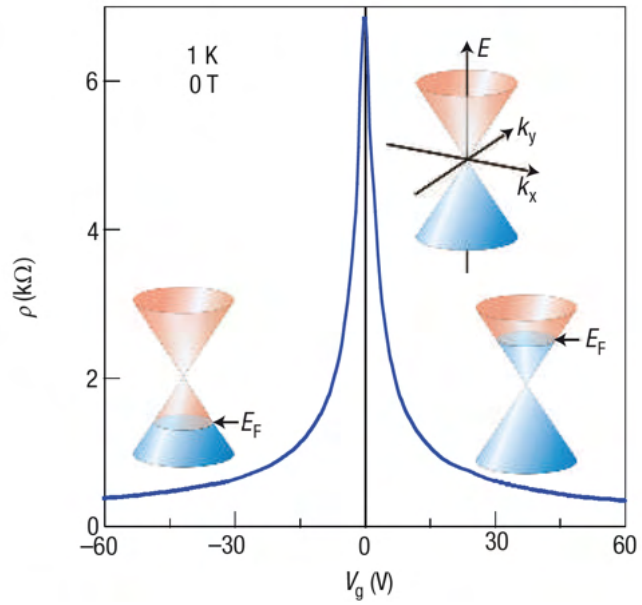

Figure 2.2.: The ambipolar field effect in single-layer graphene enables control of the charge carrier type and density by electrostatic gating. At the charge neutrality point at 0 V, E_F is located directly at the Dirac point, electron and hole concentrations become equally small, resulting in a maximum in resistance. Figure adapted with permission from Geim, A., Novoselov, K. The rise of graphene. Nature Mater 6, 183–191 (2007). Copyright 2007 by Springer Nature.[11]

The touching of the conduction and valence bands at the Dirac point is the fundamental reason behind graphene's exceptional characteristic, allowing for a seamless tunability of charge carrier density and type from electron to hole regime. The charge carrier density in graphene can be controlled by applying a gate voltage V_g which effectively shifts the Fermi energy E_F in the dispersion relation. The ambipolar electric field effect in single-layer graphene is illustrated in figure 2.2. The resistance is influenced by the electrostatic gating, since it depends on the number of available electronic states at the Fermi level. As a reflection of the band structure, this density of states is linear in graphene and vanishingly small at the Dirac point. Due to the symmetry of the cone-shaped bands, as shown in the insets of figure 2.2, graphene exhibits electron-hole symmetry. Thus, at the same energetic distance from the band crossing, the charge carrier densities of electrons and holes are expected to be equal. When E_F is located exactly at the Dirac points, the resistance reaches its maximum at the charge neutrality point (CNP), im-

plying that the concentration of electrons and holes are equally small. In addition, graphene's small density of states at the Dirac point results in an extremely small electronic heat capacity. Although graphene exhibits exceptionally high phononic thermal conductivity, the electron system is extremely well thermally isolated due to the low carrier density, single atomic thickness and low electron-phonon coupling.[53,54] These properties make graphene ideally suited for very high sensitivity bolometers and calorimeters, as discussed in chapter 2.3.1.[53,55]

The gate voltage sweep contains valuable information which can be used to assess the device quality of a graphene sample. First of all, the CNP will be shifted away from 0 V by charged impurities and doping. The voltage at which the CNP appears (V_{CNP}) is therefore a good indication of the level of doping in the graphene. Secondly, the shape and steepness of the CNP peak are a representation of the charge carrier mobility μ, which is the most prominent device quality factor. In absence of an external magnetic field, by assuming a constant mobility and neglecting different phenomena such as ballistic transport effects and quantum capacitance,[56] the Drude model can be employed to describe the resistivity of a graphene device

$$\rho_{\boldsymbol{B}=0} = \frac{1}{en\mu}, \tag{2.6}$$

with the elementary charge e, the mobility μ and the charge carrier density n. In good approximation, the field effect induced charge carrier density can be calculated by using

$$n = \frac{C_{\mathrm{g}}}{e}\left(V_{\mathrm{g}} - V_{\mathrm{CNP}}\right) + n^{*}, \text{with} \quad C_{\mathrm{g}} = \frac{\kappa\epsilon_0}{t_{\mathrm{i}}}, \tag{2.7}$$

where the gate capacity C_{g} is given by κ as the relative permittivity, ϵ_0 the vacuum permittivity and t_{i} the thickness of the gate-separating insulating layer. The residual charge carrier density n^{*} generated by charged impurities at the graphene-insulator-interface is typically in the order of a few $10^{11}\,\mathrm{cm}^{-2}$ and can be even as low as $10^{9}\,\mathrm{cm}^{-2}$ for high-quality graphene devices.[57–59] Details on the theoretical framework of n^{*} can be found in the works by Adam *et al.* and Gosling *et al.* where the effect of charged impurities on graphene transport are discussed.[56,60]

Hexagonal boron nitride and van der Waals heterostructures

As presented above, the transport characteristics of graphene samples depend on μ and n^{*}, which in turn are significantly influenced by the immediate interface to the surrounding environment. The use of SiO_2 substrates for graphene has shown to be inferior due to the surface roughness, charged impurities and surface phonons.[61,62] In 2010, Dean *et al.* identified hexagonal boron nitride as an ideal candidate in the search for a better substrate for graphene.[63] Since then, the quality of graphene devices has been massively improved by encapsulating graphene with hexagonal boron nitride.[59,64–67]

With strong in-plane bonds and weak van der Waals (vdW) interactions between layers, hexagonal boron nitride (hBN) is a layered two-dimensional material like graphite. A single layer of hBN is, similar to graphene, an atomically flat sheet with a hexagonal lattice but with alternating boron and nitrogen atoms at the A and B sites of the triangular sublattices, as shown in figure 2.3 a). Because these two elements are neighbors to carbon in the periodic table, the hBN lattice constant is only $\sim 1.8\,\%$ larger compared to graphene. The big difference to graphene lies in the electronic properties of hexagonal boron nitride. Due to the asymmetric potential energy distribution of the boron and nitrogen sites, hBN exhibits a large bandgap of $\sim 6\,\mathrm{eV}$ and is therefore considered an insulator.[68] Because of the optical appearance of its bulk crystals, hBN is also referred to as "white graphene".[69]

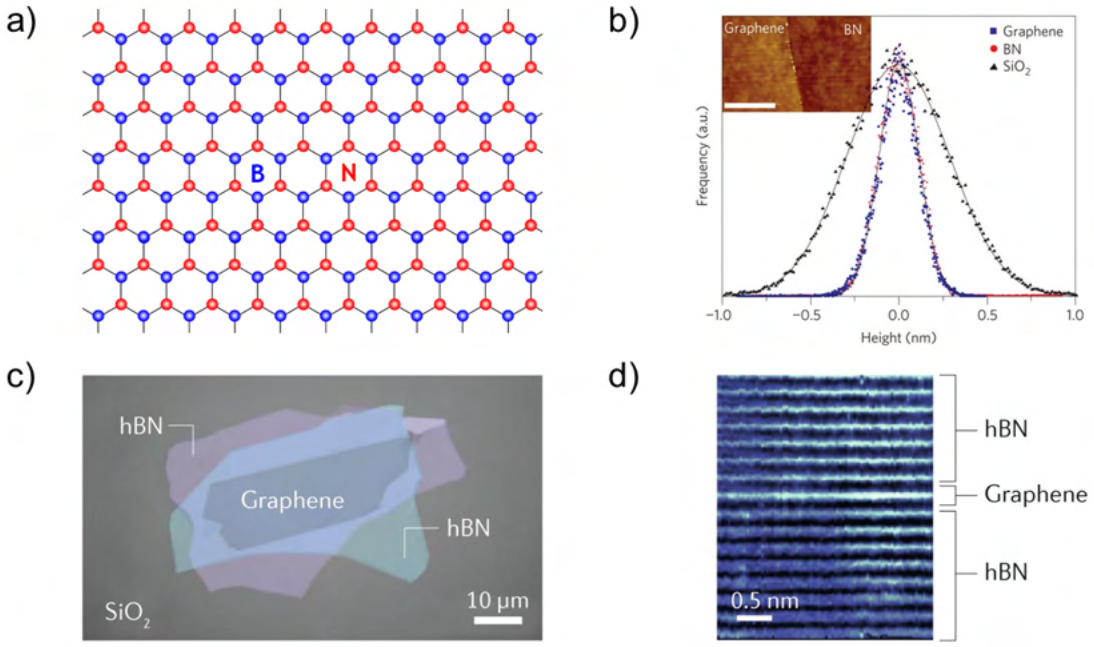

Figure 2.3.: a) Lattice structure of hexagonal boron nitride (hBN), with alternating boron (blue) and nitrogen (red) atoms at the A and B sites of the triangular sublattices. b) Histogram of the height distribution measured by atomic force microscopy (AFM), showing a greater surface roughness for SiO_2 (black triangles) compared to hBN (red circles) and graphene on hBN (blue squares). c) Optical microscope image of a very clean multilayered heterostructure of graphene encapsulated by two hBN layers. d) High-resolution transmission electron microscope image verifying the atomically sharp and impurity-free interfaces of the hBN-graphene-hBN heterostructure. Figure b) adapted with permission from Dean, C., Young, A., Meric, I. *et al.* Boron nitride substrates for high-quality graphene electronics. Nature Nanotech 5, 722–726 (2010). Copyright 2010 Springer Nature.[63] Figures c) and d) are adapted with permission from Yankowitz, M., Ma, Q., Jarillo-Herrero, P. *et al.* van der Waals heterostructures combining graphene and hexagonal boron nitride. Nat Rev Phys 1, 112–125 (2019). Copyright 2019 by Springer Nature.[70]

Typically, a layer of hBN is utilized to pick up subsequent layers with the help of vdW forces to form a stack of 2D materials.[6,71] In contrast to conventional 3D crystals such as silicon, germanium or gallium arsenide, vdW heterostructures come without the need for stringent epitaxial lattice matching. Instead, it is possible to combine materials with different crystal symmetry, structure and lattice parameters.[6]

Early on, it became clear that hBN-graphene heterostructures show a significantly smaller surface roughness compared to graphene devices on SiO_2. For comparison, a histogram of the height distribution, i.e., the surface roughness of graphene on hBN (blue squares), hBN only (red circles) and SiO_2 (black triangles) is shown in figure 2.3 b).[63] The atomically flat surface of hBN allows to assemble ultraclean hBN-graphene-hBN heterostructures with atomically sharp and impurity-free interfaces, as shown in figure 2.3 c) and d).[66,70] Apart from reducing the surface roughness, a layer of hBN separates the graphene from the silicon oxide surface that has charged impurities, leading to less charge inhomogeneity. This beneficial effect can be even enhanced by inserting a thin layer of graphite for additional screening below the bottom hBN. The dielectric constant $\epsilon_r \sim 3-4$ and the dielectric breakdown field of ~ 0.7 V/nm of hBN are excellent properties to enable electrostatic gating of the graphene layer by metal or graphite gates.[72,73] Such high-quality graphene devices with drastically enhanced mobilities that exhibit fragile fractional quantum Hall states[74] became possible because of breakthroughs in device fabrication engineering, which will be discussed in detail in section 3.1.

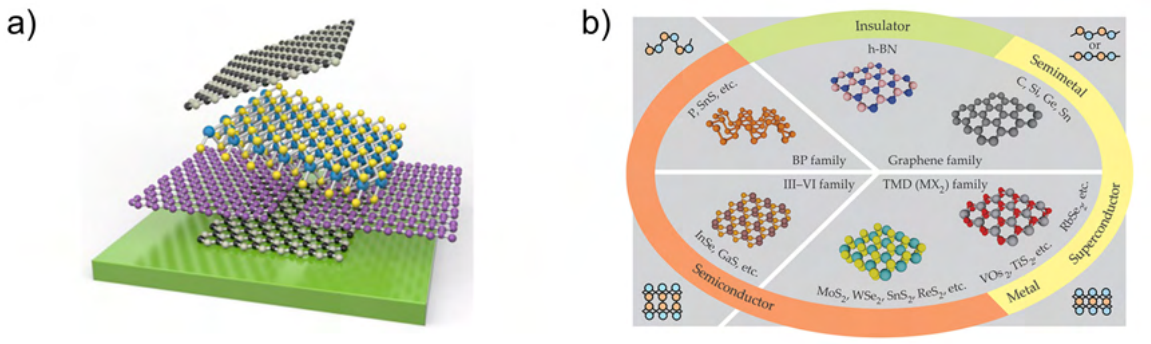

Figure 2.4.: a) Schematic assembly of different 2D crystals to form a van der Waals heterostructure. b) The extensive range of van der Waals materials can be categorized into distinct families based on their electronic properties and crystal structure. Figure a) adapted from Sander *et al.* (2017) under terms of the Creative Commons CC BY license.[75] Figure b) adapted with permission from P. Ajayan, P. Kim, K. Banerjee; Two-dimensional van der Waals materials. Physics Today 1 September 2016; 69 (9): 38–44. Copyright 2016 by AIP Publishing.[5]

Along with improved graphene device quality, the incorporation of hBN into sample processing had an enduring impact on two-dimensional material research and condensed matter physics. Starting with graphene-hBN heterostructures, it enabled the direct assembly of all

types of two-dimensional materials into vdW heterostructures, as shown in figure 2.4 a).[3–5] These structures allow for the selection of individual layers from a diverse range of vdW crystals with distinct properties, as illustrated in figure 2.4 b). The different vdW materials can be classified in families regarding their elemental composition, crystal structure and electrical properties.[5] Next to graphene and hBN, currently the most important are the transition-metal dichalcogenides (TMDs or MX_2). In this material group, a transition-metal atom (M) is combined with two atoms (X_2) from the chalcogenides. In contrast to graphene and hBN, which are semi-metallic and insulating, respectively, TMDs such as MoS_2 or WSe_2, are mostly semiconducting with a wide range of bandgaps and intriguing physical properties.[76] The possibility to combine various TMDs in a vdW heterostructure has led to remarkable discoveries such as the fractional quantum anomalous Hall effect.[77,78]

Twisted bilayer graphene

The high degree of variability of the vdW layer assembly leads to a new degree of freedom, which was impossible to access with conventional materials: the interlayer twist angle. The possibility to tune the crystallographic orientation between the layers with high precision resulted in the discovery of unconventional superconductivity and other phenomena in twisted bilayer graphene (TBG) by Cao *et al.* in 2018.[24,25] This discovery came as a big surprise because the individual graphene mono- and bilayers had been thoroughly investigated at the time and showed no signs of the effects in TBG. This illustrates the allure of the field of twistronics where the electronic properties of vdW materials can be manipulated by the twist angle θ.[79] Analogous to the plethora of different vdW heterostructures, numerous interesting observations have been made in the field of twistronics with different vdW materials. Since the focus of this thesis lies in the investigation of hybrid superconductor graphene devices, only a brief overview of twist angle physics in TBG follows.

To understand the influence of the interlayer rotation angle θ on the electronic properties of twisted bilayer graphene, we will first consider normal bilayer graphene, where two graphene monolayers are positioned on top of each other without any rotation. Bilayer graphene appears naturally in a Bernal AB-stacking configuration as shown schematically in figure 2.5 a). In contrast to the AA-stacking, where two sheets sit exactly on top of each other, in an AB-stacking one of the sheets is slightly translated in one lateral direction. Thus, atoms from sublattice A of the upper layer are positioned directly on top of atoms from sublattice B of the lower layer, as indicated by the yellow arrows. The atoms from sublattice B of the upper layer are located above the center of the hexagons of the lower layer (dashed yellow arrow). This stacking configuration results in a modified band structure with parabolic bands which touch when both layers are energetically equal. In contrast to monolayer graphene, a perpendicular electric field $\boldsymbol{E}$, generally referred to as displacement field, can induce a band gap Δ in bilayer graphene,

as shown in figure 2.5 b).[80] The possibility to induce a band gap and effectively suppress conductivity, in conjunction with the renowned properties of graphene, such as high charge carrier mobility, as well as valley and spin degrees of freedom, renders bilayer graphene highly appealing for various applications. Bilayer graphene quantum dots have been proposed as spin qubits candidates[48] early after the discovery of graphene and have been recently coupled to a microwave resonator.[81]

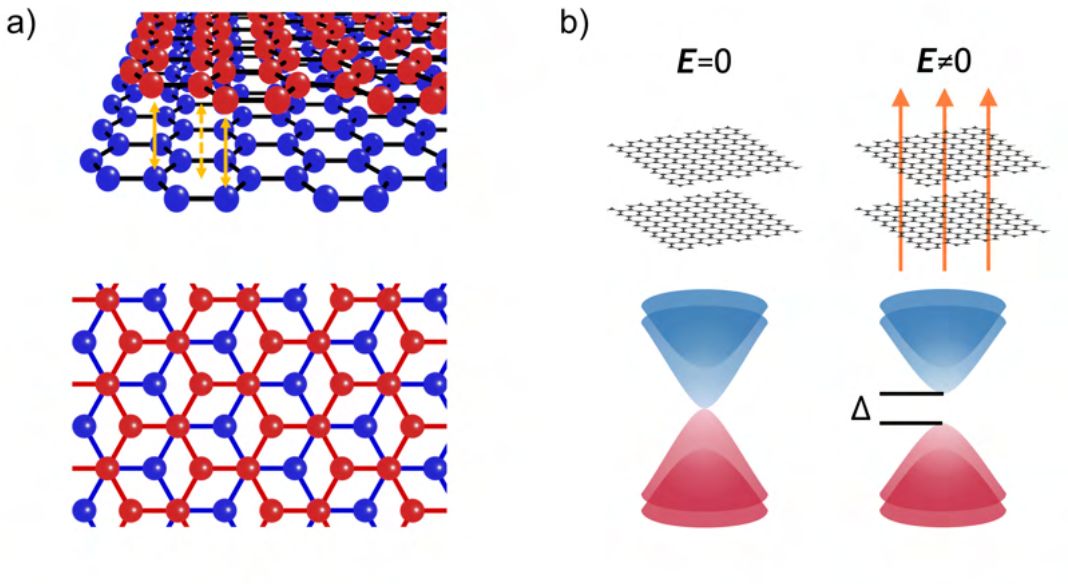

Figure 2.5.: a) Schematic representation of the Bernal AB-stacking configuration of bilayer graphene. b) Left: In equilibrium ($\boldsymbol{E} = 0$), the parabolic bands of bilayer graphene touch. Right: Upon the application of a perpendicular displacement field ($\boldsymbol{E} \neq 0$), it is possible to open up a band gap Δ.

In the case of twisted bilayer graphene, the two graphene sheets are misaligned by a twist angle θ, resulting in the emergence of a geometric interference pattern known as the moiré pattern, illustrated in figure 2.6 a). The appearance of the moiré pattern yields a superlattice potential of periodic regions with the same stacking order. To describe the resulting superlattice structure, the rotation between the sheets is defined as a change of the lattice vector $\vec{L}(m,n)$ to $\vec{L}'(m,n)$, where *m* and *n* are coordinates with respect to the lattice vectors $\vec{a}_1$ and $\vec{a}_2$[82]

$$\vec{L}(m,n) = m\vec{a}_1 + n\vec{a}_2. \tag{2.8}$$

For commensurate rotations, a superlattice vector $\vec{L}(m,n)$ exists, that brings a point in the structure on itself, fulfilling the condition for commensurability[83]

$$\cos(\theta) = \frac{n^2 + 4nm + m^2}{2\left(n^2 + nm + m^2\right)}. \tag{2.9}$$

Considering only structures with one moiré pattern per unit cell given by $|m - n| = 1$, we obtain the simplified equations

$$\cos(\theta) = \frac{3n^2 + 3n + 1/2}{3n^2 + 3n + 1} \text{ and } \vec{L} = n\vec{a}_1 + (n+1)\vec{a}_2. \tag{2.10}$$

The area A_M and number of atoms per moiré unit cell N_M can be obtained by

$$\begin{aligned} A_\mathrm{M} &= \frac{\sqrt{3}}{2}\lambda_\mathrm{M}^2 = \frac{\sqrt{3}}{8}\frac{a^2}{\sin^2(\theta/2)}, \\ N &= 4\left(3n^2 + 3n + 1\right) \end{aligned} \tag{2.11}$$

with the moiré wavelength $\lambda_\mathrm{M} = |\vec{L}|$. As the twist angle θ decreases, A_M and N_M increase drastically, resulting in $N_\mathrm{M} \sim 10^4$ atoms for small angles around 1°. Compared to monolayer or Bernal bilayer graphene, this very large number of atoms complicates the calculations with the tight binding model for moiré systems, as they become computationally demanding.

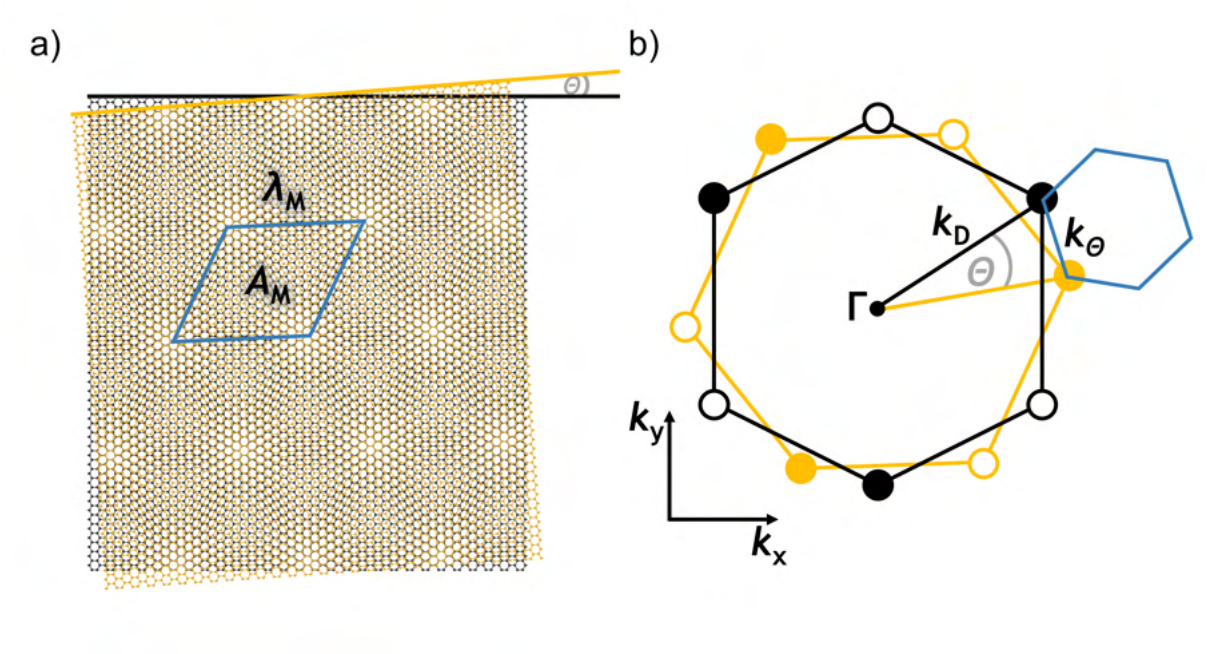

Figure 2.6.: a) Moiré pattern of twisted bilayer graphene (TBG) with twist angle θ (here 4 ° for better visibility). The superlattice unit cell (blue) with area A_M and moiré wavelength λ_M, which is in the order of 10 nm for small θ. b) Representation of the moiré pattern in reciprocal space with the original Brillouin zones of the two graphene layers (black and yellow) and the mini Brillouin zone (blue) with moiré wave vector k_θ.

This issue can be circumvented by describing the electronic structure of twisted bilayer graphene at low momentum and energies in a continuum approximation.[82,83] The rotation of the two graphene layers in real space also leads to a rotation of the reciprocal lattices. Considering a rotation around the Γ point, the difference between the *K* points of the original lattice is given by the moiré wave vector

$$k_\theta = 2\sin(\theta/2)k_\mathrm{D} \tag{2.12}$$

with the magnitude of the Dirac point wave vector $k_\mathrm{D} = 4\pi/3a$.[84] Using k_θ, a new mini Brillouin zone can be defined, as shown in figure 2.6 b), that also forms a superlattice in reciprocal space. The K_s points of this superlattice are a combination of *K* and *K'* points of opposite lattices. However, the large difference in momentum that exists in the original graphene Brillouin zone protects the valley degeneracy, resulting in an inherited four-fold degeneracy also in TBG.[85] The superlattice carrier density n_s for a completely filled mini Brillouin zone is then given by

$$n_s = 4/A_\mathrm{M} = 4\frac{8\sin^2(\theta/2)}{\sqrt{3}a^2} \approx \frac{8\theta^2}{\sqrt{3}a}\,(\text{for small }\theta)\,. \tag{2.13}$$

In experiments, this relation is useful to extract the twist angle of the investigated sample.[24,25,85]

The twist angle of TBG can be considered as a tuning knob for the electronic properties as illustrated in figure 2.7, which shows the evolution of the band structure in momentum space [figure 2.7 b)] with respect to the interlayer twist in real space [figure 2.7 a)]. Initially, at large twist angles, the band spectrum of TBG can be described by two almost decoupled monolayer Dirac cones, only very weakly affected by the moiré pattern. When θ decreases, the cones at each valley move closer together in momentum space and start to hybridize. In 2011, Bistritzer and MacDonald found, that the bands of TBG mostly depend on a single factor

$$\alpha = \frac{w}{\hbar v_\mathrm{F} k_\theta}, \tag{2.14}$$

where w is the interlayer hopping energy.[84] The parameter α describes the competition between the hybridization of the Dirac cones, expressed by w, and the kinetic energy of the electrons, expressed by $\hbar v_\mathrm{F} k_\theta$. As introduced above, for a decreasing twist angle, the increasing hybridization is expected since $w \propto k_\mathrm{D} \propto \theta$, while the kinetic energy becomes smaller as k_θ decreases. This leads to a drastic renormalization of the effective Fermi velocity $v^\star$

$$\frac{v^\star}{v} = \frac{1-3\alpha^2}{1+6\alpha^2}. \tag{2.15}$$

At particular angles, the Dirac cones flatten and converge to zero energy. This situation is

shown on the right in figure 2.7, where ultraflat bands appear in the dispersion relation of TBG. At this twist angle, the renormalized Fermi velocity approaches zero and all electrons in these flat bands have almost the same energy. As a result, the density of states for these bands is extremely large. The twist angles for which these effects are expected to appear are referred to as *magic angles*. The first magic-angle condition is found for $\alpha = 1/\sqrt{3}$ which corresponds to a twist angle of

$$\theta = \arcsin\left(\frac{\sqrt{3}w}{\hbar v_{\mathrm{F}} k_{\mathrm{D}}}\right) \cdot 2 \approx 1.1^{\circ}. \tag{2.16}$$

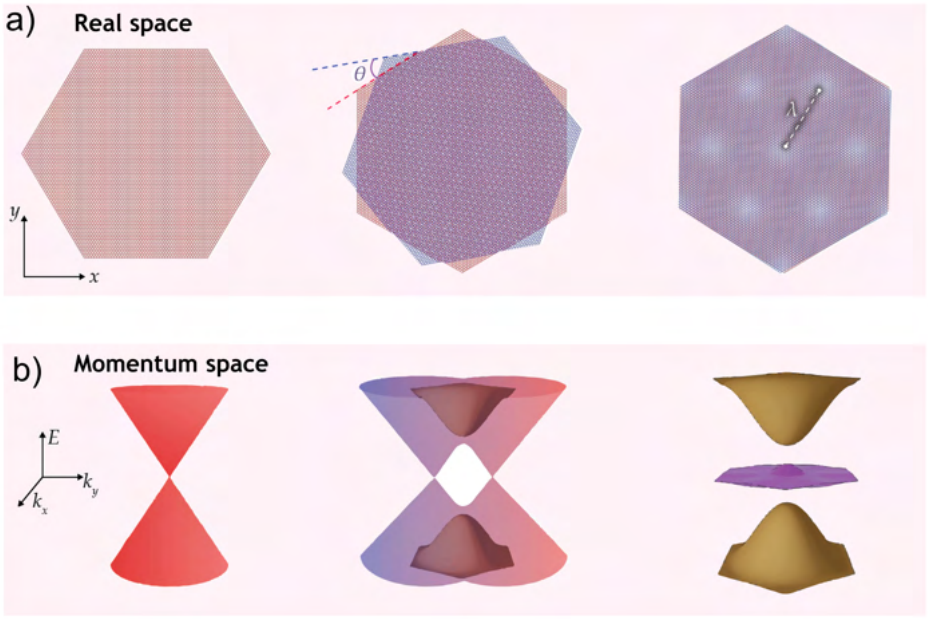

Figure 2.7.: Representation of TBG in real space a) and momentum space b). Starting at large twist angles, the band structures of the two graphene layers are almost decoupled and behave like two single Dirac cones of monolayer graphene (left). In TBG with a smaller twist angle, the bands hybridize progressively (middle). At the so-called magic angle, the pronounced moiré pattern leads to hybridized bands that form ultraflat bands with distinct properties (right). Figure adapted from B. Andrei Bernevig, Dmitri K. Efetov; Twisted bilayer graphene's gallery of phases. Physics Today 1 April 2024; 77 (4): 38–44. Copyright 2024 by AIP Publishing.[26]

Bilayer graphene that is twisted by this angle was found to host a plethora of exotic phenomena and is now known as magic-angle twisted bilayer graphene (MATBG).[24,25] The rich physics of MATBG originates from its flat band properties. Due to the combination of a very low Fermi velocity and a high density of states, the electron-electron interactions are extraordinarily enhanced. In addition, the bands appear to be topological, which means that the sample edges can be conductive, while the inside behaves as an insulator.[26] As a result, MATBG revealed ex-

otic phases such as correlated and Chern insulator states,[25,86] superconductivity,[24,87] a so-called strange-metal phase[88] and orbital magnetism.[87,89] Remarkably, these phases can coexist in a single device and are tunable by experimental parameters like electrostatic gating.

In MATBG, the gate voltage allows control over the filling factor of the flat band ν, which is defined as the number of electrons per moiré lattice site. Due to the four-fold degeneracy, the flat band is completely filled for $\nu = \pm 4$ electrons or holes. Unexpectedly, it has been observed, that the flat bands are not filled simultaneously and continuously.[90] Instead, the bands undergo a symmetry breaking phase transition every time an integer filling factor $\nu = \pm 1, 2, 3$ is reached. At these transitions, one band is filled completely, while the other bands are emptied. Until the flat bands are filled, these transitions reappear at every integer value of ν.[90]

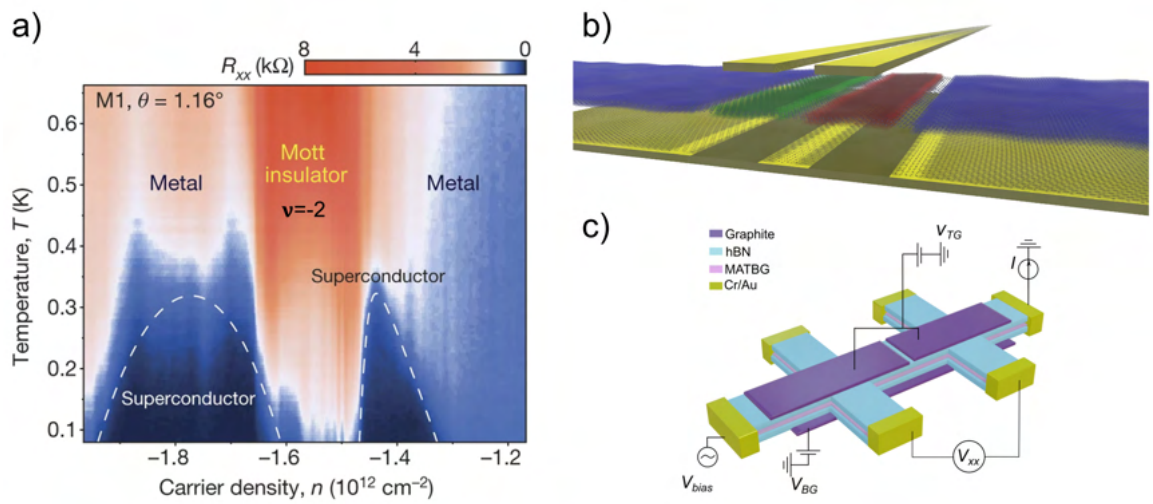

Figure 2.8.: a) Figure from the original article by Y. Cao *et al.* showing the resistance versus temperature behavior of MATBG ($\theta = 1.16°$) close to the correlated insulator state at half filling $\nu = -2$. Two superconducting domes appear in close vicinity to the insulating state, which transition into a metallic state at temperatures above 0.3 K.[24] b) MATBG offers a highly tunable system that can be insulating, metallic or superconducting, depending on the electrostatic gating, while avoiding material interfaces.[91] c) Schematic of a MATBG device with two separated top gates, which are utilized to form a MATBG Josephson junction.[92]Figure a) adapted with permission from Cao, Y., Fatemi, V., Fang, S. et al. Unconventional superconductivity in magic-angle graphene superlattices. Nature 556, 43–50 (2018). Copyright 2018 Springer Nature.[24] Figure b) adapted with permission from Prance, J.R., Ben Shalom, M. Building devices in magic-angle graphene. Nat. Nanotechnol. 16, 745–746 (2021). Copyright 2021 Springer Nature.[91] Figure c) adapted from Díez-Mérida *et al.* (2023).[92]

The groundbreaking experiments by Y. Cao *et al.* in 2018 revealed that at one particular phase

transition at half filling $\nu = \pm 2$ MATBG enters a correlated insulator phase, which is consistent with a Mott-like insulator that is driven by strong electronic interactions.[25] This state with high resistance is depicted in figure 2.8 a) as the red area in the center at $\nu = -2$ in the hole regime. If the carrier density in the system is doped slightly away from this state, two regions appear on either side where the resistance drops to zero. These regions show signs of superconductivity up to roughly 0.3 K, before they turn metallic at higher temperatures.[24] The appearance of the superconducting regime upon doping from a Mott-like insulating state is reminiscent of unconventional superconductivity as known from cuprates. The mechanism of superconductivity in MATBG is still under debate, although an electron-phonon mediated mechanism in the classical sense seems improbable. The concepts of conventional and unconventional superconductivity will be introduced in more detail in section 2.2.

The ability to move between insulating, metallic and superconducting phases by electrostatic gating makes MATBG a highly tunable system. In contrast to conventional approaches, multiple electric components can be realized in principle within the same material, thereby avoiding interfaces which typically are a source of performance loss.[91] A schematic representation of MATBG's versatility is shown in figure 2.8 b). Gate electrodes (yellow) on top and bottom of MATBG can induce insulating, metallic and superconducting states (red, green and purple) in the system. Multiple research groups have experimentally demonstrated highly tunable MATBG devices in the form of single-electron transistors,[93] Josephson junctions,[92–94] which will be discussed in detail in section 2.2, and even more complex structures.[95] For MATBG Josephson junctions devices, as depicted schematically in figure 2.8 c), two separated topgates are used in combination with the backgate to realize two superconducting regions in the device, separated by a small non-superconducting junction.[92]

After the initial discovery in MATBG, superconductivity and other correlated phases have also been observed in many other twisted moiré systems but also surprisingly in *untwisted* Bernal bilayer[96–98] and rhombohedral trilayer graphene.[99] Although these systems were studied before, the existence of such phases was probably masked by insufficient sample quality or unsuitable temperatures and fields.[96] Research is still at the beginning to determine the similarities and differences between correlated phenomena of twisted and untwisted systems. However, these findings suggest that graphene bi- and trilayers possess a nontrivial phase diagram with rich physics yet to explore.

2.2. Superconductivity in Graphene

The phenomenon of superconductivity was first discovered in 1911 by Kamerlingh Onnes in mercury.[100] Below their critical temperature T_c, superconducting materials not only behave as perfect conductors with zero resistance, but also as perfect diamagnets that expel an external magnetic field from their interior. The latter effect, discovered by Meissner and Ochsenfeld in 1933,[101] persists in so-called type-I superconductors (SC) up to their critical magnetic field H_c. The thermodynamic description of the critical field as a function of temperature is given by[102]

$$H_\mathrm{c}(T) = H_\mathrm{c}(0)\left[1 - \left(\frac{T}{T_\mathrm{c}}\right)^2\right]. \tag{2.17}$$

Due to the perfect conductivity, spontaneously generated currents that oppose the magnetic field are created at no energy cost in the superconductor to expel the magnetic field. The behavior of SCs in electric and magnetic fields is described by the London equations.[103]

$$\frac{d\vec{j}_\mathrm{s}}{dt} = \frac{n_s e^2}{m_\mathrm{e}}\vec{E} \tag{2.18}$$

$$\nabla \times \vec{j}_\mathrm{s} = -\frac{n_s e^2}{\mu_0 m_\mathrm{e}}\vec{B} \tag{2.19}$$

with the superconducting current density of the SC $\vec{j}_\mathrm{s}$, the local density of superconducting electrons n_s, the elementary charge e and mass m_e of electrons. The second London equation implies that the magnetic field still penetrates a superconductor for a certain distance even in the so-called Meissner state. Applying Ampere's law $\nabla \times \vec{B} = \mu_0 \vec{j}$ to the second London equation yields

$$\nabla^2 \vec{B} = \frac{n_s e^2}{\mu_0 m_\mathrm{e}}\vec{B} = \frac{1}{\lambda_L^2}\vec{B}. \tag{2.20}$$

Here, the characteristic length the magnetic field is able to enter the SC is expressed by the London penetration depth λ_L at zero temperature

$$\lambda_\mathrm{L} = \sqrt{\frac{m_\mathrm{e}}{\mu_0 n_\mathrm{s} e^2}} \tag{2.21}$$

This length is temperature dependent and can empirically be approximated by

$$\lambda_\mathrm{L}(T) = \lambda(0)\sqrt{1 - \left(\frac{T}{T_\mathrm{c}}\right)^4} \tag{2.22}$$

Experimental observations of superconductors that do not follow the Meissner-Ochsenfeld

effect led to an extension of the London equations to the Ginzburg-Landau (GL) theory. This theory describes SCs that screen a magnetic field at small fields below a critical field H_{c1} but allow a magnetic field to penetrate the interior of the SC in the form of vortices before returning to the resistive state at a higher critical field H_{c2}. The flux of each vortex is quantized to the superconducting flux quantum $\Phi_0 = \frac{h}{2e}$. As a result, these so-called type-II SCs reach far higher critical magnetic fields compared to type-I SCs. Based on Landau's quantum mechanical theory of phase transitions, the GL theory introduces an order parameter Ψ based on a macroscopic pseudowavefunction to describe the superconducting state. Due to the phase-locked state of the ensemble of superelectrons, the macroscopic wave function of a superconductor can be written as

$$\Psi = |\Psi| e^{i\theta}. \tag{2.23}$$

The order parameter Ψ represents the local density of superconducting electrons $n_s = |\Psi|^2$.[102,104]

A successful microscopic theory to explain superconductivity is the BCS theory, named after its developers Bardeen, Cooper and Schrieffer.[105] The main concept of the BCS theory is that SCs have a band gap, in which not single electrons, but rather *pairs* of electrons carry the current. These electron pairs form in the presence of a small phonon-mediated attractive interaction and have been conceptualized by L. Cooper in 1956 and are therefore named Cooper pairs.[106] These Cooper pairs behave as effective bosons with an integer spin. Cooper pairs consist of two electrons with opposite momentum and can be described as two identical fermions in time-reversed momentum states. A property of the wave function of such a pair of fermions must be antisymmetric regarding spin and spatial components if the fermions are exchanged. Thus, the pair states of a Cooper pair can either be spin singlets with an even-parity spatial component or spin triplets with odd parity.[107] When a SC enters its superconducting state, the electrons close to the Fermi energy create a condensate due to the bosonic nature of Cooper pairs.

The condensation of the electrons to Cooper pairs results in a band gap E_g, as shown in figure 2.9 a), which is twice the pairing energy Δ of a Cooper pair and corresponds to the required energy to break a Cooper pair

$$E_g = 2\Delta. \tag{2.24}$$

In the framework of BCS theory, the relation of the superconducting gap Δ and the critical temperature T_c is approximately

$$\Delta \approx 1.764 k_B T_c, \tag{2.25}$$

with the Boltzmann constant k_B.[104] The size of a Cooper pair is given by the coherence length ξ

and depends on the length scale of the pairing potential Δ. The coherence length is particularly important in the case of a non-superconducting material in contact with a SC. Then, the wave function of the SC will penetrate the non-superconducting material and induce superconductivity for the length of ξ in an effect called proximity effect. The wave function of the SC exponentially decays over ξ in the non-superconducting material, as shown in figure 2.9. The proximity effect is the basis for the tunneling of Cooper pairs. The coherence length depends on Δ of the superconducting material and of the Fermi velocity v_{F} of the proximitized material

$$\xi = \frac{\hbar v_{\mathrm{F}}}{\pi \Delta}. \tag{2.26}$$

The BCS theory successfully describes superconductivity in many classical superconductors through a phonon-mediated Cooper pairing mechanism. However, it is important to note that many SCs discovered towards the end of the 20th century and beyond do not conform to the BCS theory. In particular, high-T_{c} superconductors, such as cuprates ($T_{\mathrm{c}} > 70\,\mathrm{K}$),[108] exhibit superconductivity that is generally classified as *unconventional*. While conventional SCs are well described by BCS theory, the attractive potential responsible for Cooper pair formation in unconventional SCs appears to arise from electron-electron interactions.[109] Additionally, unlike conventional SCs, which typically exhibit an isotropic superconducting wave function with *s*-wave symmetry, unconventional SCs often possess an anisotropic wave function.[107] Due to the multitude and complexity of their anomalous behavior, a comprehensive theory to explain unconventional superconductivity remains elusive. As mentioned in section 2.1, the various phases observed in MATBG are also found in certain high-T_{c} superconductors. Compared to these materials, MATBG is a simpler system, consisting solely of carbon atoms. Consequently, MATBG could serve as an ideal platform for gaining deeper insights into unconventional superconductivity, that may be extended to understand other superconductors.

Josephson junctions

In addition to flux quantization, the collective quantized behavior of SCs manifests itself on a macroscopic scale in the form of the Josephson effect. This phenomenon is observed when a non-superconducting material or weak link separates two superconducting regions, as illustrated in figure 2.9 b). If the barrier is thin enough, the macroscopic wave functions of both SCs overlap and form a weakly coupled system, called Josephson junction (JJ). The two superconducting electrodes will differ in phase, as they are not directly connected. Cooper pairs that tunnel coherently from one electrode to the other result in a superconducting tunnel current, which was first theoretically described by B. Josephson in 1962.[110] The supercurrent flowing through a JJ is given by the first Josephson equation

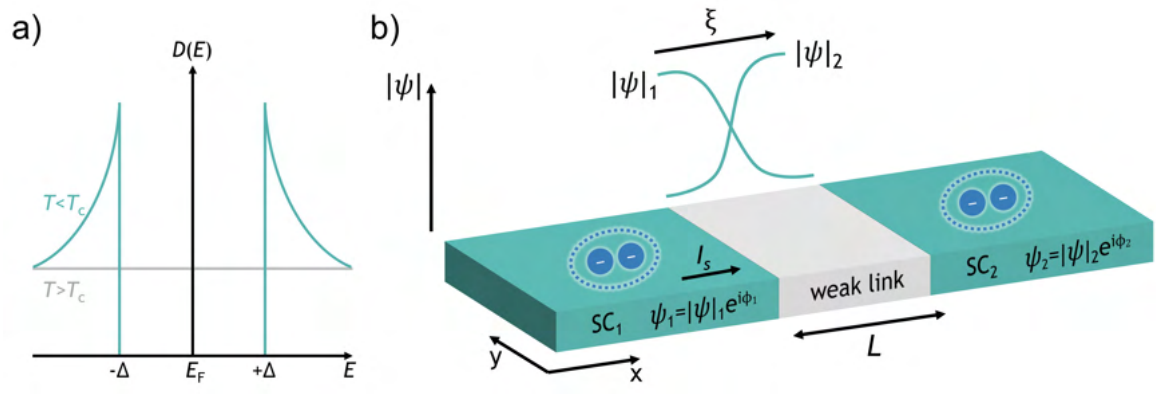

Figure 2.9.: a) In contrast to the normal state ($T > T_c$) (grey), the density of states in the superconducting state ($T < T_c$) (green) exhibit a bandgap of 2Δ around the Fermi energy E_F. b) Schematic of a Josephson junction (JJ) which consists of two superconducting electrodes (SC_1 and SC_2) separated by a non-superconducting weak link with length L. Due to the proximity effect, the macroscopic wave functions of the two superconductors overlap and Cooper pairs tunnel across the JJ.

$$I_s(\phi) = I_c \sin(\phi), \tag{2.27}$$

which is also known as the DC Josephson effect or current phase relation. Here, I_c is the critical current of the junction and ϕ the gauge invariant phase difference $\phi = |\phi_1 - \phi_2|$ of the two electrodes, with phases ϕ_1 and ϕ_2. The second Josephson equation gives an expression for the voltage across a JJ that depends on the phase difference over time, which is known as the AC Josephson effect[110]

$$V(t) = \frac{\Phi_0}{2\pi}\frac{d\phi}{dt}. \tag{2.28}$$

Combining the two Josephson equations Eq. 2.27 and Eq. 2.28 results in

$$I_s = I_c \sin\left(\frac{2\pi}{\Phi_0} V \cdot t\right), \tag{2.29}$$

which implies that a DC voltage applied to the JJ will produce an alternating current in the junction. In turn, when the JJ is irradiated with microwave frequency ν, a DC voltage is induced for multiples of $V = \frac{n\hbar\nu}{2e}$, with integer values for n. This leads to the so-called Shapiro steps in the current-voltage behavior of the JJ.

Graphene Josephson junctions

Weak links forming the JJ can be made of different materials, which determine its properties. Insulators form superconducting-insulating-superconducting (SIS) junctions while JJs of nor-

mal metals are referred to as superconducting-normal-superconducting (SNS) junctions. The weak link can also consist of van der Waals materials such as graphene, leading to a graphene Josephson junction (GJJ) that consists of a superconducting-graphene-superconducting (SGS) interface. The physics of SGS JJs can be assessed by classifying different regimes, depending on the relevant length scales: diffusive/ballistic, long/short and dirty/clean. A GJJ is considered ballistic when the junction length L is shorter than the mean free path l_{mfp} of charge carriers in graphene. For ballistic GJJs the coherence length is given by $\xi = \hbar v_{\text{F}}/\Delta$. If $l_{\text{mfp}} < L$, the junction is in the diffusive regime and the coherence length is modified to $\xi = \sqrt{\hbar D/\Delta}$, with the diffusion constant $D = v_{\text{F}} l_{\text{mfp}}/2$.[111] Depending on the coherence length, a GJJ is considered to be in the long junction regime if $\xi < L$. Vice versa, if $\xi > L$ a junction is short.[31,111] Comparing the coherence length to the mean free path determines whether a junction is clean ($\xi < l_{\text{mfp}}$) or dirty ($\xi > l_{\text{mfp}}$). As the smallest energy scale determines the behavior of the system, it is important to note that for long junctions the Thouless energy $E_{\text{th}} < \Delta$, with $E_{\text{th}} = \hbar D/L^2$, is the dominating factor. For short junctions, where $E_{\text{th}} > \Delta$, the behavior of the GJJ is determined by the superconducting gap.

To understand the behavior of GJJs in more detail, it is worth looking at effects of a simple SNS junction. An electron in the metal approaching a single NS interface can undergo different scattering mechanisms, as depicted schematically in figure 2.10 a). If the energy of the electron is smaller than Δ, it cannot enter the SC due to the superconducting gap and undergoes a regular specular reflection. However, the electron can also undergo an Andreev reflection, in which the electron is transmitted into the SC by forming a Cooper pair with another electron of opposite spin and momentum. As a result, a hole of opposite spin and momentum than the incident electron is reflected in the metal. Andreev reflection is a phase coherent process that is strongly dependent on the interface transparency $t = 1/(1 + Z^2)$, with the barrier strength Z.[112] For a perfect contact and fully transparent interface ($Z = 0$, $t = 1$), regular specular reflections are suppressed, whereas Andreev reflections are not possible for large Z, resulting in a regular tunnel barrier.[113]

In a SNS junction, multiple Andreev reflections can occur because of the presence of two NS interfaces. This case is depicted in figure 2.10 b), where a right moving electron undergoes an Andreev reflection at the right NS interface, causing a hole to be reflected. This hole also undergoes an Andreev reflection when reaching the left NS interface, resulting in another right moving electron. This process requires the destruction of a Cooper pair in the left superconductor in order to obey charge, energy, and momentum conservation, while it creates a Cooper pair in the right superconductor. Thus, the phase coherent process of Andreev reflection enables non dissipative Cooper pair transport through a SNS junction. During the two Andreev reflections described above, a phase difference $\Delta\phi$ is accumulated. For the resonance condition, $\Delta\phi$ should be a multiple of 2π, resulting in constructive interference of the two SC wave functions. This

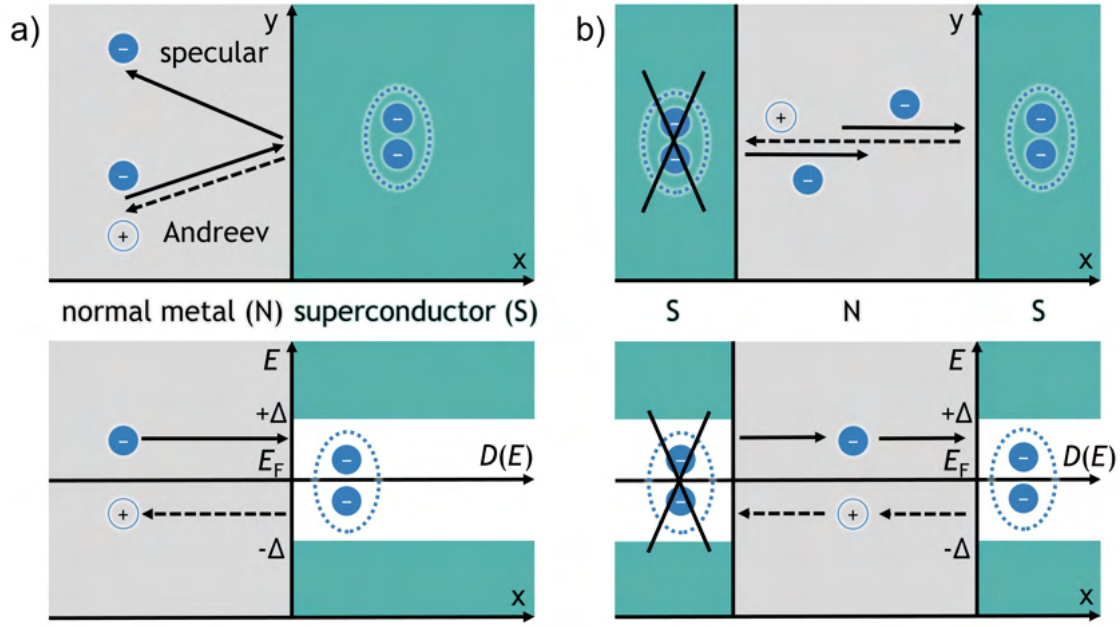

Figure 2.10.: Schematical representation of scattering mechanisms in space (top) and energy (bottom) at a single normal metal (N) (grey) superconductor (S) (green) interface a) and at a SNS junction b). a) Spatial illustration of specular and Andreev reflection of electrons (top). If Andreev reflection occurs, a Cooper pair is created in the superconducting material under the reflection of a hole with opposite spin and momentum in the normal metal. b) A right moving electron undergoes Andreev reflection at the right NS interface. The converted hole undergoes another Andreev reflection itself at the left interface, causing the destruction of a Cooper pair in the left superconductor and an electron moving to the right NS interface again. Such multiple Andreev reflections in a SNS junction lead to the coherent transfer of Cooper pairs across the junction.

leads to the formation of so-called Andreev bound states, which dominate the superconducting transport if the resonance condition is met. In the short junction regime, $\Delta\phi$ corresponds to the phase difference of the two SC wave functions and the Andreev bound state energy E_{ABS} is given by

$$E_{\mathrm{ABS}} = \pm \cos(\Delta\phi/2) \tag{2.30}$$

where two levels ($\pm$) are created for each conductive channel. This implies that discrete states are formed inside the superconducting gap, which carry the supercurrent.

Resistively and capacitively shunted junction model

A Josephson junction can adopt two fundamental states that depend on the experimental conditions. Considering $T < T_{\mathrm{c}}$ and $B < B_{\mathrm{c}}$ of the superconducting material, the carried current

I determines the state of the JJ, as depicted in figure 2.11 a). If $I < I_c$, the junction is in the *zero voltage state*, in which no voltage drops across the junction and the junction resistance R_{JJ} is zero. For currents larger than the critical current, $I > I_c$, the current flowing through the JJ can no longer be carried completely as supercurrent. Instead, Cooper pairs break up into quasiparticles which form an additional normal current I_n. This current $I_n = V/R_{JJ}$ leads to a finite voltage drop across the junction, which is referred to as the *voltage state*.[102] In this normal state, the junction resistance behaves ohmic. The total current by the junction also has contributions of a displacement current $I_d = C_{JJ}\frac{dV}{dt}$, caused by time varying voltage fluctuations and an intrinsic current noise, denoted by I_f. The junction capacitance C_{JJ} can be approximated by using the relative dielectric constant ϵ_r of the weak link with thickness d and area A to obtain $C_{JJ} = \frac{\epsilon_r \epsilon_0 A}{d}$.[104] Using Kirchhoff's law, the total current flowing through a JJ is therefore described by

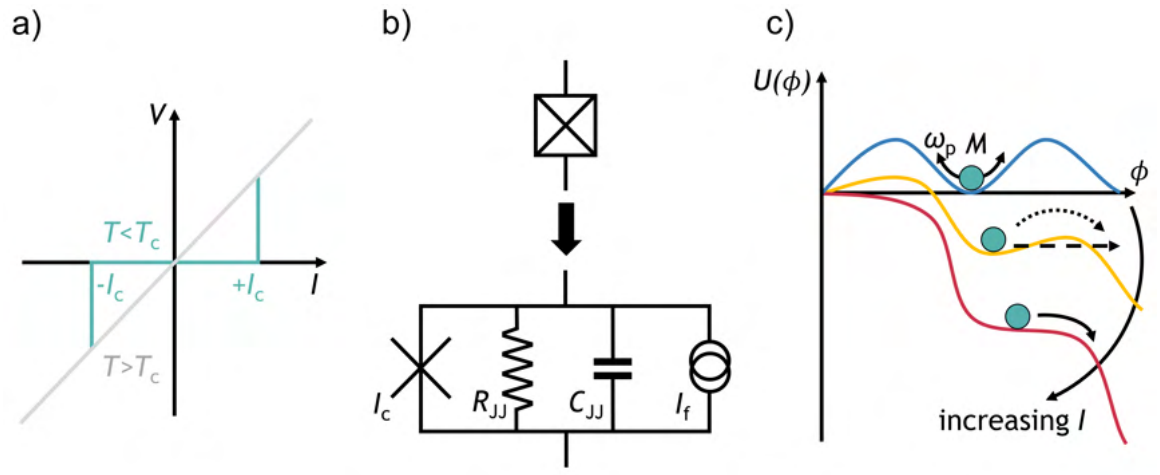

Figure 2.11.: a) A Josephson junction is in the zero voltage state for $T < T_c$ and $I < I_c$, as indicated by the green line. For $T > T_c$, $I > I_c$, the JJ is in the voltage/normal state (grey line). b) Following the RCSJ model, the electronic symbol of a JJ (top) can be represented in a circuit diagram by the characteristic critical current I_c, the junction resistance R_{JJ} and the junction capacitance C_{JJ}. Contributions from intrinsic current noise are accounted for by I_f. c) The behavior of a current-biased JJ can be described by a macroscopic quantum phase particle subjected to the tilted washboard potential in the RCSJ model. The oscillation frequency of the particle around the potential minimum at low current (blue curve) corresponds to the plasma frequency ω_p. For $I < I_c$ (yellow curve), the phase particle can escape the potential well by macroscopic quantum tunneling (dashed arrow) or thermal activation (dotted arrow). When the current is increased even further to $I > I_c$ (red curve), the phase particle is no longer trapped by the potential and escapes, representing the voltage state of the JJ.

$$I = I_\mathrm{s} + I_\mathrm{n} + I_\mathrm{d} + I_\mathrm{f} = I_\mathrm{c}\sin(\phi) + \frac{V}{R_\mathrm{JJ}} + C_\mathrm{JJ}\frac{dV}{dt} + I_\mathrm{f}. \tag{2.31}$$

Here, the supercurrent I_s is described by the first Josephson equation. Using the second Josephson equation, the Eq. 2.31 is modified to

$$I = I_\mathrm{c}\sin(\phi) + \frac{1}{R_\mathrm{JJ}}\frac{\Phi_0}{2\pi}\frac{d\phi}{dt} + C_\mathrm{JJ}\frac{\Phi_0}{2\pi}\frac{d^2\phi}{dt^2} + I_\mathrm{f}. \tag{2.32}$$

Following the equations above, the behavior of a JJ can be described effectively by a parallel circuit representation, shown in figure 2.11 b). This representation is therefore known as the *resistively and capacitively shunted junction* (RCSJ) model, which is presented in more detail below.[102]

By introducing a normalized current $i = I/I_\mathrm{c}$ and neglecting the noise current contribution I_f, it is possible to rewrite Eq. 2.32 to the following differential equation

$$C_\mathrm{JJ}\frac{\Phi_0}{2\pi}\frac{d^2\phi}{dt^2} + \frac{1}{R_\mathrm{JJ}}\frac{\Phi_0}{2\pi}\frac{d\phi}{dt} + \frac{d}{d\phi}[E_\mathrm{J0}(1-\cos\phi - i\phi)] = 0, \tag{2.33}$$

with the Josephson energy

$$E_\mathrm{J} = \frac{\Phi_0 I_\mathrm{c}}{2\pi}(1-\cos\phi) = E_\mathrm{J0}(1-\cos\phi). \tag{2.34}$$

The differential equation in Eq. 2.33 is comparable to the equation of motion for a particle with mass M moving along the coordinate X in a potential U with damping η

$$\begin{gathered} M\frac{d^2X}{dt^2} + \eta\frac{dX}{dt} + \nabla U = 0, \\ \text{with } U(\phi) = E_\mathrm{J0}(1-\cos\phi - i\phi). \end{gathered} \tag{2.35}$$

The potential U is known as *tilted washboard potential* and describes the dynamics of a macroscopic phase difference ϕ of a Josephson junction. This is visualized in figure 2.11 c), in which the tilt of the potential is determined by the current applied to the JJ.

For a very small current $I \sim 0$, the phase particle oscillates in a local potential minimum with the *Josephson plasma frequency* ω_p

$$\omega_\mathrm{p} = \sqrt{\frac{2\pi I_\mathrm{c}}{\Phi_0 C_\mathrm{JJ}}}. \tag{2.36}$$

If the current is increased to values below but close to I_c, the potential is tilted and a finite probability exists, that the particle tunnels through the potential barrier in a process called macroscopic quantum tunneling. The particle can also escape the potential well by thermal activation. When the applied current is increased to values larger than I_c, the phase particle is

no longer trapped in a local potential minimum and escapes. This state represents the voltage state of the JJ.[102] The magnitude of the local potential minimum is determined by the damping, which is correlated to the quality factor Q_{J} of a junction. This is defined as

$$Q_{\mathrm{J}} = \sqrt{\frac{2\pi}{\Phi_0} I_{\mathrm{c}} R_{\mathrm{JJ}}^2 C_{\mathrm{JJ}}} = \sqrt{\beta_{\mathrm{C}}}, \tag{2.37}$$

with the Stewart McCumber parameter β_{C} that is a measure for the damping of a JJ. A weakly damped JJ has a high β_{C} and a high Q_{J}. In turn, a highly damped junction with a low β_{C} has also a low Q_{J}.[102]

The tilted washboard potential and its dependency on the applied current is the key element of the model that can be utilized to assess the current voltage characteristics of a current-biased JJ. The RCSJ model draws a simple picture of the dynamics of a Josephson junction to understand its behavior in quantum information processing or single-photon detection contexts.

2.3. Photosensing with Graphene-based Devices

2.3.1. Graphene-based Josephson Junctions as Photon Detectors

Superconducting photon detectors feature a variety of detection mechanisms. Most of the conventional detectors such as transition edge sensors and superconducting nanowire single photon detectors rely on the photon-induced breaking of Cooper pairs.[114–116] For superconducting nanowire single photon detectors, the excitation of Cooper pairs above the superconducting gap creates a locally expanding hot spot in the superconducting detector material, finally resulting in a resistive switching of the material before returning to its superconducting state. This mechanism has been proven to be very sensitive, enabling the detection of single photons.[116] However, the energy resolution of this mechanism is intrinsically limited by the superconducting gap, which sets a cutoff. To solve this issue, a different detection mechanism is required that creates an energy resolving environment. Instead of just using a superconducting material alone, a promising approach is to combine materials with different properties in the form of a Josephson junction. In the past, it has been revealed that the critical current in SNS junctions is dramatically dependent on the temperature of the electrons in the metal of the weak link.[117,118] An increase in the effective electron temperature leads to a rapid decrease of I_c.

However, the choice of material in the SNS junction is paramount to maximize the sensitivity of such a photon detector. Graphene is an exceptionally well suited material for photon detection applications. As introduced in section 2.1, graphene exhibits a linear band structure without a band gap, which enables broadband absorption of light down to microwave frequencies, which are typically difficult to detect due to their low energy of only a few µeV. Additionally, at the Dirac point of graphene, the density of states is vanishingly small. This results in an extremely low heat capacity and weak electron-phonon coupling. This is combined with the ultrafast electron-electron thermalization timescale of only a few hundred femtoseconds of graphene. Consequently, when a photon is absorbed by the graphene, it is immediately converted to electronic heat that is kept by the electron system since it does not dissipate as fast to phonons.

These properties make graphene Josephson junctions ideally suited for bolometric applications. A bolometer is sensitive to the power of incident photons. As schematically shown in figure 2.12 a), a bolometer is a device in which energy of absorbed photons leads to a heat increase in the material and subsequently to thermally-induced resistance alterations. Upon absorption of photons with power P, the heat increase ΔT of the thermal mass depends on its temperature T and heat capacity C. The thermal mass is linked to a thermal reservoir by the thermal conductance G. The detector speed of a bolometer is limited by the energy relaxation in the thermal mass, given by the thermal time constant $\tau = C/G$. The ability of SGS GJJs

to act as ultrasensitive and ultrafast bolometers for microwave and infrared photons has been first demonstrated by Lee *et al.*[36] and Kokkoniemi *et al.*[35] in 2020, followed by Walsh *et al.* in 2021.[37] Their findings are briefly summarized below.

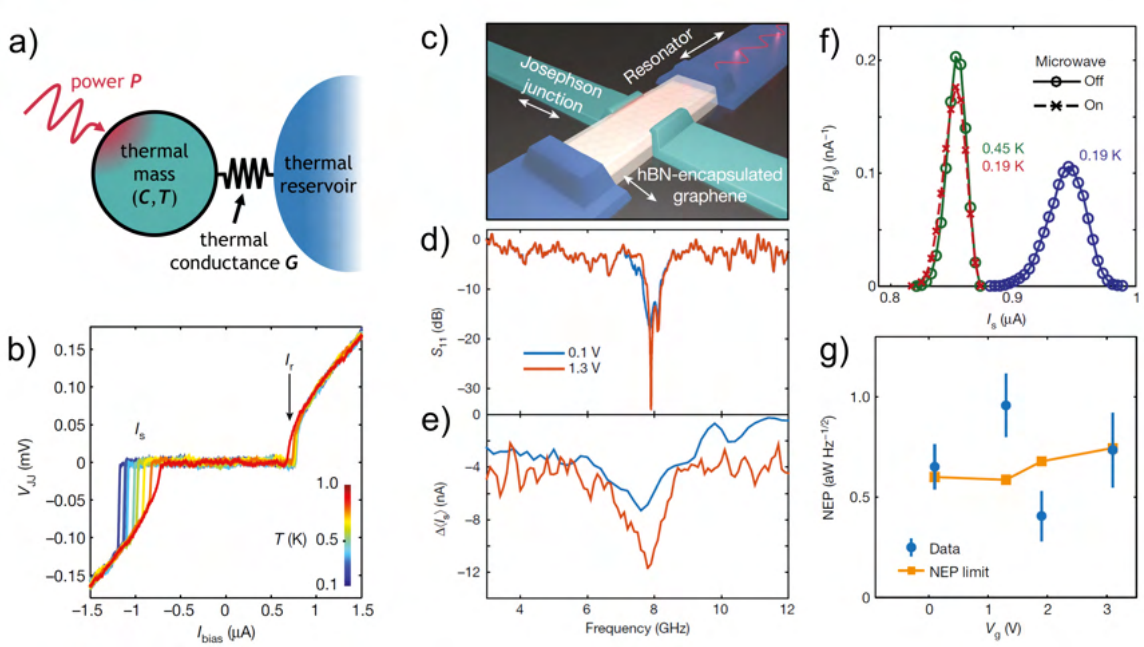

Figure 2.12.: a) Schematic of a bolometer. Photon with power P is absorbed by the thermal mass with temperature T and intrinsic heat capacity C. Cooling is provided to the thermal reservoir via the thermal conductance G. b) Voltage across the GJJ as a function of bias current I_{bias} for different temperatures. The switching current I_{s} of the junction is highly temperature dependent. c) Illustration of the GJJ bolometer, where a GJJ is coupled to a microwave resonator. d) The microwave resonator has a resonance frequency near $8\,\text{GHz}$. e) At the resonance frequency, the average observed switching current ΔI_{s} exhibits a clear decrease, indicative of microwave coupling to the junction. f) The microwave response at 126 fW and 0.19 K (red) of the switching probability distribution $P(I_{\text{s}})$ is compared to measurements at 0.19 (blue) and 0.45 K (green) without microwave input. g) Measured NEP (blue) and fundamental thermal fluctuation limit of the NEP (orange). The average NEP of the GJJ bolometer is $0.7 \pm 0.2\,\text{aW Hz}^{-1/2}$, corresponding to an energy resolution of a single $32\,\text{GHz}$ photon. Figure b)-g) adapted with permission from Lee, GH., Efetov, D.K., Jung, W. et al. Graphene-based Josephson junction microwave bolometer. Nature 586, 42–46 (2020). Copyright 2020 Springer Nature.[36]

The GJJ-based bolometer reported by Lee *et al.*[36] was developed in the group of Prof. K. C. Fong and consists of a GJJ coupled to a microwave resonator as shown schematically in figure 2.12 c). The current voltage characteristics of the GJJ shown in 2.12 b) display the behavior of an underdamped JJ. For underdamped JJs, the determination of the critical current I_{c} is non-trivial because the transition from the voltage to the zero voltage state is hysteretic, depending

on the current sweep direction. Therefore, the downswept current measurement in figure 2.12 b), exhibits a retrapping current I_r when the JJ enters the zero voltage state and a switching current I_s, when the transition to the normal state appears.

Interestingly, I_s is extremely sensitive to temperature as indicated by the colors. The microwave resonator, explained in detail in section 2.5, is utilized to couple microwave radiation at the resonance frequency of approximately $8\,\mathrm{GHz}$, depicted in figure 2.12 d), to the GJJ. Remarkably, the average observed switching current ΔI_s of the device in figure 2.12 e) exhibits a clear decrease at the resonance frequency, signaling the microwave responsivity of the GJJ. The switching rate of the junction from superconducting to normal state is stochastic and can therefore be described by a probability distribution. This rate is also known as the escape rate from the RCSJ model. In figure 2.12 f) the switching probabilities $P(I_\mathrm{s})$ at 0.19 K and 0.45 K with zero input power show a clear separation. For a very low microwave power of 126 fW and 0.19 K, the switching histogram overlaps well with that at 0.45 K and zero input power, indicating the same switching probability under these two conditions. This suggests that the suppression of I_s occurs due to the microwave radiation. It is possible to infer the sensitivity of the GJJ bolometer from the suppression of I_s in terms of noise-equivalent power (NEP). The NEP is defined as minimum power to result in a signal-to-noise ratio of one over a bandwidth of 1 Hz. The sensitivity of the bolometer is determined for different gate voltages and compared to the fundamental thermal fluctuation limit of the NEP in figure 2.12 g). The NEP achieved by the GJJ-based bolometer is on average $0.7 \pm 0.2\,\mathrm{aW\,Hz^{-1/2}}$.[36] Compared to bolometers based on superconducting nanowire single photon detectors, the SGS device operates $\sim 10^5$ times faster and with much lower energy resolution, equivalent to a $32\,\mathrm{GHz}$ photon, due to the small heat capacity C of the graphene electron system.

Using a different readout technique, Kokkoniemi *et al.* reported a NEP of $30\,\mathrm{zW\,Hz^{-1/2}}$ at 55 mK with an energy resolution of $30\,\mathrm{GHz}$.[35] Later Walsh *et al.* used an optical fiber to irradiate a graphene Josephson junction with photons of 1550 nm wavelength. In this experiment, the near-infrared photons excite localized surface plasmons at the SGS interfaces, resulting in a highly sensitive single photon detector.[37] In the most recent study, Huang *et al.* reported the calorimetric detection of single photons, i.e., the measurement of the internal energy of a photon, using a GJJ.[38] Following the work of Walsh and Huang *et al.*, recent studies investigated the use of magic-angle twisted bilayer graphene for the bolometric detection of single near-infrared photons.[119,120] Di Battista *et al.* illuminated MATBG devices with near-infrared radiation and assessed the thermal response. Although these MATBG devices are not based on JJs, they illustrate the unique thermal properties of graphene, which make graphene-based superconducting photodetectors appealing for a wide range of applications such as dark matter axion search and quantum information science.[44,121]

2.3.2. Graphene-based Plasmonic Photodetectors

In the previous section, the extraordinary properties of graphene-based Josephson junction bolometers and their ultrahigh sensitivity down to the single photon regime have been introduced. However, the application of these superconducting devices is restricted by their operation in a cryogenic environment. Therefore, significant advancements have been made to realize sensitive graphene-based photodetectors aimed for operation at room temperature. Based on the original idea of Dyakonov and Shur,[122] graphene detectors for frequencies in the THz regime have caught significant attention due to their potential use in various applications. These graphene-based detectors operate on the excitation of plasmons, i.e., collective oscillations of charge carriers, facilitated by various top gate structures. Such plasmonic graphene terahertz field-effect-transistors (GTeraFETs) are able to rectify THz radiation if an asymmetry is present in the system. An effective approach is to equip devices with so-called asymmetric dual-grating gate (ADGG) structures, which serve multiple purposes that are explained in the following.[123]

Modern GTeraFETs consist of hBN-encapsulated graphene heterostructures and are based on the THz excitation of graphene surface plasmon-polaritons (GSP).[40,124] These plasmons are a graphene-specific subtype of surface plasmon-polaritons (SPP), which propagate along the interface of a dielectric and a conductive medium. In conventional metals, the dispersion relation for bulk plasmons $\omega_{\mathrm{bp}} = \sqrt{\frac{ne^2}{\epsilon_0 m}}$ and SPP $\omega_{\mathrm{spp}} = \frac{\omega_{\mathrm{bp}}}{\sqrt{1+\epsilon_{\mathrm{r}}}}$ depend on the carrier density n of the conductor and the dielectric constant ϵ_{r} of the dielectric. Since the carrier density in graphene is not only much lower, but also gate tunable, the dispersion relation of GSP $\omega_{\mathrm{gsp}} \propto \sqrt{E_{\mathrm{F}}}$ and therefore $\omega_{\mathrm{gsp}} \propto n^{1/4}$.[125]

However, it is generally impossible to directly excite GSPs with THz radiation, since the dispersion relations of light and GSPs do not intersect, resulting in an energy and momentum mismatch as shown in figure 2.13 a). This problem is solved by the addition of a grating structure as illustrated in figure 2.13 b), which in the case of GTeraFETs is the ADGG.[123,124] According to Bragg's law, the grating adds an extra momentum to overcome the mismatch every time the wave vector of the GSP q_{gsp} matches with a component of the diffracted incident light $k \sin\theta$

$$q_{\mathrm{gsp}} = k \sin\theta \pm nG, \tag{2.38}$$

where n is an integer and with the reciprocal grating vector $G = \frac{2\pi}{R}$ and grating lattice constant R.[125] Although, the periodic grating structure itself already enables the excitation of graphene surface plasmon-polaritons, an additional asymmetry is necessary to generate a finite net photocurrent, without the need to apply a bias current.[123]

The ADGGs as shown in figure 2.13 c) significantly enhance THz rectification in GTeraFETs. In combination with the global backgate, the topgate grating structure can be utilized to induce

periodic abrupt pn-junctions in the graphene channel. This periodic electrostatic modulation gives rise to various mechanisms such as the photo-thermoelectric (PTE) effect,[126,127] resistive self mixing (RSM),[128] plasmonic ratchet effect[129–131] and the plasmonic drag effect,[132] that result in the conversion of incident THz radiation into a rectified DC photocurrent. The photocurrent signal has contributions from these multiple mechanisms of which the disentanglement is complex and non-trivial. A significant signal change is typically expected whenever ω_{spp} matches the incident THz frequencies near the CNP. This is shown in figure 2.13 d) as a function of topgate voltage for different temperatures. Note that a finite photocurrent of tens of pA is still detectable even at room temperature.[40]

Close to 4 K, the ADGG-GTeraFET reaches a maximum signal of approximately 4 nA, which can be used to extract an important figure of merit, i.e., the current responsivity R_I

$$R_I = \frac{\pi}{\sqrt{2}} \frac{S}{P} \frac{S_{\text{T}}}{S_{\text{D}}}, \tag{2.39}$$

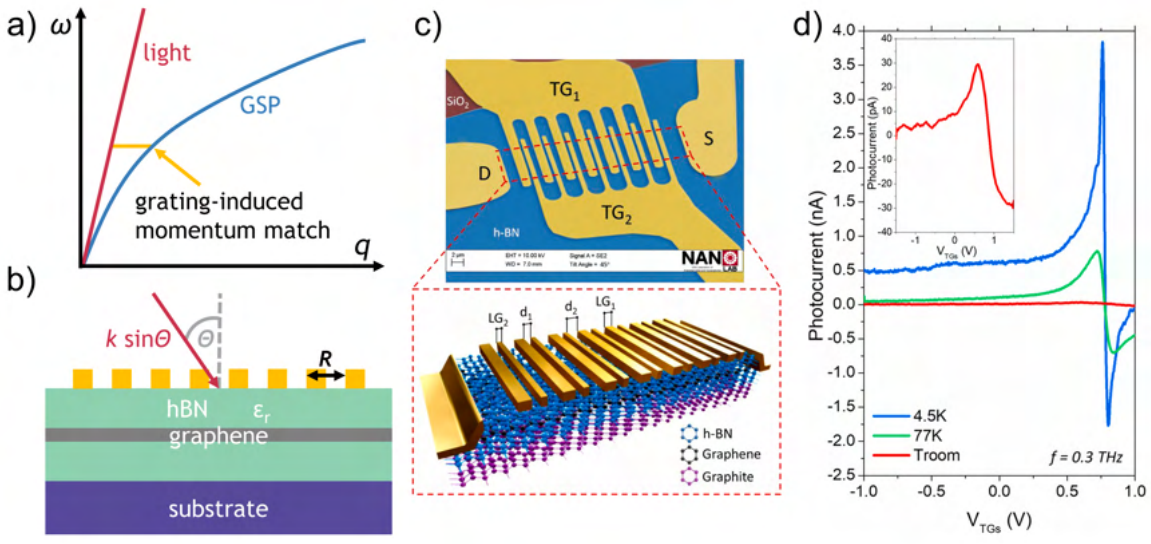

Figure 2.13.: a) The momentum mismatch between the dispersion relation of light and graphene surface plasmon-polaritons (GSP) can be resolved by additional momentum from the grating. b) Schematic of a hBN-encapsulated GTeraFET with topgate grating, which is required for the excitation of GSPs by incident THz radiation (red arrow). c) (top) Exemplary ADGG GTeraFET device from Delgado-Notario *et al.*, with metallic source and drain contacts to the hBN-encapsulated graphene stack that also includes a graphite backgate. (bottom) Highlighted image of the asymmetric dual-grating gate with its characteristic distances. d) THz-induced photocurrent as function of topgate voltage for different temperatures. Figure c) and d) adapted from Delgado-Notario *et al.* (2022) under terms of the Creative Commons CC BY license.[40]

where S is the detected signal, P is the power of the THz radiation with spot size S_T at the detector area S_D. With R_I, the measured channel resistance R_ch and the noise spectral density N, the NEP of these graphene-based THz detectors can be determined with[40]

$$\mathrm{NEP} = \frac{N}{R_I R_\mathrm{ch}} = \frac{\sqrt{4 k_\mathrm{B} T R_\mathrm{ch}}}{R_I R_\mathrm{ch}}. \tag{2.40}$$

Using Eq. 4.18 and Eq. 4.19, maximum values of $0.216\,\mathrm{A/W}$ and $0.002\,\mathrm{A/W}$ could be determined for R_I at 4.5 K and room temperature, respectively. This results in minimum values of $0.81\,\mathrm{pW/Hz^{1/2}}$ and $0.67\,\mathrm{nW/Hz^{1/2}}$ for the NEP at 4.5 K and room temperature, respectively. These values are in good agreement with similar devices.[124,128,131]

Compared to the graphene Josephson junction-based detectors presented before, even at low temperatures, the NEP of the ADGG-GTeraFET devices is orders of magnitude higher and therefore still far away from single-photon detection level. Additionally, these detectors are not able to provide energy resolution yet. However, significant performance improvements can be expected in the future by gaining a better understanding of the detection mechanisms[128] or the utilization of lenses and antennas.[39,133] Another interesting approach to further improve the performance of GTeraFET THz detectors is to replace the asymmetric dual-grating gate with a tunable grating provided by surface acoustic waves (SAW).[134,135] In contrast to ADGGs where the frequency range is determined by the fabricated gate pattern, a SAW grating can be excited at various SAW frequencies and wavelengths by the use of so-called *chirped* interdigital transducers (IDTs).[136] SAW-induced phenomena in graphene devices have been investigated in the past and showed signatures of pseudomagnetic field effects.[137,138] A SAW-based GTeraFET could therefore be within reach and provide possibly high detection sensitivity combined with unprecedented tunability.

2.4. Microwave Spectroscopy

The preceding sections illustrated graphene's capability to detect high frequency electromagnetic radiation spanning from the radiofrequency to the microwave and terahertz regime. This ability arises from the linear and gapless band structure of graphene, allowing broadband absorption. From a fundamental research perspective, it is equally intriguing to reverse this approach and instead of using graphene to sense radiation, use radiation as a tool to probe the properties of graphene.

Magnetic resonance spectroscopy, which combines high magnetic fields with electromagnetic radiation, is a powerful technique used to investigate electron and nuclear spin states. The microwave spectroscopy of electron spins in experimental physics is typically referred to as electron spin resonance (ESR) and is closely related to the investigation of nuclear spins, known as nuclear magnetic resonance (NMR). ESR is a highly suitable method to study two-dimensional charge carrier systems such as graphene. An external magnetic field $\boldsymbol{B}$ applied perpendicular to the graphene electron system will energetically separate the spin up and down states. The energy of a spin state is given by the Zeeman energy

$$E_{\mathrm{Z}} = g\mu_{\mathrm{B}}\boldsymbol{s}\boldsymbol{B}, \tag{2.41}$$

with the electron g-factor ($g = 2.0023$ for the free electron) and electron spin $\boldsymbol{s}$.[20] The Zeeman energy increases linearly with magnetic field and is proportional to the g-factor, as shown schematically in figure 2.14 a). The energy difference between the two electron spin states with $m_{\mathrm{s}} \pm 1/2$ is referred to as Zeeman splitting energy ΔE_{Z}

$$\Delta E_{\mathrm{Z}} = h\nu = g\mu_{\mathrm{B}} \left|\Delta m_{\mathrm{s}}\right| \boldsymbol{B} = g\mu_{\mathrm{B}}\boldsymbol{B}. \tag{2.42}$$

Eq. 2.42 represents the resonance condition for ESR, allowing spin flip transitions, if the microwave energy $h\nu$ matches ΔE_{Z}.[20] In addition to the energy of the photon, the orientation of its magnetic field component with respect to the orientation of the electron magnetic moment $\boldsymbol{\mu}_{\mathrm{s}} = g\mu_{\mathrm{B}}\boldsymbol{s}$ is important. In order to act as a tipping field and induce spin flips, the microwave radiation effectively needs to be aligned perpendicular to the magnetic field.[20]

The Zeeman splitting ΔE_{Z} for electrons lies in the µeV or GHz range. Therefore, the method of ESR can be employed to investigate the low energy spectrum of graphene in a resistively-detected electron spin resonance (RD-ESR) approach. A schematic of RD-ESR is shown in figure 2.14 b), where a graphene Hall bar is subjected to microwave radiation provided by a simple loop antenna under an external magnetic field. By measuring the longitudinal resistance, resonance-induced resistance alterations can be detected. Although this approach is well known in classical semiconductor science, Mani *et al.* pioneered RD-ESR in epitaxial graphene

on SiC and deduced an energy splitting even at $\boldsymbol{B} = 0\,\mathrm{T}$.[15] A few years later, Sichau *et al.* resolved this energy splitting in more detail in large-area graphene, obtained by chemical vapor deposition (CVD), which is described in section 3. Their study revealed that the observed splitting can be attributed to a small energy gap in the graphene band structure of approximately 40 µeV, resulting from carbon's intrinsic spin orbit coupling.[17] Previously, Lyon and Sichau *et al.* also determined the electron g-factor in graphene to be $g = 1.952 \pm 0.002$.[16] Using the same approach, Singh *et al.* investigated large-area graphene on hBN, where the hBN-induced sublattice symmetry breaking leads to a small gap of approximately 20 µeV in the graphene band structure.[18] These studies on large-area graphene illustrate the allure of RD-ESR microwave spectroscopy. Due to its high sensitivity and ability to probe spin states, this method recently has been used to investigate (naturally small) exfoliated graphene samples, in particular ADGG-GTeraFETs and twisted bilayer graphene.[139,140] These studies verified the results of the ESR studies on large-area graphene, although some claims about moiré effect-induced resonances in TBG are under dispute.[141]

In materials with a nuclear spin, the electron spin resonance can be influenced by nuclear effects. In graphene, nuclear spin effects are typically neglected due to the low natural abundance of the spin carrying isotope $^{13}\mathrm{C}$ ($I = 1/2$) of only 1.1 %. In addition, the hyperfine interaction is expected to be small. This interaction describes the coupling of electron and nuclear magnetic moments arising from their individual spins. The effective Hamiltonian of the hyperfine interaction can be expressed as

$$\hat{H}_{\mathrm{HFI}} = \boldsymbol{s}\bar{\boldsymbol{A}}\boldsymbol{I}, \tag{2.43}$$

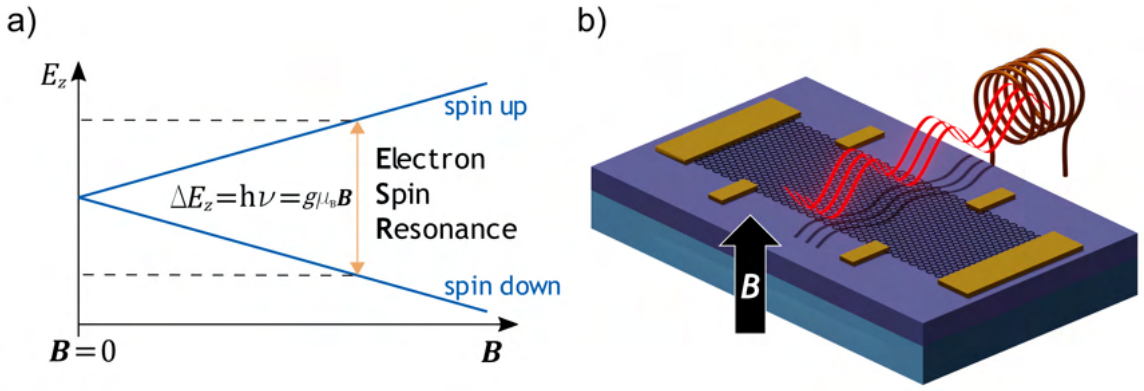

Figure 2.14.: a) Linear magnetic field dependence of the electron Zeeman splitting. At the resonance condition, microwave radiation with energy $h\nu$ matches the Zeeman splitting energy ΔE_{Z} and induces electron spin flip transitions. b) Schematic of a resistively-detected ESR measurement. A graphene Hall bar sample under a perpendicular external magnetic field is irradiated with microwaves provided by a loop antenna.

with the hyperfine interaction tensor $\bar{\boldsymbol{A}}$, that mediates the coupling between electron spin $\boldsymbol{s}$ and nuclear spin $\boldsymbol{I}$. The hyperfine interaction is effectively constructed by two contributions. The first interaction is the dipole-dipole interaction between the magnetic moments $\boldsymbol{\mu}_\mathrm{s}$ and $\boldsymbol{\mu}_\mathrm{N}$ and their local stray fields as shown in figure 2.15 a). The second contribution describes the interaction when the electron is close to the nucleus and is referred to as the Fermi contact interaction. This mechanism is the major contribution to the overall hyperfine interaction and depends on the density of the conduction electron wave function at the nucleus. In contrast to materials with conduction electrons in s-orbitals and thus a large isotropic overlap at the site of the nuclei, graphene's conduction electrons have p-orbital character, as shown schematically in figure 2.15 d). This corresponds to a vanishingly small Fermi contact interaction and therefore small overall hyperfine interaction in graphene. However, a possible approach to enhance nuclear effects in graphene is the use of isotopically purified ^{13}C graphene with a ^{13}C content close to 100 %.

Analogous to its electron counterpart, a nuclear spin is aligned by an external magnetic field, leading to nuclear Zeeman splitting of its ground states. However, the nuclear spin degeneracy $(2I + 1)$ can be larger than 2 and due to the large proton mass, the nuclear Zeeman splitting is generally two or three orders of magnitude smaller than the electron Zeeman splitting, as illustrated in figure 2.15 b).[20] According to the Maxwell-Boltzmann law, the spin state population is temperature dependent and the distribution for the number of spin up (down) $N_\uparrow$ ($N_\downarrow$) is given by

$$\frac{N_\uparrow}{N_\downarrow} = \exp\left(-\frac{\Delta E_\mathrm{Z}}{k_\mathrm{B}T}\right) = \exp\left(-\frac{g\mu_\mathrm{B}\boldsymbol{B}}{k_\mathrm{B}T}\right). \tag{2.44}$$

The resulting Boltzmann distributions for electrons and nuclei in ^{13}C graphene are depicted in figure 2.15 c). For magnetic resonance spectroscopy, a finite spin state imbalance is required to yield a sizeable signal from resonance-induced spin flip transitions. While the ratio $N_\uparrow/N_\downarrow$ for electrons differs significantly from unity at temperatures below 10 K and moderate magnetic field strengths, this is not the case for nuclear spins. Due to the much smaller Zeeman splitting, a significant spin imbalance is reached only at high magnetic fields and ultralow temperatures in the mK-range. In addition, the low number of atoms in a single graphene layer limits the maximum signal. These experimental boundary conditions make direct NMR measurements in ^{13}C graphene extremely challenging.

Motivated by the use of ^{13}C nuclear spins as qubits for quantum information processing and a precise determination of the hyperfine interaction strength in graphene, studies have investigated ^{13}C carbon nanotubes and ^{13}C graphene.[19,50,142–144] While the study on ^{13}C carbon nanotube quantum dots reported a surprisingly large hyperfine interaction,[142] transport studies on ^{13}C graphene did not show any signs of nuclear effects.[143,144] Dynamic nuclear polarization

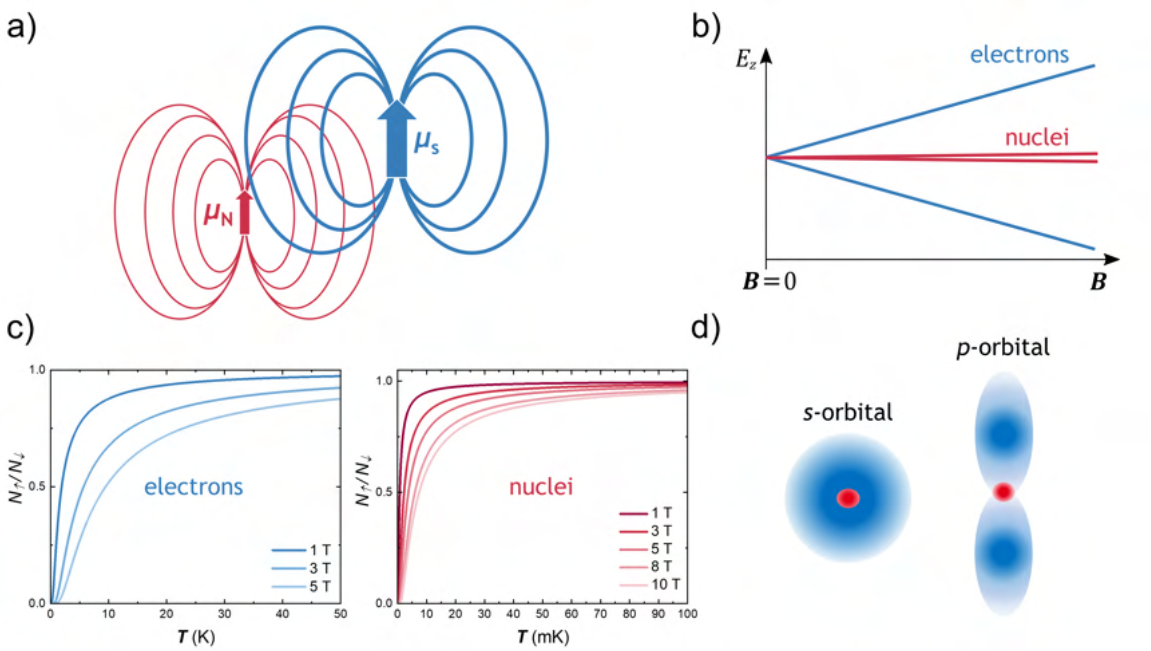

Figure 2.15.: a) Visualization of the hyperfine interaction between the electron spin and nuclear spin. The stray field of the electron magnetic moment μ_s (blue) acts on the magnetic moment of nuclear spin μ_N (red) and vice versa. b) Oversimplified comparison of the electron Zeeman splitting (blue) and the nuclear Zeeman splitting (red), which is much smaller due to the much larger proton mass. c) Temperature dependency of the ratio of opposing spin states $N_\uparrow/N_\downarrow$ following the Maxwell-Boltzmann law at different magnetic fields for electron spins (blue, left) and nuclear spins (red, right). For nuclear spins, the temperature scale of significant spin polarization is three orders of magnitude smaller. d) Comparison between s-orbitals and p-orbitals and their respective conduction electron density (blue) at the nucleus (red). ^{13}C graphene exhibits a small Fermi contact interaction due to the p-orbital character of the charge carriers.

(DNP) through the application of ESR that continuously excites electron spins to enhance the nuclear polarization in ^{13}C graphene has shown signatures of hyperfine effects.[19,145] To study these nuclear effects in more detail, experimental limitations need to be overcome. For example, the low nuclear Zeeman splitting energy requires mK-temperatures. In ESR and NMR experiments, the application of microwaves via simple loop antennas, as introduced in figure 2.14 b), is usually very inefficient. Due to high losses and subsequently high radiation power, this technique leads to an unavoidable heat increase at the position of the sample, destroying any nuclear spin imbalance $N_\uparrow/N_\downarrow$. Thus, a more efficient way to couple microwave radiation to graphene devices with less introduced heat is necessary. Possible approaches to address this challenge will be discussed in the next section 2.5.

2.5. Enabling Technologies

The electromagnetic frequency range spanning from the low MHz range to several hundreds of GHz encompasses wavelengths ranging from hundreds of meters to millimeters. These are enormous distances compared to typical van der Waals device sizes discussed in this thesis and commonly used in industrial micro-electromechanical systems (MEMS) fabrication. Nevertheless, high-frequency electromagnetic signals are integrated on-chip as an essential part of micro- and nanostructured circuits in research and applications. However, compared to low frequency circuits, it is possible that the electromagnetic wavelength at high frequencies is smaller than the circuit that is under investigation. The propagation of electromagnetic signals with smaller wavelengths than the electrical circuit dimensions is described by transmission line theory.[146]

The foundation of transmission line theory is the distributed element model, which describes the propagation of electromagnetic waves along transmission lines in good approximation. This representation treats the transmission line as being composed of infinitesimally small elements distributed continuously along its length, instead of a single lumped element with resistance R, inductance L, capacitance C, and conductance G concentrated at a single point.[146] Since transmission lines always consist of two conductors (signal and ground), they are often schematically represented as two-wire lines as shown in figure 2.16 a). Here, a piece of line with infinitesimal length Δx is modeled as a lumped-element circuit. Applying Kirchhoff's law to this infinitesimally small piece circuit leads to the *telegrapher equations*

$$\begin{aligned} \frac{\partial v(x,t)}{\partial z} &= -Ri(x,t) - L\frac{\partial i(x,t)}{\partial t}, \\ \frac{\partial i(x,t)}{\partial z} &= -Gv(x,t) - C\frac{\partial v(x,t)}{\partial t}. \end{aligned} \tag{2.45}$$

These equations describe how voltage and current waves propagate and are affected by the distributed resistance, inductance, capacitance, and conductance of the line. By applying these equations, the characteristic impedance of a transmission line can be expressed as

$$Z_0 = \sqrt{\frac{R + j\omega L}{G + j\omega C}}, \tag{2.46}$$

with the circular frequency ω of the transmitted signal. The impedance is defined as the ratio of the voltage and current amplitudes of the signal V/I and has the unit Ohm (Ω). The transmission of a signal between two interfaced parts of a transmission line depends on the impedance of each part. Perfect transmission only occurs in the case of impedance matching, avoiding reflection and losses. Hence, the impedance of most components in microwave engineering is designed to match a standard impedance of $50\,\Omega$.

Among the most popular transmission line concepts are coplanar waveguides (CPWs), which

are heavily used in today's quantum information science as an essential building block of circuit quantum electrodynamics (QED). CPWs were first introduced by C. P. Wen in 1969 and consist of a central signal transmission line and its two neighboring ground planes, all sitting on a dielectric substrate.[147] A schematic drawing of a CPW with the most important geometric lengths is depicted in figure 2.16 b). The transmission behavior of the CPW depends on the thickness of the conductor t and the dielectric substrate h, as well as on the width of the signal line w and the distance from the signal line to the ground planes s.

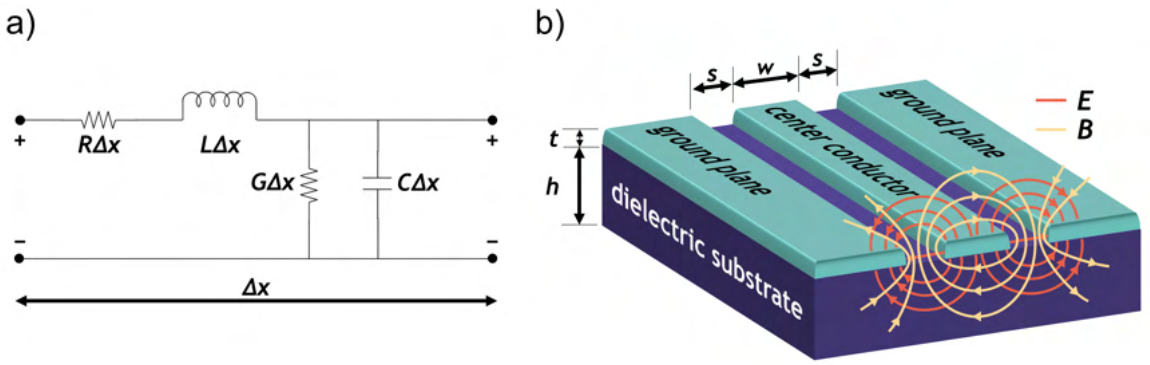

Figure 2.16.: a) Lumped element representation of an infinitesimal length Δx of a transmission line inside the distributed element model framework. b) Schematic drawing of a coplanar waveguide (CPW) with its characteristic lengths. The conductor is shown in green, the dielectric in dark violet. The electric and magnetic field lines of the CPW are illustrated in orange and yellow, respectively.

The characteristic impedance of a CPW can be fine tuned by designing w and s, which construct the geometrical parameters $k = \frac{w}{w+2s}$ and $k' = \sqrt{1-k^2}$. Approximating a lossless CPW, the characteristic impedance is given by

$$Z_0 = \sqrt{\frac{L_l}{C_l}} \approx \frac{30\pi}{\sqrt{\epsilon_{\text{eff}}}} \frac{K(k)}{K(k')}. \tag{2.47}$$

This is the result of a conformal mapping approach, which will not be presented here and is described in detail in different books.[148–150] $K(k)$ and $K(k')$ are elliptic integrals and their ratio $K(k)/K(k')$ can be simplified to:

$$\frac{K(k)}{K(k')} = \frac{\pi}{\ln\left(2\frac{1+\sqrt{k'}}{1-\sqrt{k'}}\right)} \quad \text{for} \quad 0 \leq k \leq 0.707, \tag{2.48}$$

$$\frac{K(k)}{K(k')} = \frac{\ln\left(2\frac{1+\sqrt{k'}}{1-\sqrt{k'}}\right)}{\pi} \quad \text{for} \quad 0.707 \leq k \leq 1. \tag{2.49}$$

The effective permittivity is given by $\epsilon_{\text{eff}} \approx \frac{\epsilon_r+1}{2}$, with the dielectric constant ϵ_r of the substrate.[148,149] The phase velocity of the wave propagating along the transmission line has the

relation

$$v_{\text{ph}} = \frac{1}{\sqrt{L_l C_l}}, \tag{2.50}$$

with L_l and C_l defined as[151]

$$L_l = \frac{\mu_0}{4}\frac{K(k')}{K(k)}, \tag{2.51}$$

$$C_l = 4\epsilon_0\epsilon_{\text{eff}}\frac{K(k)}{K(k')}. \tag{2.52}$$

In practice, many approximations made in the considerations above do not hold completely. Even superconducting coplanar waveguides are not lossless. The thickness of the conducting layer, the size of the ground planes and many additional effects will influence the transmission. The loss of transmission, i.e., the attenuation of a CPW, consists of at least three categories: dielectric loss α_{d}, conductor loss α_{c} and radiation loss α_{r}. The total attenuation is a sum of these three contributions: $\alpha_{\text{t}} = \alpha_{\text{d}} + \alpha_{\text{c}} + \alpha_{\text{r}}$.[150]

The dielectric loss α_{d} is proportional to the dielectric loss tangent of the substrate $\alpha_{\text{d}} \propto \tan\delta_{\text{e}}$, which is material dependent. Good dielectric materials with low losses are high-resistivity silicon or sapphire for example. The choice of dielectric material always depends on the intended application of the coplanar waveguide. Generally, insulating materials with as high resistivities as possible are desirable. The opposite is true for the conducting material where a high conductivity is desirable. However, at high frequencies, the main contribution to conductor loss α_{c} is the skin effect, which describes the concentration of AC currents at the surface of the conductor. This effect scales with increasing frequency. The skin depth δ is the distance below the surface of the conductor that still contributes significantly to transport and is defined as

$$\delta = \sqrt{\frac{2\rho}{\omega\mu_{\text{c}}}}, \tag{2.53}$$

with the resistivity ρ and permeability μ_{c} of the conductor. The film thickness of the conductor t should be sufficiently large (multiple δ) to reduce conductor loss.[150] Compared to conventional microstrips, which only consist of the signal line without groundplanes, CPWs have less radiation loss due to the shielding by the ground planes. Nevertheless, CPWs still show significant radiation loss in the out-of-plane direction because of their open structure. The dominant radiation loss mechanism is the so-called leaky mode, which occurs if the phase velocity in the line exceeds the phase velocity in the substrate. This effect increases with increasing signal transmission line width. In superconducting CPWs, the phase velocity ($v_{\text{ph}} \propto \frac{1}{\sqrt{L_l}}$) is reduced due to the kinetic inductance L_l^{k}, allowing for ultralow loss transmission.

For superconductors, the inductance $L_l = L_l^{\mathrm{m}} + L_l^{\mathrm{k}}$ is a sum of the geometric (magnetic) inductance L_l^{m} and the kinetic inductance L_l^{k} given by[102]

$$L_l^{\mathrm{k}} = \frac{\hbar R_{\mathrm{N}}}{\pi \Delta}. \tag{2.54}$$

Here, R_{N} is the normal state resistance and Δ the superconducting gap of the superconductor. The kinetic inductance describes the inertia of moving Cooper pairs in a superconductor and can contribute significantly to the overall inductance.[151,153]

Microwave resonators

CPWs are often used in the form of microwave resonators. Such a resonator is formed when a part of the center conductor is separated from the rest of the transmission line by two coupling gaps, as shown in figure 2.17 a). The transmission behavior of resonators is different from transmission lines, which transport the signal ideally without any reflections on a broadband frequency range. Because of the two coupling gaps, a standing wave can form at the correct frequency, depending on the length of the resonating piece of the center conductor. This is schematically depicted in figure 2.17 b), where the voltage profile along the resonator distance is illustrated. The case of two gaps leads to a voltage profile of a standing wave with twice the wavelength λ of the resonator length $l = \lambda/2$. However, one side of the resonator can be terminated differently. Instead of an open circuit (gap), one side is shorted to ground, leading to a fixed voltage of zero at this point. This results in a voltage profile, where only a quarter of the wavelength matches the resonator length $l = \lambda/4$. Thus, the termination of a resonator, open or short, determines whether it is a $\lambda/2$ or a $\lambda/4$ resonator.

The frequency which matches the resonator length is the fundamental resonance frequency f_0 given by[153]

$$f_0 = \frac{v_{\mathrm{ph}}}{\lambda} = \frac{c}{\sqrt{\epsilon_{\mathrm{eff}}}} \frac{1}{\lambda}, \tag{2.55}$$

with $\lambda = 2l$ ($\lambda = 4l$) for an open (short) terminated resonator, respectively. Around the resonance frequency, the properties of a microwave resonator can be approximated by a lumped element, parallel LCR circuit, as shown in figure 2.17 c). The input impedance into such a parallel LCR-circuit is

$$Z_{RLC} = \left(\frac{1}{R} + \frac{1}{j\omega L_{\mathrm{R}}} + j\omega C_{\mathrm{R}} \right)^{-1}, \tag{2.56}$$

with the resistance R, magnetic inductance L_{R} and capacitance C_{R} of the resonator.[146] The angular resonance frequency of this circuit is given by

$$\omega_n = n\omega_0 = \frac{1}{\sqrt{L_\mathrm{R} C_\mathrm{R}}}, \tag{2.57}$$

where n denotes the resonance mode number.

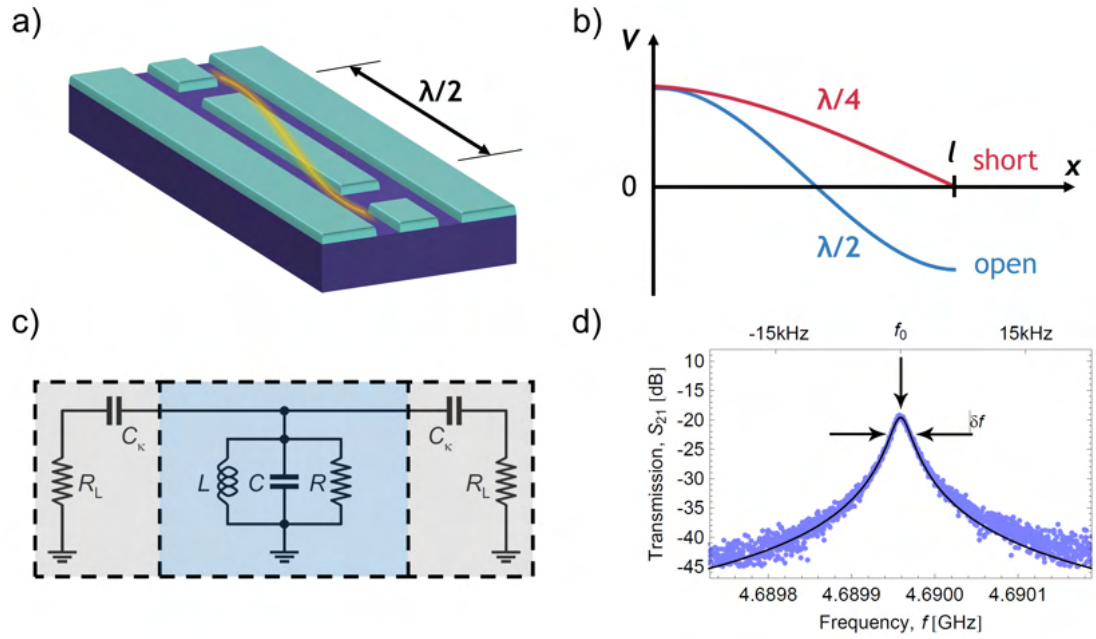

Figure 2.17.: a) By separating a part of the center conductor with two gaps from the rest of the transmission line, a $\lambda/2$ microwave resonator is formed with length l. b) Voltage profile of a standing electromagnetic wave in open (blue) and short (red) terminated resonator. Depending on the termination, the resonator becomes a $\lambda = 2l$ or $\lambda = 4l$ resonator. c) Representation of the resonator by a parallel LCR-circuit. The grey shaded parts provide input and output coupling while the parameter inside the blue shaded region constitute the internal quality factor Q_int. d) Exemplary resonance peak of a $\lambda/2$ resonator from Göppl *et al.*, with $f_0 \approx 4.7\,\mathrm{GHz}$ and $Q_\mathrm{L} \approx 10^5$. Figure c) and d) adapted with permission from M. Göppl, A. Fragner, M. Baur, R. Bianchetti, S. Filipp, J. M. Fink, P. J. Leek, G. Puebla, L. Steffen, A. Wallraff; Coplanar waveguide resonators for circuit quantum electrodynamics. J. Appl. Phys. 1 December 2008; 104 (11): 113904. Copyright 2008 by AIP Publishing.[153]

The quality factor Q of a resonant circuit is a quantity that compares the amount of stored energy to the amount of energy loss. The higher the loss, the lower the quality factor. The quality factor can be divided in the internal quality factor of the resonator Q_int and an external quality factor Q_ext.[146] These two contributions are used to calculate the loaded quality factor Q_L

$$\frac{1}{Q_\mathrm{L}} = \frac{1}{Q_\mathrm{int}} + \frac{1}{Q_\mathrm{ext}}. \tag{2.58}$$

This loaded quality factor can be determined from the measured transmission spectrum of the resonator. An exemplary resonance of a $\lambda/2$ resonator is shown in figure 2.17 d), with

$f_0 \approx 4.7\,\mathrm{GHz}$. At the resonance of the $\lambda/2$ resonator, the input power is transmitted instead of being reflected, leading to a peak in transmission. The loaded quality factor can be calculated from the measured peak with

$$\frac{1}{Q_\mathrm{L}} = \frac{f_0}{\delta f}, \tag{2.59}$$

where δf is the full width half maximum of the resonance peak.[153] The loaded quality factor decreases due to resistive loading R_L resulting from the capacitive coupling of the resonator to external input and output lines. In addition, the simultaneous capacitive loading leads to a frequency shift of f_0. Generally, a larger coupling capacitance C_K leads to more microwave power coupled into the resonator, but leads to a decrease in Q_L.[153]

While early research on coplanar waveguides for circuit QED and microwave spectroscopy often used $\lambda/2$ resonators,[153] modern approaches focus on transmission feedline coupled $\lambda/4$ resonators.[154] These architectures allow the coupling of multiple $\lambda/4$ resonators with different resonance frequencies to a single feedline that is used for readout. This simple frequency-domain approach to multiplexing enables the coupling and readout that is necessary for certain microwave spectroscopy applications and scalable quantum processors.[155,156]

Employing coplanar waveguides or microstrip lines offers the possibility to efficiently couple high frequency electromagnetic radiation on-chip to other structures such as vdW devices. Different approaches that were realized as part of this thesis are presented in the next chapter 3. In contrast to loop antennas, on-chip transmission lines are advantageous due to their close proximity to the structures of interest. Since the intensity of radiation is inversely proportional to the square of the distance $I \propto \frac{1}{r^2}$, this allows the use of much lower applied microwave power to reach the same AC fields at the sample. As explained previously, this can be crucial to enable ultralow temperature microwave spectroscopy of fragile and sensitive states, such as the nuclear spin polarization of ^{13}C graphene. Although microwave spectroscopy with high-frequency waveguides at low temperatures is an established technique,[155,157,158] its huge potential for the investigation of vdW materials remains largely unexplored. However, vdW materials were identified as a highly valuable addition to high-quality circuit QED and the first *vdW-only* qubit could be within reach.[81,159]

3. Device Fabrication and Experimental Techniques

3.1. Van-der-Waals Devices

During the time of this project, a substantial amount of work was spent to optimize the device architecture and to improve the quality of the investigated vdW structures. At the start of this work, three main categories were identified where significant improvements are necessary to achieve the set goals: vdW materials, electrical contacts and high-frequency circuit integration. Substantial advancements in these areas also provide a solid foundation for future scientific progress in this group. The following chapter will summarize the experimental details and advancements made in vdW device fabrication. Starting with the preparation of vdW materials, two different graphene sources are introduced: large-area polycrystalline graphene and small-sized exfoliated graphene. While large-area graphene was mainly used in the beginning, device fabrication focused on exfoliated vdW materials towards the end of this work. Notably, isotopically purified ^{13}C graphene could initially only be obtained in the form of large-area graphene.

3.1.1. Large-Area Graphene

The large-area graphene used in this work is either commercially available ^{12}C monolayer graphene grown by chemical vapor deposition (CVD) (Graphenea) or isotopically purified ^{13}C few-layer graphene grown by molecular beam epitaxy (MBE). The ^{13}C few-layer graphene was provided by Dr. Joao Marcelo J. Lopes from the Paul-Drude Institut für Festkörperphysik Berlin. Both types of graphene are grown on thin copper foil, which acts as a catalyst and substrate during growth. Thus, the Cu foil needs to be removed from the graphene before it is transferred onto a target substrate. The whole large-area graphene fabrication process is adapted with modifications from Lyon *et al.*[23] and presented in short below.

The fabrication of large-area graphene devices is based on the widely used wet transfer approach.[23,160] First, a large piece of graphene on Cu foil is spin coated for 60 s with 4000 rpm with a protective layer of PMMA (950 K, AR-P 672.045, Allresist). This polymer resist also acts as a supporting layer during the wet transfer process to avoid crumbling of the

fragile graphene sheet. After cutting the PMMA-coated graphene on Cu foil into small pieces ($< 1 \times 1\,\mathrm{cm}^2$), individual pieces are placed floating for several hours in an aqueous solution of $Fe_3(NO_3)_3 \cdot 9\,H_2O$ to remove the Cu foil. After the copper foil is fully dissolved, the graphene piece with PMMA on top is transferred to clean DI water for 10 min at least three times. Subsequently, the graphene/PMMA piece is cleaned in a solution of 5 ml 32 % HCl, 4 ml 30 % H_2O_2 and 100 ml DI H_2O for 15 min to remove inorganic contaminants, followed by an additional DI water step. A second cleaning step is performed in a solution of 1 ml 30 % NH_4OH, 1 ml 30 % H_2O_2 and 100 ml DI H_2O for 3 min to reduce organic contaminants. After three more DI water steps, the graphene/PMMA piece is ready to be transferred onto the target substrate. This substrate and its preparation can vary depending on the intended experiment and device design. Before the graphene transfer, the substrate is cleaned with acetone and isopropanol before performing an O_2 plasma cleaning step. To transfer the graphene/PMMA on the target substrate, the floating graphene piece is carefully scooped up from below with the substrate. Any remaining water trapped in between the substrate and the graphene/PMMA is removed by drying the sample in an oven at 50 °C. The temperature is slowly increased to 150 °C and baked for another 15 min. The protecting PMMA layer is removed by immersing the sample in AR 600-76 PMMA remover (Allresist) for 30 min, followed by acetone and isopropanol cleaning. Finally, the graphene is annealed to the substrate in a rapid thermal annealer (RTA) at 180 °C for four hours. Afterwards, the large-area graphene is ready for further processing steps.

Due to the large-area of graphene grown by CVD and MBE, it is useful for applications and wafer scale fabrication.[161,162] However, CVD and MBE graphene typically exhibit a substantial amount of defects such as grain boundaries, wrinkles, folds and contamination from the transfer process.[22] Therefore, the electronic quality of CVD and MBE graphene is inferior to that achieved in single crystalline, exfoliated graphene.

3.1.2. Exfoliated 2D Materials

Exfoliated van der Waals materials offer unparalleled electronic quality and are the building blocks for complex vdW heterostructures. Small flakes of vdW materials are obtained after exfoliation, which can be stacked, twisted and encapsulated by hBN, hardly possible with CVD or MBE grown 2D materials. In the following, the exfoliation recipe is presented for graphene and hBN, which are the two vdW materials used in this work.

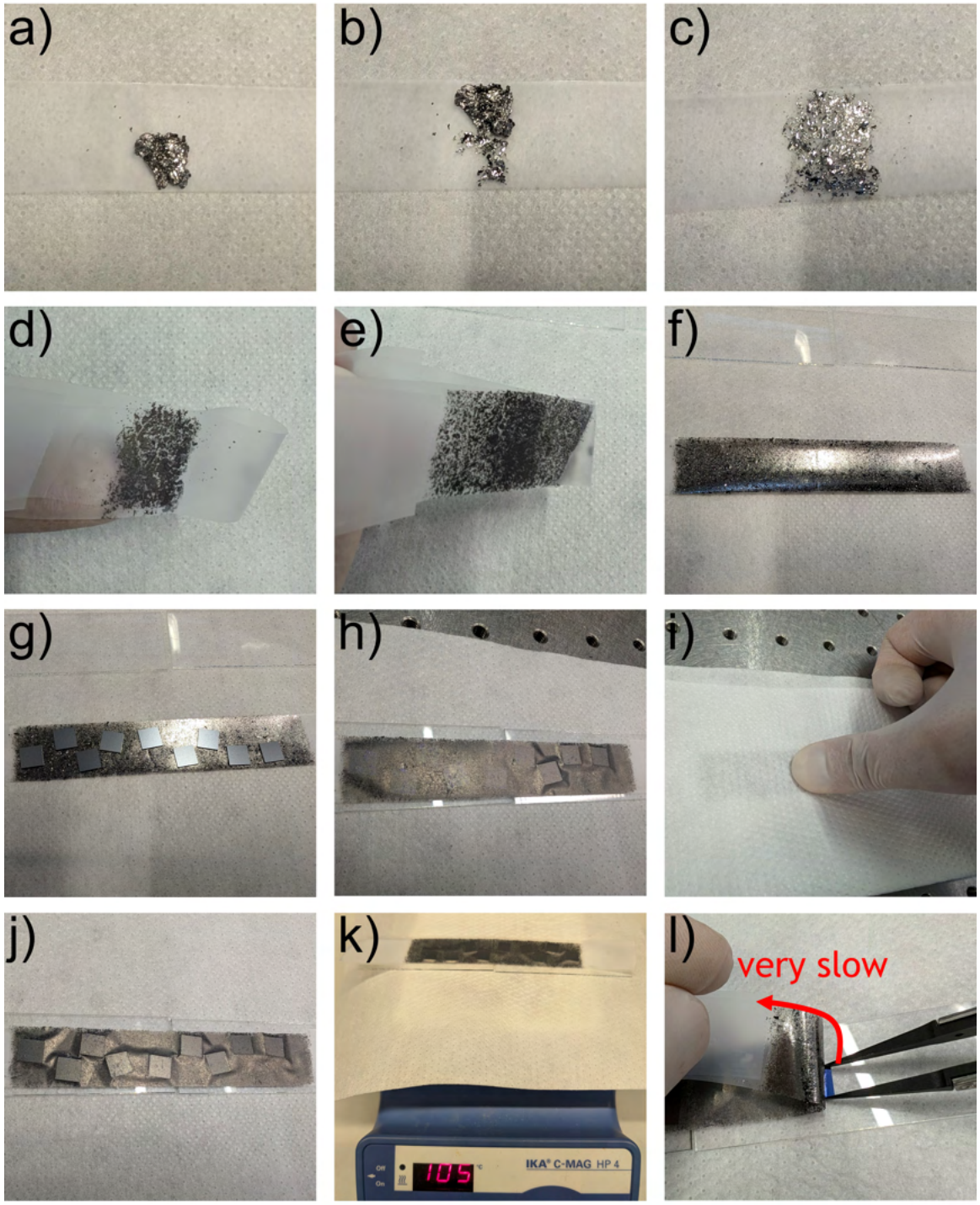

Figure 3.1.: a), b) A large graphite flake is placed on a piece of Scotch tape several times. c) A small but densely covered area should be the result. d) The graphite is first distributed along the width of the tape. e) With the minimum number of folds, the graphite is distributed across the entire length of the tape. f) The resulting tape should be very homogeneous and densely covered. g) Si chips are placed on the most homogeneous spots on the tape. h) The tape with the attached chips is flipped. i) The tape is covered with a wipe and pressed on the chips with a finger from the top. j) Applying pressure attaches the tape and its graphite to the Si surface and removes trapped air. k) The chips with the tape on top are heated at $\sim 100\,^{\circ}\mathrm{C}$ for 3 min. l) At room temperature, the tape is removed as slowly as possible.

Exfoliation

The flakes for subsequent fabrication steps are obtained by mechanical exfoliation from bulk crystals on silicon substrates with 285 nm dry thermal SiO_2 (Microchemicals). The 285 nm oxide layer is used to optimize the optical contrast of thin graphene, facilitating the identification of the desired flakes.[163] Small chips of $\sim 7 \times 7\,mm^2$ are cut from the silicon wafer after which dust is removed with nitrogen gun. Note that any wet cleaning steps including solvents are avoided. Following the process by Huang *et al.*, the Si chips are treated with strong O_2 plasma (> 2 min at 200 W and 20 sccm O_2) by reactive ion etching (RIE) immediately prior to exfoliation.[164] The O_2 plasma cleaning removes organic residues and ambient adsorbates, drastically increasing the yield of usable flakes. The same wafer treatment is used for all 2D materials.

The complete exfoliation process for graphene is shown in figure 3.1. The first step of exfoliation is the tape preparation. A large bulk graphite flake (flaggy flakes, NGS graphite) is placed several times on a small area of Scotch tape, leading to a densely covered region. The amount of material needs to be adjusted according to the length of the tape and requires training to obtain the best tapes. The tape is folded to cover as much tape as possible with the minimum number of folds (< 10 folds), as each fold will reduce the size of potential graphene flakes. Therefore, the first folds are used to spread the graphite across the width of the tape and to increase graphite spot density. The remaining folds are used to distribute the graphite material homogeneously across the entire length of the tape. Note, that for exfoliated ^{13}C graphene only small graphite crystals are available (NIMS Japan), which are placed directly on the tape.

Once the Si chips are treated with O_2 plasma, as many chips as possible (~ 5 - 10) are positioned upside down on the prepared graphite tape. Chips are placed on the most homogeneous areas on the tape. The tape with the attached chips is flipped and placed on a clean glass slide and covered with a clean room wipe. For graphene exfoliation, the tape is now pressed as hard as possible to the Si chips from the top with a finger for 1 min each. Note that the force should only by applied in vertical direction, avoiding any lateral movements that would destroy large flakes by shear forces. The pressing removes any trapped air between the graphite and the wafer, maximizing the contact area of the graphite flakes to the wafer, which will be important for the yield of large flakes. The glass slide with the mounted Si chips and attached tape is placed on a hot plate for three minutes at 100 °C. Longer heating periods and higher temperatures do not improve yield and instead lead to increased glue residues. After cooling down to room temperature the actual act of *exfoliation* is performed. While keeping the chips in place with a tweezer, the tape is peeled off as slow as possible. The slow motion is very important to avoid breaking of larger flakes. During the removal of the tape, the van der Waals forces of the graphene in contact to the silicon and of the graphene to its adjacent layers in the graphite compete. In the best case, the adhesion of the graphene to the SiO_2 surface is larger, resulting in cleaving of the graphite flake, which remains with the tape, leaving a monolayer graphene

flake on the chip. However, not only monolayers, but also bilayers, few-layers (3 - 10 layers) and multilayers (> 10 layers) will result from exfoliation on a wafer.

A similar approach is used for hBN flakes. The bulk hBN crystals are provided by Takashi Taniguchi and Kenji Watanabe from NIMS, Japan. These crystals have the best quality and yield the largest flakes after exfoliation. However, compared to graphite, their supply is limited and material efficiency is important. Hence, after a homogeneously covered hBN tape with a shiny, bright and colorful appearance is prepared from a few small hBN bulk crystals, an additional tape is attached to the first *mother* tape and subsequently peeled off. This process can be repeated three times, resulting in a total of four tapes (including the mother tape). This approach also results in thinner flakes in the end, which is desired for the stacking procedure. After placing as many chips as possible on a hBN *daughter* tape, the tape is gently pressed to the wafers with much less force since the hBN crystals tend to break into smaller pieces much easier. Without heating, the tape is left on the wafers for a few minutes before peeling off. Again, the tape is removed as slowly as possible.

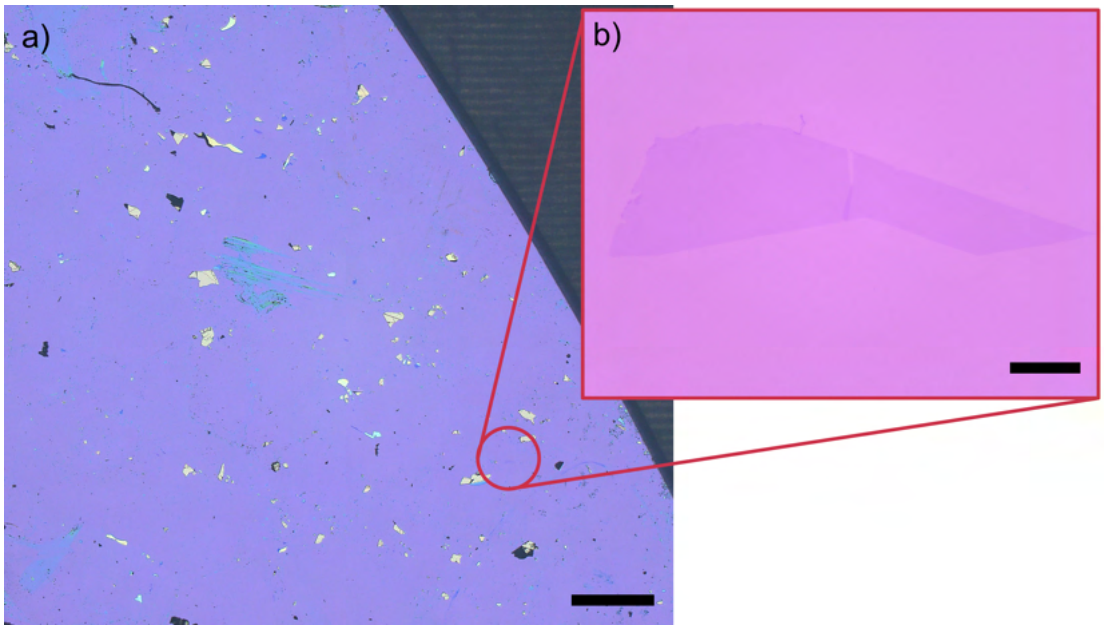

Figure 3.2.: a) Exemplary Si chip after mechanical exfoliation of graphene. Among glue residues and thick graphite flakes, thin graphene can be found as marked by the red circle. Scale bar is 1 mm. b) Magnified view of a large monolayer graphene flake found after exfoliation. Scale bar is 20 µm.

The identification of usable hBN and graphene flakes is performed with a good optical microscope (here Olympus BX51, other groups often use a Nikon Eclipse LV150 with NIS Elements software). Six criteria are used to evaluate the flakes: thickness, size, homogeneity, form, isolation and cleanliness. For each Si chip of an exfoliation run, a wafer map is created, capturing the location in combination with an optical image of good flakes. An exemplary Si chip after

mechanical exfoliation of graphene is shown in figure 3.2 a), with a magnified view of a monolayer graphene flake that can be found on this chip in b). To illustrate the selection criteria, figure 3.3 compares optical images of different graphene flakes. The three flakes shown in figure 3.3 a) to c) have a good size and thickness (< 3 layers), but are either inhomogeneous or badly isolated from other flakes, making them difficult to use during the stacking process. In contrast, the graphene flakes in d) to f) are well isolated, mostly homogeneous and have a large size. The flake in d) has a small crack at its center, which is actually an ideal position to cut the flake. This would allow cutting and twisting this flake, to fabricate twisted bilayer graphene. The same selection criteria also apply for hBN, although a few differences have to be considered. Figure 3.4 compares optical images of different hBN flakes. Since the used hBN flakes are typically multilayers with thicknesses between 10 nm and 40 nm, cracks and folds in hBN flakes, as shown in figure 3.4 a), can lead to tearing and folding of flakes during the stacking process. Additionally, thinner flakes generally lead to less *bubbles* trapped in between stacked layers and improve the visibility of graphene after stacking. Suitable hBN flakes should fully encapsulate the graphene flake and therefore require a large size in addition to good homogeneity, isolation and thickness. The thickness of hBN flakes can be measured by AFM or identified from their colorful appearance.[165] For 300 nm and 285 nm SiO_2 substrates, hBN flakes with the correct thickness range from a dark blue (10 nm) to a light green (40 nm).

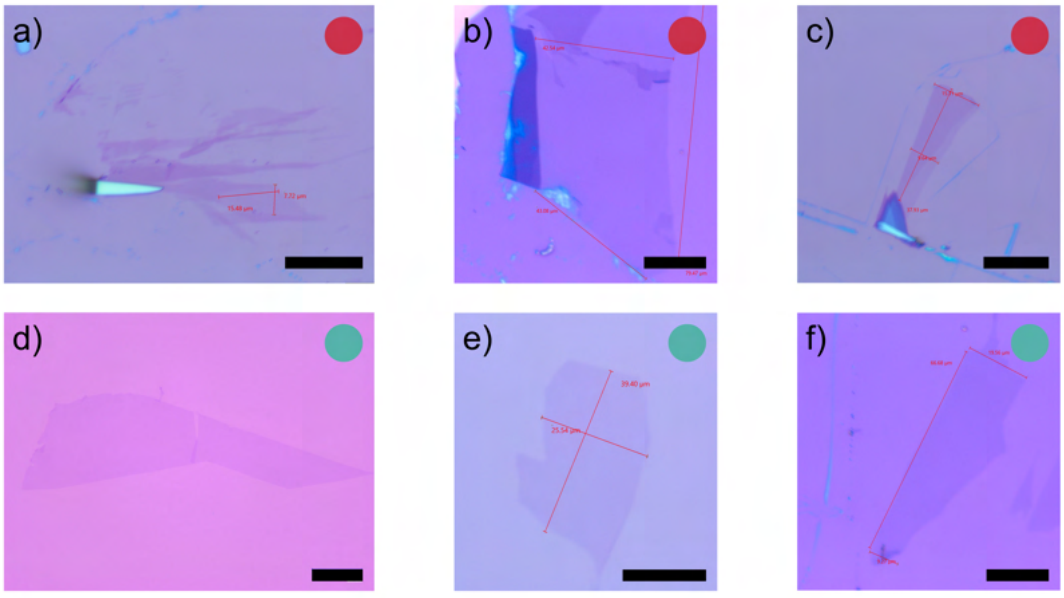

Figure 3.3.: a) to c) Unsuitable graphene flakes as indicated by the red dot. Although the flakes have a good size, they are inhomogeneous or not well isolated. d) to f) Suited graphene flakes that are homogeneous, well isolated and have a good size. The flake in d) could be used for twisted bilayer graphene due to the large size and a small crack in the center that could be used for cutting. All scale bars are 20 µm.

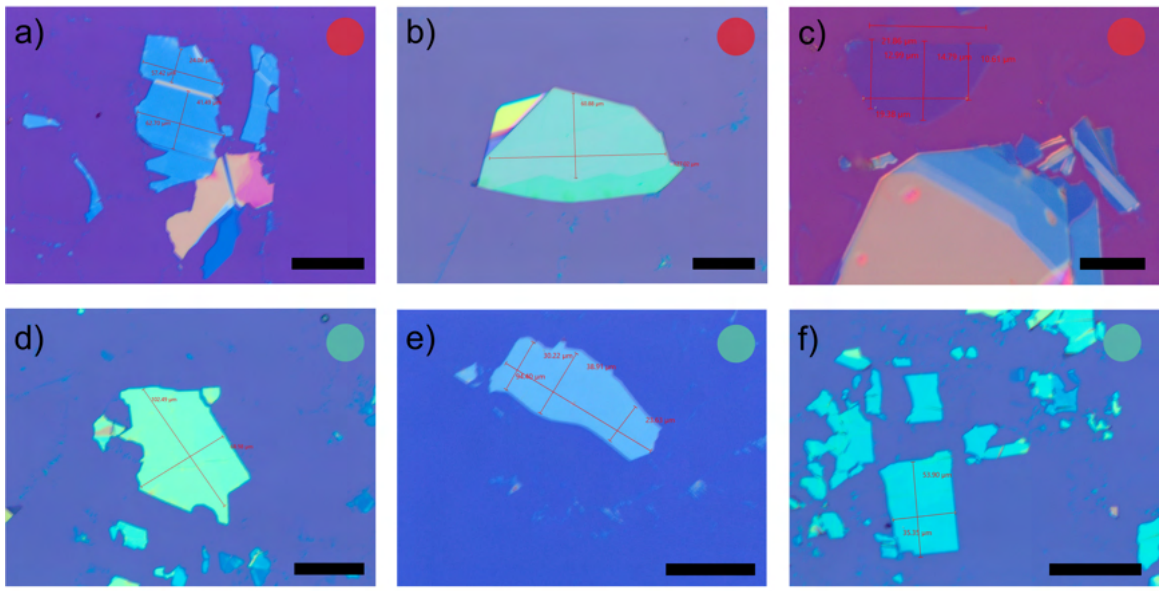

Figure 3.4.: a) to c) Unsuitable hBN flakes as indicated by the red dot. a) Due to the cracks and folds, this hBN flake is likely to disintegrate during stacking. b) Although this flake is very large, the flake is too thick to fabricate a stack. c) Although the thin hBN flake itself would be suited for stacking, the very thick flake in close proximity would lead to problems during the stacking procedure. d) to f) Well-suited hBN flakes for stacking with decent thickness, size, homogeneity and isolation. All scale bars are 50 µm.

The thickness of graphene flakes is mainly determined by optical contrast.[165] Without the necessary experience, optical contrast analysis can be performed with the open source software Gwyddion. However, a calibration and verification of the optical contrast values is recommended either by AFM or Raman spectroscopy.[166] The so-called G and 2D peaks in Raman spectroscopy allow for the reliable and accurate determination of the number of graphene layers.[166,167] Monolayer graphene typically exhibits an intensity ratio of the two peaks $I_{2D}/I_G > 2$ and a full width half maximum (FWHM) of the 2D peak of ≤ 30.[167,168] Raman spectroscopy excites vibrational modes that are inversely proportional to the square root of the atomic mass, making it sensitive to the mass constituents of carbon. Therefore, this method allows differentiation of natural ^{12}C graphene and isotopically purified ^{13}C graphene. The 2D and G Raman peaks display a shift toward lower wave numbers by a factor of $\sqrt{13/12}$ due to the mass difference between the isotopes.[169,170] The Raman spectra of different graphene species are compared in figure 3.5. The I_{2D}/I_G ratio for exfoliated monolayer graphene is significantly higher than for CVD monolayer graphene. The MBE-grown ^{13}C few-layer graphene shows a reduced I_{2D}/I_G ratio and a high 2D-FWHM, indicating 4 to 5 layers. The spectrum of this ^{13}C few-layer graphene also exhibits a large D peak, suggesting a high defect density. The characteristic

shift of the 2D and G peak to lower values is visible for both exfoliated and MBE-grown ^{13}C graphene.

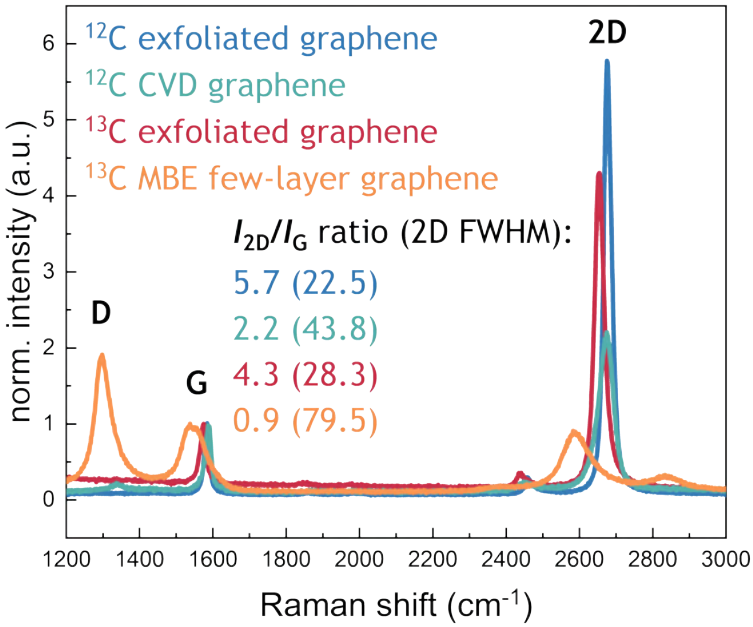

Figure 3.5.: Raman spectra of different graphene species: ^{12}C exfoliated monolayer graphene (blue), ^{13}C exfoliated monolayer graphene (red), ^{13}C CVD monolayer graphene (green), ^{13}C few-layer graphene (orange). The values for the respective I_{2D}/I_G ratios and the full width half maximum (FWHM) of the 2D peak are given, which are used to determine the number of layers. For comparison, all spectra are normalized to a G peak value of 1.

After identifying potentially useful hBN and graphene flakes, the final stack has to be planned. The active layer, i.e., the graphene, has to fit to the required geometric dimensions according to the intended experiment and device design. For small sized GJJs, even graphene flakes with just $10 \times 10\,\mu m^2$ are acceptable while other devices such as GTeraFETs may require elongated flakes with a minimum size of $40 \times 10\,\mu m^2$. For hBN-encapsulated graphene heterostructures, the hBN flakes should be large enough to comfortably cover the complete graphene flake, leaving space for potential misalignment or shifts during the stacking procedure.

Stamp preparation

The assembly of vdW materials can be performed in different ways. In this work, a modified dry-transfer technique is used that is based on polymer stamps.[171,172] These stamps need to be prepared prior to the stacking procedure and consist of two different polymers. The first step is to fabricate small hemispheres from polydimethylsiloxane (PDMS), in the following referred to as *PDMS bubbles*. The PDMS acts as a transparent, soft viscoelastic cushion for the vdW flakes during stacking. Approximately 5 g to 8 g of base component silicone elastomer is mixed with

its polymerization initiator (Sylgard 184) in a ratio of 10:1. After trapped air from the mixing of the two components is removed in vacuum for at least 30 min, small droplets of the PDMS mixture are placed on a hydrophobic 4" Si wafer. The functionalized hydrophobic surface of the wafer results in an increased contact angle of the droplets that promotes a stronger curvature. This method yields small droplets that should have a diameter of 2 nm to 3 mm. Typically, around 100 PDMS bubbles can be prepared in one run. The full polymerization of the PDMS bubbles takes 48 hours, after which they can be picked up carefully with a tweezer and moved into storage.

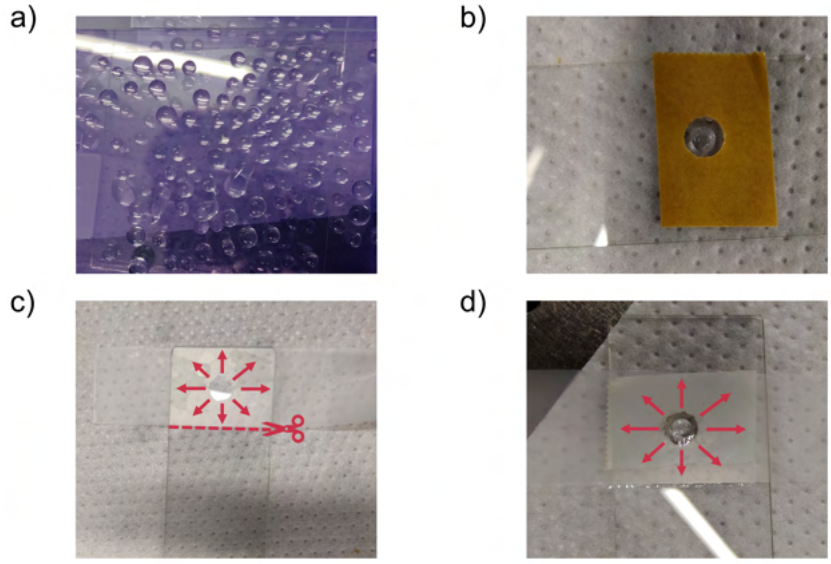

Figure 3.6.: a) Multiple PDMS bubbles with varying sizes stored on large glass slides. b) For the polymer stamp, a small PDMS bubble is placed in the hole in the center of double sided Kapton tape on a glass slide. c) Scotch tape with a hole is attached to a small piece of the prepared PC film. By making a cut, the remaining PC film is separated from the part which will be used for the stamp. d) The free standing PC film is positioned on top of the PDMS bubble and the Scotch tape is carefully attached to the Kapton tape.

In the next step, a thin film of polycarbonate (PC) is prepared, which acts as an adhesive layer to pick up the flakes. First, PC pellets are dissolved in chloroform to form a solution of 5 wt. % PC. The solution is left overnight and stirred on the next day to ensure that the PC pellets are completely dissolved. The final PC solution can be used for several weeks. As chloroform will evaporate over time, the concentration will become incorrect after extended use, making the solution no longer usable. To fabricate the PC film, two very clean glass slides are required that are cleaned thoroughly with acetone and isopropanol and blow dried with N_2 beforehand. One of the glass slides is used as a substrate for 5 to 8 droplets of PC solution. Then, the second glass slide is placed on top to homogeneously distribute the PC between the glass slides. By sliding

the two glass slides apart, a thin and homogeneous film is obtained on both glass slides. Both glass slides with PC film on top are heated for 5 min at 95 °C to remove solvent residues and to improve the homogeneity of the film. The fabricated PC films should be used within two weeks.

When the PC films and PDMS bubbles are prepared, it is possible to fabricate the complete PDMS/PC stamps as depicted in figure 3.6. For this, a $1 \times 1\,\mathrm{cm}^2$ piece of double sided Kapton tape is placed on one end of a clean glass slide after punching a hole in the center of the Kapton tape piece. A small PDMS bubble is placed in the center of this hole as shown in figure 3.6 b). A piece of Scotch tape is also equipped with a hole in its center and subsequently placed on the glass slide with the fabricated PC film. Since the PC film will be used for multiple stamps, only a minimum region of PC film is covered to maximize the yield. The Scotch tape is carefully pressed to the PC film to optimize contact and a cut is made with a scalpel next to the tape. The tape can be slowly peeled off together with the PC film, resulting in a freestanding PC film in the hole region. Finally, this PC film is aligned and transferred on top of the PDMS bubble and the double sided Kapton tape. By carefully removing any trapped air between the Scotch tape and the Kapton tape, the PC film is slightly stretched and conforms tightly to the PDMS surface. After cutting any excess Scotch tape, the stamp is finished and ready for stacking.

It was found that other stamp preparation methods did not result in reproducible and good results. For example, spin coating the PC solution on the glass slides equipped with PDMS bubbles tends to result in thinner films which are prone to tear during the stacking process. This is independent of the spin coating parameters and probably a result of the hemispherical shape of the PDMS. Furthermore, for an extended time, polypropylene carbonate (PPC) was used as an alternative adhesive polymer before moving to PC. Earlier reports on the dry transfer technique used the temperature dependent adhesion of PPC to vdW materials to pick-up and release individual flakes.[173] However, the general adhesion of PPC is much lower than for PC, which often results in unsuccessful stacking steps. For the PPC-based technique, temperatures between 40 °C and 110 °C are used during the stacking process. For the PC-based technique, much higher temperatures up to 180 °C are necessary which only became available in a new setup towards the end of this work.

van der Waals aligner

The assembly of vdW flakes is very delicate and requires high-precision control of their positioning. This is possible by the use of a so-called *van der Waals aligner*. In this work, two different setups are used which were built in-house by Dr. Chithra H. Sharma. The main features of such a van der Waals aligner are described below.

The aligner is shown in figure 3.7 and can be divided into three main sections which are the sample stage (A), the stamp stage (B) and the optical microscope (C). Each of these sections can be divided again into individual subsections. The chips with different vdW materials are

placed on a sample heater plate (A1) and are kept in place by either vacuum or Kapton tape. The chips on the sample heater plate can be rotated with a precision of 0.04 ° by a motorized rotation stage (A2) below. A high precision in angle control is important for the fabrication of twisted moiré structures such as TBG. Three micromanipulators (A3) enable position control in X-, Y- and Z-direction. With the Z-control, the chips are brought into contact with the polymer stamp, which is held in place by vacuum on a metallic arm (B2). To position the stamp correctly, the metallic arm can be moved in X- and Y-direction by an additional manipulator (B1). The stacking process is controlled via an optical microscope equipped with different objective lenses (C1) ranging from 10× to 50× magnification. The microscope is also equipped with a camera and the associated imaging software that allows to capture images, videos and to draw shapes on screen (C2). The quality of the camera is important to identify even thin flakes such a monolayer graphene during the stacking process. Taking images during the stacking process and marking individual flakes is essential to ensure proper alignment of the flakes to each other and to the electrical connections in the subsequent device fabrication.

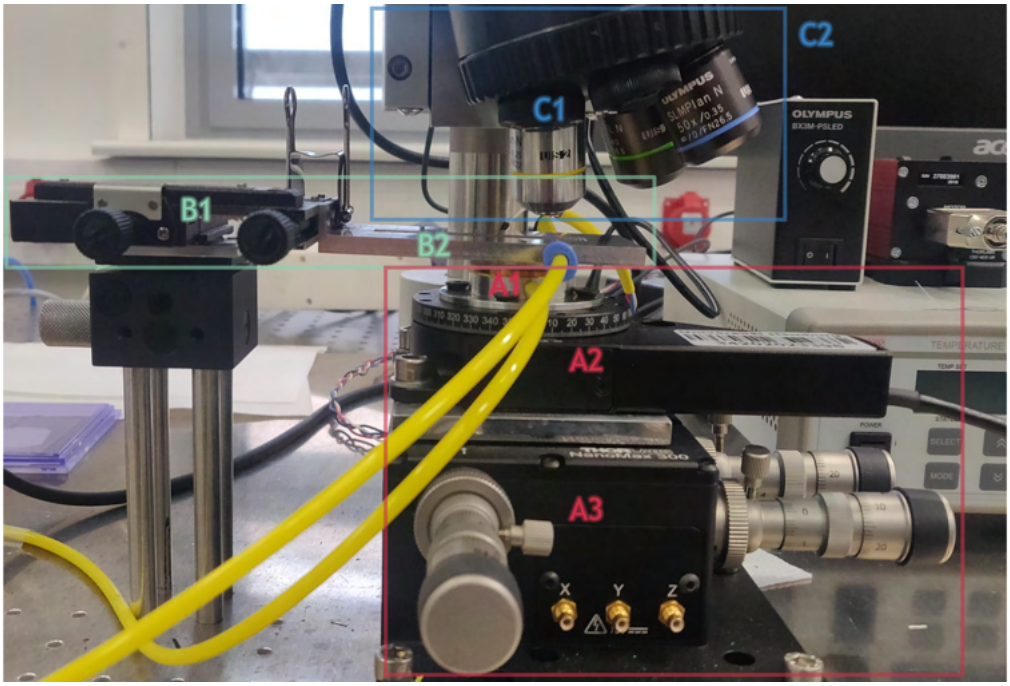

Figure 3.7.: Overview of the home-built van der Waals aligner setup, that can be divided into three sections. The sample stage (A) consists of the sample heater plate (A1), a motorized rotation stage (A2) and three micromanipulators (A3), which enable control in X-, Y- and Z-direction. The stamp stage (B) allows positioning in X- and Y-direction (B1) of the stamp on a glass slide, that is attached by vacuum to a metallic arm (B2). Visual control of the stacking process is provided by an optical microscope (C) equipped with different objective lenses (C1) and a camera connected to a monitor (C2).

Cutting graphene

In the first experimental reports on TBG, device fabrication included a method referred to as *tear-and-stack* technique that was used to align two graphene sheets with a controlled and small twist angle.[24,85] By tearing a single graphene flake in half, two graphene pieces with the same crystallographic orientation are obtained, which is the precursor for small twist angle alignment. However, this method introduces a lot of strain to the graphene sheet due to the large tension during the tearing process. The so-called *cut-and-stack* technique circumvents this by cutting the graphene flake first, for example with an AFM cantilever.[92] It is worth mentioning that this technique was adopted from the group of Prof. Dmitri Efetov (LMU München) to our fabrication process after our research visit to the Efetov lab. Optical images that illustrate the technique are shown in figure 3.8.

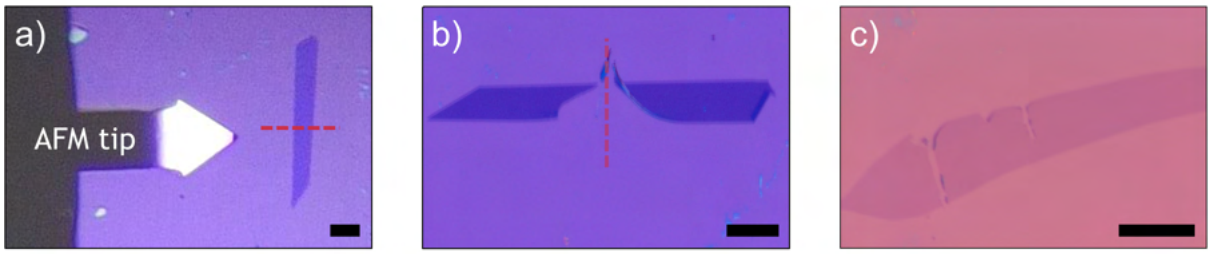

Figure 3.8.: a) Cutting graphene flakes can be performed with an AFM tip attached to a polymer stamp. The cantilever deflects the light when brought in contact with the graphene wafer and appears bright. The graphene flake is cut along the dashed red line in one continuous movement of the AFM tip. b) Optical image after cutting the flake in a). Due to the mechanical rigidity of thicker flakes, as the one shown here, the flake folds onto itself during the cutting. c) Cutting thin graphene flakes typically results in a small cut. Elongated flakes can be cut multiple times to obtain more graphene pieces with identical crystallographic orientation. All scale bars are 10 µm.

To cut graphene flakes with an AFM tip, a modified polymer stamp is used. Instead of the PC-film, an AFM cantilever is positioned on the PDMS bubble and fixed with Scotch tape. Subsequently, this AFM tip stamp can be attached to the stamp holder arm of our aligner setup. A Si chip with exfoliated graphene is loaded and the AFM tip is positioned close to the desired graphene flake as shown in figure 3.8 a). When the AFM tip is brought into contact with the wafer, the optical reflectance of the cantilever changes and the tip starts to appear bright instead of dark. The tip can then be moved across the graphene flake in one continuous movement to perform the cut. Ideally, the graphene flake is cut in two pieces separated by a gap of approximately 1 µm width without any folding. However, this only works for thin graphene flakes up to ~ 5 layers. Thicker flakes can also be cut, but typically fold onto themselves as shown in figure 3.8 b), which is not acceptable for high-quality devices. Graphene flakes with high aspect ratios can be cut several times as indicated in figure 3.8 c), which is necessary for

twisted trilayer graphene.

Compared to graphene cutting techniques based on optical laser systems,[93] the AFM tip cutting technique has two advantages. First, the method is technically undemanding and cost-effective because it only requires additional AFM cantilevers. Secondly, it can be implemented with ease in the device stacking process, since it is conducted at the aligner setup, thereby avoiding an extra sample transfer. Additionally, the AFM tip-based technique is very versatile and allows to remove undesired thicker graphene or hBN flakes on the Si chip surface, i.e., to clean the pick-up area.

Stacking process

After the exfoliation and identification of appropriate graphene and hBN flakes, the graphene heterostructure can be assembled in a stacking process, using the previously prepared polymer stamp. Images of each step of this stacking process are shown in figure 3.9. Prior to the first pick-up of the top hBN flake, the sample stage is heated to 110 °C to remove moisture from the wafer surface. While maintaining the temperature, the stamp is brought into contact with the hBN wafer. As depicted in figure 3.9 b), the area of the polymer stamp in contact with the Si surface is clearly visible. The hBN flake should be positioned off-center in a clean area of the PC film. This allows a continuous and slow movement of the contact front across the desired flakes, which is controlled by carefully adjusting the micromanipulator of the Z-direction. After marking the flake in the software and maintaining contact for 30 s to 60 s, the contact front is carefully pulled back to pick up the hBN. When the wafer is fully retracted, the heater is turned off until the graphene wafer is loaded on the sample stage of the aligner. To pick up the next flake, care should be taken in the rotational alignment of the wafer in regard to the positioning of the previous flake. When the top hBN is aligned correctly to the desired graphene flake, the stamp is again slowly brought into contact, as shown in figure 3.9 d). Note, that the contact front will push out contaminants in between the flakes towards their edges. If controlled correctly, bubbles of trapped contaminants can be reduced significantly.[174] Due to the strong adhesive forces between the hBN and the graphene flake, the graphene will be picked up when the stamp is pulled back similarly to the first pick-up. This process is repeated for the third pick-up of the bottom hBN [figure 3.9 f)] before the hBN-graphene-hBN stack will be released on a target wafer. This target wafer [figure 3.9 g)] is equipped with prepatterned alignment markers and bonding pads. For the release, a different aligner setup enables the use of higher temperatures. The target wafer is treated with strong O_2 plasma for a minimum of 5 min prior to the release to increase the adhesion of the released stack to the Si. After loading the target wafer to this aligner, the temperature is set to 140 °C. At this temperature, the wafer is brought into contact with the stamp and the previously assembled stack. The temperature is raised to 160 °C to melt the PC film. When the wafer is now slowly separated from the polymer

stamp, the PC film delaminates from the PDMS bubble while sticking to the target substrate. If this is successful, the temperature is subsequently increased to 180 °C to melt the PC even further, while continuously separating the substrate from the stamp and releasing the stack on the substrate.

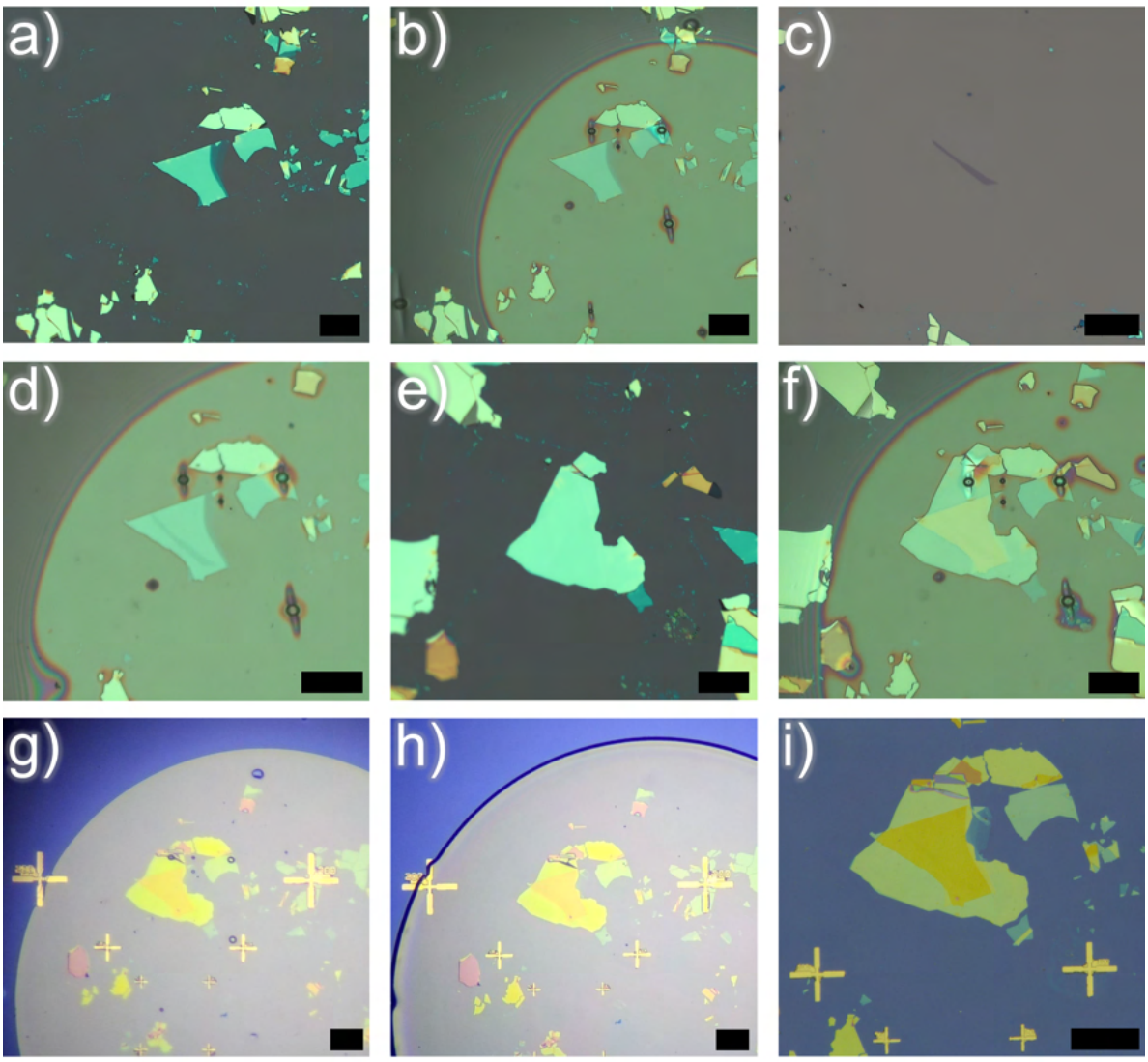

Figure 3.9.: Optical images representing the steps of the stacking process for a hBN-graphene-hBN heterostructure. a) Optical image of the top hBN flake. b) The polymer stamp is in contact with the wafer surface and the circular contact front is moved across the hBN flake. c) Target graphene flake. d) After aligning the top hBN flake to the graphene, it is carefully brought into contact. e) Bottom hBN flake. f) The pick-up process is repeated for the bottom hBN, thereby fully encapsulating the graphene. g) The stack is brought into contact with the target wafer for the release. h) The stack is released after melting the PC film from the stamp. i) Optical image of the finalized stack on the target substrate. All scale bars are 50 µm.

After the release, the fabricated stack and the melted PC film remain on the target substrate as shown in figure 3.9 h). For increased adhesion, a minimum period of 24 hours is kept in between the release and the subsequent removal of the PC film. The PC is removed by immersing the sample in chloroform, followed by rinsing in isopropanol and nitrogen blow dry. Finally, the sample is annealed at 180 °C for four hours in the RTA to reduce contaminants between the flakes and to further increase adhesion of the stack.

3.1.3. Lithographic Processing and Contact Engineering

In addition to the assembly of van der Waals materials on the target substrate, lithographic processes are employed to fabricate the final electronic devices. The lithographic fabrication is mainly composed of four different techniques: photolithography, electron beam lithography (EBL), reactive ion etching (RIE) and metal evaporation by physical vapor deposition (PVD).

Photolithography

Lithographic processes in micro- and nanofabrication use a temporary sacrificial layer, which is referred to as resist, that can be patterned in a controlled way. The pattern of the resist layer is transferred to another material layer, either by etching (RIE) or deposition (PVD), before the resist is removed.

In photolithography, the resist is sensitive to UV light, which is provided in this process by a mask aligner equipped with a mercury lamp source. All resists can be divided into positive resists (exposed areas will be removed in the development process) and negative resists (exposed areas stay after development). For our fabrication processes, mostly a double layer of positive photoresist consisting of LOR-5A (Microresist, spin coated at 6000 rpm for 1 min) and S1813 (Microresist, 4000 rpm, 1 min) is used to create an undercut. After each spin coating step, the samples are baked at 160 °C (LOR-5A) and 115 °C (S1813). The samples are loaded to the mask aligner (MJB3 or MJB4, Süss MicroTec) and aligned to the desired design on the photo mask. After UV exposure for 10 s, the samples are developed in MF-319 (Microresist) for 45 s and stopped in DI water. Subsequently, the samples can be treated with the next process such as metal deposition. The photoresists can be removed in PG remover (Microresist), followed by acetone and isopropanol cleaning.

Numerous photo masks with different patterns have been designed and fabricated during this work. The 4 inch mask blanks (g-materials) consist of borosilicate glass and are fully coated with a layer of chromium and AZ 1500 positive photoresist. In some cases, this resist is replaced with S1813 for compatibility reasons with other process chemicals. The design pattern is written with a laser writer (Heidelberg DWL 66^+) and developed. Afterwards, the mask is immersed in a bath of chrome etch (Microresist) for 1 min to transfer the design pattern into the Cr-layer,

before stopping in DI water for 1 min. The mask is finished after resist removal. Possible resist residues can be removed either in O_2 plasma or a Piranha solution wet etch.

Depending on the available equipment, either photolithography or electron beam lithography is used to write the mask design. The main differences are the process resist and the extended exposure time during EBL.

Electron beam lithography (EBL)

In EBL, the resist is sensitive to the dose deposited by a focused electron beam. The resolution achieved by EBL can be below 10 nm and is therefore much smaller than the resolution limit of photolithography. In contrast to photolithography, EBL is a maskless technique, which allows to draw custom designs and pattern. However, this leads to long writing and exposure times for large areas. For our EBL process, a combination of two positive PMMA resists with different molecular weights (600 K, AR-P 662.04, Allresist and 950 K, AR-P 672.045, Allresist) is used to create an undercut after development, which improves lift-off results. The PMMA resist layers are spin coated at 4000 rpm for 1 min and subsequently baked at 150 °C for 3 min. Note that all lithographic processes should be performed within 24 hours after spin coating the PMMA resist to ensure easy and reproducible resist removal. The spin coated samples are transferred into the EBL Voyager system (Raith) and exposed with a previously calibrated dose. Larger structures need a lower dose while small nanoscale structures require a larger dose. For our purposes, doses ranging between 290 µC/cm^2 to 350 µC/cm^2 lead to good results, after development for 60 s in AR 600-55 (Allresist) and stopping in isopropanol. After treating the samples with the intended process, the PMMA resist is removed in AR 300-76, followed by acetone and isopropanol cleaning.

Reactive ion etching (RIE)

In order to pattern materials, RIE is employed, which utilizes plasma etching with physical and chemical etching contributions. The samples are loaded into the vacuum chamber of the RIE instrument (Sentech SI 500), which is subsequently flooded with reactive gases. Upon plasma ignition, the etching process starts as the process gas is ionized and reacts with the material to be etched. The RIE uses a radiofrequency (RF) plasma and an inductively-coupled plasma (ICP), whose plasma power can be adjusted to achieve the desired etching behavior. The etching rate of a material is a combination of many different parameters and requires careful tuning. The most important parameters are the process gases and their ratios, chamber pressure, plasma power and temperature. For our device fabrication mainly three different etching processes are used. One etching recipe is based on O_2 plasma that is typically used for 30 s to remove organic contaminants and excess graphene. The parameters for the RIE process are 2 Pa, 50 °C, 20 W RF power, 300 W ICP power and 20 sccm of O_2. Another etching recipe uses a combination

of O_2/CHF_3 in a 1:10 ratio to etch exfoliated hBN-graphene heterostructures. The process is conducted at 3 Pa, 0 °C, 60 W RF power, 4 sccm O_2 and 40 sccm CHF_3, resulting in an etching rate of $\sim$ 30 nm/min. The resulting etch profile was verified by AFM measurements and is in agreement with previous reports,[66] as shown in the appendix A.1. To pattern Nb, NbN and NbTiN thin films, a third RIE process is conducted for 5 min to 7 min with 3 Pa, 23 °C, 40 W RF power, 120 W ICP power and 20 sccm SF_6 gas. More details on the use of these RIE processes are discussed in the individual device fabrication below.

Physical vapor deposition (PVD)

For the fabrication of devices in this work, metals are used either as electrical contact material, gate or as a conductor in microwave circuits. Generally, the term physical vapor deposition can be divided into different types which are thermal evaporation, electron beam evaporation and sputtering. The feasibility of each PVD subtype depends on the melting point of the metal to be deposited. For most metals electron beam evaporation is used. In section 3.3, the sputtering of superconducting niobium and niobium nitride thin films is discussed in detail. Compared to the sputtering setup, the PVD deposition chamber for thermal and e-beam evaporation (Balzers, PST) reaches lower vacuum pressures during evaporation of $\sim 10^{-7}$ mbar and allows lower deposition rates (typically 1 - 3 Å/s). During this work, the available materials mounted in the PVD chamber are Cr, Au, Cu, Ti, Al, and Ni.

Electrical contact engineering

Forming high-quality metallic electrical contacts to the 2D electron system is paramount to enable quantum transport measurements in vdW materials. Due to its semimetallic nature, contacting graphene is significantly easier compared to semiconducting materials such as MoS_2, where device contacts often suffer from Schottky barriers. However, even for graphene, contact performance can be degraded by defects and impurities from the fabrication process leading to non-functional contacts at cryogenic temperatures. Hence, contact engineering is important to increase the overall contact yield in fabrication and to optimize the contact transparency. Looking for means to maximize these two factors, three electrical contact architectures are presented and evaluated below.

Top contacts

For large-area graphene, metallic contacts are typically fabricated by depositing the metal on top, followed by lift-off. This approach can also be used for exfoliated graphene samples that are not encapsulated, leaving the graphene exposed for the metal deposition.

After the transfer of CVD or MBE graphene to the target substrate, a large-area of the substrate is covered by graphene as shown in figure 3.10 a). To define a Hall bar geometry, the

excess graphene has to be removed in an EBL step to avoid electrical shorts between the contacts. The samples are spin coated with a double layer of PMMA 950 K resist, exposed with 290 µC/cm^2 and developed as described above. Strong O_2 plasma in the RIE is used for 30 s to remove the excess graphene, before removing the PMMA resist. As a result, multiple separate graphene Hall bars are obtained, as shown in figure 3.10 b), which can be electrically contacted by an additional EBL step. A double layer of PMMA 600 K and 950 K resist is used, exposed again with 290 µC/cm^2 and developed. Metallic contacts are formed by depositing 7 nm chromium as adhesion promoter and 70 nm gold by electron beam evaporation. This is followed by lift-off in AR 300-76, acetone and finally isopropanol to remove the excess metal. In some cases, short and mild ultrasonic treatment is used to facilitate the lift-off. The finalized device is shown in figure 3.10 c).

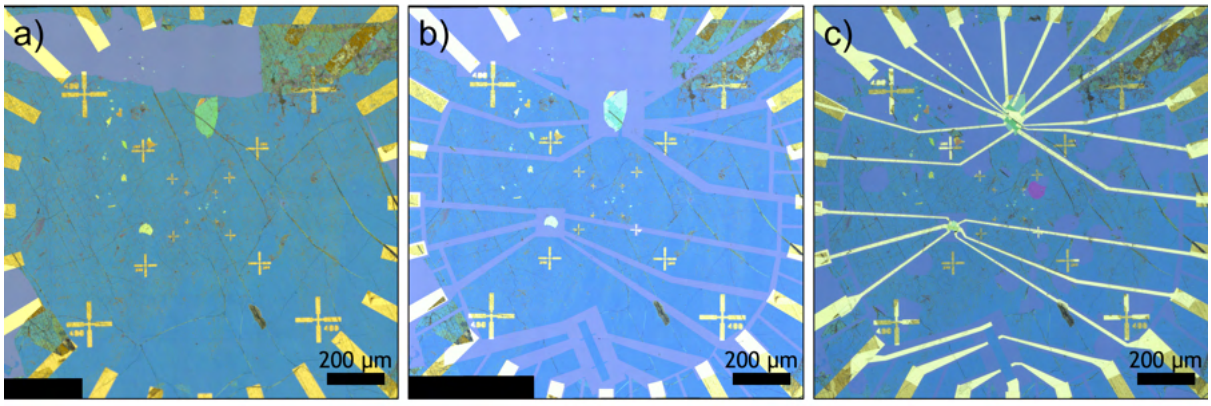

Figure 3.10.: a) Optical image of a large-area MBE-grown graphene sheet after its transfer on the target substrate, covering many of the prepatterned gold electrodes. b) After the first EBL step, excess graphene is removed and the individual graphene Hall bars are separated from the remaining graphene. c) After the second EBL step and lift-off, the final device is obtained with Hall bars that are electrically connected by Cr/Au electrodes.

A schematic of metallic top contacts is depicted in figure 3.11 a). Such top contacts are used mostly for large-area graphene as shown in figure 3.11 b), but can also be employed to electrically probe exfoliated graphene devices on Si [figure 3.11 c)] or hBN [figure 3.11 d)]. Since the electrical properties of exfoliated graphene are preserved much better by hBN-encapsulation, top contacts are rarely used.

Electrical contacts to graphene fabricated from the top suffer from several drawbacks. The direct evaporation of metal on the graphene surface can lead to defects resulting from the bombardment with high-energy metal species. Moreover, residues from the lithographic processes can remain on the graphene surface and act as a barrier layer in between the graphene and the metal. Furthermore, it has been shown that top contacts to graphene generally exhibit a larger

contact resistance compared to other contact geometries.[66,175] As a result, non-functional top contacts are found repeatedly and on a regular basis.

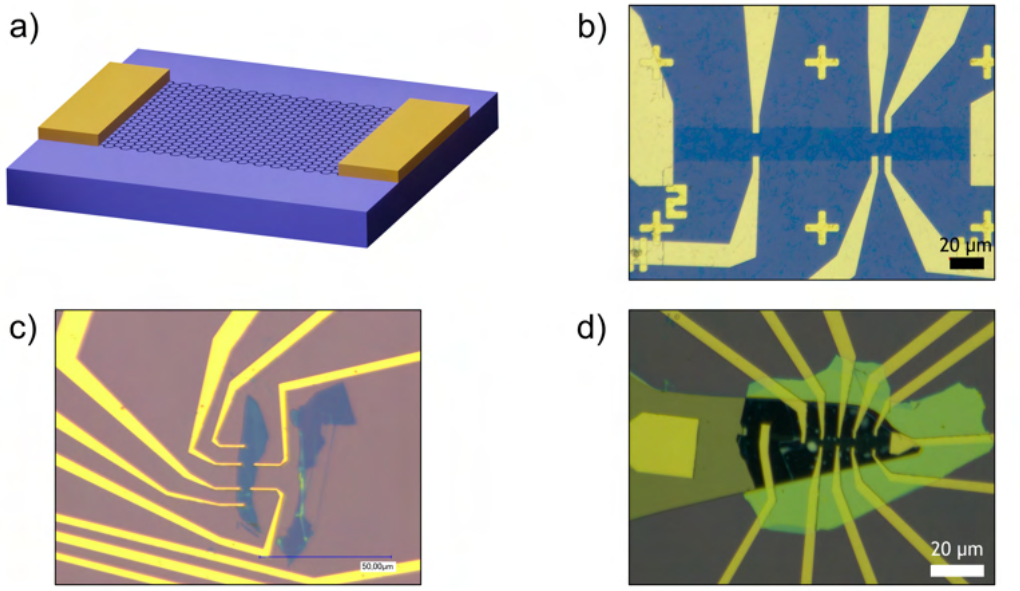

Figure 3.11.: a) Schematic of metallic gold electrodes on top of the graphene sheet. b) Optical image of a large CVD graphene Hall bar with Cr/Au top contacts. c) Optical image of an exfoliated few-layer graphene sample on Si with metallic contacts from the top. d) Graphene heterostructure, involving a graphite backgate separated by a bottom hBN layer and gold top contacts.

Graphite contacts

Graphite flakes can be used as an alternative approach to circumvent the issue of non-functional metallic top contacts. This approach is inspired by the works of Zhou *et al.* and Seiler *et al.*, which demonstrated high-quality transport measurements by using graphene devices equipped with graphite contacts.[96,98] A schematic representation of the graphite contacting approach is displayed in figure 3.12 a). The hBN-encapsulated graphene sample is connected to two graphite flakes, which protrude beneath the top hBN. These graphite layers can subsequently be contacted by large Cr/Au contacts.

However, this approach requires more steps during the stacking procedure, which increases the difficulty and risk of an unsuccessful assembly. If the stacking is successful, a complex heterostructure is obtained, as shown in figure 3.12 b). The metal Cr/Au electrodes to the graphite that were fabricated in an additional EBL step are indicated by the yellow dashed lines. The major drawback of this approach is the reduced number of contacts due to the extra pick-up step for each contact. Therefore, this approach is mostly intended for the GTeraFET project, where

only two contacts to the graphene are required.

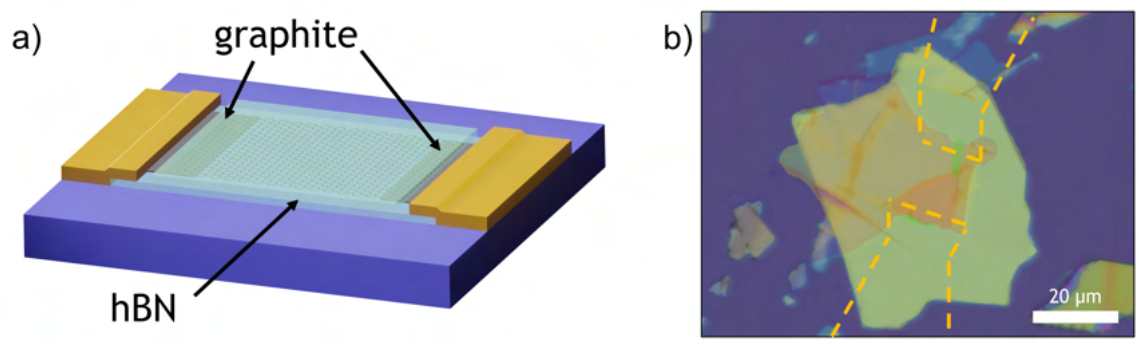

Figure 3.12.: a) Schematic of the approach using graphite flakes as contact material. The two graphite flakes contacting the graphene sheet and protruding the stack can be contacted by metal electrodes. b) Optical image of a finished stack equipped with two graphite contacts, indicated by the green marking. The graphene flake (dark orange) is encapsulated by the top (smaller, brown) and bottom (larger, green) hBN flakes. The metallic electrodes connecting the graphite contacts are indicated by the yellow dashed lines.

Edge contacts

The encapsulation of graphene with hBN protects the graphene from environmental conditions. However, this also means that the hBN has to be removed locally to electrically contact the buried graphene sheet. Based on the initial work by Wang *et al.*,[66] most of today's research on graphene devices utilizes edge contacts, as shown schematically in figure 3.13 a). In this approach, the hBN-encapsulated graphene is contacted along its edge, where additional σ bonding orbitals are exposed.[66,175,176] Hence, the resulting graphene heterostructures show higher electronic performance.[66] Since the metal only contacts the edge instead of an area from the top, this contacting approach is also referred to as 1D contacts to a 2D material.[66]

In this work, this contacting approach was adopted to improve the contacts to graphene devices. The contacts are fabricated by defining a pattern by EBL on top of the hBN-graphene stack, followed by a RIE etching step in a O_2/CHF_3 plasma with a 1:10 ratio as described above. The etching process removes the stack, resulting in an etch profile with an angle ($\sim 45°$).[66] Immediately after the etching, the sample is transferred to the PVD chamber to minimize contaminants at the exposed graphene edges. After deposition of Cr/Au contacts (7 nm/70 nm), lift-off is performed to remove the PMMA resist (600 K/950 K double layer) and the excess metal. Since the same PMMA mask is used for the whole process, the method is also referred to as *etch-and-fill* technique.

One of the first fabricated graphene devices with edge contacts was investigated by scanning electron microscopy (SEM), which is illustrated in figure 3.13 b). The inset shows a magnified

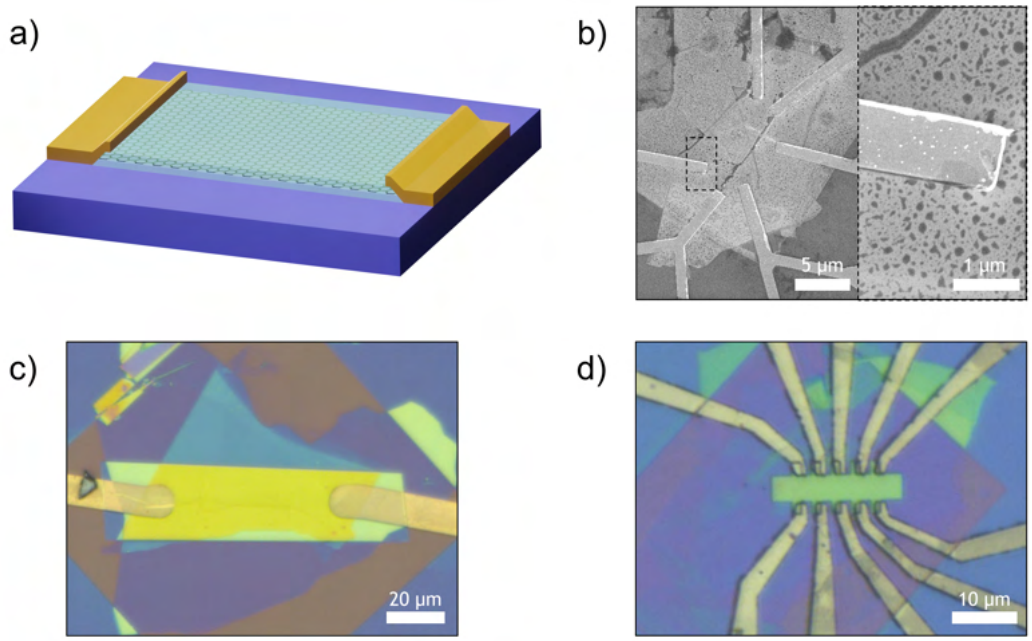

Figure 3.13.: a) Schematic of edge contacts to graphene devices. A CHF_3-based plasma etch process exposes the graphene edge. Metal deposition is carried out directly afterwards to reduce surface contamination. b) Scanning electron microscope (SEM) image of one of the first graphene devices with edge contacts. The inset shows a magnified view of one contact. However, the etch profile is not easy to identify. c) A rectangular shape is carved out of the hBN-graphene-hBN stack in a first etching step using the same etch process. In the second step, the edge contacts are formed using the *etch-and-fill* technique. d) More advanced devices are patterned into a Hall bar shape with arms first, before the final contacts are fabricated.

view of one contact, however, the etch profile is difficult to identify. Therefore, the etch profile was verified by AFM measurements, as shown in the appendix A.1. To obtain a defined graphene structure, hBN-graphene-hBN stacks can be first patterned in a rectangular shape by the same etching process before the contacts are fabricated. An exemplary sample is depicted in figure 3.13 c). Since the Si surface is also slightly etched, the surrounding Si surface appears is a different color. More advanced devices are patterned into Hall bar shapes with small arms, to optimize the contact configuration, as shown in figure 3.13 d). The edge contact method generally results in a significant increase in contact transparency and contact yield.

Electrostatic gating

In order to tune the charge carrier density in graphene, electrostatic gates are employed. In this work, mostly backgates are used, consisting of a highly p-doped Si substrate. However, some devices are equipped with a local graphite or gold backgate. For transport measurements, a combination of a global p-Si and a local graphite backgate is ideal. In this case, the global p-Si

backgate can be used to tune the small contact arms to high transparency/low resistance, while the local graphite gate allows control of the carrier density in the graphene layer.

Devices equipped with high-frequency circuits are fabricated on insulating substrates to avoid dielectric losses. In these cases and for graphene terahertz field-effect-transistors (GTeraFETs), the fabrication of top gates is necessary. To enable plasmonic excitations in the GTeraFETs, metallic gold topgates are mostly fabricated in this work. Two example devices are compared in figure 3.14 a) and b).

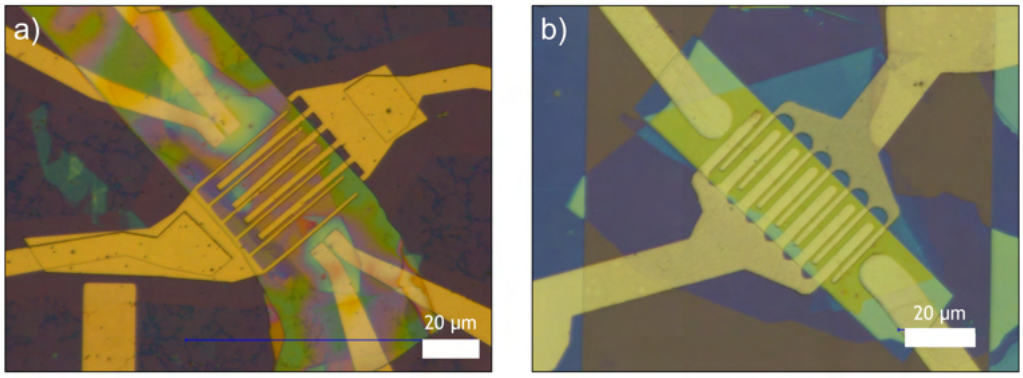

Figure 3.14.: a) Optical image of an asymmetric dual-grating gate graphene terahertz field-effect-transistor device of the first generation, consisting of CVD graphene on hBN. The graphene is covered by a second large hBN flake before the metallic topgates can be fabricated by EBL and PVD. A few gate fingers have detached due to the thick top hBN. b) Optical image of GTeraFET device made from hBN-encapsulated exfoliated graphene. The asymmetric gold topgates have a rounded design to optimize the lift-off results after EBL and PVD.

The first generation GTeraFET device in figure 3.14 a) consists of large-area CVD graphene on hBN with source and drain top contacts. After the contact fabrication by EBL (PMMA 600 K/950 K) and PVD, the top hBN is placed on the graphene before the metallic topgates can be fabricated in a second EBL and PVD run. Due to the large size and thickness of the hBN layers, some of the fabricated topgate finger have detached. The device in figure 3.14 b) belongs to the newest generation of asymmetric dual-grating gate GTeraFETs, consisting of a high-quality hBN-encapsulated graphene heterostructure. After shaping the stack by EBL and RIE, the source and drain edge contacts are fabricated by EBL and PVD. The asymmetric gold topgates are then fabricated in a third EBL run (PMMA 600 K/950 K/950 K), followed by PVD and lift-off. The gate design is rounded to optimize the lift-off performance. Note that the fabrication of these topgate structures is not possible, if metallic whiskers on the hBN exist from previous fabrication runs.

Lithographic issues: PMMA cracks and metallic whiskers

In the fabrication of edge contacts and other small structures by EBL on top of smooth hBN flakes, recurring cracks in the PMMA resist appeared after development. These cracks lead to metallic whiskers after metal deposition and lift-off. Optical images of multiple examples of such cracks and whiskers are shown in figure 3.15 a) to c).

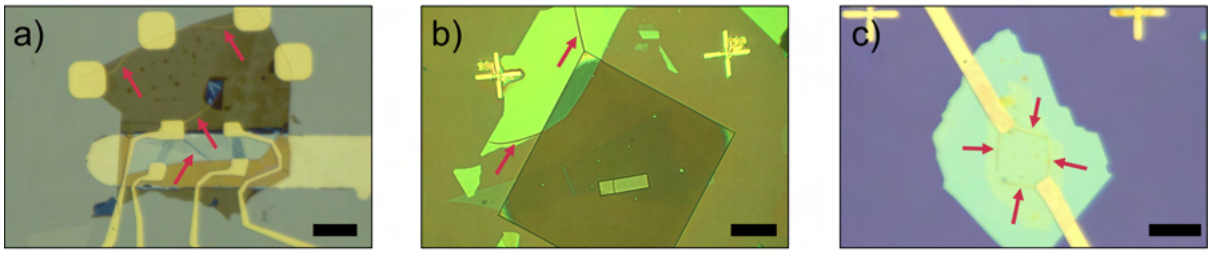

Figure 3.15.: Exemplary optical images of whiskers resulting from cracks in the PMMA resist, indicated by red arrows. a) Gold whiskers on a graphite contacted graphene device. b) Cracks in the PMMA layer during the plasma etching-based patterning step of a graphene stack. c) Gold whiskers on a graphene device with edge contacts, preventing the fabrication of top gate structures. All scale bars are 20 µm.

Multiple approaches can help to prevent or at least minimize the occurrence of such cracks in the PMMA layer. The cracks result from insufficient resist adhesion on the smooth hBN surface combined with tensile film stress in the PMMA layer. They predominantly appear at sharp corners, but even rounded designs do not fully prevent the cracks. However, by patterning the graphene stack into a small island, the hBN area is minimized, which significantly reduces the formation of PMMA cracks. Additionally, resist adhesion can be increased by letting the PMMA resist rest on the wafer for ~ 60 s before starting the spin coating. In this time, the thin water layer that is present on the wafer surface at ambient conditions is replaced by the resist. Another approach is the use of a trilayer PMMA resist (600 K/950 K/950 K) because the 950 K PMMA resist has higher mechanical stability. Furthermore, employing cold development close to 0 °C also reduces the number of PMMA cracks and can even improve the lithography resolution. For cold development, an increased dose of 750 µC/cm^2 is used, while maintaining a development time of 60 s.

3.2. Microwave Circuits

The previous sections have highlighted the optimization and fabrication details regarding vdW materials and electrical contacts. In this section, different approaches to optimize the high-frequency circuit integration of vdW materials are presented in detail.

3.2.1. Metallic Waveguides Equipped with Large-Area Graphene

In an approach to optimize the coupling of high-frequency electromagnetic radiation to large-area graphene, metallic waveguides have been utilized for the use in magnetic resonance spectroscopy. An overview of the fabrication process flow is given in figure 3.16 a), along with optical images of a device at different stages of the fabrication [figure 3.16 b) to d)].

Here, dielectric substrates consisting of high-resistivity silicon (Siegert Wafer, prime grade, $>3\,\mathrm{k}\Omega$ resistivity, 500 nm wet oxide) or *c*-plane sapphire are coated with a 400 nm thick layer of Cu by e-beam evaporation with a 10 nm thin Cr adhesion layer.

To achieve $50\,\Omega$ impedance matching of the CPW for silicon substrates ($\epsilon_{\mathrm{eff}} \approx 6.35$), the width of the center conductor is designed to be 50 µm with a spacing of 30 µm to the ground planes. For sapphire substrates, the center conductor is 60 µm wide, with a 25 µm spacing. The design parameters are evaluated using the circuit simulation software QucsStudio.

The coplanar waveguide (CPW) structures are defined via photolithography and a wet etch approach. Here, only S1813 is used to minimize underetching of the resist. The wet etch is based on an aqueous solution of Iron(III) nitrate ($Fe_3(NO_3)_3 \cdot 9\,H_2O$). A lower concentration (1.5 g Iron(III) nitrate in 200 mL DI water, corresponding to 31 mmol/L) is used compared to the large-area graphene Cu etching to achieve longer etching times that facilitate reproducible and controlled etching behavior. The Cr/Cu films are typically etched for 3 min and stopped in DI water for 1 min. The photoresist is removed in acetone, followed by isopropanol rinsing and N_2 blow dry.

In the next step, the metallic waveguides are conformally coated with an insulating layer of approximately 20 nm Al_2O_3 by atomic layer deposition (ALD). The insulating Al_2O_3 is supposed to electrically decouple the waveguide from the graphene layer to be placed on top. This is necessary to avoid electrical shorts between the center conductor and the ground planes of the waveguide. Additionally, this enables the fabrication of metallic contacts to the graphene used for low-frequency lock-in detection of the electrical resistance. After the ALD-growth of Al_2O_3, the waveguides are ready for the large-area graphene transfer described earlier. However, the O_2-plasma cleaning step is not performed prior to the graphene transfer to avoid damaging the insulating oxide layer. Either CVD-grown ^{12}C monolayer graphene or MBE-grown ^{13}C few-layer graphene are transferred onto the metallic waveguides.

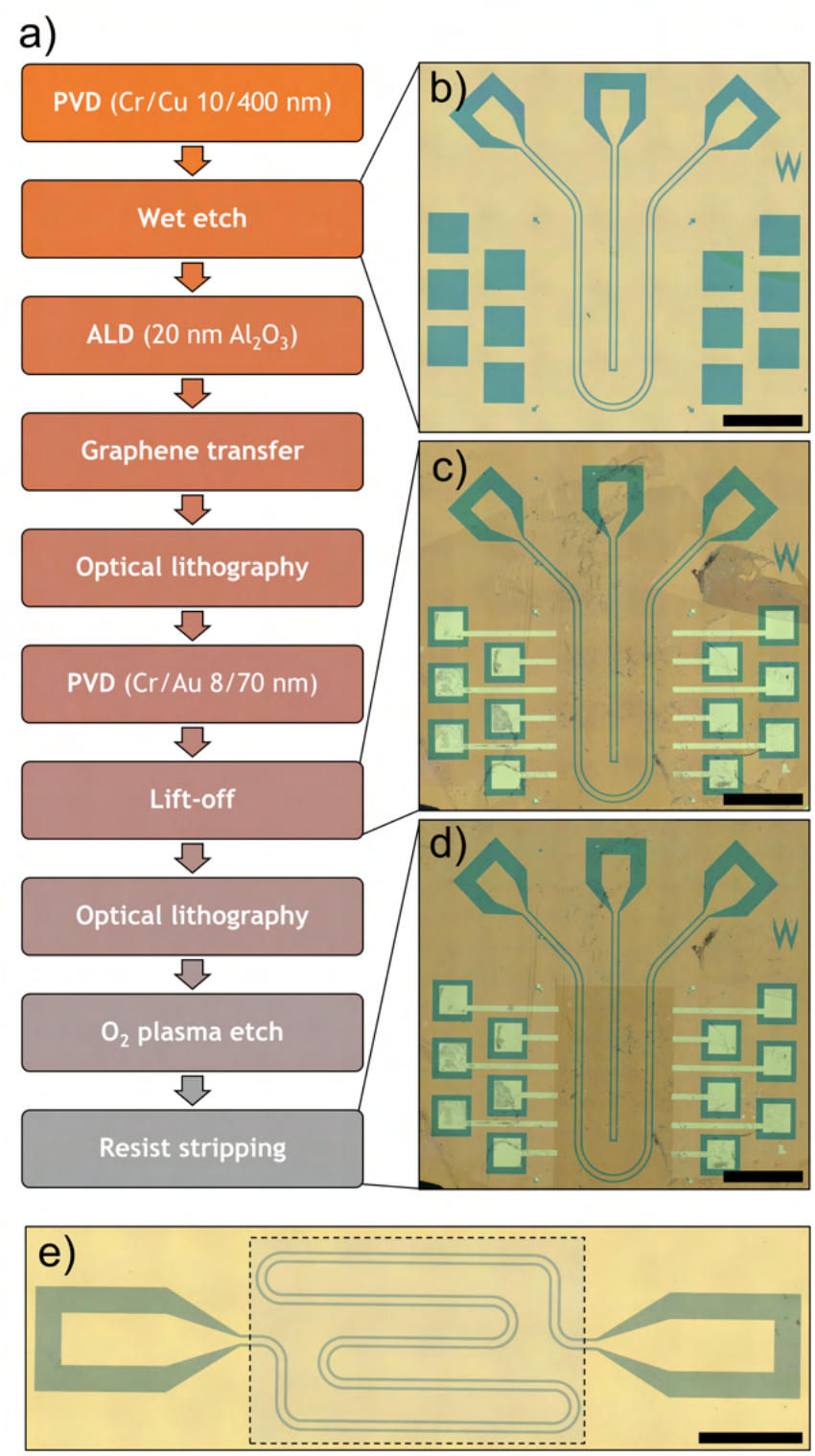

Figure 3.16.: a) Overview of the fabrication process flow. b) to d) Optical images of a device during different stages of fabrication, as indicated by the arrows: b) after the wet etch of the Cu film, c) after contact fabrication to the transferred CVD graphene sheet and d) after patterning the graphene with O_2 plasma. e) Coplanar waveguide of the first generation of devices, which maximizes the area between the CPW and the graphene (indicated by the dashed area). All scale bars are 1 mm.

After the PMMA removal and the RTA annealing step, metallic contacts are fabricated by optical lithography. A double layer resist consisting of LOR-5A and S1813 is used to facilitate lift-off. After exposure and development, metallic contacts with 8 nm Cr and 70 nm Au are evaporated, followed by lift-off in PG remover, acetone and finally isopropanol. Electrical contact fabrication is performed before patterning the large-area graphene layer to reduce photoresist residues at the graphene-metal interface resulting from the additional lithography step. Although this improves the contact quality, some contacts suffer from bad adhesion to the chip due to the underlying graphene layer and are also removed during lift-off. In the last step, the double layer resist with LOR-5A and S1813 is used to pattern the large-area graphene into a rectangle to avoid electrical shorts between the contact pads. The excess graphene is removed in O_2 plasma at 300 W for 3 min. The metallic waveguides equipped with large-area graphene are finished after resist removal in PG remover, acetone and isopropanol, followed by N_2 blow dry. An optical image of a finished device is shown in figure 3.16 d).

The fabrication of these metallic waveguides equipped with large-area graphene is challenging. The major challenge is to avoid electrical shorts between the CPW circuit and the graphene circuit. Although they are electrically isolated by the ALD-grown oxide, this layer could only be made 20 nm thick. A significantly higher yield of functional devices is expected for thicker oxide barriers, such as 200 nm thick silicon oxide, which can be achieved by plasma-enhanced CVD. Unfortunately, during the time of this work, the instrument was out of order.

The first generation of these devices was based on a different CPW design, which maximized the waveguide area below the graphene as shown in figure 3.16 e). This design of broadband CPW transmission lines is based on previous reports on CPWs optimized for magnetic resonance spectroscopy.[158] While this design is advantageous for transmission-based readout, the fabrication of additional electrical contacts to the graphene, enabling simultaneous resistive readout, often results in electrical shorts with the CPW ground planes. To address this issue, the next generation of the device incorporates space in the ground plane to accommodate the electrical contacts. Furthermore, the final devices [figure 3.16 d)] feature an additional CPW structure in the center, which allows to apply two different frequencies simultaneously. This capability is particularly valuable for ^{13}C graphene-based devices, where electron spins and nuclear spins can be addressed.

3.2.2. Metallic Waveguides Coupled to Exfoliated Graphene Heterostructures

In order to probe high-quality exfoliated graphene devices with high-frequency radiation, metallic waveguides are integrated on chip. The design considerations and fabrication details are described in the following.

Similar to the metallic waveguides for large-area graphene, dielectric substrates are used, consisting of high-resistivity silicon (Siegert Wafer, prime grade, $>3\,\mathrm{k}\Omega$ resistivity, 500 nm wet oxide), that are equipped with prepatterned markers and bonding pads for electrical connections and high-frequency lines. However, for the first generation of devices, sometimes n-doped silicon wafers with native oxide are used to conduct initial tests and safe material cost. After a hBN-encapsulated graphene heterostructure is released on such a substrate, metallic electrical contacts and high-frequency waveguides are fabricated by EBL, PVD of Cr/Au (7 nm/70 nm) and lift-off.

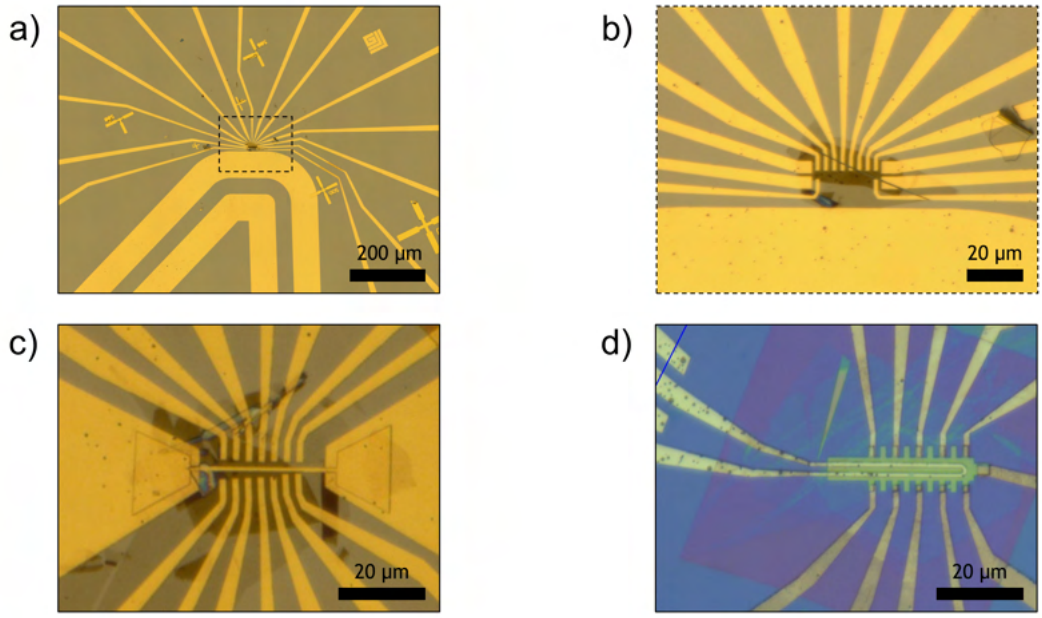

Figure 3.17.: a) First generation exfoliated graphene device equipped with coplanar stripline on chip. b) Magnified view of the marked area containing the graphene Hall bar in a). The signal transmitting line is in close proximity of the graphene flake. c) By fabricating the waveguide on top of the Hall bar, it can also act as a gate. d) More advanced devices are fabricated in a Hall bar shape with small contact arms and a U-shaped waveguide on top.

Different approaches were tested to couple the waveguide to graphene. For these devices intended for magnetic resonance spectroscopy experiments, mainly a capacitive coupling approach is employed, based on previous experiments conducting microwave transmission line spectroscopy of 2D electron systems in conventional semiconductors.[177,178] The first generation of devices are equipped with a coplanar stripline in close proximity to the graphene Hall bar, as depicted in figure 3.17 a) and b). The side of the coplanar stripline, which faces the Hall bar is coupled to the signal line, while the other side is connected to ground. This design leads to lower losses compared to a regular stripline.[150] Additional losses are reduced by increasing the

general width of the conducting lines. For all fabricated waveguides, geometric parameters of signal and ground lines are optimized for impedance matching. The first samples faced several drawbacks. The major problem was the inability to tune the charge carrier density, since neither a graphite nor a p-Si backgate were available. To solve this issue and to increase the coupling, the next generation of devices were designed with the signal line on top of the graphene Hall bar [see figure 3.17 c)]. Here, the waveguide acts both as a transmission line and as a gate. In the latest version, the graphene heterostructure is patterned into a Hall bar shape with small contact arms to optimize the contact behavior. The waveguide on top is then patterned into a U-shape, as shown in figure 3.17 d), in order to study also the transmitted signal through the waveguide. To minimize losses, the additional ground lines run alongside the signal line, extending up to the vicinity of the Hall bar.

For future experiments, it could be interesting to explore the possibility of resistively-coupled waveguides. In a recent study, monolayer graphene is placed as a shunt resistor of the signal line to ground, thereby modulating the transmission of the waveguide via its resistance.[179]

3.2.3. Metallic Coplanar Waveguide Resonators

In order to understand the behavior of the high-frequency setup and to evaluate various design parameters, such as coupling strength, metallic coplanar waveguide resonators are fabricated. While these resonators are primarily designed for simple measurements at room temperature, they are also suited for cryogenic measurements. To reduce resistive losses, metals such as copper or gold are used, which have a high room temperature conductivity. Different metallic microwave resonators are fabricated with resonance frequencies between 1 GHz and 10 GHz. To minimize dielectric losses, substrates consisting of high-resistivity silicon (Siegert Wafer, prime grade, > 3 kΩ resistivity, 500 nm wet oxide) or sapphire (c-plane) are used. However, for the first generation of devices, sometimes n-doped silicon wafers with native oxide are used to conduct initial tests and reduce material cost.

For practical reasons, simple microstrip resonators are fabricated by EBL using a double layer PMMA resist (600 K and 950 K), followed by PVD of Cr/Au (7 nm/120 nm) and lift-off. An optical image of a fabricated half-wavelength resonator with a resonance frequency of ~ 8 GHz is shown exemplary in figure 3.18 a). These microstrip resonators typically have a high fabrication yield and can be reliably fabricated using the lift-off technique. However, the long exposure times for these large structures in EBL are unsuitable to fabricate a larger number of devices. This issue could be solved at a later stage of this work when a new photomask was fabricated.

The fabrication of metallic coplanar waveguide resonators required significant process optimization. Initial attempts to fabricate CPWs by lift-off failed due to the long and thin lines

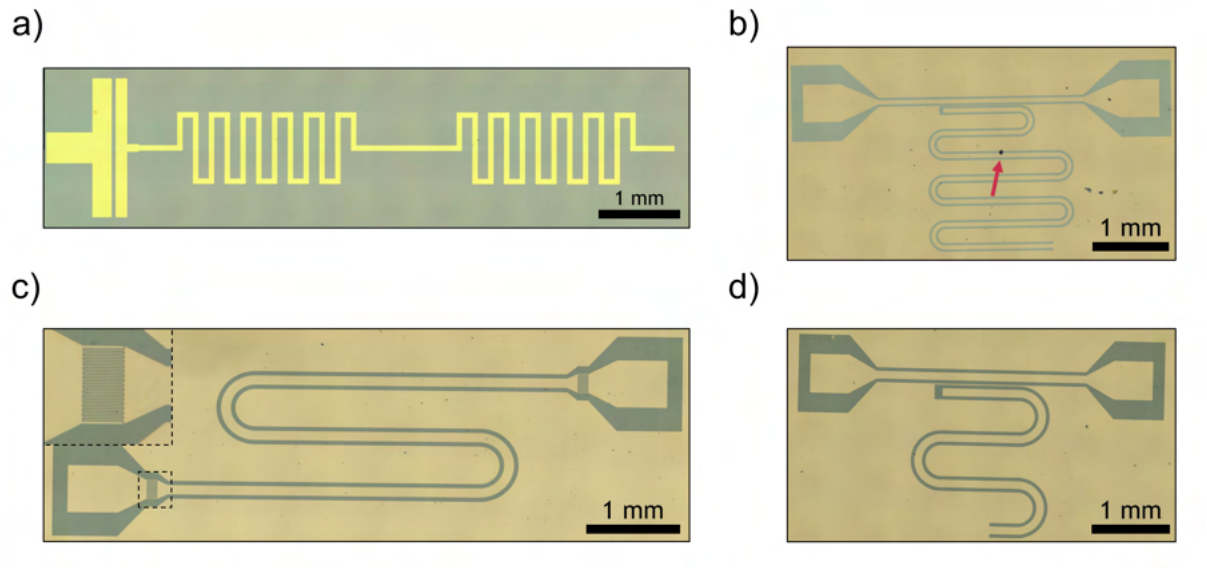

Figure 3.18.: a) Metallic (Cr/Au) microstrip $\lambda/2$ resonator fabricated by EBL and lift-off. b) Metallic (Cr/Cu) $\lambda/4$ resonator fabricated by photolithography and wet etching of the CPW structure. An impurity from the fabrication process (marked by the red arrow) shortens the signal line to ground. c) Two bonding pads are coupled to this $\lambda/2$ resonator on sapphire by 32 interdigitated finger pairs for increased coupling. d) This $\lambda/4$ resonator is designed for a resonance frequency of 5 GHz and is coupled to a short feedline.

separating the center conductor from the ground planes. The high aspect ratio of these structures leads to poor lift-off results and thus a low fabrication success rate. Consequently, the predeposited Cr/Cu thin films were patterned by etching. Different Cu thin film thicknesses are used, ranging from 100 nm to 500 nm. However, for most samples, a 400 nm thick layer of Cu is deposited by PVD together with a 10 nm thin Cr adhesion layer.

In order to pattern the metal film, the samples are prepared for etching by using optical lithography with a single layer of S1813 resist. In a first approach, using the RIE, a dry etching recipe with Ar-plasma is employed. For Cu, no chemically reactive process gases are available which transfer the resulting etching products into the gas phase. The Ar-plasma-based process therefore only physically etches the metal films, which is not very effective and leads to a significant amount of resputtered metal species on the sample and its surroundings. This contaminates the RIE process chamber with metal species and additionally alters the resist properties, which is significantly harder to remove afterwards.

Hence, a wet etching approach is utilized, which was introduced earlier in the fabrication of coplanar waveguides for large-area graphene. This approach chemically etches chromium and copper and solves both problems which are associated with the dry etching approach. As mentioned earlier, the wet etch is based on an aqueous solution of Iron(III) nitrate ($Fe_3(NO_3)_3 \cdot 9\,H_2O$)

with a low concentration (1.5 g Iron(III) nitrate in 200 mL DI water, corresponding to 31 mmol/L) to gain more control of the etching behavior. The Cr/Cu films are typically etched for 3 min and stopped in DI water for 1 min. The photoresist is subsequently removed in acetone, followed by isopropanol rinsing and N_2 blow dry.

Several challenges are encountered during the fabrication of these samples since the access to the clean room was restricted. Therefore, all lithographic processes were conducted in a regular lab atmosphere under yellow light, but without laminar flow, air filtering and controlled humidity. This leads to a significantly higher dust particle accumulation at the sample surface. In some cases, such impurities during the lithographic process result in electrical shorts between the signal line and the ground plane, rendering the device unusable, as shown exemplary for a $\lambda/4$ resonator in figure 3.18 b).

The directionality of wet etching is inherently isotropic, leading to a significant underetch of the resist that affects fine structures. After compensating the underetch in a newly designed photo mask, CPWs with optimized geometries can be fabricated as illustrated in figure 3.18 c) and d). The CPW in figure 3.18 c) is a $\lambda/2$ resonator coupled via two finger capacitors, consisting of 32 interdigitated finger pairs each with a width of $3\,\mu$m and $100\,\mu$m length, resulting in a coupling capacity of $100\,$fF. For optimized impedance matching on the sapphire substrate, the center conductor is designed to be $100\,\mu$m wide, with a spacing of $44\,\mu$m to the ground planes. The $10.5\,$mm long resonator has an expected resonance frequency of $6.11\,$GHz. The $\lambda/4$ resonator in figure 3.18 d) is designed for a resonance frequency of 5 GHz and is coupled to a short feedline.

3.3. Superconducting Devices

3.3.1. Superconducting Microwave Resonators

Before a graphene Josephson junction can be embedded in a superconducting microwave resonator, it is necessary to study the behavior of unloaded resonators first. Hence, multiple superconducting resonators are fabricated with varying designs and materials. Again, high-resistivity silicon substrates are used (Siegert Wafer, prime grade, $>3\,\mathrm{k\Omega}$ resistivity, 500 nm wet oxide).

At the beginning of this work, a $\lambda/2$ resonator design is adopted from a previous study in our group on superconducting CPWs. Prior to the lithography, the Si substrates are coated by Isabel González Díaz-Palacio with a superconducting NbTiN thin film by plasma-enhanced atomic layer deposition.[180] These films typically have a thickness of only 25 nm, since the ALD-growth of thicker layers is very time consuming. The NbTiN films are annealed at 1000 °C to improve the thin film quality, resulting in a high critical temperature of 15.9 K.[180] The superconducting films are patterned into CPW structures by photolithography with S1813 resist and subsequent dry etching. Based on the SF_6 RIE process, the thin films are etched for 5 min to 7 min. In some cases, the etching time is increased to obtain a deeper etching of the structures into the silicon substrate. This deep etching approach was found to reduce intrinsic losses associated with two-level systems at the Si-surface.[181] An exemplary finished superconducting NbTiN resonator is shown in figure 3.19 a).

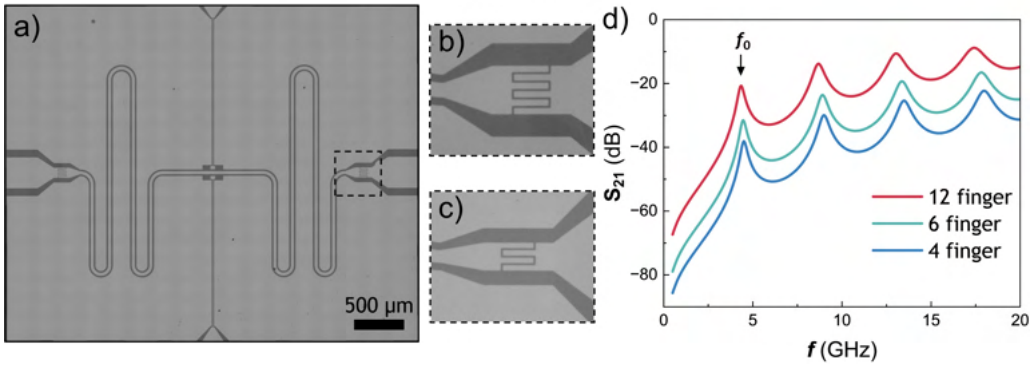

Figure 3.19.: a) Optical image of a superconducting plasma-enhanced ALD-grown NbTiN $\lambda/2$ resonator. b) Magnified view of the coupling capacitor in a) with three finger pairs. c) Different CPW resonator design with a finger capacitor with two finger pairs. d) Simulation of the resonator's transmission (S_{21}) spectrum upon increasing the number of finger pairs in the coupling capacitors.

For these NbTiN $\lambda/2$ resonators, different coupling strengths are tested by increasing the amount of finger pairs at the coupling capacitors, as illustrated in figure 3.19 b) to d). A simulation with the circuit simulation software QucsStudio of the transmission (S_{21}) spectrum of the resonator illustrates the influence of the coupling capacity by adjusting the number of finger

pairs. While a low coupling (less finger) generally leads to a higher Q_{L}-factor, the transmission decreases.[153] After testing several resonators, it became apparent that the $\lambda/2$ resonator design with two coupling capacitors proves to be a challenging starting point. Due to the overall low transmission through the CPW, real resonance peaks are difficult to identify in a background spectrum with numerous box and parasitic modes.

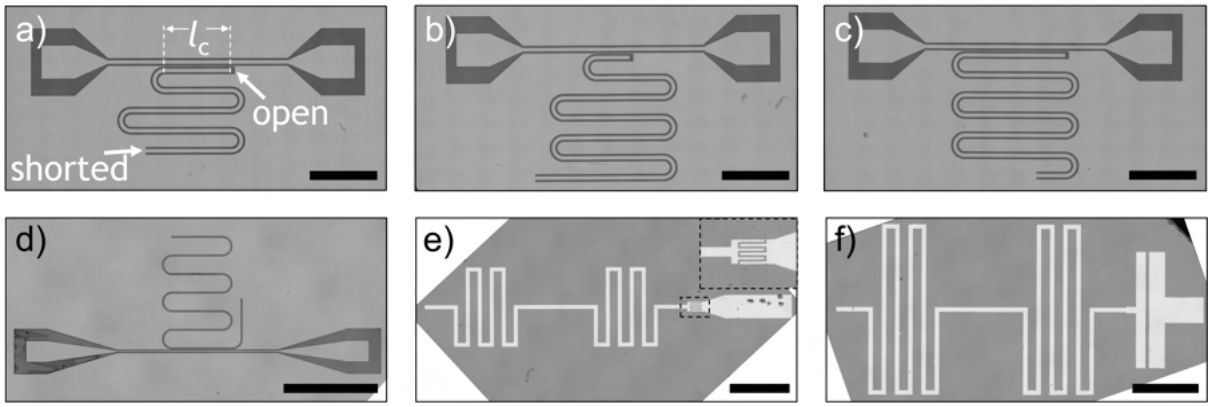

Figure 3.20.: a) NbN $\lambda/4$ resonator with a designed resonance frequency f_0 of $3.75\,\mathrm{GHz}$ and a coupling section length l_{c} of $1\,\mathrm{mm}$. The open and short end of the resonator are indicated by the white arrows. b) NbN $\lambda/4$ resonator with $f_0 = 2.5\,\mathrm{GHz}$ and $l_{\mathrm{c}} = 0.5\,\mathrm{mm}$. c) NbN $\lambda/4$ resonator with $f_0 = 2.5\,\mathrm{GHz}$ and $l_{\mathrm{c}} = 1.5\,\mathrm{mm}$. d) Fabricated Nb $\lambda/4$ resonator with a high quality factor design at $f_0 = 5\,\mathrm{GHz}$. e) Nb microstrip half-wave resonator coupled via a finger capacitor. f) Nb microstrip half-wave resonator coupled via a 200 fF parallel plate capacitor. All scale bars are 1 mm.

This problem is solved by using a feedline-coupled resonator design, which is the most common approach in modern CPW resonator studies.[154,156] The feedline leads to a generally high transmission with a sharp minimum at the resonance frequency. In the work by Besedin *et al.*, more details and a very useful tool to study the influence of design parameters on the quality factor and first-order frequency corrections in feedline coupled CPW resonators are given.[182] Multiple feedline coupled $\lambda/4$ resonators with different parameters are designed and fabricated as illustrated in figure 3.20 a) to d). Here, instead of ALD-grown NbTiN, sputtered Nb or NbN thin films are used as a superconducting material. More details on the sputtering process will be given in the next section. The CPW structures are again obtained by photolithography and subsequent RIE etching. Three different $\lambda/4$ resonators of the first generation are displayed in figures 3.20 a) to c). The resonator in a) is designed for a resonance frequency f_0 of $3.75\,\mathrm{GHz}$ with a coupling section of $1\,\mathrm{mm}$ length. The two resonators in b) and c) share a designed resonance frequency of $2.5\,\mathrm{GHz}$, but have different coupling strengths with $0.5\,\mathrm{mm}$ and $1.5\,\mathrm{mm}$ coupling section length for b) and c), respectively. The design of these $\lambda/4$ resonators is not

yet optimized for a high quality factor. A fabricated quarter-wave resonator with an advanced design for a high Q_{L} at $f_0 = 5\,\mathrm{GHz}$ is depicted in figure 3.20 d).

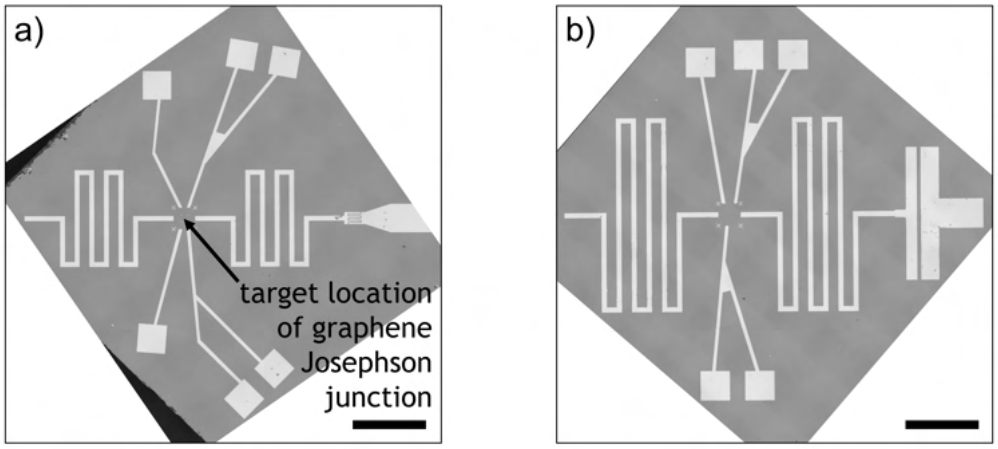

Figure 3.21.: a) Optical image of prepatterned superconducting circuit for embedding graphene Josephson junctions including a Nb microstrip half-wave resonator with finger capacitor. b) Equivalent prepatterned circuit with different resonator design. All scale bars are 1 mm.

Many resonators are not functional due to the delicate fabrication process and defects such as shorted signal lines, as discussed earlier for metallic CPWs. Thus, for practical reasons and to mitigate these issues, superconducting microstrip resonators are designed and fabricated in a first step towards hybrid resonator coupled GJJs, which is one goal of this thesis. These superconducting microstrip resonators are less susceptible to manufacturing defects that affect their functionality. Two different half-wave resonator designs are used for fabrication as shown in figure 3.20 e) and f). Both designs are intended to study the behavior of these resonator in the unloaded case, without GJJ. These microstrip resonators are fabricated by photolithography with LOR-5A and S1813 resist, followed by Nb-sputtering and lift-off. Finally, modified versions of these microstrip resonators are fabricated as part of a prepatterned superconducting circuit for embedding GJJs, as shown in figure 3.21 a) and b).

3.3.2. Superconducting Contacts

One goal of this thesis is the realization of graphene Josephson junctions, which require the fabrication of highly transparent superconducting edge contacts to hBN-encapsulated graphene. The available deposition techniques and materials, i.e., plasma-enhanced atomic layer deposition of NbTiN, sputtering of Nb and NbN, and electron beam evaporation of Al dictate the fabrication methods and various approaches that are summarized below.

Niobium titanium nitride

Superconducting niobium titanium nitride (NbTiN) thin films are deposited via plasma-enhanced ALD by Isabel González Díaz-Palacio and Dr. Robert Zierold, who are also members of the Blick group. The NbTiN films have high critical temperatures up to $15.9\,\mathrm{K}$ and critical magnetic fields higher than $7\,\mathrm{T}$. For details on the deposition process and the annealing treatment that improve the thin film quality, the interested reader is referred to a recent publication.[180] Here, the compatibility of these thin films with various fabrication processes is assessed to determine their suitability as superconducting contacts for graphene.

The primary drawback of these high-quality NbTiN thin films lies in their demanding deposition conditions (high temperature and plasma), which are incompatible with available resists. Additionally, in contrast to PVD, the conformal coating of ALD does not result in an undercut of the deposited material film. Thus, contact fabrication by lift-off is not possible, which also rules out the fabrication of highly transparent edge contacts. As a consequence, alternative contact architectures have to be developed. A simple structure is fabricated in order to assess whether NbTiN can serve as an electrical contact by placing graphene on top of a prepatterned contact structure. After performing photolithography to define two separate contact regions, a deep and $280\,\mu\mathrm{m}$ wide trench is etched into a NbTiN thin film by the SF_6-based RIE dry etching process. The two resulting NbTiN planes are connected by a large sheet of CVD graphene, which is transferred on top by the wet transfer method. The resulting sample, shown in figure 3.22 a), demonstrates sufficiently low electrical resistance of $\sim 4\,\mathrm{k}\Omega$ through the graphene across the trench.

Following this successful test, a Josephson junction pattern with four individual junctions of different lengths and large bonding pads is designed, which is illustrated in figure 3.22 b). This design is intended for small exfoliated graphene flakes, which are transferred after prepatterning the superconducting NbTiN contacts. However, due to the small size of these nanostructures, EBL is necessary which is based on a PMMA resist. Unfortunately, the PMMA resist does not withstand the prolonged dry etching process required to pattern the NbTiN thin film. Another problem is that the dry etched regions of the Si from figure 3.22 a) are extremely rough, which renders them unsuitable as a graphene substrate.

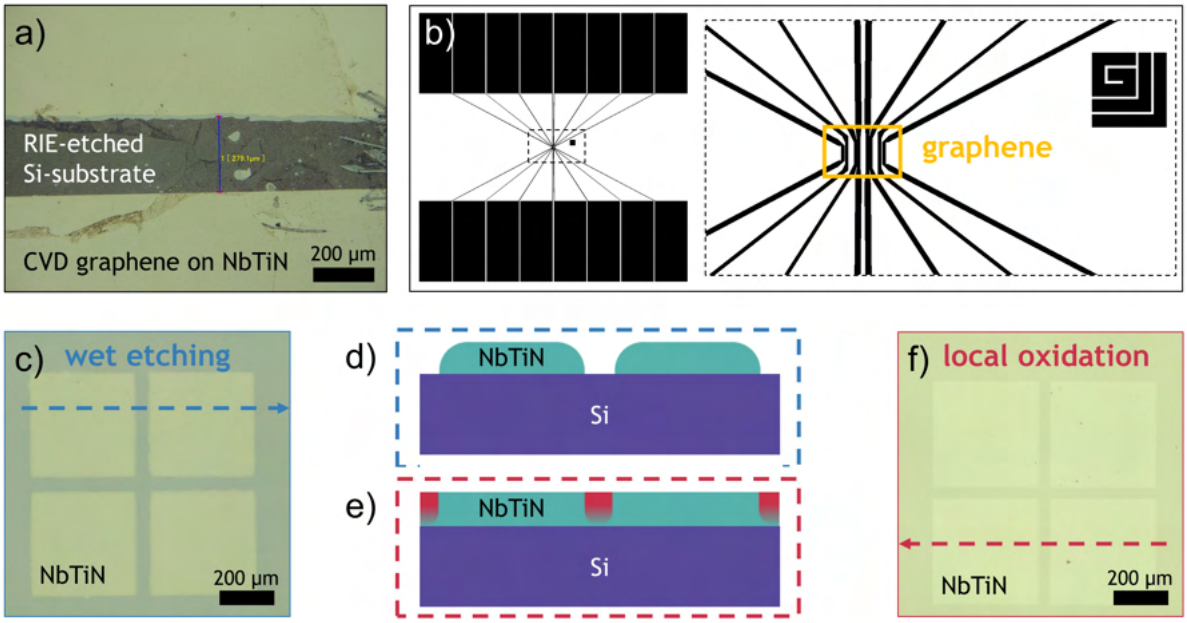

Figure 3.22.: a) Optical image of two NbTiN planes separated by a trench which is etched into the Si substrate with a dry etching process. The two superconducting NbTiN regions are electrically connected by a large-area CVD graphene sheet placed on top. b) Design of multiple Josephson junctions with different lengths and large bonding pads. NbTiN films are prepatterned into this shape before transferring a small exfoliated graphene flake on top of the superconducting electrodes, as indicate by the yellow box. c) NbTiN thin films can be patterned into square electrodes with a wet etch approach. d) Schematic cross section along the blue dashed line in c). Islands of superconducting NbTiN are separated by a smooth and even Si surface. e) Schematic cross section along the red dashed line in f), representing the local oxidation approach described in the text. The oxidation renders the NbTiN insulating as indicated by the red shading, while keeping a smooth and flat surface. Thick films are not oxidized entirely. f) The locally oxidized NbTiN areas are optically well visible.

To mitigate this problem, a wet etching method is used instead. After photolithography with S1813 to define four square contacts, the NbTiN films samples are etched in a mixture of $NH_4OH/H_2O_2/H_2O$ in a 1:2:5 ratio at $T > 60\,°C$. For 25 nm thick NbTiN thin films, the wet etching takes 90 s to remove any unprotected area. An optical image of the resulting squares is depicted in figure 3.22 c). The associated cross section is illustrated schematically in figure 3.22 d). Separate islands of NbTiN are obtained with a slightly rounded edge profile. Most importantly, the Si substrate remains smooth with small topographic height differences corresponding to the NbTiN film thickness. Although these initial results are promising, the wet etching of nanostructures proves to be impossible. One issue is the poor lateral resolution of the

method. The primary issue, however, is the delamination of the PMMA resist during the wet etching process, caused by insufficient adhesion of the resist. This issue can not be mitigated by a hard bake of the resist or a short O_2 plasma treatment of the NbTiN surface. Note that a chromium hard mask is not a solution either, since the NbTiN is attacked by the chrome etchant used for Cr removal.

During these experiments, it was observed that prolonged oxygen plasma treatments oxidize NbTiN, rendering the material electrically insulating. Thus, the local oxidation presents an alternative and novel approach to pattern the NbTiN films. For this, photolithography with S1813 resist is performed again to define four square contacts. Subsequently, the RIE process with strong O_2 plasma is utilized for 2 min to oxidize the unprotected NbTiN areas. The oxidized areas in the NbTiN film are optically visible as depicted exemplary in figure 3.22 f).

The schematic cross section in figure 3.22 e) illustrates a major advantage of this method: the method does not impact the surface morphology, which remains smooth and flat. Placing graphene on top of NbTiN structures prepatterned by local oxidation could thus be a novel and promising way to build devices. However, this method also has two drawbacks. First, the oxidation depth into of the NbTiN thin film is limited. For the 25 nm thick films, a remaining low conductivity is observed between the apparently separated NbTiN islands, which could be explained by a thin NbTiN layer below the oxide, as shown schematically in figure 3.22 e). However, this issue could be solved by using NbTiN films with a sufficiently small thickness, enabling complete oxidation throughout the entire film depth. The second drawback is the instability of most EBL resists such as PMMA when exposed to O_2 plasma. A simple hard bake of PMMA does not improve the resist stability enough to withstand even shorter O_2 plasma treatments of 60 s. Reducing the O_2 plasma process time even further leads to insufficient oxidation of the NbTiN films. Additional O_2 atmospheric treatments or baking of the NbTiN films after O_2 plasma treatment to increases the oxygen diffusion deeper into the material do not result in the required improvements.

In summary, nanostructuring NbTiN thin films to construct GJJs could not be realized due to various process incompatibilities. The available EBL resists can not be used to pattern the NbTiN thin films by lift-off due to the harsh deposition conditions. Moreover, the nanostructuring of already deposited NbTiN thin films attacks EBL resists in a similarly aggressive way. The most promising approach is to locally oxidize very thin NbTiN films which seems within reach as long as a nanostructured mask survives a sufficiently long O_2 plasma treatment. A fine tuning of process parameters could lead to successful results, but was unfortunately not possible within the time of this thesis.

Niobium and Niobium nitride

Nb and NbN exhibit relatively high critical temperatures, critical currents, and critical magnetic fields, making these superconductors particularly advantageous for experiments, as measurements can be performed at liquid helium temperatures. In this work, niobium and niobium nitride thin films are obtained by RF sputtering in a modified Torr International Compact Research Coater System (CRC600), which is shown during operation in figure 3.23 a). For all sputtering processes, small (0.5 cm^2) pieces of a n-doped silicon wafer with native oxide are ultrasonically cleaned in acetone and isopropanol, followed by a mild oxygen plasma treatment to remove any organic contaminants. The plasma treatment was conducted a few days before the deposition to prevent the introduction of reactive oxygen species into the deposition process. The substrates are placed on a rotating metallic sample holder inside the sputtering chamber, which is pumped below 5×10^{-5} Torr prior to the sputter deposition. However, pumping to lower pressures 5×10^{-6} Torr reduces the amount of residual oxygen in the chamber. This is beneficial to minimize run-to-run variations and improve the thin film quality.[183] In the current state, the vacuum system of the sputter setup reaches a minimum pressure of 1×10^{-6} Torr. At ambient temperature, films are deposited from a 2 inch pure Nb target (99.95 %) in an argon (Ar) atmosphere provided by the flow control unit. For the deposition of NbN thin films by reactive sputtering, a new Sensirion SFC5500-50sccm mass flow controller (MFC) is installed at the sputter system, to control the nitrogen (N_2) (99,999 %) gas flow. This MFC enables fine tuning of the deposition atmosphere with different Ar/N_2 ratios. After plasma ignition, the chamber pressure and plasma power are brought to deposition conditions and stabilized for several minutes before the actual deposition. This period serves to clean the Nb target and condition the chamber, which is important to reduce run-to-run variations.[184,185]

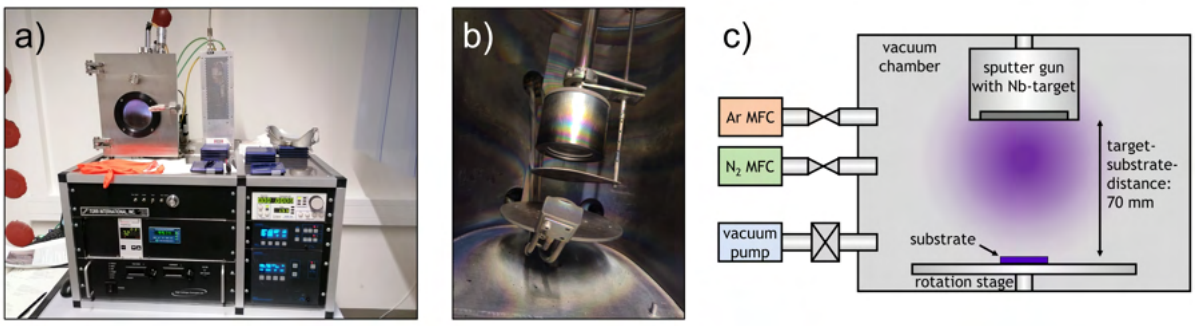

Figure 3.23.: a) Overview of the CRC600 sputter system during Nb deposition. b) Deposition chamber with rotation stage, shutter and sputter gun. c) Schematic representation of the sputter chamber, including the newly installed N_2 mass flow controller for reactive NbN sputtering.

The deposition rate is regulated by setting power and argon flow and ranges from 30 nm/min

to 70 nm/min. Lower deposition rates facilitate manual operation of the shutter to achieve the desired thickness. For each deposition, a dedicated film thickness reference sample is prepared, without the need for lithographic preprocessing. An area of the substrate is simply covered with a marker pen, lifted off post-deposition to create a film edge. Deposition rates and film thicknesses are determined by measuring multiple height profiles along this step between the bare substrate and the film with a Bruker Dektak surface profilometer.

For the fabrication of superconducting Nb and NbN edge contacts to hBN-encapsulated graphene, EBL lithography with a PMMA double layer resist (600 K/950 K) is used, followed by RIE, sputtering and lift-off. The first generation of Nb and NbN GJJs are formed directly at the released graphene stack, while later iterations pattern the graphene heterostructure into a rectangle and into individual islands by RIE-etching. This development is represented by exemplary optical images of finished devices in figure 3.24 a) to c).

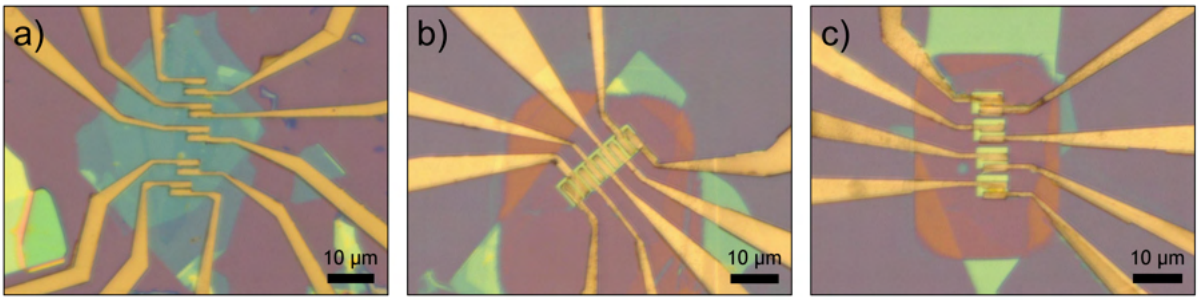

Figure 3.24.: a) Optical image of the first generation of graphene based Nb JJs. The superconducting electrodes are formed without prepatterning the graphene heterostructure. b) Optical image of a niobium GJJ-array, fabricated from a single graphene flake, with different junction distances ranging from 400 nm to 750 nm. c) Optical image of four different Nb GJJs on separate graphene-hBN islands.

Compared to the lift-off of PVD deposited metal contacts, the lift-off of sputtered Nb and NbN contacts is more complicated and often requires ultrasonic treatment. The lift-off results can be improved if the PMMA resist is hard baked after the development. However, the presence of PMMA-coated samples during the sputter deposition generally tends to deteriorate the superconducting film quality due to contamination from outgassing. More details and the associated data are discussed in chapter 4.3.2 and in our publication.[49]

In an alternative lithographic process that prevents the contamination by organic polymers through the resist, an aluminum (Al) mask is used instead of a PMMA mask. First, the entire sample is covered with approximately 800 nm of Al by PVD. The sample is then coated with PMMA (950 K), and the desired structure is patterned by EBL. After the usual PMMA development, the alkaline TMAH-based photoresist developer MF-319 is used for 5 min to remove the Al in the unprotected areas and impose the pattern of the PMMA into the Al layer. The resulting

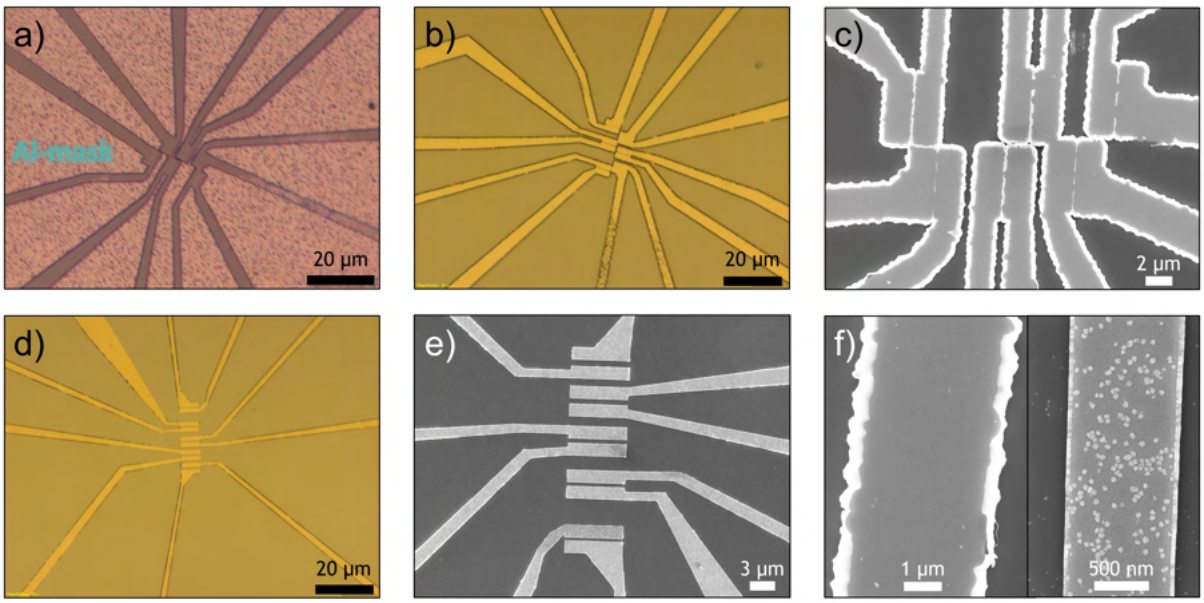

Figure 3.25.: a) Optical image of a finished Al-mask after removing the Al in the unprotected areas and imposing the pattern of the PMMA into the Al layer. b) Optical image of the same sample from a) after RF-sputtering of Nb and subsequent lift-off in alkaline developer. c) SEM image of the same sample from a) and b). A rough edge shape is observed. d) Optical image of sputtered Nb JJs patterned by PMMA-based EBL. e) SEM image of the sample from d) with Nb JJs obtained by conventional PMMA lift-off. f) SEM images to compare Nb contacts fabricated by the Al-mask approach (left) and conventional PMMA-based EBL (right). The edge shape roughness of the Nb structures one the left is twice as rough.

patterned Al-mask is shown in figure 3.25 a). After removing the PMMA, Nb and NbN sputter deposition can proceed without any organic polymers on the sample. The finished superconducting Nb structures are obtained after lift-off in the same alkaline developer for 10 min, which selectively etches the Al. An optical image and a SEM image of an exemplary sample with Nb contacts are shown exemplary in figure 3.25 b) and c), respectively. These structures are compared to structures obtained by conventional EBL with PMMA, shown in figure 3.25 d) and e). A significant increase in edge shape roughness is visible. By directly comparing the SEM images shown in figure 3.25 f), it becomes clear that contacts fabricated by the Al-mask approach (left) are twice as rough compared to the contacts fabricated by PMMA-based EBL (right).

Due to the novelty and the complex wet etching behavior resulting from natural oxide formation on the Al surface, the Al-mask method requires further process optimization tailored to the specific feature sizes and application to achieve high-precision lithography results. It is worth mentioning that from these first preliminary Nb-structures obtained by the unoptimized

Al-mask approach, a lateral resolution of $< 350\,\text{nm}$ can be deduced. This indicates that minor optimization to the process could result in major improvements. More importantly, as discussed later in chapter 4.3.2, the Al-mask approach is more compatible with the RF-sputtering of high-quality Nb and NbN thin films. Hence, Al presents a promising alternative to polymer-based masks to obtain RF-sputtered nanostructures.

Aluminum

Compared to the superconducting materials of the previous sections, aluminum has the lowest critical temperature, critical magnetic field and critical current. However, its deposition is more compatible with our nanostructuring processes and the deposition of Al could yield superconducting contacts with higher transparency. Here, Al is deposited by electron beam evaporation which offers multiple advantages: the deposition of Al is carried out under high vacuum conditions ($\sim 5 \times 10^{-8}\,\text{mbar}$) and a thin titanium (Ti) adhesion layer can be deposited beforehand without breaking the vacuum. The PVD chamber also allows to cool the samples during deposition to control the wetting process.

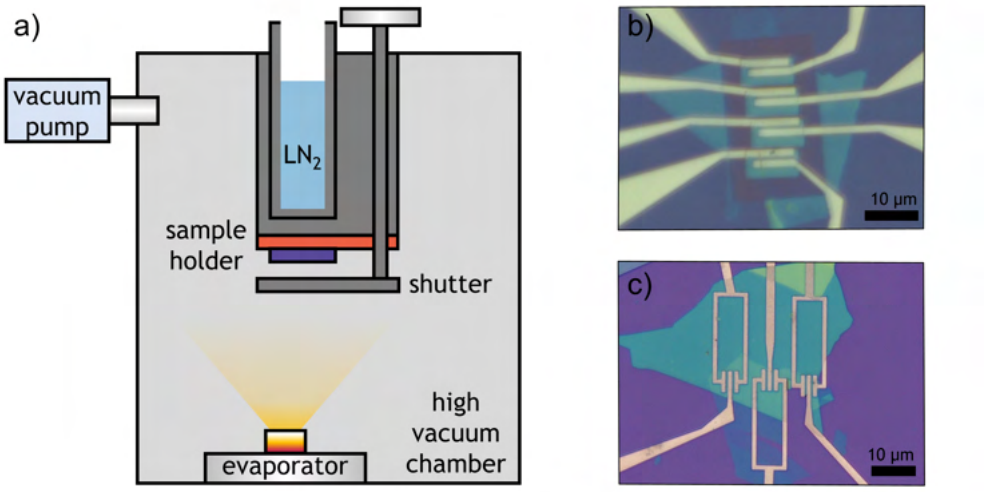

Figure 3.26.: a) Schematic drawing of the cold deposition setup of the PVD. A modified sample holder equipped with a container filled with liquid nitrogen (LN_2) is utilized to cool down the samples during Al-deposition. b) Optical image of four individual aluminum GJJs with different junction lengths, as small as 300 nm. c) Optical image of three fabricated Al-graphene SQUID loops.

The samples are patterned by EBL (600 K/950 K PMMA resist), RIE etched and afterwards immediately mounted with the sample holder in the PVD chamber which is pumped to $\sim 5 \times 10^{-7}\,\text{mbar}$. At this point, a shutter is engaged to protect the samples from the initial deposition. In this way, a small amount of Ti ($\sim 15\,\text{nm}$) can be evaporated to reduce the cham-

ber pressure even further to $\sim 5 \times 10^{-8}$ mbar, without coating the samples. Subsequently, the shutter is removed and the actual deposition can proceed by evaporating a trilayer of Ti/Al/Ti (8 nm/70 nm/10 nm) at deposition rates of 1 Å/s/2 Å/s/1 Å/s. The first Ti-layer is crucial for enhancing the quality of the edge contact to the graphene; however it is unfortunately not available for our Nb contacts.[186,187] The second Ti-layer on top of Al protects the Al from oxidation at ambient conditions. In some cases a significant amount of Al ($\sim$ 200 nm) is deposited with the samples protected by the shutter prior to the actual deposition, to clean the Al material source. After the deposition, the samples are removed and lift-off is performed to obtain Al-GJJs.

During conventional electron beam evaporation, the sample is slightly heated by the incoming highly energetic metal species. Cooling of the samples to liquid nitrogen temperatures can be beneficial to control nucleation and wetting and improve the contact quality to vdW materials.[188,189] In order to perform such a *cold deposition*, a modified sample holder is utilized, which is equipped with a container on the outside that can be filled with liquid nitrogen. A schematic representation of the cold deposition PVD setup is given in figure 3.26 a). After mounting the samples and pumping the deposition chamber, the samples are cooled down to temperatures < 100 K with three to four fillings of liquid nitrogen. The deposition of the Ti/Al/Ti metal trilayer can be conducted as described above, while refilling the liquid nitrogen two more times. After the deposition, the liquid nitrogen container at the sample holder is replaced by a heater that is set to 40 °C to accelerate the warm up of the samples. The samples can be removed from the deposition chamber safely after waiting for 2 to 3 hours, to prevent freezing or condensation on the sample surface. In the next step, lift-off is performed as usual.

These processes are reliable, reproducible and result in a high yield and small junction lengths of 300 nm, as shown in figure 3.26 b). This inspires the design of more advanced devices such as superconducting quantum interference devices (SQUIDs) consisting of two Al-GJJs. An exemplary optical image of such a fabricated device is shown in figure 3.26 c).

Finally, the promising fabrication of Al-GJJs motivates the integration of GJJs into high-frequency microwave circuits as depicted in figure 3.27 a). The optical image shows an Al-GJJ embedded in a prepatterned microwave resonator, as described in section 3.3.1. Here, the Nb resonator is connected to the graphene by aluminum edge contacts. If fully functional, such a device would enable direct coupling of microwaves to hybrid superconductor-graphene junctions. A different device is shown in figure 3.27 b), where multiple Al-GJJs with varying junctions lengths are coupled to two IDTs, which are designed for a resonance frequency at 1.5 GHz. These IDTs are fabricated by EBL and PVD of Cr/Au (7 nm/70 nm) on the piezoelectric material $LiNbO_3$ and can be employed to launch SAWs to the GJJs. Such a device enables strain dependent measurements in GJJs, which is predicted to modulate the supercurrent of the junction.[111]

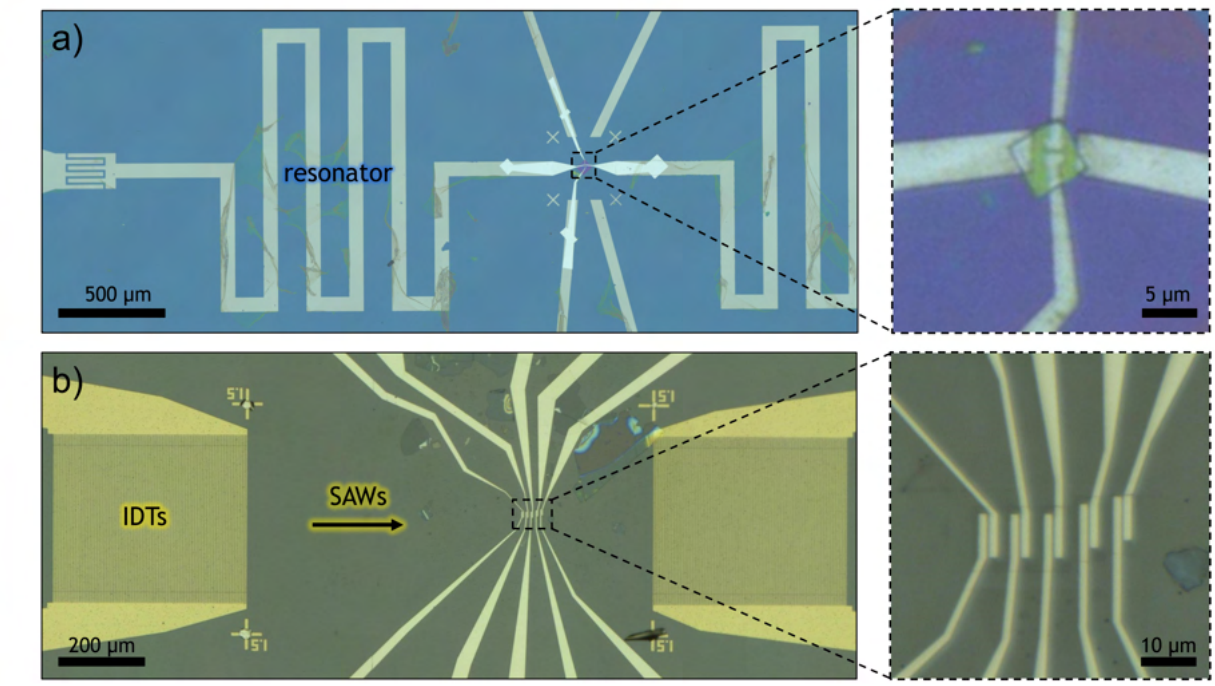

Figure 3.27.: a) Aluminum GJJ embedded in a Nb microstrip resonator. The inset shows a magnified view of the junction that is connected to the resonator via edge contacts. b) Al-GJJ-device with multiple junctions fabricated on the piezoelectric material $LiNbO_3$. Two interdigital transducers (IDTs) can be used to launch surface acoustic waves (SAWs) to the GJJs.

3.4. Measurement Procedures and Setup

The fabricated samples are investigated using various measurement techniques across different setups, tailored to the specific experimental conditions required. Most measurements are conducted at or below liquid helium temperatures to cool superconducting devices below their critical temperature. This section outlines the various standard measurement procedures and describes the corresponding cryogenic setups in detail.

3.4.1. Measurement Procedures

Transport measurements

The main probing technique employed in this thesis to characterize graphene devices is electrical transport. In a measurement method that is generally referred to as low frequency lock-in technique, the sample is excited with a small AC current at frequencies below 200 Hz. As shown schematically in figure 3.28, a large resistor R (1 MΩ to 100 MΩ) is placed in series with the device to convert the AC voltage provided by the oscillator output of a lock-in to a small AC current (≤ 5 nA). In a classical Hall bar geometry, the device response, e.g., in longitudinal voltage V_{xx}, is detected in a four-terminal configuration by the lock-in amplifier, which improves the signal-to-noise ratio by phase-sensitive detection.

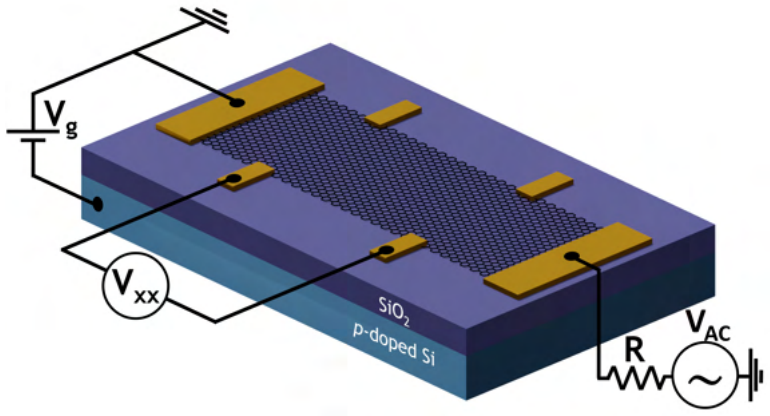

Figure 3.28.: Schematic representation of standard low frequency lock-in transport measurements on a graphene Hall bar with a global p-Si backgate.

Simultaneously, transverse contacts can be used to record the Hall voltage V_{xy} when a perpendicular magnetic field is applied. In this work, Stanford Research SR830 lock-in amplifiers are used for these transport measurements. The backgate voltage V_g is supplied by a Keithley 2400 Source Measure Unit, which is capable of detecting gate leakage that harms the sample. The same approach is employed to apply topgate voltages.

Current-biased measurements

Superconducting graphene Josephson junctions can also be characterized by standard low frequency lock-in measurements. However, to study the different regimes of GJJs, a modification is made to the previously described technique. A large DC current is added to the small AC current $I = I_{AC} + I_{DC}$ to exceed the critical current and tune the junction out of the zero resistance state. A low noise voltage Stanford Research 560 preamplifier is utilized (without gain) to couple AC and DC voltages supplied by the lock-in oscillator and a DC voltage source such as a Yokogawa GS200. A series resistor R with a much larger impedance than the GJJ converts $V_{AC} + V_{DC}$ in $I_{AC} + I_{DC}$. The value of this resistance R is chosen based on the desired current flow through the GJJ, e.g., $V_{DC} = 1\,\mathrm{V}$ with a $1\,\mathrm{M\Omega}$ resistor corresponds to $I_{DC} = 1\,\mu\mathrm{A}$. The contacts to each side of the two-terminal GJJ are split in two and connected to different bonding pads. In the superconducting state, the voltage drop across these superconducting leads is negligible, enabling simultaneous four-terminal current-biasing and voltage V_{JJ} detection. A schematic drawing of the GJJ measurement circuit is presented in figure 3.29.

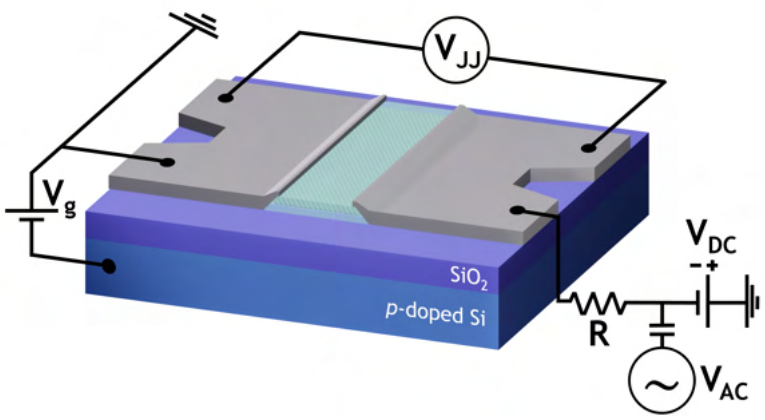

Figure 3.29.: Schematic representation of current-biased measurements of a graphene Josephson junction with a global p-Si backgate.

The voltage V_{JJ} measured across the junction, consists of an AC and a DC component, which are measured simultaneously by routing connections at room temperature to two differential voltage amplifiers with $1000\times$ gain (Physics Basel SP1004), set to AC and DC coupling, respectively. The DC voltage signal V_{DC} is measured by a HP 34401A digital multimeter. The AC component of V_{JJ} is detected with a SR830 lock-in amplifier and can be converted to the differential resistance $R_{JJ} = dV/dI = V_{AC}/I_{AC}$.

Microwave measurements

In experiments where microwave radiation is applied to the sample, a frequency generator (e.g. Anritsu MG3965c) at room temperature is connected via high-frequency coaxial cables to the

(cryogenic) setup. In order to assess the microwave reflection and transmission response of devices, scattering parameter (S-parameter) measurements are conducted with a vector network analyzer (VNA). The definition of the four S-parameters S_{11}, S_{12}, S_{21} and S_{22} is given in figure 3.30 a). The VNA (Agilent N5222A) is equipped with two ports that alternately measure the reflected and transmitted microwave signals in a given frequency range. The reflected (transmitted) signal for port 1 is S_{11} (S_{21}), respectively, and vice versa for port 2.

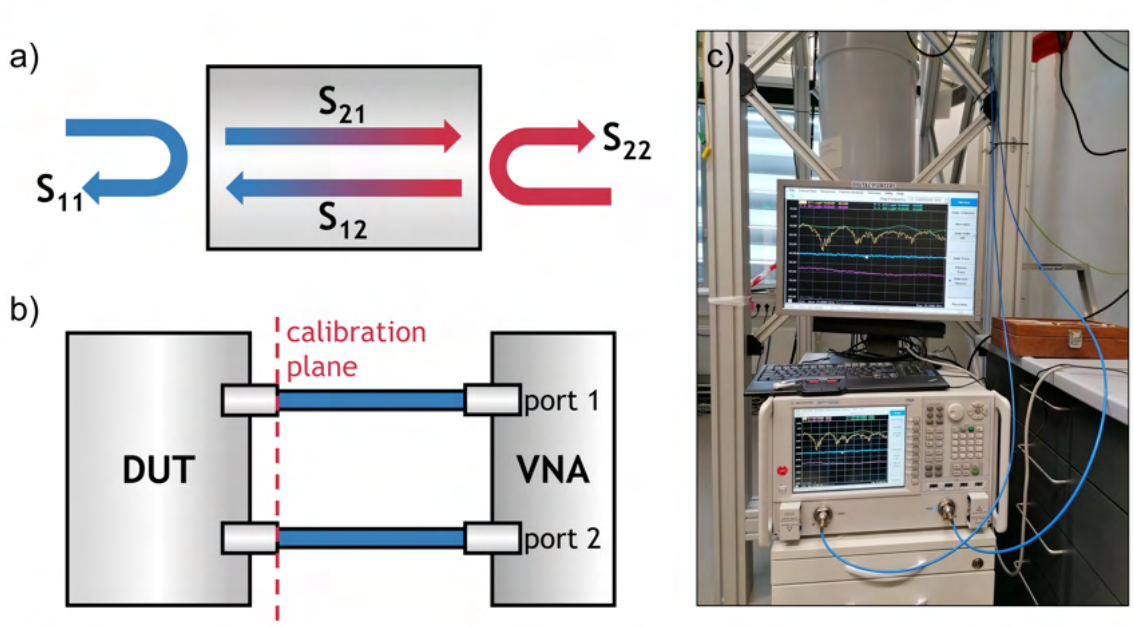

Figure 3.30.: a) Schematic representation of the four S-parameters. b) The point in the circuit where the calibration pieces are connected is defined as the calibration plane and should be close to the DUT. c) Image of a VNA connected to a cryogenic setup.

The accurate determination of the microwave response of a device under test (DUT) requires calibration of the high-frequency circuit including all components such as the coaxial cables, except the DUT. A so-called SOLT calibration is performed by connecting standard calibration pieces corresponding to short (S), open (O), load (L) and finally through (T) of a calibration kit (Agilent 85033E) to the microwave lines connected to the VNA. The open and short standard pieces ideally lead to total reflection, while the 50 Ω load has total absorption. All components of the microwave circuit can be de-embedded from the measurement up to the point where these calibration pieces are connected. This point in the circuit is defined as the calibration plane and should be as close as possible to the sample plane to minimize parasitic signals. The schematic drawing in figure 3.30 b) illustrates the calibration plane. In some cases, however, the calibration plane has to be placed further away from the actual device, such that the entire cryogenic setup can be the DUT for example. After calibration, the VNA is connected to the setup and measurements are performed, as shown in figure 3.30 c).

Photocurrent detection

Measurements on ADGG GTeraFETs for THz-detection are performed by grounding both sides of the device to enable a current flow. The photocurrent I_{ph} can be detected by using the virtual ground of a lock-in instead of a physical ground. In some measurements, a second lock-in is used to measure the photocurrent on both ends of the device. Another lock-in can be utilized to simultaneously measure the photovoltage across the device. No bias voltage is applied to the device. The lock-in AC frequency is set to several hundred Hz to kHz and used to perform amplitude modulation of the sub-THz-signal. This is generated by a millimeter wave source module (OML Inc.) operated by a frequency generator (Keysight E8257D). Different source modules with varying frequency ranges can be used. For most THz-detection measurements in this thesis, a source module is employed with a frequency range from 110 GHz to 170 GHz.

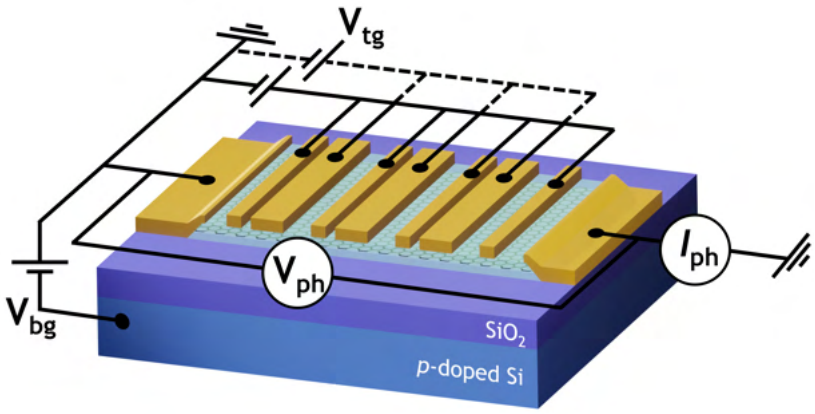

Figure 3.31.: Schematic representation of sub-THz-detection measurements with a ADGG GTeraFET. The two different topgates are connected either together or independently, as indicated by the dashed lines.

The gate voltages to the backgate and to the two topgates is controlled by a Keithley 2400 Source Measure Unit. Depending on the experiment, the two different topgates are connected either in parallel or independently, as depicted in figure 3.31.

3.4.2. Cryogenic Setups

The resolution limit of the physical phenomena is dictated by thermal noise, which amounts to ~ 25 meV at room temperature. To investigate the electronic properties of graphene devices and JJs, where the relevant energy scales are on the order of tens of meV, the samples are cooled to cryogenic temperatures. The following section presents an overview of the cryogenic systems used in this work.

Liquid helium cryostats

Cryogenic systems are generally categorized in "wet" or "dry" fridges, depending on whether their operation is based on liquid helium or not. During this work, different liquid helium cryostats (Oxford Instruments) are used. These systems have different working principles and operation temperatures. In the simplest form, the vacuum sample insert is immersed in a bath of liquid helium (^{4}He), cooling the device down to ~ 4.2 K. In another system, the vacuum sample insert is placed in a pumped chamber, which is connected to the helium bath by a small needle valve. This valve is adjusted to control the He vapor pressure in the chamber to cool the sample down to ~ 1.5 K.

Lower temperatures can be reached with the HelioxVL (Oxford Instruments). This system has a ^{3}He insert which enables base temperatures of < 300 mK for a duration of ~ 24 h. The operation of the system is based on pumping of liquid ^{3}He in a single-shot mechanism. Since ^{3}He liquefies only below 2.2 K, this low temperature has to be achieved first by cooling the system to ~ 1.5 K by pumping of ^{4}He through a pick-up line from the surrounding liquid ^{4}He bath. This setup is also used for the measurements on the graphene-based Josephson junction bolometer device, presented in chapter 4.3.1.

All of these liquid helium systems are equipped with superconducting magnet coils to create strong magnetic fields of several Tesla perpendicular to the devices. In some setups, a three-axis vector magnet allows for additional in-plane field directions. In addition to standard electric DC lines (twisted pair loom), most inserts of the setups are equipped with one or more semi-rigid coaxial line to route high-frequency signals to the sample space. In some experiments, the coaxial line is terminated by a loop antenna for microwave excitation, positioned approximately 1 cm from the device.

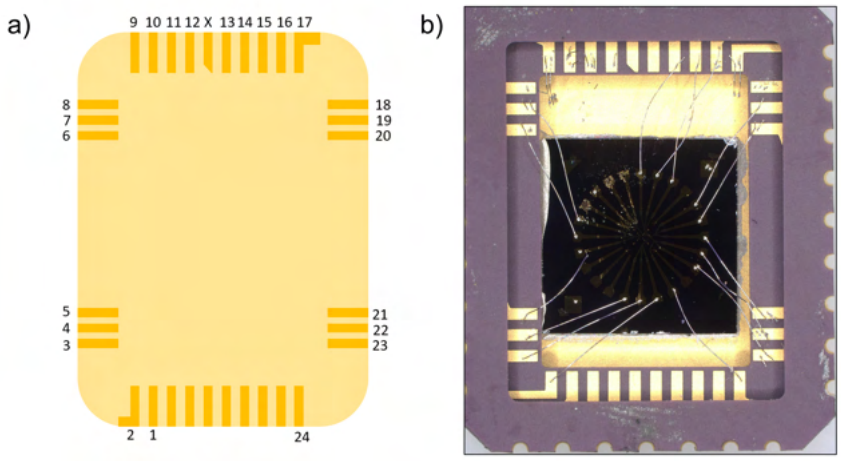

Figure 3.32.: a) Schematic representation of a chip carrier with 24 bonding pads. b) Optical image of a fully wirebonded Al-GJJ device chip inside the chip carrier.

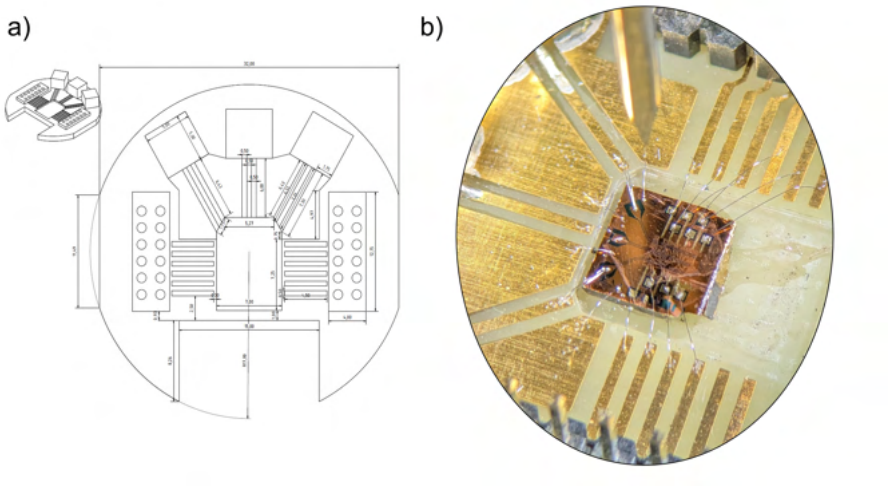

Figure 3.33.: a) Technical drawing of the printed circuit board (PCB) layout used in liquid helium cryostats. b) Microscope image after bonding a chip of a metallic CPW equipped with large-area graphene to the PCB. In addition to the standard DC connections, high-frequency SMP connectors enable the efficient coupling of microwaves via coplanar transmission lines to the signal lines of the device.

For the wet systems, two different kinds of samples holders are used. Devices for pure DC measurements are glued into 24-pin chip carriers with silver paint. A schematic drawing of the chip carrier layout is shown in figure 3.32 a). Note that for all available cryogenic setups only a maximum chip size of $\sim 5 \times 5\,\mathrm{cm}^2$ is possible. An optical image of a fully wire bonded device (Al wedge bonding) is depicted in figure 3.32 b). This chip carrier is mounted on a socket that connects the 24 pins to the wiring of the cryogenic sample insert.

For devices with high-frequency components such as CPWs, a printed circuit board (PCB) equipped with DC connections and coplanar transmission lines connected to high-frequency SMP connectors is used. A technical drawing of the PCB layout is given in figure 3.33 a). The chip is glued on the PCB with Fixogum before connecting the DC lines of the device, as well as signal lines and ground of its high-frequency components, as shown in figure 3.33 b).

Dilution refrigerator

Even lower temperatures are achieved in the dilution refrigerator Triton (Oxford Instruments), which has a base temperature of approximately 14 mK. The working principle of a dilution refrigerator exploits the separation of the mixture in ^{4}He and ^{3}He phases at very low temperatures. This arises because ^{3}He (nuclear spin $I = 1/2$) follows fermionic statistics, while ^{4}He (nuclear spin $I = 0$) behaves as a boson and becomes a superfluid at low temperatures. Below 800 mK, the ^{3}He/^{4}He mixture separates in a ^{3}He-rich phase and a mixed phase of ^{3}He/^{4}He. For decreasing temperatures, the concentration of this mixture changes continuously until a stable

equilibrium of $\sim 6\,\%$ is reached. By heating a still and pumping on this mixture, ^{3}He is selectively removed due to its higher vapor pressure and consequently ^{3}He atoms from the ^{3}He-rich phase cross the phase boundary into the mixed phase. This evaporation of ^{3}He atoms into the mixed phase yields the cooling power of the mixing chamber.

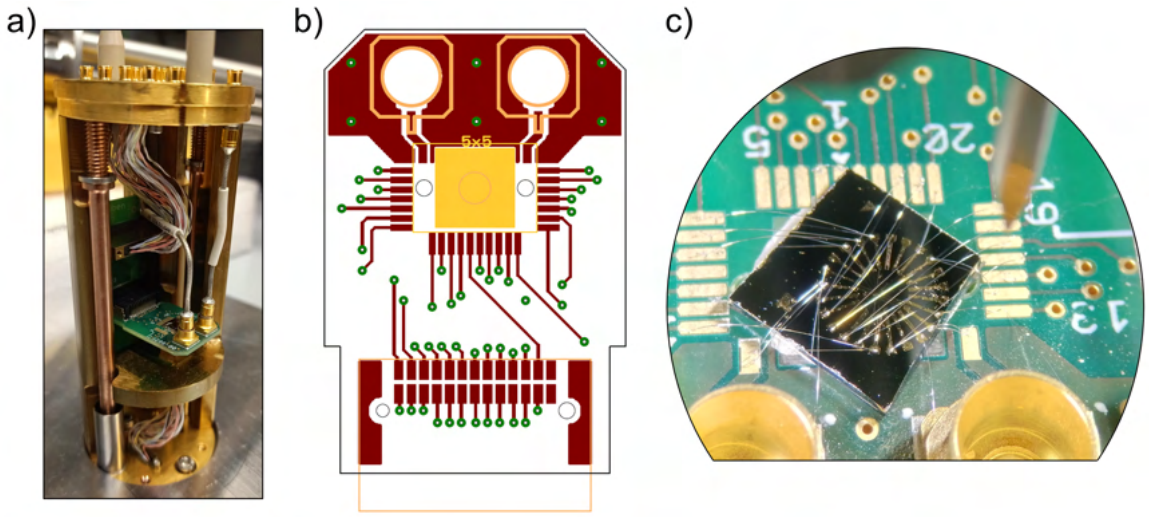

Figure 3.34.: a) Schematic representation of PCB layout intended for combined DC and high-frequency measurements at mK-temperatures in the Triton dilution refrigerator. b) Microscope image of a wire bonded graphene Hall bar sample with metallic waveguide on top. The two high-frequency SMP connectors of the PCB are visible in the front of the image.

For standard DC transport and current-biased measurements, typically the standard chip carriers are used to mount the devices in the sample puck. This puck is inserted into the cryostat via a bottom-loading mechanism and attached to the mixing chamber. The Triton dilution refrigerator is equipped with two coaxial lines without any additional filtering or attenuators. For experiments where high-frequency radiation is applied on-chip, a different PCB with two SMP high-frequency connectors is used for the sample puck. In this configuration, the two coaxial lines are fed in the puck to the PCB SMP connectors via two short flexible coaxial cables, as shown in figure 3.34 a). A schematic drawing of the PCB with its DC connections and SMP connectors is shown in figure 3.34 b). A fully wire bonded device on such a PCB is shown in figure 3.34 c).

Physical Properties Measurement Setup

Another dry cryogenic setup is the physical property measurement system (PPMS) DynaCool (Quantum Design), which allows temperature dependent measurements from room temperature to 2 K. Additionally, perpendicular magnetic fields up to 9 T can be applied, independent of

the sample temperature. Hence, this system is ideally suited to characterize materials such as the sputtered Nb and NbN thin films. A standard four-terminal measurement scheme is used to determine the critical temperature and upper critical magnetic field of superconducting thin films. The samples are contacted either by wire bonding or by the available press contacts for this setup.

Stirling Setup

In order to conduct sub-THz-detection measurements at lower temperatures, a different cryogenic setup is utilized, which allows optical access to the device. The sample is mounted with the standard chip carrier sockets on the cold finger of a table-top-sized Stirling cryocooler (Lihan), with a variable temperature between 40 K and 300 K. The system operation is based on the Stirling cycle with He gas and enables very fast cool down times < 1 h. The sample space housing is decorated with an optical polyethylene window (QMC Instruments) with almost 100 % transmission from 600 MHz to 2.1 THz.

4. Results and Discussion

The following sections present the experimental results and their analysis. In several sections, the transition from large-area graphene towards exfoliated graphene devices will be illustrated. First, nuclear-spin-induced effects in large-area and exfoliated ^{13}C graphene will be discussed in section 4.1, followed by an evaluation of the results from microwave spectroscopy performed with hybrid circuits in section 4.2. The section 4.3 about superconducting graphene devices includes data acquired from a graphene Josephson junction device of an external collaborator, but primarily focuses on results obtained from superconducting graphene junctions fabricated within our group. Lastly, preliminary results of sub-THz-detection measurements conducted with graphene-based photodetectors are shown in the last section 4.4 to briefly illustrate the significant progress in this side project. While this last section reflects our current interpretation of the data, the experiments are still ongoing and a comprehensive analysis of the observed photoresponse, which is beyond the scope of this work, is still required.

4.1. Nuclear-Spin-induced Effects in ^{13}C Graphene

This section presents nuclear-spin-induced effects in large-area ^{13}C graphene. Before discussing more advanced devices in the following sections, here simple graphene Hall bar structures with metallic top contacts (see section 3.1.3) are used. The graphene samples consist of CVD-grown ^{13}C monolayer graphene (sample A) and MBE-grown ^{13}C few-layer graphene (sample B and sister sample). First, the influence of the nuclear spins on quantum interference effects is discussed for sample A, before evaluating the hyperfine interaction and possible nuclear spin effects in magnetic resonance spectroscopy experiments for ^{13}C few-layer graphene. Some of these results have been published in Strenzke *et al.* Phys. Rev. B 105, 144303 (2022).[19]

4.1.1. Quantum Interference

Magnetotransport measurements on sample A show a pronounced weak localization (WL) peak in the longitudinal resistance at $\boldsymbol{B} = 0\,\mathrm{T}$, which is used to probe the presence of nuclear spins. The WL phenomenon is a quantum correction to the Drude resistance in the absence of a magnetic field. It arises from the constructive interference of two time-reversed electronic paths

enclosing a loop in the clockwise and anticlockwise direction. If the phase is preserved over both paths, the increased possibility of backscattering leads to constructive interference at the point of origin.[19] This quantum interference effect is illustrated in figure 4.1 a). By applying an external magnetic field $\boldsymbol{B}$, the time reversal symmetry is broken which cancels constructive interference by introducing a phase difference between the two paths. Weak localization thus diminishes monotonically with $\boldsymbol{B}$, resulting in a resistance peak at $\boldsymbol{B} = 0\,\mathrm{T}$, as shown exemplary in figure 4.1 b).[19] For graphene, this behavior is well described by the theory of McCann *et al.*[190] who developed a mathematical description given by

$$\Delta\rho = \rho(B) - \rho(0) = -\frac{e^2\rho^2}{\pi h}\left[F\left(\frac{B}{B_\phi}\right) - F\left(\frac{B}{B_\phi + 2B_i}\right) - 2F\left(\frac{B}{B_\phi + B_i + B_*}\right)\right] \quad (4.1)$$

with $F(z) = \ln z + \Psi\left(\frac{1}{2} + \frac{1}{z}\right)$ and $B_{\phi,i,*} = \frac{\hbar}{4De}\tau^{-1}_{\phi,i,*}$ which include the diffusion coefficient $D = \frac{1}{2}v_\mathrm{F}l_\mathrm{mfp}$ and the mean free path for elastic scattering l_mfp.

This model can be employed to fit the experimental resistance values, as shown in figure 4.1 b). The red solid line is a fit using equation 4.1 that yields the scattering times $\tau_{\phi,i,*}$ for phase coherence (ϕ), intervalley (i) and intravalley (*) scattering. Magnetotransport measurements were conducted at different gate voltages and the resulting WL peaks are fitted to evaluate the carrier density dependence of the scattering times.

The charge carrier density is carefully extracted from the transport measurements by considering imperfections in our large-area graphene samples. Near the CNP, the carrier density is generally not zero at finite temperatures and potential fluctuations induce electron-hole puddles. Hence, both electrons (n) and holes (p) contribute to transport which is not captured by a simple one-carrier capacitive model. Thus, the two-carrier model by Hilke *et al.*[191] is employed to determine the total charge carrier density $p + n$.[19] A more detailed explanation of the two-carrier model can be found in the original publication by Hilke *et al.*[191] or in my Master's thesis.[145] Far away from the CNP, the carrier density is determined from the Hall resistivity. The corrected charge carrier concentration is shown in the inset in figure 4.1 b) as a function of gate voltage.

The analysis of the WL peak fitting over a range of charge carrier densities is presented in figure 4.1 c) to e). The phase coherence time τ_ϕ, the intervalley scattering time τ_i and intravalley scattering time τ_* for sample A (blue circles) are compared to the data of a CVD-grown ^{12}C monolayer graphene reference sample. Additional free parameters that account for nuclei-enhanced electron spin-scattering terms are not introduced into the original WL theory by McCann *et al.*, to have a direct comparison between both graphene species within a compact model. As a result, an anomaly in the deduced scattering times can be expected, as hyperfine coupling enhances both elastic and inelastic processes.[192]

The most striking feature in these plots is the pronounced drop of all scattering times in the

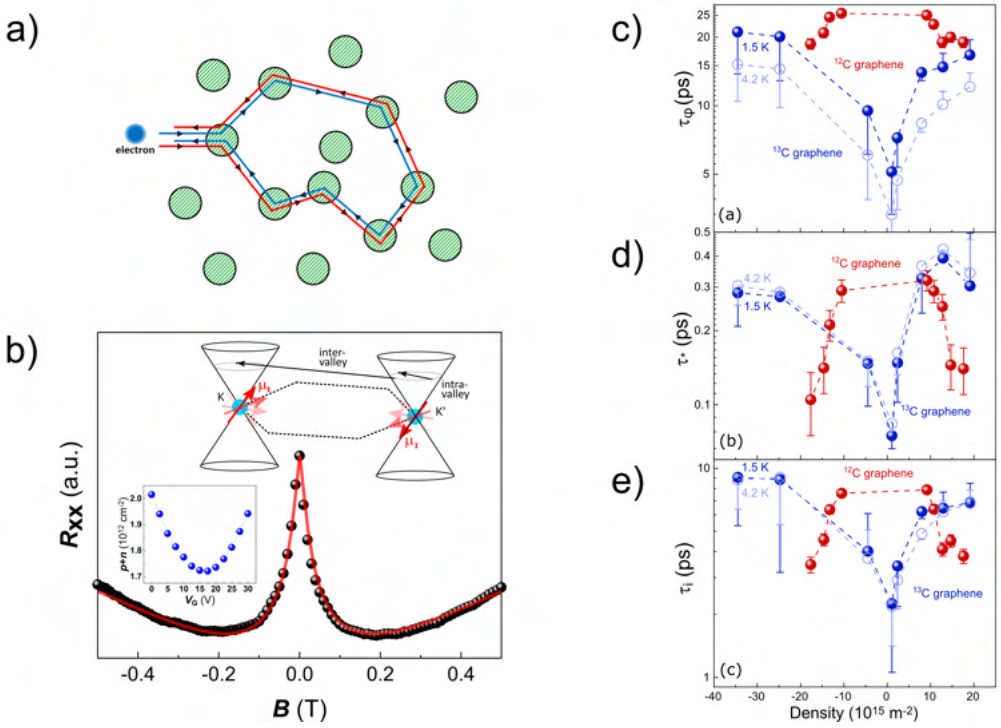

Figure 4.1.: a) Illustration of the weak localization (WL) effect which leads to an increased resistivity at $\boldsymbol{B} = 0\,\mathrm{T}$. b) Exemplary magnetotransport data (black dots) of sample A at 1.5 K, which are fitted by Eq. 4.1 (red solid line). The upper inset illustrates two Dirac cones in the honeycomb lattice with intra- and intervalley scattering events. The circles at the Dirac points represent ^{13}C nuclei with their spin magnetic moments (red arrows) μ_I around $\boldsymbol{B} \approx 0\,\mathrm{T}$. The lower inset displays the corrected charge carrier density using the two-carrier model. c) phase-breaking scattering time τ_ϕ, d) intravalley scattering time τ_* and e) intervalley scattering time τ_i measured on sample A (monolayer ^{13}C graphene, blue dots) and a reference sample of ^{12}C graphene (red dots). The measurements were performed at 1.5 K (closed dots) and 4.2 K (open dots). Figure a) is adapted from my master's thesis.[145] Figure b) to e) are adapted with permission from V. Strenzke, J. M. Meyer, I. Grandt-Ionita, M. Prada, H.-S. Kim, M. Heilmann, J. M. J. Lopes, L. Tiemann, and R. H. Blick. Nuclear-induced dephasing and signatures of hyperfine effects in isotopically purified ^{13}C graphene. Physical Review B 105, 144303 (2022). Copyright 2022 American Physical Society.[19]

^{13}C sample when approaching the CNP. This effect can be interpreted by noting that near the CNP the magnetic moment densities of electron spins and nuclear spins become comparable. Despite the significantly smaller magnetic moment of ^{13}C nuclei, the nuclear density N is much larger than typical carrier concentrations in graphene,[143] especially near the CNP. Moreover, at low carrier concentrations, a significant fraction of carriers becomes locally trapped while at the same time carrier screening of the nuclear moments is weak. Since locally trapped carriers are susceptible to fast spin exchange,[193,194] similar effects could result in the suppression of all scattering times, mediated by the hyperfine interaction and the large number of weakly

screened nuclei.[19]

Except for an overall shift, the phase coherence time τ_ϕ of the ^{13}C graphene sample in figure 4.1 c) shows a similar behavior at 1.5 K (closed blue dots) and 4.2 K (open blue circles). Considering the dephasing rate as linear with temperature, $\tau_\phi^{-1} = \tau_s^{-1} + AT$,[195,196] a faster spin spin relaxation rate τ_s^{-1} is obtained as the carrier concentration is close to the CNP. Moreover, τ_s^{-1} for the ^{13}C sample is roughly one order of magnitude faster than for ^{12}C, which is in agreement with the arguments presented above.[19]

The dichotomy between the ^{12}C and ^{13}C graphene scattering times near the CNP can be further evaluated by the scattering mechanisms that enhance or subdue WL, as visualized in the upper inset in figure 4.1 b). The nuclear spins will influence the scattering mechanisms as atomically sharp impurities[192] and (time-dependent) randomly fluctuating spin moments that are linked to the electron spins via the hyperfine interaction.[19]

WL originates from interference of two paths, which makes it sensitive to inelastic phase-breaking scattering parameterized by τ_ϕ and its competition with intervalley and intravalley scattering. Phase-breaking scattering is generally associated with inelastic phonon scattering, where the scattering target changes with time. There are, however, also elastic scattering events that can contribute to phase-breaking, such as spin-flip events. Since nuclear moments are coupled to the electron spins via the hyperfine interaction, randomly fluctuating nuclear moments can transfer spin momentum to the electrons, which represents phase-breaking scattering.[19]

Intervalley elastic scattering (τ_i) is promoted by sharp defects or edges that flip the direction of the carriers. We may expect this to be dominant at low densities, where the potential landscape consists of electron-hole-puddles. Intervalley scattering mixes two valleys that have opposite chirality and can thus restore WL. As nuclear spins can be considered atomically sharp defects, it is feasible that their existence will enhance intervalley scattering, as represented in the data in figure 4.1 d).[19]

Intravalley elastic scattering (τ_*) originates from scattering on defects with sizes comparable to interatomic distances and the trigonal warping effect, i.e., a trigonal deformation of the Dirac cone. Trigonal warping will appear as we shift away from the DP. Although intravalley scattering is elastic, it still breaks the chirality within each of the two graphene valleys in k-space. Owing to the relative Berry phase of π, the backscattering interference is destructive at $\boldsymbol{B} = 0$. Intravalley scattering is thus a dephasive process that competes with the constructive WL interference. Nuclear spins exist on interatomic distances on all atomic sites and may contribute to intravalley scattering, resulting in the behavior of τ_* shown in 4.1 e).[19]

Various defects exist that influence intra-, inter- and phase-breaking scattering regardless of the nuclear isotope. Graphene synthesized by CVD is comprised of grains that form during growth when the nucleation centers fuse into a continuous layer and can exhibit additional lattice defects such as vacancies, line defects and folds.[197,198] Vacancies in the crystal lattice are

associated with localized states that possess magnetic moments[199,200] and induce spin scattering. The same types of defects will be present in both the ^{12}C CVD graphene and ^{13}C CVD graphene but their concentration differs such that the mobility of the ^{13}C graphene is smaller by a factor of 3 as compared to the ^{12}C reference sample. We emphasize that the lower mobility alone can not account for the opposite trends of the scattering times for ^{13}C and ^{12}C graphene near the CNP.[19]

The experimentally observed suppression of τ_ϕ implies fast electron spin diffusion by momentum transfer between the electrons and nuclei. This type of momentum transfer is a precursor for dynamic nuclear polarization (DNP). In the following section, this method is exploited to generate a sizable nuclear field via ESR.[19]

4.1.2. Magnetic Resonance Spectroscopy of ^{13}C Graphene

Electron spin resonance spectroscopy of large-area ^{13}C graphene

As introduced in section 2.4, microwave activated magnetic resonance spectroscopy methods, such as electron spin resonance (ESR) and nuclear magnetic resonance (NMR), can provide valuable information about the spin physics of graphene. In these experiments, a loop antenna in close proximity irradiates the sample with microwave radiation, as shown in figure 4.2 a). The Hall bar consists of MBE-grown isotopically purified ^{13}C few-layer graphene (sample B and sister sample). Similar to the CVD-grown large-area graphene of sample A, it is comprised of grains and exhibits inhomogeneously distributed curvature existing as a large number of folds, bends and ripples.[19,50] In ^{13}C carbon nanotubes, curvature induces sp hybridization of the electron orbitals that affects the spin-orbit coupling[201,202] and the hyperfine interaction. The magnitude of the hyperfine interaction in carbon nanostructures and how it is influenced by curvature is still a controversial topic.[142,203–207] The unintentional curvature represented by random folds and nanoripples in the ^{13}C few-layer graphene sample might result in a slightly larger overall hyperfine interaction than anticipated for single crystalline exfoliated graphene.[19,50]

Resistively-detected ESR experiments on GaAs two-dimensional electron systems have shown the sensitivity of ESR to nuclear magnetic fields $\boldsymbol{B}_\mathrm{N}$, where the electron spin resonance is subjected to an *Overhauser shift*.[208,209] More recently, Shchepetilnikov *et al.* have demonstrated the detection of nuclear fields using resistively-detected ESR measurements on an AlAs 2D system,[210] which has p-type conduction electrons, similar to graphene. Hence, the p-orbital character and the weak hyperfine interaction in graphene should not generally preclude such an experimental approach.[19,50]

The ESR measurements shown in figure 4.2 b) are conducted by monitoring the longitudinal sample resistivity ρ_{xx} in a ramping magnetic field $\boldsymbol{B}$ under continuous irradiation with microwaves of constant power and frequency ν at nominally 1.5 K. Once the varying electron

Zeeman splitting matches the constant energy of microwave quanta, $h\nu$, electron spins are resonantly excited, resulting in a change in resistivity. The expected frequency-dependent dispersion of the resonance is clearly observed. For a substantially polarized nuclear spin system, a nuclear magnetic field $\boldsymbol{B}_{\mathrm{N}}$ is present which acts on the electron Zeeman energy and shifts the resonance position by $\Delta\boldsymbol{B} \propto \bar{\boldsymbol{A}}/\mu_{\mathrm{B}}g$, with the electron g factor and the hyperfine interaction tensor $\bar{\boldsymbol{A}}$. A strong nuclear polarization out of thermal equilibrium can be achieved by means of DNP. DNP pumps the nuclear level polarization by exploiting momentum transfer when an electron flips its spin and transfers momentum to the nuclei.[19,20,193]

At first glance, four different resonances can be identified in the resistively-detected ESR measurements shown in figure 4.2 c), corresponding to multiple resonant excitations between bands of opposing spin and chirality in the low-energy regime of the graphene band structure that can be modified by intrinsic spin-orbit splitting[15,17] and sublattice splitting.[18] The ESR measurements under microwave excitation in figure 4.2 c) are compared to a background measurement without microwave radiation, where the resonances are absent. For these measurements, the charge carrier density was tuned close to the CNP. The four resonances are marked with Greek letters, using α for excitations between the pure Zeeman levels and β for excitations between bands that are split by intrinsic spin-orbit coupling.[17] The two γ lines result from sublattice splitting.[18] Sublattice splitting can originate from a symmetry breaking due to the substrate but also from a (local) Bernal stacking in graphene multilayers.[211] Following previous reports,[15,17,18] each resonance is fitted with a Lorentzian function to analyze the amplitudes and (center) magnetic field occurrences. The results are summarized in figure 4.2 d), showing the linear dispersion of microwave energy versus magnetic field position of all resonances. The plot combines the data of ESR measurements on sample B and an additional sister sample, which are nearly identical and both fabricated from the same processing batch. Measurements at much higher carrier density do not result in a shift of the resonance position, confirming that Rashba spin-orbit interaction is negligible. However, other types of spin-orbit interactions, arising from a hBN substrate for example, could modify the effective g factor.[18] For these measurements, such effects can be excluded since exclusively the same SiO_2 substrate is used for all samples in addition to the same fabrication methods to process the graphene.[19]

The data in figure 4.2 d) exhibit two signatures that are consistent with the presence of a small nuclear field. First, from a linear regression of the data points of the α resonance that directly follow $h\nu = g \cdot \mu_{\mathrm{B}} \cdot B$, the effective electron g factor of $g = 1.896 \pm 0.021$ is deduced, which is about $2.95 \pm 1.16\,\%$ smaller than determined from ESR measurements on ^{12}C graphene on a SiO_2 or SiC substrate.[15–17,212,213] Second, an asymmetry is observed for the intercepts of the γ resonances which represent the energy splitting of sublattice and spin degrees of freedom.[19]

First, the reduction of the g factor will be discussed: I. Unlike the *nuclear* Zeeman splitting that is probed in nuclear magnetic resonance experiments, the *electron* Zeeman energy, or more

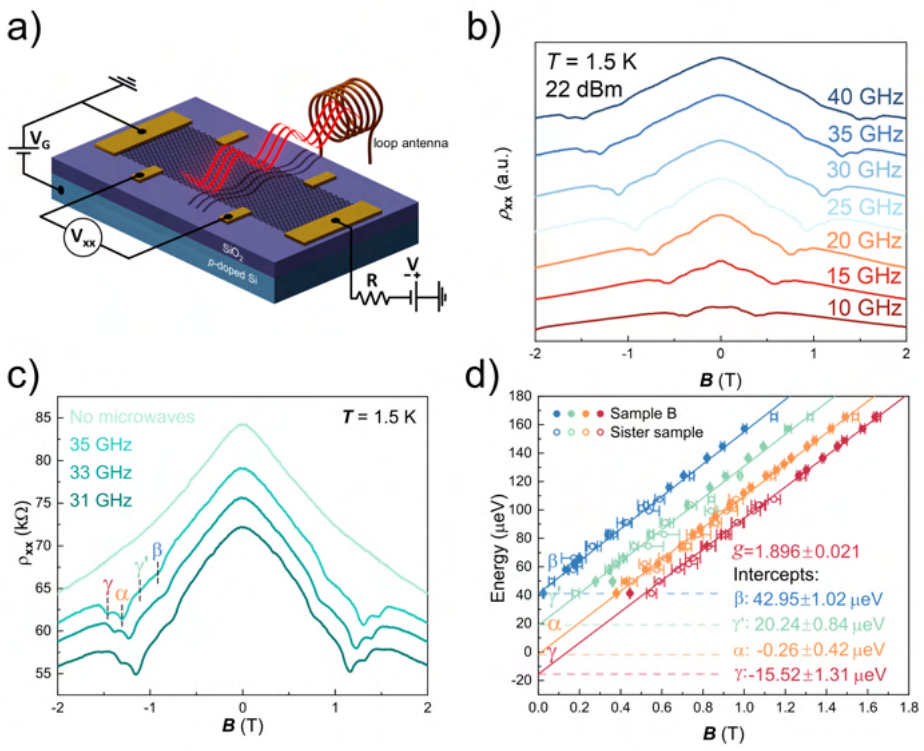

Figure 4.2.: a) Schematics of the ^{13}C graphene Hall bar sample and electron spin resonance (ESR) measurement setup utilizing a simple loop antenna. b) Resistively-detected ESR measurements of sample B (^{13}C few-layer graphene) are conducted at various constant microwave frequencies at 22 dBm power while sweeping the external magnetic field $\boldsymbol{B}$. The expected linear shift of the resonances with increasing microwave frequency is clearly visible. The data are vertically shifted for clarity. c) In contrast to the background measurement without microwave excitation (light green solid line), ρ_{xx} for 35 GHz, 33 GHz and 31 GHz (shades of darker green lines) shows four resonances that are labeled by the Greek letters α, β, γ and γ'. The charge carrier density is tuned close to the CNP, while a microwave power of 22 dBm is used at 1.5 K. d) Analysis of all resonances (including those from an identical sister sample from the same processing batch) shows the linear energy dispersion with magnetic field. The deduced g factor from the slope is $g = 1.896 \pm 0.021$. The intercepts are 42.95 ± 1.02 μeV (β), 20.24 ± 0.84 μeV (γ') and -15.52 ± 1.31 μeV (γ). The linear fit was not forced through the origin resulting in a tiny offset for the pure Zeeman energy represented by α.[19] Figure a), c), and d) are adapted with permission from V. Strenzke, J. M. Meyer, I. Grandt-Ionita, M. Prada, H.-S. Kim, M. Heilmann, J. M. J. Lopes, L. Tiemann, and R. H. Blick. Nuclear-induced dephasing and signatures of hyperfine effects in isotopically purified ^{13}C graphene. Physical Review B 105, 144303 (2022). Copyright 2022 American Physical Society.[19]

precisely μ_B, does not depend on the isotope mass. II. Since the g factor of bulk graphite is significantly larger and exceeds a value of 2, a possible layer-dependence should lead to higher but not smaller values. It was also demonstrated that even the g factor of trilayer graphene is still

independent on the number of layers[15] and still smaller than for bulk graphite.[19] III. There exists no dependence on carrier concentration and carrier type.[16–18] IV. Effects from varying substrates or varying sample preparation are excluded. The reduction of the g factor, however, is consistent with the presence of a nuclear field since a sizable nuclear field will affect the electron Zeeman splitting.[208–210] This will be reflected in the experimentally deduced, i.e., effective g factor. The small variance between the electron g factors for ^{12}C and ^{13}C graphene which is of the order of $\Delta g \approx 0.054 \pm 0.023$ may thus signal a small nuclear field.[16,17,19]

The nuclear magnetic field can be expressed as[193]

$$\boldsymbol{B}_{\mathrm{N}} = f \cdot \boldsymbol{b}_{\mathrm{N}} \frac{\boldsymbol{B} \cdot \langle S \rangle \boldsymbol{B}}{\boldsymbol{B}^2}, \tag{4.2}$$

where $\boldsymbol{B}$ is the external magnetic field, $\langle S \rangle$ represents the average electron spin polarization, f a spin relaxation factor and $\boldsymbol{b}_{\mathrm{N}}$ the effective magnetic field as a result of nuclear spin polarization. $\boldsymbol{b}_{\mathrm{N}}$ has been estimated to be $-5.2\,\mathrm{mT}$ for ^{13}C graphene.[143] For our experiments, it is not possible to calculate $\boldsymbol{B}_{\mathrm{N}}$ because unambiguous absolute values for f and $\langle S \rangle$ are not available. However, it is possible to estimate the hypothetical nuclear field that results in a certain effective g factor.[19]

A nuclear magnetic field will slightly reduce the electron Zeeman splitting. Since the microwave frequency is constant, the resonance condition for electron spin flips now requires a slightly larger external magnetic field $\boldsymbol{B}$, as illustrated in the inset of figure 4.3 a). The larger magnetic field converts to a smaller effective g factor. An extrapolation of the experimental value of the ^{12}C graphene g factor (dashed line) and their uncertainties (light blue band of confidence) is shown in figure 4.3 a). The extrapolation assumes a nuclear Overhauser field that acts on the Zeeman energy and thus the g factor. This estimation illustrates that $\Delta g \approx 0.054$ between ^{12}C and few-layer ^{13}C (lower solid black horizontal line) would be consistent with an Overhauser field of the order of $-29.8\,\mathrm{mT} \pm 8.3\,\mathrm{mT}$ (lower black horizontal line). We also obtained an experimental g factor of 1.957 ± 0.016 from sample A (monolayer ^{13}C graphene) (upper horizontal line). This value is close to those for ^{12}C graphene, but the large uncertainty still allows for a possible Overhauser field smaller than $-5\,\mathrm{mT}$. A layer effect on the g factor was ruled out in earlier studies[15] but for ^{13}C graphene multilayers may simply be required to achieve nuclear fields.[19]

The intercepts of the two γ resonances with the energy axis at $\boldsymbol{B} = 0\,\mathrm{T}$ in figure 4.2 d) exhibit a significant asymmetry. The intercept of the upper γ' resonance (green) has a value of approximately $20.2\,\mu\mathrm{eV}$, whereas the lower γ line (red) indicates a gap of $-15.5\,\mu\mathrm{eV}$. This asymmetry is consistent with a nuclear magnetic field that increases the sublattice splitting gap Δ_γ at the *K* point and lowers it at the *K'* point as illustrated in figure 4.3 b). Note that Δ_γ has a different sign (and magnitude) at each Dirac cone, owing to the nontrivial band topology of graphene,[21] where spin and sublattice (pseudospin) degrees of freedom are related by chirality.

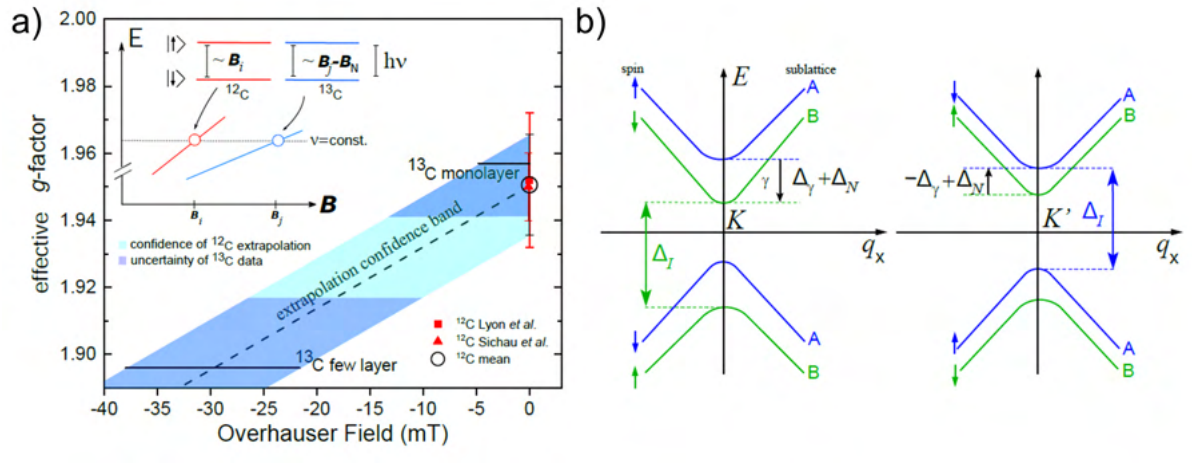

Figure 4.3.: a) Extrapolation of the ^{12}C g factor[16,17] in the presence of an Overhauser field (dashed line). The light blue band of confidence includes the measurement uncertainty. The g factors deduced from few-layer and monolayer ^{13}C graphene are shown by the intersecting dark shaded areas (black solid horizontal lines indicate mean values). The inset is a qualitative energy dispersion of the electron Zeeman splitting with a nuclear field $\boldsymbol{B}_\mathrm{N} < 0$ (blue) and $\boldsymbol{B}_\mathrm{N} = 0$ (red). A nuclear field will reduce the electron Zeeman splitting, i.e., for a constant ν a larger $\boldsymbol{B}$ is needed to match the resonance condition. b) Band diagram at K and K' in the presence of spin and sublattice splitting,[18] modified by a shift in energy of Δ_N induced by a nuclear field.[19] Figure a) and b) are adapted with permission from V. Strenzke, J. M. Meyer, I. Grandt-Ionita, M. Prada, H.-S. Kim, M. Heilmann, J. M. J. Lopes, L. Tiemann, and R. H. Blick. Nuclear-induced dephasing and signatures of hyperfine effects in isotopically purified ^{13}C graphene. Physical Review B 105, 144303 (2022). Copyright 2022 American Physical Society.[19]

This results in spin-polarized subbands with opposite ordering at the two K points,[18] causing the depicted band inversion (blue and green bands that represent the sublattice degree of freedom). Solving the zero-field splitting gaps $\Delta_\gamma + \Delta_\mathrm{N} \approx 20.24 \pm 0.84\,\mu\mathrm{eV}$ and $\Delta_\gamma - \Delta_\mathrm{N} \approx -15.52 \pm 1.31\,\mu\mathrm{eV}$ with $\Delta_\gamma = 17.88 \pm 1.1\,\mu\mathrm{eV}$, we obtain an effective $|\Delta_\mathrm{N}| \approx 2.36 \pm 0.24\,\mu\mathrm{eV}$ which converts to a nuclear field of $|\Delta_\mathrm{N}/g\mu_\mathrm{B}| \approx 21.5 \pm 2.2\,\mathrm{mT}$.

Strikingly, the two estimated Overhauser fields from the reduced g factor and the asymmetric γ resonances are in good agreement with each other, but also consistent with theoretical predictions and other experimental studies.[142,143,192,207,214] The ESR experiments presented here might have benefited from the aforementioned occurrences of local curvature in the large-area MBE-grown few-layer graphene. However, it is important to mention that the observed nuclear-induced variations are very small and approach the uncertainty limits of our measurements.

In the following, the temperature and microwave power dependence of the ESR experiments on ^{13}C graphene will be discussed. The resistively-detected ESR measurements on the ^{13}C few-layer graphene sister sample were repeated at millikelvin (mK) temperatures in a dilution

refrigerator. Figure 4.4 a) compares these measurements to the previous measurements that were conducted at 1.5 K. The γ resonance is the first resonance to appear at low microwave powers and low temperature while the main α resonance is still buried in the background. To resolve the α resonance, more electron spin-flip excitations are required, which can be provided by increasing the microwave power, as shown in figure 4.4 b). As indicated, the increasing power also results in an increase of the effective sample temperature.

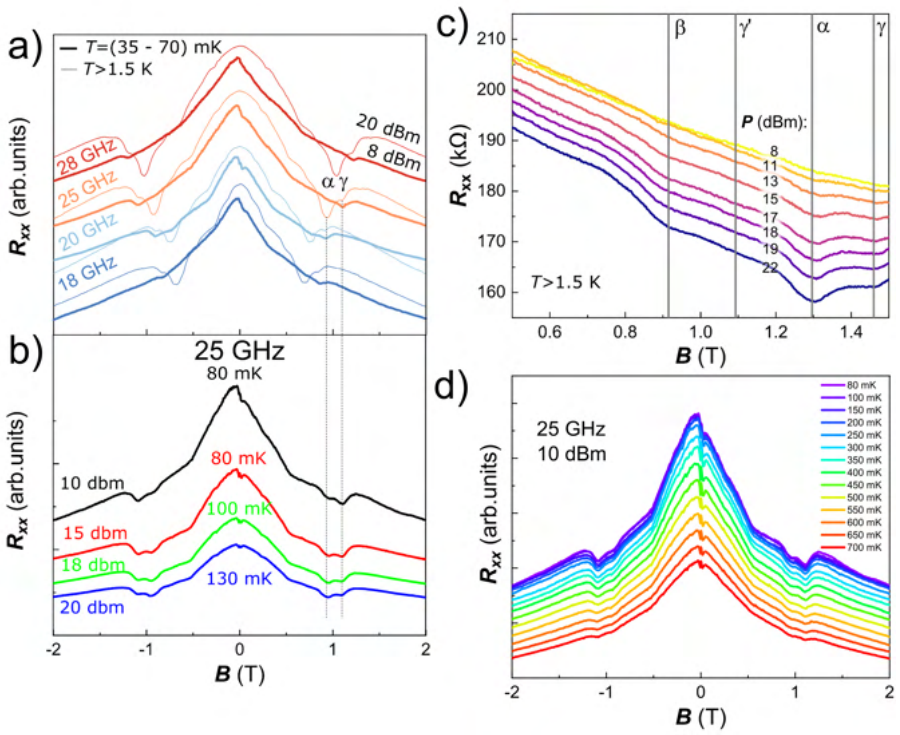

Figure 4.4.: a) Direct comparison of resistively-detected ESR measurements in the millikelvin (mK) regime (thick solid lines, all 8 dBm) and at higher temperatures (thin solid lines, all 20 dBm) on ^{13}C few-layer graphene (sample B). At low temperatures, the γ resonance is the first to appear. Measurements are performed close to the CNP and vertically shifted for better visibility. b) When the microwave power is increased, other resonances become pronounced. The effective sample temperature increases at higher power. c) Power dependence at nominally 1.5 K (the effective sample temperature is estimated to reach up to 3 K for 22 dBm). Here, all resonances appear simultaneously upon microwave power increase. d) Temperature-dependence of the resonances at mK-temperatures for constant microwave conditions. The resonances disappear equally fast for rising temperature.

A contrasting behavior is observed for ESR experiments on sample B at higher temperatures (1.5 K), depicted in figure 4.4 c). The cryostat is nominally at 1.5 K but the effective sample temperature is higher due to radiative heating of the sample space. We estimate the effective sample temperature to reach up to 3 K for the highest microwave power of 22 dBm. In this high

temperature regime, the γ resonance appears simultaneously with the other resonances when the microwave power is increased. In contrast, at low temperatures, the continuous heating of the sample at a constant microwave power reduces all resonances equally, as shown in figure 4.4 d).

We propose that in the low power and low temperature regime, a finite $\boldsymbol{B}_{\mathrm{N}}$ can exist due to a sizable $\langle S \rangle$ and the external magnetic field difference for α and γ (see Eq. 4.2). This nuclear magnetic field is too small to be detected directly as an Overhauser shift of the resonances due to our measurement uncertainty and linewidth. It becomes evident only through a detailed analysis of the resonance positions, revealing signatures of nuclear effects, as discussed above for figure 4.2 d). Here, a small $\boldsymbol{B}_{\mathrm{N}}$ can act on the electron Zeeman splitting and slightly enhance the γ resonance within the onset parameters for ESR detection where electron spin-flips can effectively transfer momentum to the nuclear spin system. Conducting such ESR experiments with improved microwave-coupling to the graphene electron system, e.g., by incorporating coplanar waveguides, could shed new light on low energy spectrum of the graphene band structure and probe nuclear-induced effects with minimized radiation heating.

Electron spin diffusion times τ_{s} are sensitive to spin-flip scattering and can be deduced from the ESR linewidth $\Delta \boldsymbol{B}_{\mathrm{res}}$[15]

$$\tau_{\mathrm{s}} = \frac{h}{4\pi \Delta E_{\mathrm{res}}} = \frac{h}{4\pi g \mu_{\mathrm{B}} \Delta \boldsymbol{B}_{\mathrm{res}}}. \tag{4.3}$$

Spin diffusion times were reported to be mostly independent of the carbon isotope and ranged between 60 ps and 80 ps, with a weak carrier density dependence.[143] From a Lorentzian fit of the resonances close to the CNP, spin diffusion times of $\tau_{\mathrm{s}}^{12\mathrm{C}} \approx 70 \pm 37$ ps (^{12}C graphene reference sample), $\tau_{\mathrm{s}}^{13\mathrm{C,\,A}} \approx 9 \pm 8$ ps (sample A) and $\tau_{\mathrm{s}}^{13\mathrm{C,\,B}} \approx 12 \pm 9$ ps (sample B) are obtained. The significantly shorter spin diffusion times for our ^{13}C samples are in agreement with the WL results and support the picture of nuclear spin-enhanced electron spin scattering.

The ESR measurements on ^{13}C few-layer graphene samples exhibit exceptionally well pronounced resonances. Exemplary measurements in both magnetic field sweeping directions were recorded with high resolution and are displayed in figure 4.5 a). These data were collected at two different gate voltages, but at the same frequency of 20 GHz. The coinciding resonance positions underline that Rashba spin-orbit coupling is negligible in our experiments. Note that the pronounced resistance dip around $\boldsymbol{B} = 0$ T will be discussed later. Although the resonances are already well visible in the raw data, the ESR signal can be enhanced by subtracting the ESR data from a background measurement, resulting in the ΔR_{xx} trace (blue solid line) in figure 4.5 b). The resonance positions of the four resonances (α, β, γ and γ') are marked by vertical lines, while their energetic separation is also labeled. Two unexpected and distinct features can be noticed in this ESR measurement. First, two symmetric shoulders appear around the α resonance, with a energetic separation of 1 GHz ($\sim 4\,\mu$eV) from α. The physical implications of such

ultralow-energy excitations in the graphene band structure would be intriguing. However, due to the line width and the signal intensity of the pronounced α resonance, these shoulder-features are sometimes difficult to identify for other frequencies. This impedes a more detailed analysis of this feature in the scope of this work, but which is certainly interesting for future studies.

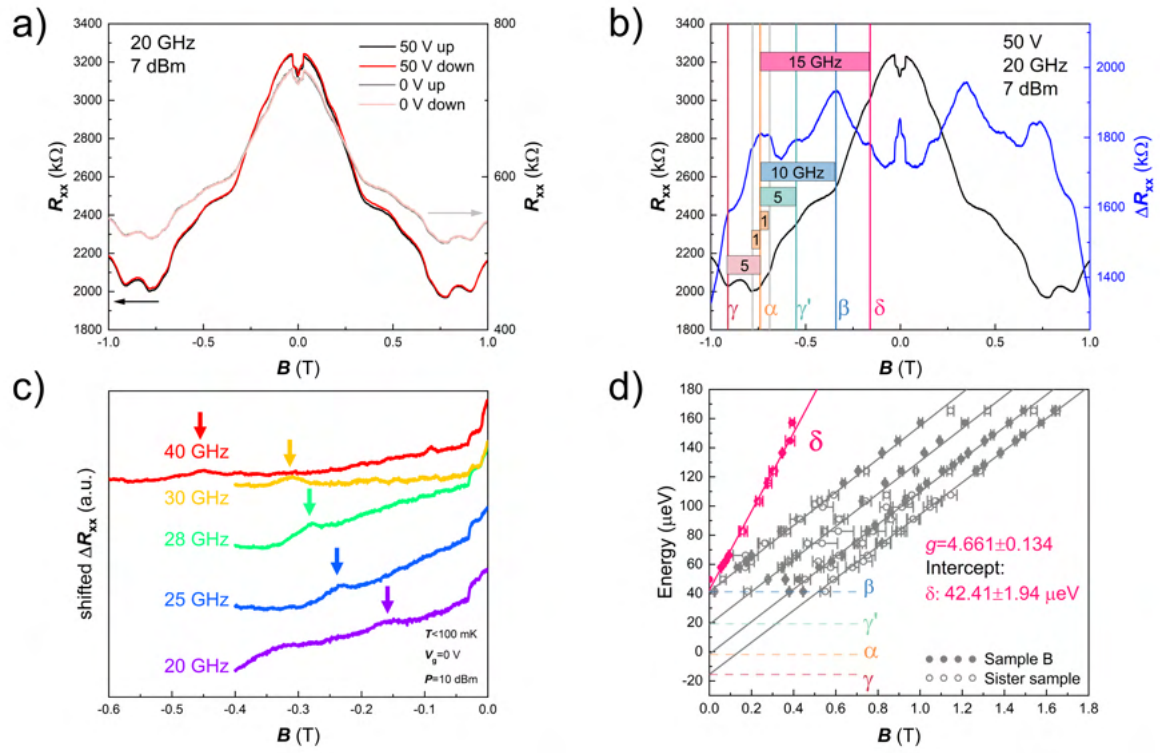

Figure 4.5.: a) Comparison of ESR measurements at two different gate voltages (0 V and 50 V) for both magnetic field sweeping directions. The measurement was performed on the ^{13}C few-layer graphene sister sample at mK-temperatures at a constant frequency of 20 GHz. b) Subtracting the ESR data (black data trace) from the background measurement yields ΔR_{xx} (blue data trace) which exhibits an enhanced ESR signal. The four resonances α, β, γ and γ' are marked by vertical lines along with their energetic separation. Two shoulders appear for the α resonance. A fifth resonance (δ) is observed at low magnetic fields. c) Detailed ESR measurements resolve the frequency shift of δ. d) Including δ in our detailed analysis yields an intercept of $\sim 42\,\mu$eV (similar to β) and a g factor of 4.661 ± 0.134.

The second unexpected feature is the appearance of an additional resonance towards lower magnetic field that is energetically separated by 15 GHz ($\sim 60\,\mu$eV) from α in this measurement. The resonance position of this feature can also be resolved for other frequencies, which is marked by arrows in figure 4.5 c). By including this additional fifth resonance in the detailed analysis from above, the intercept and g factor of this resonance are determined, as shown in figure 4.5 d). This fifth resonance, which will be referred to as δ, shares a similar intercept with β of $\sim 42\,\mu$eV. However, from the linear fit (bright red line) in figure 4.5 d) a g factor of

4.661 ± 0.134 is deduced, which is approximately 2.5 $\times$ higher than the g factor of the other four resonances. This δ resonance has appeared in ESR measurements on two ^{13}C few-layer graphene samples (sample B and sister sample)[145] and was also reported in a recent ESR study on twisted bilayer graphene.[140,141] In a recent study, Morissette *et al.* proposed an entirely different framework based on magnon geometric resonances[140] to explain the observed resonances in their study. Following their picture, the δ resonance originates from a two-magnon mode. However, their interpretation forcefully disregards the *experimental findings* of other ESR studies conducted on completely different (non-moiré) graphene devices.[19,139,141,215]

Thus, the δ resonance must have a different origin, which captures the results in ^{13}C few-layer graphene and those in TBG. Microwave-induced resistance-oscillations (MIROs) that have been observed in GaAs 2D electron systems also exhibit a linear microwave frequency dependence, although these oscillations are not strictly resonant features.[216] However, these radiation-induced oscillations are typically found in high-mobility electron systems, which is not the case for our ^{13}C few-layer graphene. Moreover, MIROs in graphene depend on the Fermi energy E_F and are expected to shift for different gate voltages.[217] As discussed above, this is not observed in our data and the δ resonance is found in at least *three different* samples, with varying carrier densities and impurity levels.[140,145] Hence, we rule out MIROs as a possible origin of δ. Based on the g factor of ~ 4.6, which is approximately twice as high as for the other resonances, an excitonic picture may be considered. Applying a perpendicular magnetic field results in quantized Landau levels with discrete energies. Under these conditions, excitonic states may form under microwave irradiation due to enhanced Coulomb interactions between carriers in the same Landau level.[218,219] As excitons in graphene are expected to be unstable it is unclear whether δ is related to them or not. However, these results highlight the rich physics that can be probed by ESR experiments, while the origin of some additional resonances, in particular δ, remains an open question.

Nuclear magnetic resonance in ^{13}C graphene

In order to probe the nuclear spins directly, the ^{13}C graphene samples were also exposed to radio frequencies to match the *nuclear* Zeeman splitting. Throughout this work, numerous approaches were employed to resistively detect NMR. The approaches differ in their method to polarize the nuclear spin system and in their detection technique.

Since the NMR signal is proportional to the nuclear spin imbalance, as discussed in section 2.4, the nuclear spin polarization should be maximized. The nuclear polarization is a fragile and extremely temperature-sensitive state. Hence, for the NMR experiments a balance must be found that allows sufficient polarization and readout signal-to-noise ratio while minimizing radiation-induced heating effects. NMR measurements are conducted either at the highest magnetic fields, which benefits thermal polarization,[145,220] or ESR is used for DNP.[19,50,145] ESR can

be utilized either in parallel to achieve a continuous polarization pumping or only ahead of the NMR probing, to minimize additional ESR-induced microwave heating of the sample.

In contrast to conventional NMR spectroscopy, solid state NMR typically indirectly probes the effect of nuclear spins on the 2D electron system.[20] As introduced earlier, one way is to identify the Overhauser shift of the electron spin resonance. Due to the narrow linewidth of the nuclear resonance, NMR measurements are usually not conducted by sweeping the magnetic field $\boldsymbol{B}$ at a constant nuclear RF frequency ν. Instead $\boldsymbol{B}$ is kept constant while ν is varied with high resolution around the expected resonance value. In addition, an RF on/off-switching technique was explored.[145,220,221]

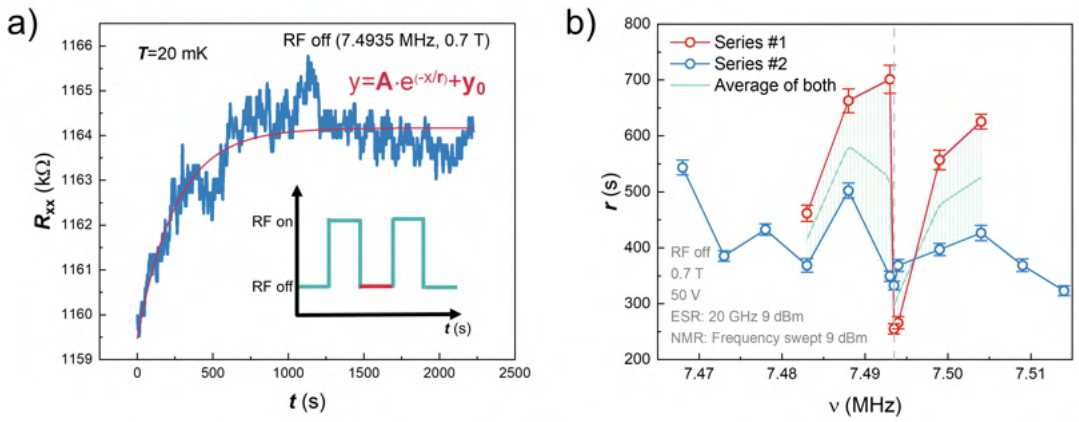

Figure 4.6.: a) Time-dependent R_{xx} relaxation of RF-off-switching, as indicated by the schematic inset, in the large-area ^{13}C graphene sister sample. The data is well described by a single exponential fit function (red solid line). The NMR experiment was conducted at 20 mK under ESR DNP at 0.7 T. b) The resistance relaxation time r of two measurement series (red and blue data points) and their average values (green line) exhibits a drop at the expected nuclear resonance frequency ν_r.

For this, R_{xx} is studied as a function of time over multiple on- and off-switching events of the radiation, for varying frequencies. When the RF radiation is turned on, the resistance decreases due to radiation-induced heating effects. The resulting resistance level can be studied as this may be affected significantly by nuclear effects at ν_r. When the RF radiation is turned off, the system equilibrates according to the Korringa law and an exponential fit to the resistance curve can be used to extract the relaxation time.[20,222] An exemplary fit of an RF-off-switching event in the large-area ^{13}C graphene sister sample is shown in figure 4.6 a). In this NMR experiment, DNP was performed by ESR at 20 GHz at a constant magnetic field of 0.7 T. For this magnetic field, the nuclear resonance frequency is expected at $\nu_r = \boldsymbol{B}\gamma = 7.494$ MHz, with the gyromagnetic ratio $\gamma = 10.705$ MHz/T for ^{13}C. The NMR frequency was switched on and off in small steps around ν_r under continuous ESR DNP. The time dependency of the resistance response to "RF off", i.e., the relaxation and cooling, is evaluated by fitting a single

exponential decay function $y = A \cdot e^{-\frac{x}{r}} + y_0$ to the data, as shown in figure 4.6 a). The spin-lattice relaxation of nuclear spins back to their equilibrium is mediated by conduction electrons and depends on the electron density of states, as described by the Korringa law.[20,222] Note that the observed resistance relaxation is also dominated by a thermal response, where the nuclear spin relaxation is encoded in a modulation of the thermal resistance relaxation time r. However, at the nuclear resonance frequency, a different resistance relaxation behavior is expected that should be reflected in the fitting results. The fit results of two series of RF-switching studies are given in figure 4.6 b) for the resistance relaxation time r. A drop towards ν_r is observed in the first series (red data points). While this feature is not as well pronounced in the second series (blue data points), the drop is visible in the average of both series (green line). The observed minimum in r at exactly ν_r signals a modulation of the resistance by nuclear spin relaxation. While these initial results are promising, it was not possible to consistently reproduce these observations, which may hint at an extremely slow/inefficient nuclear re-polarization.

In a modified version of this technique, the RF-radiation is switched between on- and off-resonant frequencies instead of on- and off-states. This minimizes thermal effects and may allow the determination of nuclear spin relaxation times.[221] An overview of the various conducted modifications of the RF-switching technique is given in D. v. Krosigk's bachelor's thesis.[220]

So far, it was not possible to clearly and reproducibly demonstrate NMR in ^{13}C graphene devices, using simple loop antennas as radiation sources. The nuclear resonance feature is expected to be small[19,203,204,214] and could be masked by radiative heating effects. However, in particular RF-switching NMR experiments could be explored in more detail in future studies.

Exfoliated hBN-^{13}C graphene heterostructures

The previously discussed large-area CVD- and MBE-grown ^{13}C graphene samples on silicon substrates suffer from inferior electronic quality compared to high-quality exfoliated graphene devices on hBN substrates. Improving the electronic quality of ^{13}C graphene devices could be beneficial to resolve nuclear effects. Thus, once the fabrication technologies were available, hBN-^{13}C graphene heterostructures were prepared and assessed by magnetotransport and microwave spectroscopy.

The influence of the hBN substrate was evaluated in ^{13}C few-layer graphene Hall bars on exfoliated hBN. However, it is still difficult to draw clear conclusion from these measurements. The interested reader is referred to D. v. Krosigk's bachelor's thesis.[220]

In a different approach, exfoliated and hBN-encapsulated ^{13}C graphene devices were prepared, which displayed a high electronic quality compared to the large-area, polycrystalline graphene samples. This brief section illustrates the advancements achieved in (^{13}C) graphene device fabrication.

An optical image of one exfoliated ^{13}C graphene sample with metallic one-dimensional edge

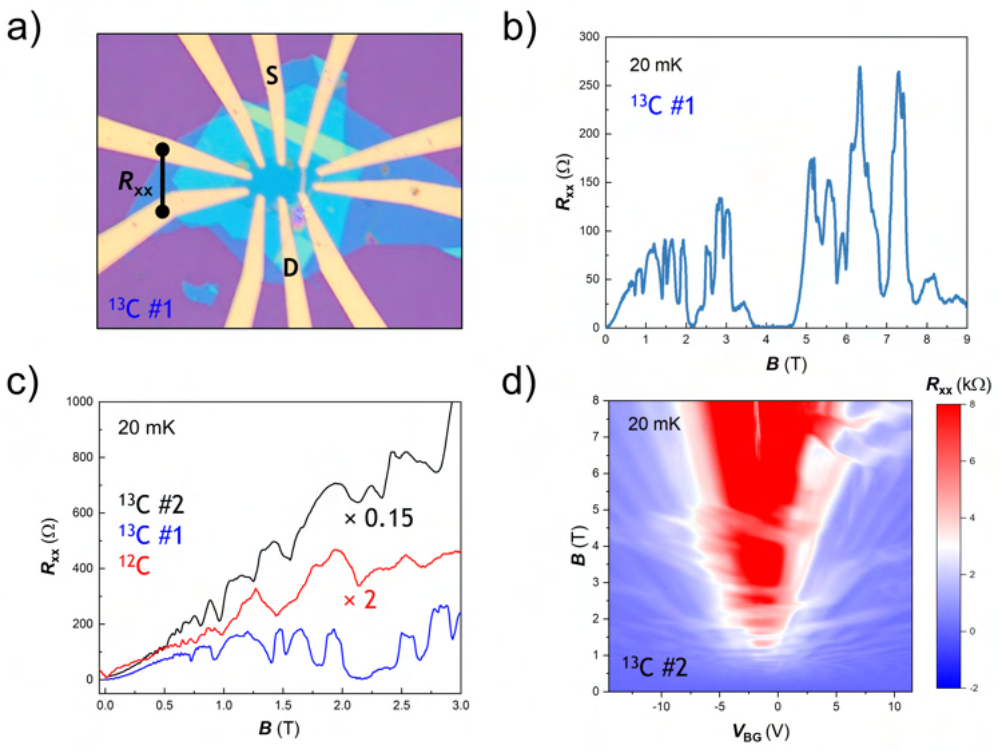

Figure 4.7.: a) Optical image of a hBN-encapsulated exfoliated ^{13}C graphene device (^{13}C # 1) with metallic one-dimensional edge contacts. b) The longitudinal resistance R_{xx} of this device exhibits clear Shubnikov-de Haas (SdH) oscillations and the quantum Hall effect. c) Comparison of the magnetotransport behavior of two ^{13}C graphene devices (^{13}C # 1 (blue) and ^{13}C # 2 (black)) and one ^{12}C sample (red). d) Landau fan diagram of ^{13}C # 2, mapping the gate voltage (V_{BG}) and magnetic field dependence of R_{xx}.

contacts (^{13}C # 1) is given in figure 4.7 a). The sample is few-layer ^{13}C graphene with 5 to 10 layers. A four-terminal magnetotransport measurement of the longitudinal resistance R_{xx} at 20 mK up to 9 T is shown in figure 4.7 b). The device exhibits pronounced Shubnikov-de Haas (SdH) oscillations, with R_{xx} dropping to zero. Unfortunately, the device configuration did not yield a well developed quantized Hall resistance[223] and the backgate was unavailable.[220]

Nevertheless, the classical Drude model can be employed to estimate the mobility μ and charge carrier density n with the classical Hall effect relation at low magnetic fields (≤ 100 mT) $R_{xy} = \rho_{xy} = \frac{B}{ne}$. The R_{xx} magnetotransport characteristics of this device (^{13}C # 1, blue trace) are compared with those of a second similar hBN-encapsulated exfoliated ^{13}C graphene sample (^{13}C # 2, black trace) and one hBN-encapsulated exfoliated ^{12}C graphene sample (^{12}C, red trace) in figure 4.7 c). Although the absolute resistance values of the ^{13}C # 2 and ^{12}C samples are much larger, they also display pronounced SdH oscillations, which start already at low magnetic fields, indicating high charge carrier mobilities.[144] The ^{12}C sample will be discussed

in more detail later in section 4.2. However, from its Hall resistance, a charge carrier density of $n \sim 5.8 \times 10^{12}\,\mathrm{cm}^{-2}$ and a high mobility of $\mu \sim 5 \times 10^{5}\,\mathrm{cm}^2/\mathrm{Vs}$ is deduced, using $\mu = \frac{1}{\rho_{xx}(\boldsymbol{B}=0)} \frac{d\rho_{xy}}{d\boldsymbol{B}}$ with the longitudinal resistivity $\rho_{xx} = R_{xx}\frac{W}{L}$ (W and L are width and length of the sample).[144] Note that there might be an overestimation of μ with a factor of $\sim$5 due to additional conductance pathways in the ^{12}C sample. The mobility for ^{13}C #1 is determined as $\mu \sim 2.6 \times 10^{4}\,\mathrm{cm}^2/\mathrm{Vs}$, although this time, the mobility is probably underestimated due to asymmetry in the Hall voltage.[220] For the other ^{13}C #2 sample, no Hall resistance could be measured and consequently n and μ could not be determined. However, in this sample a backgate was available that allowed mapping of the gate voltage (V_{BG}) and magnetic field dependence as shown in figure 4.7 d). This Landau fan diagram clearly shows the dispersion of the SdH oscillations towards higher magnetic fields, caused by the separation of the Landau levels. The expected SdH oscillations are intersected by diagonal features which may correspond to secondary Dirac peaks that result in additional Landau fans. This phenomenon, known as the Hofstadter butterfly, can be caused by the alignment of the hBN with the graphene that leads to the formation of a moiré superlattice.[224–226] For these hBN-graphene moiré superlattices, Brown-Zak oscillations are likely to arise from quantized magnetic flux through a superlattice unit cell.[225,227,228] However, the detailed analysis of the data in figure 4.7 d) is ambiguous and it remains unclear whether Brown-Zak oscillations are observed or not.

These results highlight the superior electronic quality of hBN-encapsulated exfoliated graphene devices compared to large-area graphene. For completeness, it is worth mentioning that ESR was carried out on these exfoliated ^{13}C graphene samples by using a simple loop antenna. However, no resonant signals could be observed which is mainly attributed to insufficient microwave coupling.

Resistance anomalies in ^{13}C graphene at low magnetic fields

Multiple MBE-grown ^{13}C few-layer graphene samples from different growth-batches showed resistance anomalies at low magnetic fields ($\leq 50\,\mathrm{mT}$). In the first sample, two steps appeared at $\pm 10\,\mathrm{mT}$ and $\pm 30\,\mathrm{mT}$ under microwave irradiation at mK-temperatures, as shown by the dark blue line in figure 4.8 a). The appearance of these steps is slightly hysteretic and dependent on the sweep rate. The height of the steps amounts to several tens of kΩ resistance and is also sensitive to the applied microwave power, as illustrated by the colored data points in figure 4.8 a). Measurements at different power values are compared in figure 4.8 b). The resistance steps are absent for measurements without microwave radiation (background), ruling out weak-antilocalization as possible explanation. Although the steps are observed for various microwave frequencies, the step position is frequency-independent, as shown in the appendix A.2 figure A.2. The observed effect appears to be non-resonant and is not induced by simple heating as discussed below.

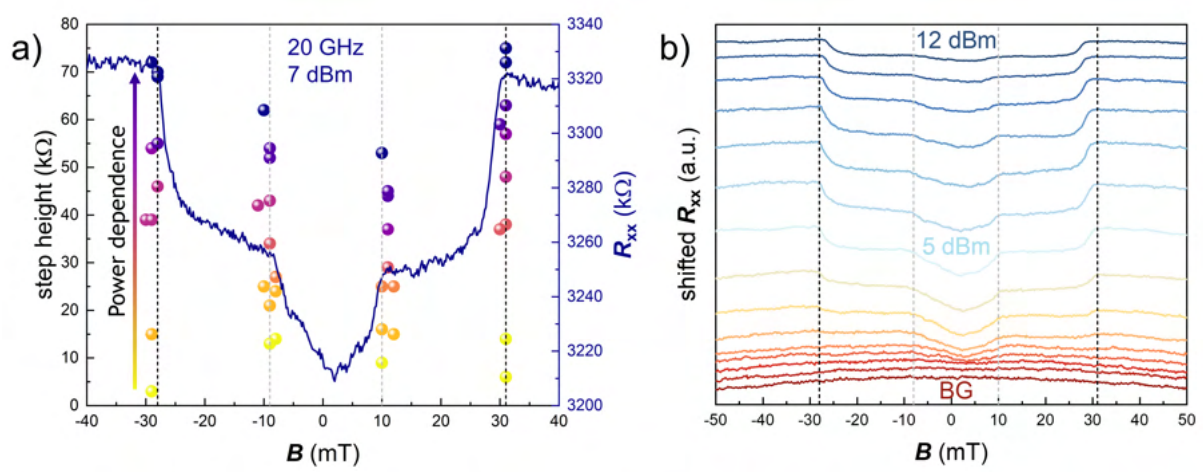

Figure 4.8.: a) Microwave-induced resistance steps (dark blue curve) at low magnetic fields in MBE-grown ^{13}C few-layer graphene at mK-temperatures. The step height is dependent on the applied power, as indicated by the colored data points. b) Comparison of measurements at different power levels including a background (BG) measurement without microwaves. All depicted measurements are conducted at 20 GHz and shifted for better visibility.

The step height of both steps can be extracted for negative and positive magnetic fields and compared for different microwave powers, as shown in figure 4.9 a). Here, the measured and calibrated effective electron temperature T_e is included to assess the radiation induced heating. Details on the determination of T_e can be found in the appendix figure A.3. The step height distribution over applied microwave power of both steps exhibits a bell curve shape with a maximum at intermediate power values. However, the maximum of the two steps is shifted by 4 dBm. The inner step is first to appear at low powers, followed by the outer step, before vanishing at high power. The disappearance of the steps at high power can be attributed to the high electron temperature, which approaches 1 K at > 12 dBm due to radiation induced heating. This sets the upper energy limit of this effect, corresponding to $k_B 1\,\mathrm{K} \sim 90\,\mu\mathrm{eV}$. In comparison, the magnetic field positions of the two steps correspond to magnetic field energies of $\mu_B \boldsymbol{B} \approx 0.6\,(1.8)\,\mu\mathrm{eV}$ for 10 mT (30 mT), respectively. The ratio R of the outer to inner step height is depicted as a function of applied microwave power in figure 4.9 b). In the given parameter range, R generally increases with increasing microwave power. An equal step height is observed for $R = 1$ at 5 dBm and $T_e \approx 650\,\mathrm{mK}$.

Various effects could be the origin of these steps. The magnetic field values fit well to the typical critical magnetic field of the aluminum wire bonds, but the magnitude of the resistance changes of tens of kΩ is too large for a superconducting transition of a metal. CVD-grown large-area ^{12}C graphene samples that were fabricated by the same methods did not show similar effects, which makes magnetic impurities from the wet transfer process an unlikely scenario.

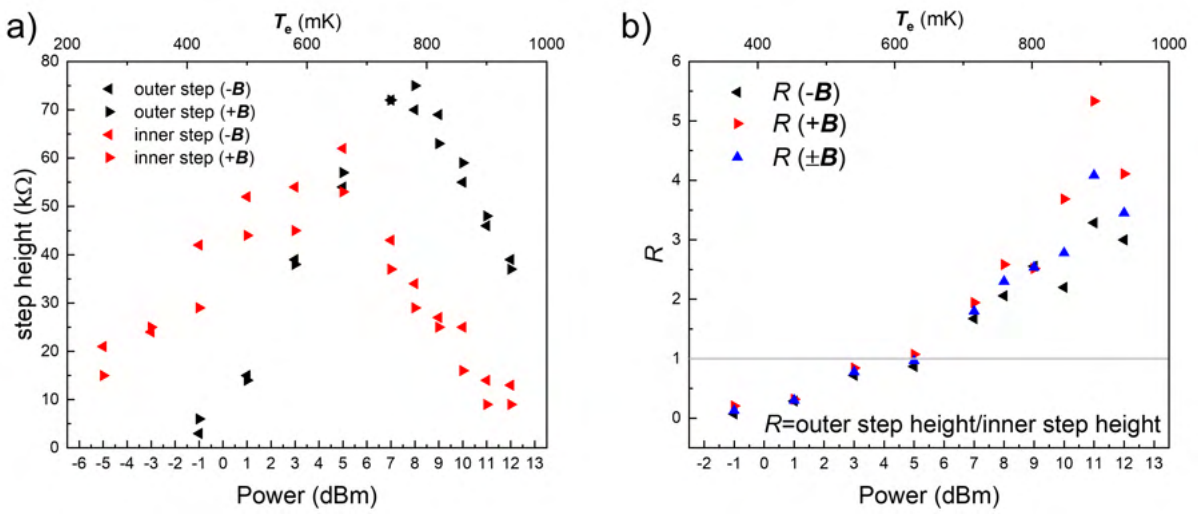

Figure 4.9.: a) Quantitative analysis of the step height of the inner (red triangles) and outer (black triangles) steps for negative and positive magnetic fields as a function of applied microwave power. The measured and calibrated effective electron temperature T_e is included as the upper x-axis. b) The ratio R of the outer to inner step height as a function of applied microwave power for negative (black triangles) and positive (red triangles) magnetic field values and their average (blue triangles). The equal step height at $R = 1$ is indicated by the grey solid line.

The lack of frequency dependence rules out resonant effects. Further, the magnetic field positions are independent of the charge carrier density and appear at identical positions for measurements at 0 V and 50 V backgate voltage. For resistance steps related to quantum effects and localized states a shift of the steps would be expected. This also makes effects improbable that result from charge domains such as electron-hole puddles. The large size of the sample geometry excludes magnetic flux quantization effects. The observed flux through the graphene area A ($20 \times 180\,\mu m^2$) ranges between $\boldsymbol{B} \cdot A \approx 1 - 5 \times 10^5$ flux quanta $\Phi_0 = \frac{h}{e}$ for 10 mT to 30 mT.

While nuclear effects are a possible reason, the application of kHz-frequencies (corresponding the nuclear resonance frequencies) by a lock-in oscillator output did not yield meaningful results. Instead, if we focus on the absence of the steps without microwave radiation, nuclear effects could result from a (partially) polarized spin system resulting from DNP. At $\boldsymbol{B} \approx 0$ T, microwave-induced non-resonant electron spin excitations could result in hyperfine-mediated non-equilibrium DNP of the nuclear spin system. The applied magnetic field could reach threshold values at ± 10 mT and ± 30 mT where the nuclear spins become polarized. The observed values of magnetic field (few tens of mT) are in good agreement with the estimations for nuclear magnetic fields from our ESR measurements.[19,50,143] However, this is purely speculative and additional measurements of these effects are needed in the future.

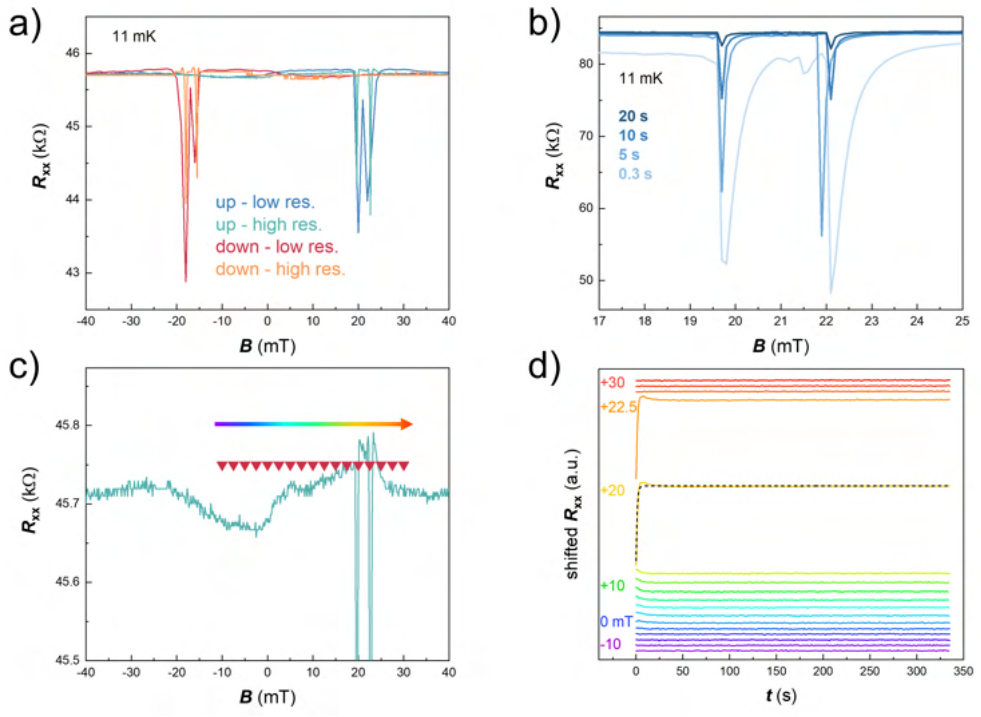

Figure 4.10.: a) Resistance anomalies at low magnetic fields *without* microwave radiation in another MBE-grown ^{13}C few-layer graphene sample. Depending on the magnetic field sweep direction and resolution, two resistance dips appear around ± 20 mT. b) The high resolution upsweep from a) is repeated with different integration time, revealing a time dependence of the two dips. c) The high-resolution upsweep exhibits the two resistance dips at 20 mT and 22.5 mT. The constant magnetic field positions of time-dependent resistance measurements are indicated by the red arrows. The colored arrow above serves as a reference for the magnetic field positions in d). d) Time-dependence resistance traces at various magnetic field values ranging from -10 mT (purple) to $+30$ mT (red). Most measurements do not exhibit a significant time dependence. However, at $+20$ mT and $+22.5$ mT (position of the dips), a rapid resistance increase is observed. An exponential fit (black dashed line) to the resistance curve yields a relaxation time of ~ 1 s.

In another MBE-grown ^{13}C few-layer graphene sample from a different growth-batch, resistance anomalies appeared at similar magnetic field values as shown in figure 4.10 a). However, this time the resistance anomalies were found *without* microwave radiation. Two resistance dips of several kΩ magnitude appear hysteretically at ~ 20 mT at negative *or* positive magnetic fields, depending on the sweeping direction. The measurements in figure 4.10 a) are conducted with either low (1 mT) or high (0.16 mT) magnetic field resolution, but with the same integration time per data point, which results in different sweep rates. The two resistance dips appear more narrow for higher resolution, i.e., slower sweep rate. This reveals a time-dependence of these dips, which is assessed by repeating the high resolution measurement with different integration

times, as shown in figure 4.10 b). Strikingly, the highest magnitude of the dips is observed for the shortest integration time of 0.3 s (light blue), while the dips almost vanish for an integration time of 20 s (dark blue).

The time dependence is evaluated in more detail by measuring the resistance over time at different constant magnetic fields, indicated by the red arrows in figure 4.10 c). The magnetic field value, ranging from -10 mT to $+30$ mT, of the resulting resistance measurements over time in figure 4.10 d) is indicated by colors. For most magnetic field positions, the resistance does not exhibit any significant time dependence. However, at the position of the two dips (20 mT and 22.5 mT), the resistance rapidly increases before reaching a stable resistance value. An exponential fit to the resistance curve yields a relaxation time of ~ 1 s at both peak positions, which may correspond to the spin-lattice relaxation time.[222] This time dependence strongly implies a spin-diffusion-based origin of the dips.

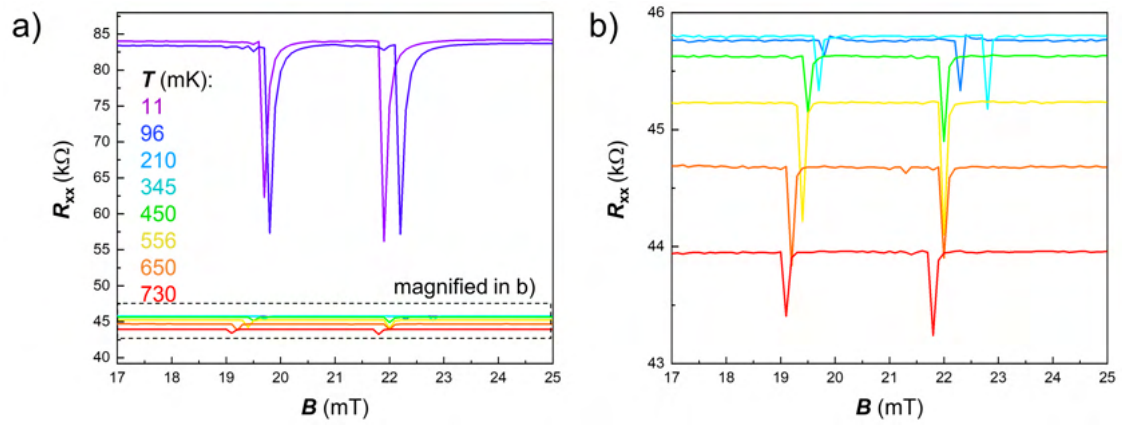

Figure 4.11.: a) Temperature dependence from 11 mK to 730 mK of the two resistance dips. All measurements performed with 5 s integration time in upsweep-direction. b) Magnified view of higher temperatures from a).

The temperature dependence of this effect is presented in figure 4.11. These measurements were recorded with 5 s integration time by sweeping the magnetic field from negative to positive values at temperatures between 11 mK to 730 mK. While no significant difference is observed between 11 mK and 96 mK, a large decrease in amplitude and overall resistance is apparent for higher temperatures. Surprisingly, the amplitude of the two resistance dips does not decrease much further when the temperature is increased from 210 mK to 730 mK. The reason for the shifts in the magnetic field positions of the dips between different temperature measurements remains unclear. These shifts appear to be irregular and not continuous.

The origin of this effect remains an open question. However, the appearance of the resistance anomaly at ~ 20 mT is again in good agreement with signatures of nuclear magnetic fields from previous measurements on MBE-grown ^{13}C few-layer graphene.

In summary, we find indications of nuclear spin effects in WL, ESR and magnetotransport measurements. If the enhanced electronic quality observed in hBN-encapsulated exfoliated ^{13}C graphene devices is combined with more efficient microwave coupling, experiments with higher sensitivity can be achieved that could be capable to resolve nuclear spin effects directly.

4.2. Microwave Spectroscopy with Hybrid Circuits

In order to optimize the coupling of microwaves to graphene, microwave spectroscopy was performed with hybrid circuits which integrate graphene with metallic contacts into high-frequency waveguides. First, the results based on large-area graphene will be discussed, before presenting advances with exfoliated graphene samples.

4.2.1. Microwave Circuits with Large-Area Graphene

The first generation of devices combined large-area CVD graphene with broadband metallic coplanar waveguides (CPWs), as presented in figure 4.12 a) and explained in detail in section 3.2.1. The CPW acts as an ultimately close microwave source directly below the large-area CVD graphene, only separated by a thin oxide. The metallic contacts on top of the graphene enable a low-frequency lock-in resistive readout technique that can be referenced to the transmission-based readout of the high-frequency signal of the CPW.

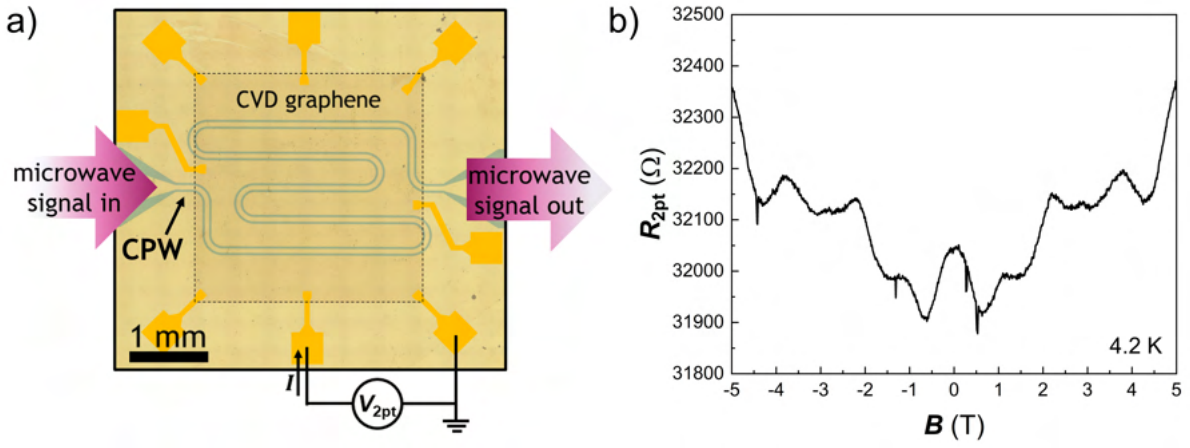

Figure 4.12.: a) Optical image of large-area CVD graphene on top of a broadband metallic coplanar waveguide (CPW) structure. This device is capable of a simultaneous high-frequency transmission-based readout of the CPW and low-frequency resistive readout via metallic contacts to the graphene. b) Exemplary two-terminal magnetotransport of the graphene at 4.2 K without microwave radiation.

The sample was cooled down to 4.2 K and two-terminal measurements on the graphene were performed as indicated in figure 4.12 a). The resulting magnetotransport behavior *without* any

high-frequency signal is shown in figure 4.12 b). Note, that other contacts were functional in this device, but left floating for these measurements. The resistance exhibits oscillations and a peak at $\boldsymbol{B} = 0\,\mathrm{T}$. Although this peak could originate from WL, its wide shape is unusual for large-area CVD graphene samples with equally inferior electronic quality. A density deduced from the $\frac{1}{\boldsymbol{B}}$ periodicity of the oscillations did not yield meaningful results and the geometry of the sample is much larger than the estimated cyclotron radius $r_\mathrm{c} = \hbar k_\mathrm{F}/e\boldsymbol{B} = \hbar\sqrt{\pi n}/e\boldsymbol{B}$.

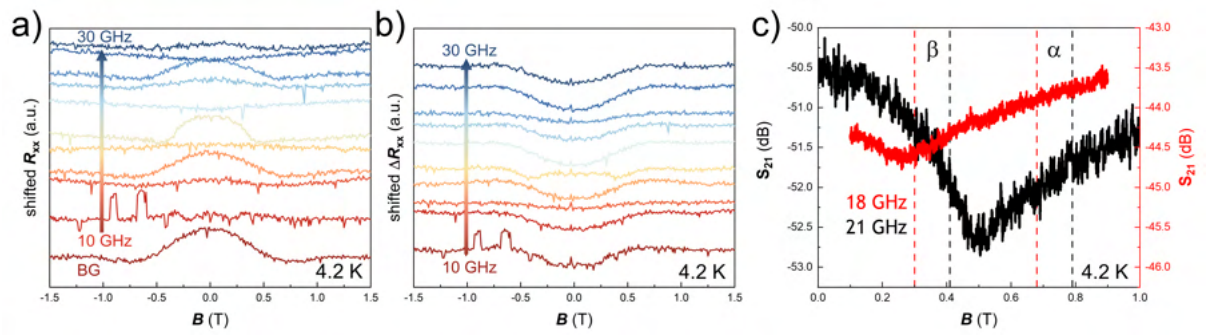

Figure 4.13.: a) Magnetic field dependence of the two-terminal resistance of the graphene under constant microwave radiation, supplied by the CPW, at various frequencies (10 GHz to 30 GHz in 2 GHz steps). The background (BG) measurement without microwaves is also included (dark red). All measurements are vertically shifted for clarity. b) BG-subtracted resistance ΔR_{xx} of the ESR measurements in a). No dispersing resonance peaks can be identified. c) Exemplary CPW transmission signals (S_{21}) at 18 GHz and 21 GHz as a function of magnetic field. The dashed lines indicate the expected resonance positions for the α and β resonance. The transmission shows a minimum that shifts with frequency, reminiscent of ESR.

When the signal generator was connected to the high-frequency lines of the CPW, the magnetotransport displayed a significant increase of the noise level. This implies potential issues of the device circuitry, which were considered in the design of the next generations of these devices (see section 3.2.1). ESR experiments were conducted by sweeping the magnetic field at a constant microwave frequency and power applied to the CPW. Resistively-detected ESR measurements at various frequencies ranging from 10 GHz to 30 GHz are displayed in figure 4.13 a). Although the microwave-induced heating leads to a decrease of the sample resistance, no clear ESR signal is observed. Subtracting the background measurement to obtain ΔR_{xx} [figure 4.13 b)], a method used in previous ESR studies,[16–18] did not reveal any ESR signal either.

The transmission of the microwaves S_{21} through the graphene-loaded CPW is detected with a VNA in parallel to the resistive readout via lock-in amplifiers. For two exemplary frequencies (18 GHz and 21 GHz), the behavior of S_{21} is shown in figure 4.13 c). The dashed lines indicate the expected magnetic field positions of the α and β resonance. For both measurements, a minimum is detected in close proximity to the expected position of the β resonance. This minimum shifts with frequency, as expected for the Zeeman energy. Under the assumption that

the observed minima are caused by ESR-induced attenuation of microwaves in the sample, it remains unclear why only the β resonance is detected. Hence, the observed peaks from the transmission-based readout should be taken with caution. Nevertheless, the presented CPW-based ESR experiments on large-area graphene serve as a proof-of-concept which should be repeated with optimized devices in future studies. An optical image of an exemplary device of the next generation is shown in figure 4.14. Due to time constraints it was not possible to study these devices within the scope of this work.

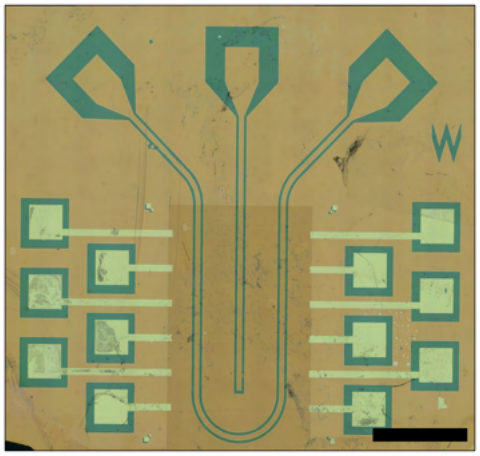

Figure 4.14.: Exemplary optical image of a metallic CPW device of the next generation, equipped with CVD graphene on top. The scale bar is 1 mm.

4.2.2. Microwave Circuits with Exfoliated Graphene

High-frequency microwave radiation can be coupled to exfoliated graphene devices in different ways. In this thesis, hBN-encapsulated exfoliated graphene heterostructures were combined with on-chip microwave transmission lines. These waveguides are only partially equipped with groundplanes, due to space limitations caused by the additional electrical contacts used for resistive readout. Strictly speaking, the utilized waveguides are thus not *coplanar* waveguides. Hence, the term CPW will not be used in this context.

Different approaches in transmission line coupling to the graphene were assessed, as illustrated in figure 4.15, a) within close proximity to the graphene or b) directly on top of the graphene. In order to reduce losses in microwave transmission, these samples are prepared on insulating high-resistivity (high-res) silicon substrates without a global backgate.

First, results are presented that were obtained on a graphene sample with a waveguide in close proximity, as shown in figure 4.16 a). Unfortunately, the Hall resistance could not be measured due to non-functional contacts. Four-terminal (black) and two-terminal (red) magnetotransport

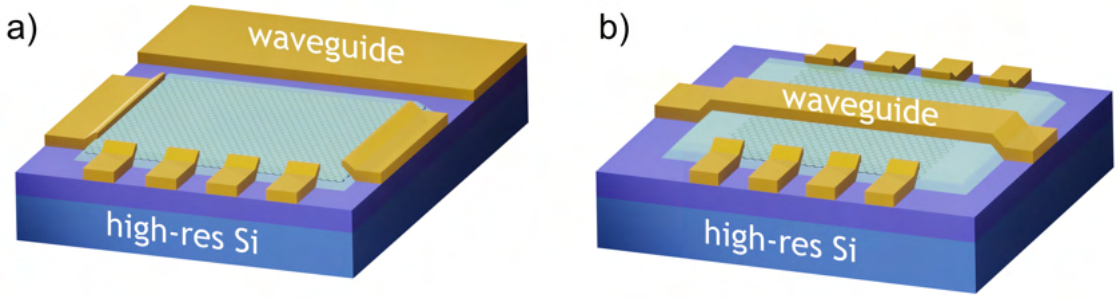

Figure 4.15.: Schematic drawings of different approaches to couple microwave radiation from a high-frequency waveguide to an exfoliated graphene device with metallic contacts. Approach where the waveguide is a) in close proximity to the graphene device and b) on top of the graphene heterostructure.

measurements were conducted, as shown in figure 4.16 b). From the SdH oscillations, the charge carrier density n can be estimated by

$$n = \frac{4e}{h}\left(\Delta\left(\frac{1}{\boldsymbol{B}}\right)\right)^{-1} = \frac{4e}{h}\left(\frac{1}{\boldsymbol{B}_{\mathrm{i+1}}} - \frac{1}{\boldsymbol{B}_{\mathrm{i}}}\right)^{-1}, \tag{4.4}$$

with the magnetic field separation of two neighboring SdH oscillations $\Delta\left(\frac{1}{\boldsymbol{B}}\right)$. For this sample, a value of $n \approx 3 \times 10^{11}\,\mathrm{cm}^{-2}$ is estimated. Since neither a global nor a local gate was available in this sample, the charge carrier density could not be controlled electrostatically.

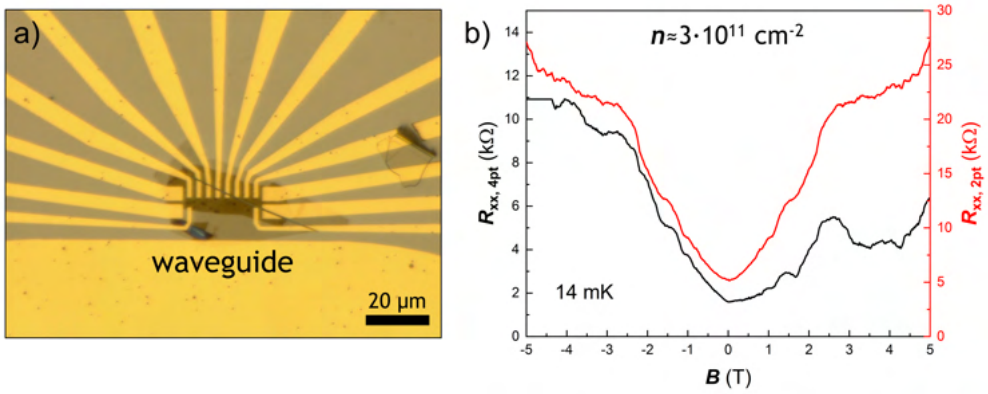

Figure 4.16.: a) Optical image of hBN-encapsulated graphene Hall bar in close proximity to a high-frequency waveguide. b) Magnetic field dependence of the four-terminal (black) and two-terminal resistances. The four-terminal configuration exhibits a pronounced asymmetry. The charge carrier density is estimated from the SdH oscillations using Eq. 4.4.

For ESR measurements, primarily the two-terminal resistance is evaluated due to the pronounced asymmetry in the four-terminal configuration. The microwave dependence of R_{xx} at various frequencies at 18 dBm power is shown in figure 4.17 a). The raw data of this resistance-

based ESR readout exhibit a significant microwave-induced resistance decrease due to heating. Additionally, the increased temperature of up to 200 mK evens out the resistance oscillations. This causes pronounced oscillations in the background-subtracted ΔR_{xx}, shown in figure 4.17 b), which complicates the identification of potential resonances. The data in figure 4.17 a) are the averaged values of three individual measurements to enhance the signal-to-noise ratio. Despite our efforts, no ESR signal can be found at the expected resonance positions, that are exemplary marked by the dashed lines in figure 4.17 b) for the α resonance.

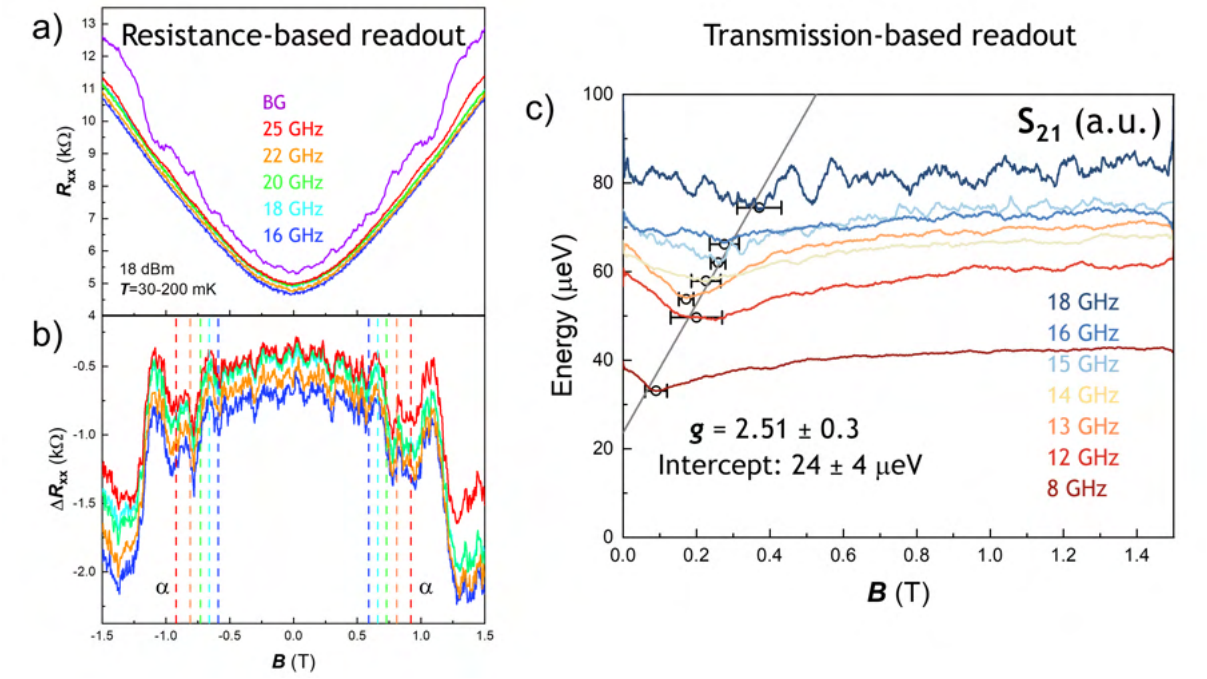

Figure 4.17.: a) Resistive readout of ESR measurements at mK-temperatures on the hBN-encapsulated graphene devices with a microwave transmission line in close proximity. Data are the average of three individual resistance curves at multiple exemplary frequencies and the background (BG) without radiation. The resistance oscillations vanish under microwave irradiation due to heating. b) BG-subtracted resistance data ΔR_{xx} from a). The colors correspond to the various frequencies. The dashed lines indicate the expected magnetic field positions of the α resonance. c) Transmission-based readout of ESR measurements, showing the magnetic field dependence of S_{21}. A minimum can be identified in the transmission that shifts in magnetic field, depending on the applied microwave energy. A linear fit to the position of this minimum yields $g = 2.51 \pm 0.3$ with an intercept at $24 \pm 4\,\mu\mathrm{eV}$.

In addition to the resistance-based readout, the attenuation of the microwave transmission S_{21} was recorded by a VNA. Similar to the measurements presented in figure 4.13 c), the magnetic field dependence of S_{21} on this exfoliated graphene device exhibits a minimum that shifts with the applied microwave frequency, as shown in figure 4.17 c). A linear fit to the magnetic field position of this minimum at frequencies ranging from 8 GHz to 18 GHz yields a g factor of

2.51 ± 0.3 with an intercept at $24 \pm 4\,\mu$eV. Even under the assumption of a large error, the resonance is unlikely to intercept the energy axis around zero, which could point towards an origin in the β resonance. However, these results should be interpreted with caution due to the large uncertainty and the limited number of data points. The origin of this minimum remains an open question and could be the result of an unknown artifact in our measurement approach.

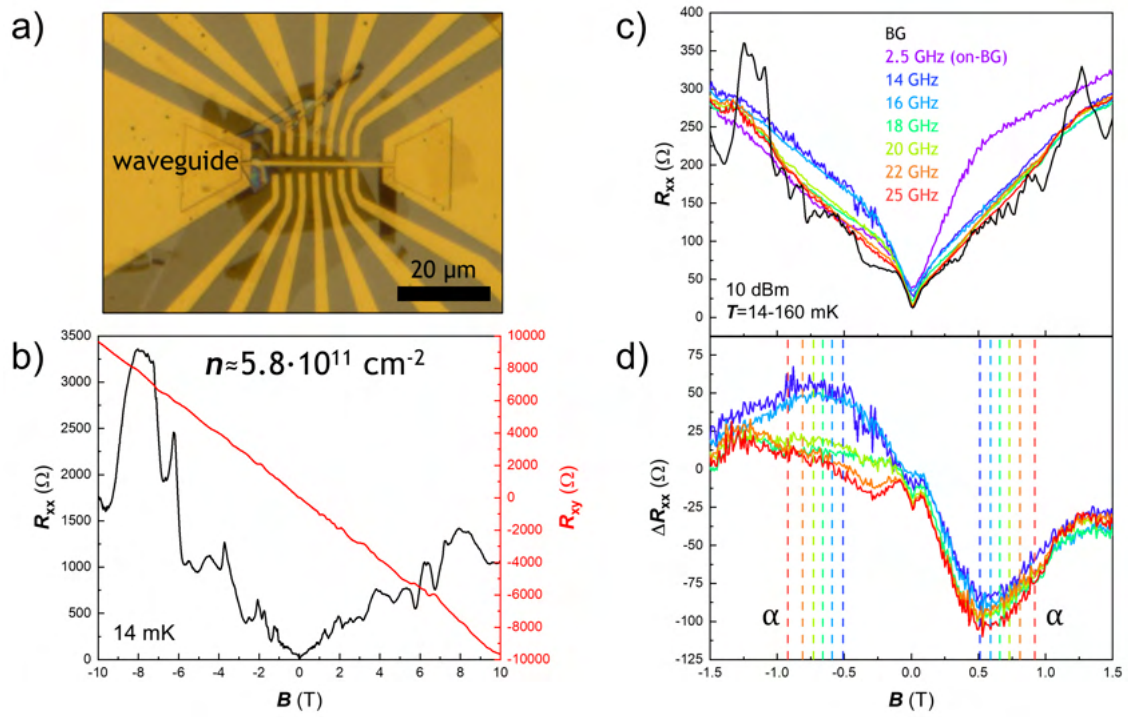

Figure 4.18.: a) Optical image of hBN-encapsulated exfoliated few-layer graphene Hall bar embedded in a hybrid microwave circuit with a waveguide on top. b) Low-temperature transport behavior showing the longitudinal and Hall resistance, R_{xx} (black) and R_{xy} (red), respectively. c) Resistively-detected ESR measurements at 10 dBm power and various constant microwave frequencies. In addition to the standard background (BG, black) measurement without radiation, a measurement at 2.5 GHz serves as on-background (on-BG, purple). d) Resulting ΔR_{xx} using the on-BG shown in c). However, no resonance peaks can be identified at the expected magnetic field positions (indicated by the colored dashed lines for α).

The optical image in figure 4.18 a) shows the second design with the waveguide running across the graphene. The metallic waveguide can act as a top gate to locally tune the carrier concentration, however, in this sample it was electrically shorted to a non-functional contact. The graphene flake in this sample consisted of two to four layers. Using a four-terminal contact configuration, pronounced SdH oscillations are observed in the longitudinal magnetoresistance (black), as shown in figure 4.18 b). Around zero field, R_{xx} reaches values of only a few tens of Ω, which is unexpectedly low. The slope of R_{xy} at low fields is used to extract a density of $n \approx 5.8 \times 10^{11}$ cm^{-2} and a charge carrier mobility of $\mu \sim 5 \times 10^5$ cm^2/Vs, which is a factor of 5

to 10 higher than for our typical samples. The sample exhibits high-mobility transport behavior, which is combined with microwave radiation in the next step to perform ESR experiments.

The magnetotransport properties of this sample without microwave radiation are compared to measurements under illumination with various frequencies at 10 dBm in figure 4.18 c). Here, a measurement at 2.5 GHz is included that serves as a new background measurement (on-BG, purple) to include radiation-induced heating effects and to avoid oscillating artifacts in ΔR_{xx}. However, due to the asymmetry of R_{xx} in the on-BG, a varying offset is introduced to the on-BG-subtracted ΔR_{xx} curves in figure 4.18 d). Again, resonance features are absent at the expected magnetic field positions (indicated by the colored dashed lines for α) despite significant radiative heating of the sample. Other approaches such as frequency-swept ESR experiments have been conducted, as shown in the appendix in figure A.4. Transmission-based readout measurements which are shown in figure A.4 c) showed similar signs of a shifting resistance minimum as discussed for the previous sample.

ESR experiments on exfoliated graphene devices have shown to be experimentally challenging, despite their elevated electronic quality compared to large-area graphene and improved microwave coupling. Certain impurities in large-area graphene that typically limit the electronic quality may actually be beneficial for ESR experiments. Especially impurities and defects with a magnetic moment such as magnetic adatoms or vacancies could promote electron spin effects in graphene.[195,229] The role of such defects has been discussed as a major contribution to electron spin dephasing in graphene.[195,199,229] In our MBE-grown large-area ^{13}C few-layer graphene samples, a large defect peak in the Raman spectra (see figure 3.5) indicates the presence of a significant amount of vacancies. This level of vacancies is much larger compared to our other graphene materials. In the previously discussed ESR experiments on ^{13}C few-layer graphene (section 4.1), the observed ESR resonance peaks were extremely well pronounced. In contrast, large-area CVD-grown ^{12}C graphene with a much lower defect peak in the Raman data, did not show as well developed ESR signals.[16,17] The absence of resonances in exfoliated graphene devices could also be due to inefficient coupling of the microwaves, despite our efforts to employ novel high-frequency circuits. Following the results of recent experiments on asymmetric dual-grating gate graphene terahertz field-effect-transistors, it could be beneficial to fabricate metallic coupling structures to the graphene to achieve reliable ESR detection.[139,215]

Microwave Circuits with Exfoliated ^{13}C Graphene

The design with the waveguide situated on top of graphene was also employed for exfoliated ^{13}C graphene devices, as shown in the optical image in figure 4.19 b). This device consists of a hBN-encapsulated trilayer ^{13}C graphene Hall bar with metallic Cr/Au contacts. Using a bias-tee, also a DC voltage for electrostatic gating of the carrier concentration can be applied to the waveguide, as shown in figure 4.19 a), with the CNP located at $V_\mathrm{g} \approx -6\,\mathrm{V}$. However, it only partially covers the sample and gating will be inhomogeneous. The accessible voltage range is limited to $\pm 10\,\mathrm{V}$ due to gate leakage. The magnetotransport characteristics for $V_\mathrm{g} = 6\,\mathrm{V}$, shown in figure 4.19 c), exhibit oscillatory features. The largest minima at approximately $\pm\,2\,\mathrm{T}$ and $\pm\,4\,\mathrm{T}$ show little response to varying gate voltage, as shown in figure 4.19 d). The cyclotron radius r_c and SdH oscillations depend on the charge carrier density, which is not affected in areas far away from the waveguide, such as between contacts.

Resistively-detected ESR and NMR experiments on this device were performed between $V_\mathrm{g} = -8\,\mathrm{V}$ and $+8\,\mathrm{V}$, but resonant features remained absent, as shown in the appendix in figure A.5.

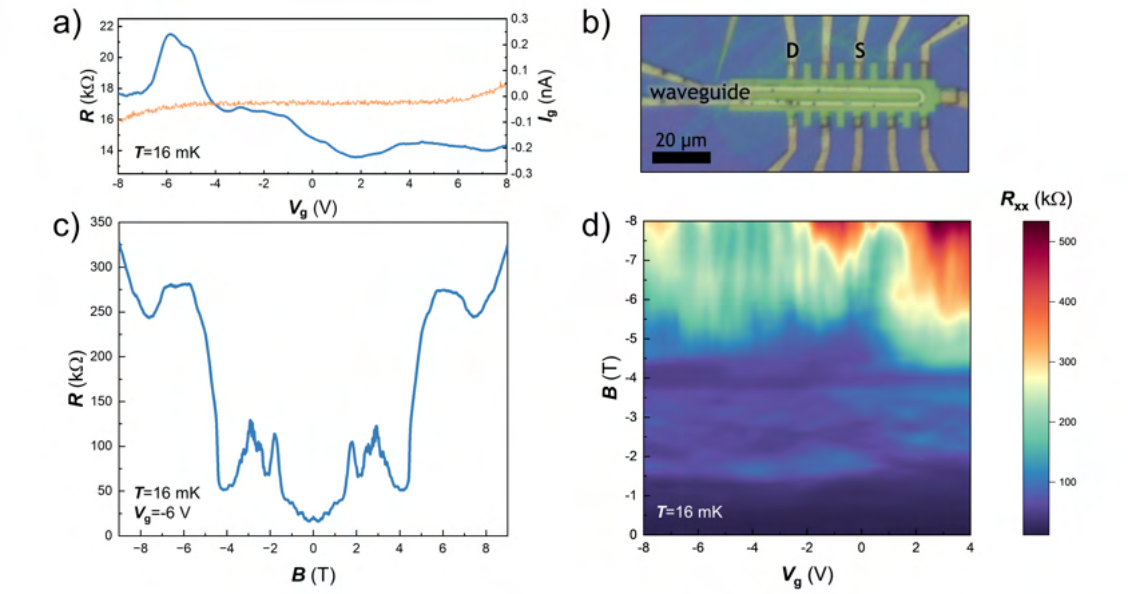

Figure 4.19.: a) Gate voltage (V_g) dependence of the two-terminal resistance (blue line) and the leakage current (orange line). b) Optical image of the ^{13}C graphene device with a waveguide on top, that can also be used as a topgate. c) Resistance as a function of magnetic field at $V_\mathrm{g} = 0\,\mathrm{V}$. d) Resistance as a function of magnetic field and gate voltage. All measurements were performed at 16 mK.

Analogous to experiments MBE-grown few-layer ^{13}C graphene from section 4.1, at small magnetic fields of $\sim 20\,\mathrm{mT}$ two resistance dips appear hysteretically at negative *or* positive

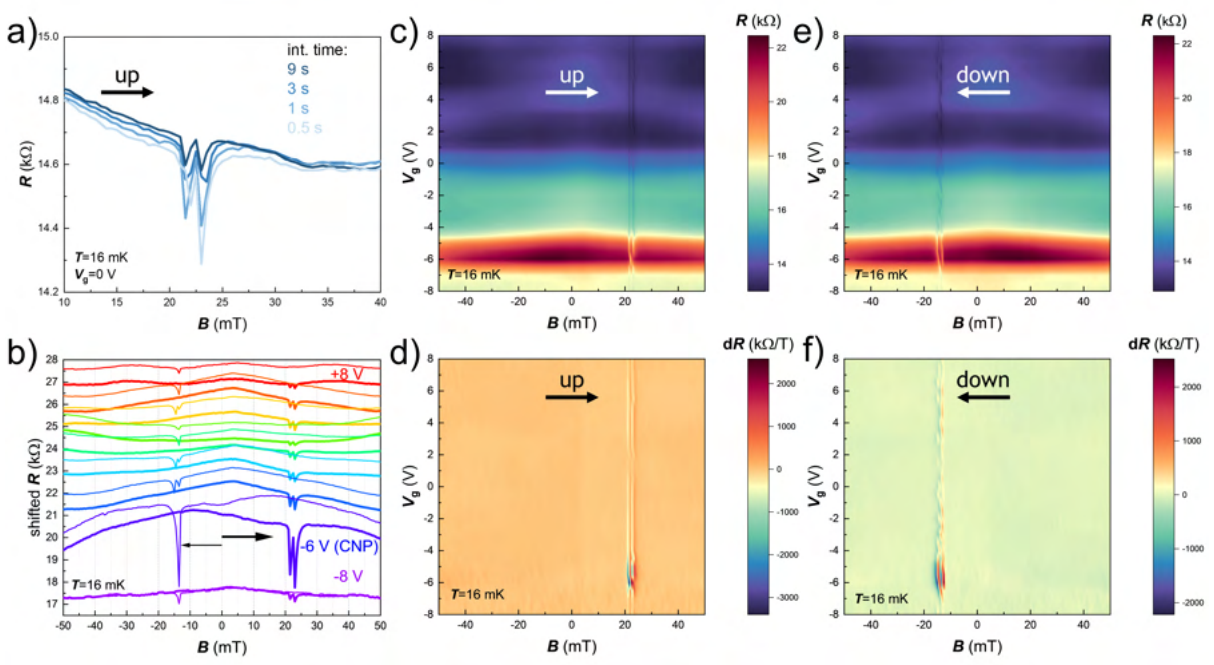

Figure 4.20.: a) At $\sim 20\,\mathrm{mT}$ two resistance dips appear hysteretically at negative *or* positive magnetic fields. The peak amplitude decreases with increasing integration time. b) Magnetic field up- (thick lines) and down-sweeps (thin lines) showing the peaks at various gate voltages. c) Detailed gate voltage dependence of the resistance and d) the differentiated resistance dR at small magnetic fields in up-sweep and e), f) down-sweep direction, respectively. All measurements were performed at 16 mK.

magnetic fields. Figure 4.20 a) shows that the amplitude of the two peaks depends on the integration time for each magnetic field data point, which signals a time-dependent origin.

The measurements shown in figure 4.20 b) to f) reveal a significant dependence of the peaks on the gate voltage, which are most pronounced at the CNP. Note that the zero of our magnetic field power supply is offset by $+3.3\,\mathrm{mT}$, which is not corrected in data presented here. The amplitude of the peaks reaches its maximum at low densities around the CNP, where charge carrier screening, e.g., of nuclear moments, is weak. Hence, this observation is attributed to nuclear spin effects in the ^{13}C few-layer graphene, which influence charge carrier transport especially at low densities (as seen for the density dependence of scattering times in section 4.1).[19, 193, 194]

Figures 4.21 a) and b) show the resistance as a function of time at magnetic fields around the peak positions to evaluate their time dependence. Only for the magnetic field values of the two peaks, a resistance relaxation is found. The associated T_1 relaxation time can be extracted from an exponential fit, which yields $T_1 \sim 3\,\mathrm{s}$. This behavior is very similar to the one observed in the previously discussed ^{13}C graphene sample. When this experiment was repeated at multiple gate voltages, the most pronounced resistance relaxation was found at the CNP ($V_\mathrm{g} = -6\,\mathrm{V}$). Density dependent studies of the T_1 relaxation time in GaAs show a pronounced dependence on

the carrier concentration in the quantum Hall regime.[230] Here, the T_1 time is mostly constant, with a slightly larger value at the CNP, as shown in the inset in figure 4.21 b).

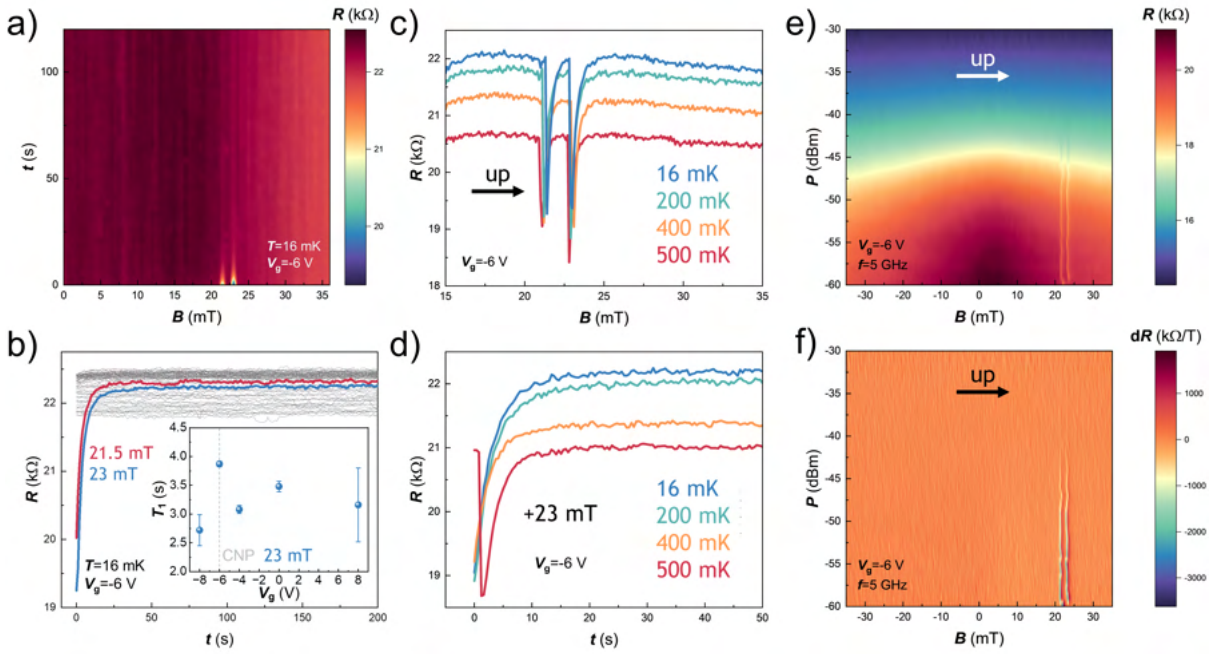

Figure 4.21.: a) Resistance as a function of time at small magnetic fields around the two peak positions. b) A time dependent resistance relaxation observed at $21.5\,\mathrm{mT}$ (red line) and $23\,\mathrm{mT}$ (blue line) and not for all other magnetic fields (grey lines). The inset shows the T_1 relaxation time extracted from exponential fits at $23\,\mathrm{mT}$ for multiple gate voltages. c) The overall resistance and the peak amplitude decreases for increasing temperatures up to $500\,\mathrm{mK}$. d) Time dependence of the resistance at $23\,\mathrm{mT}$ for increasing temperatures. Extracted T_1 times show a decrease with increasing temperature. e) Microwave radiation at $5\,\mathrm{GHz}$ is applied to the waveguide to induce local heating. The resistance and f) the differentiated resistance dR show that both peaks vanish at $\sim -40\,\mathrm{dBm}$.

According to the Maxwell-Boltzmann distribution, a temperature of $\sim 20\,\mathrm{mK}$ ($k_\mathrm{B}T \sim 2\,\mu\mathrm{eV}$) results in a non-zero nuclear spin polarization at finite magnetic fields, although the thermal energy is typically much larger than the energetic difference of nuclear spin states even at $1\,\mathrm{T}$ (^{13}C: $\Delta E = h\gamma\,1\,\mathrm{T} \sim 44\,\mathrm{neV}$). Hence, the nuclear spin polarization at $20\,\mathrm{mT}$ is still expected to be very small. Figure 4.21 c) shows the temperature evolution up to $500\,\mathrm{mK}$. The peaks decrease in height due to the increasing thermal activation which equilibrates the nuclear spin polarization.[20] Similarly, the time dependence for the peak at $+23\,\mathrm{mT}$ is exhibits a shorter relaxation time, as shown in figure 4.21 d). For temperatures above $500\,\mathrm{mK}$, where a stable operation of the dilution fridge becomes difficult, radiative local heating was used instead. Here, a high-frequency signal of $5\,\mathrm{GHz}$ is applied via the waveguide as shown in figures 4.21 e) and f). Although the exact sample temperature can not be determined in this measurement, the ap-

proximate temperature increase due to this local heating can be estimated from the microwave-induced resistance decrease. At ~ -40 dBm, the resistance reads $\sim 16\,\mathrm{k}\Omega$, from which a sample temperature of 1 K to 1.5 K is inferred. The amplitude of both peaks decreases with increasing power before vanishing at ~ -40 dBm. Note that the peak positions remain fixed within the given magnetic field resolution and no signs of resonant excitation are observed.

In summary, the gate voltage and temperature dependence of the peaks indicates a nuclear-spin-based origin. The magnetic field position of the peaks at approximately $\pm\,20$ mT is strikingly similar to the estimated nuclear magnetic fields of ^{13}C graphene[19,143] and to the resistance anomalies discussed previously. However, the exact mechanism that causes the peaks remains unclear and speculative. Both exfoliated and MBE-grown ^{13}C graphene devices consist of few-layer graphene, which potentially leads to interlayer spin-ordering effects.[231] In a different picture, a hyperfine-mediated interaction could affect the resistance similar to the Ruderman–Kittel–Kasuya–Yosida (RKKY) interaction, which arises from the coupling of magnetic moments via conduction electrons.[232,233] Another possible mechanism is based on intrinsic DNP of the nuclear spins that arises from randomly fluctuating electron spins at small fields and results in a sizable nuclear magnetic field B_N. This process promotes electron spin scattering that leads to enhanced resistance. The field B_N is aligned along the direction of the externally applied magnetic field B. When the external magnetic field switches sign and increases towards the *opposite* field direction, the nuclear spins system initially remains polarized in its previous state. Once the external magnetic field value matches the nuclear magnetic field $|B| \approx |B_\mathrm{N}|$, the effective magnetic field felt by the conduction electrons is canceled, which can result in a sudden decrease of spin scattering events. However, additional measurements on other samples in the future are necessary to understand the effect and to evaluate the possible influence of the number of graphene layers.

4.3. Superconducting Graphene Devices

This section presents the experimental results obtained on graphene Josephson junction (GJJ) systems. The low-temperature characterization of a GJJ-based bolometer device from an external collaborator is discussed in the first section. Afterwards, the advancements in the deposition of superconducting thin film are presented, which are the foundation for superconducting circuits. Finally, results of in-house fabricated GJJs will be shown and analyzed in detail.

4.3.1. Graphene-based Josephson Junction Microwave Bolometer

Within a collaborative project on dark matter axion research including groups of Prof. Dieter Horns (University of Hamburg) and Dr. Kin Chung Fong (Northeastern University and Raytheon BBN Technologies), a graphene-based JJ bolometer[36] was characterized at low temperatures in one of the cryogenic setups in the group of Prof. Robert H. Blick. The device was developed and fabricated in the Fong group, before it was made available for experiments at the University of Hamburg. The device consists of a GJJ coupled to a superconducting half-wavelength microstrip resonator, similar to the bolometer device presented by Lee *et al.* in 2020 (see section 2.3.1).[36] The charge carrier density n in the graphene can be controlled by a topgate. The chip is mounted inside of a shielding sample box, that is equipped with high-frequency SMP connectors, as shown in figure 4.22 b). This device was cooled down in a ^{3}He-based cryostat to study the transport properties of the GJJ as part of this thesis. Due to space limitations, additional measurements under microwave excitation could not be conducted in the existing cryogenic setup, which will be discussed later.

To characterize the device, the four-terminal resistance R is monitored while sweeping the topgate voltage V_g, to identify the position of the CNP. The resistance displays a large peak at $0.29\,\mathrm{V}$, as shown in figure 4.22 a). Above this value, the Fermi level is located in the conduction band resulting in electron conduction (*n*-doped regime). Below the CNP, the Fermi energy lies in the valance band (*p*-doped regime), as indicated by the insets in figure 4.22 a). In the hole regime, reproducible oscillations of R are observed as a function of V_g. These oscillations can be attributed to *pn*-junctions in graphene near the superconducting contacts. Each contact slightly *n*-dopes the contact region resulting in a *npn*-doping distribution across the graphene when tuned to the hole regime. The *pn*-junctions at the contact interfaces lead to a small asymmetry of the resistance values of the electron and hole regime. Furthermore, the interference of reflected charge carriers between opposing *pn*-junctions gives rise to Fabry-Pérot (FP) oscillations, analogous to an optical FP cavity of light waves between two mirrors. The Fermi wavelength of electrons in graphene depends on the charge carrier density n and is given by

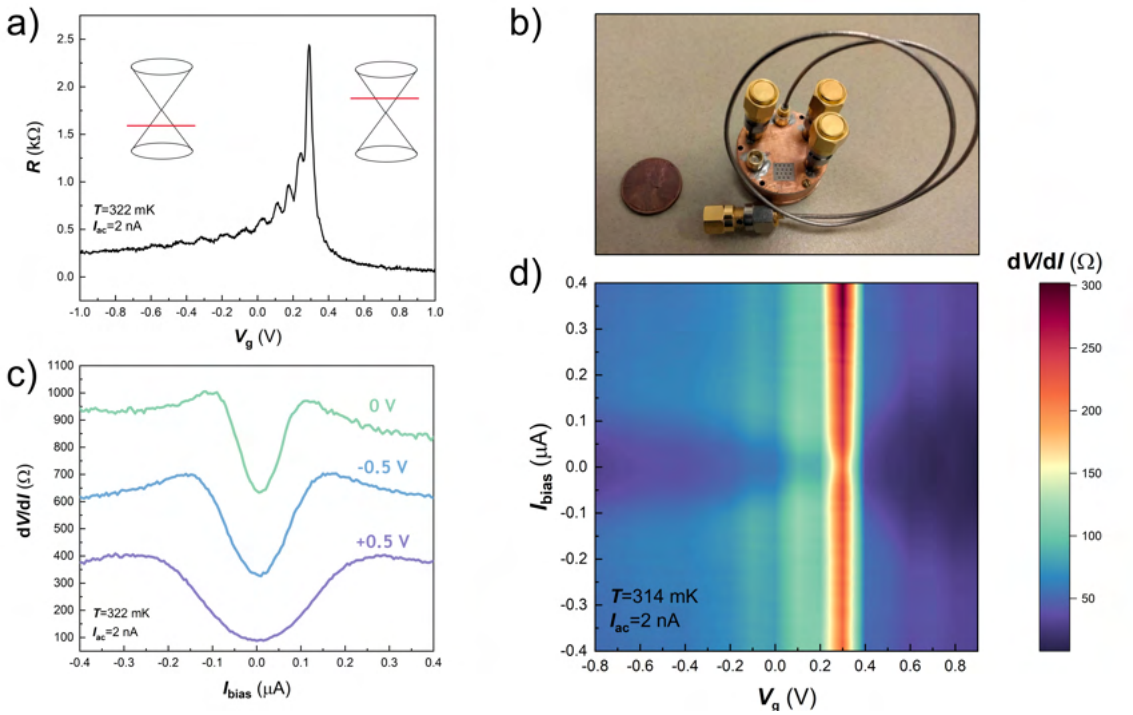

Figure 4.22.: a) Resistance across the graphene Josephson junction as a function of gate voltage. The graphene is in the electron regime (*n*-doped) at gate voltages above the CNP ($V_\mathrm{g} > 0.29\,\mathrm{V}$) and in the hole regime (*p*-doped) below the CNP. In this hole regime, *pn*-junctions in graphene near the superconducting contacts lead to FP oscillations in the resistance.[30,234–236] b) Optical image of the graphene-based JJ bolometer device, which was characterized in electrical transport in this thesis. The device was fabricated in the group of Dr. Fong at Raytheon BBN Technologies. c) Differential resistance $\mathrm{d}V/\mathrm{d}I$ as a function of applied DC bias current I_bias for three different gate voltages. Although the resistance does not fully extend to zero, the superconducting state of the GJJ can be identified. Compared to $0\,\mathrm{V}$, the superconducting minimum widens for *p*- and *n*-doping (blue and purple, respectively). d) Detailed gate voltage dependence of the superconducting regime of the GJJ. All measurements are performed at approximately 320 mK, although the effective sample temperature could be higher.

$$\lambda_\mathrm{F} = \frac{2\pi}{k_\mathrm{F}} = \frac{2\pi}{\sqrt{\pi n}}, \tag{4.5}$$

with the Fermi wavevector $k_\mathrm{F} = \sqrt{\pi n}$. By varying the gate voltage, the Fermi wavelength changes and constructive and destructive interference alternate, depending on the condition $2d = m\lambda_\mathrm{F}$, with the effective junction length d and integer m.[234] This leads to the observation of FP resistance oscillations, which is generally understood as a characteristic of ballistic transport.[30,234–236] From the periodicity of the FP oscillations in figure 4.22 a), an effective junction length in the range of $d = 130 - 230\,\mathrm{nm}$ is estimated, as shown in the appendix in figure A.6.

This value is in good agreement with reported junction lengths.[36,37,234,235]

In order to assess the critical current I_c of the GJJ, a DC current bias I_{bias} is applied while monitoring the differential resistance dV/dI at various gate voltages. At $V_g = 0\,V$, a minimum in dV/dI is observed around $I_{bias} = 0\,\mu A$, with a switching current at $\sim 0.1\,\mu A$, as shown in figure 4.22 c). Although the differential resistance does not fully decrease to zero, the resistance minimum is a sign of superconducting transport across the junction. As expected for a GJJ, the critical current is dependent on the applied gate voltage.[30] The resistance minimum at zero bias current widens when the measurement is repeated at higher gate voltages in the electron ($+0.5\,V$, purple) and hole ($-0.5\,V$, blue) regime, as depicted in figure 4.22 c).

These measurements can also be plotted as a function of DC source-drain voltage V_{SD}, as shown in the appendix in figure A.6 c). The extracted superconducting energy gap $\Delta \approx 80\,\mu eV$ is smaller than the bulk values of common superconducting materials such as Al ($\Delta = 180\,\mu eV$) or Nb ($\Delta = 1400\,\mu eV$).[102,104] Furthermore, a hysteresis of the switching current depending on the current sweep direction is typically a signature of underdamped GJJs.[30,36,37] However, in our measurement the switching current appears to be symmetric and without any hysteresis and the superconducting state of the junction does not fully extend to zero resistance. Hence, it is suspected that the effective sample temperature could be higher than $\sim 320\,mK$, due to a small thermal short in the cryogenic setup. Elevated temperatures would weaken superconductivity in the GJJ and reduce the superconducting gap Δ, which could explain the apparent transport behavior.

The gate tunability of the superconducting current is shown in more detail in figure 4.22 d), where the critical current vanishes at the CNP but extends to $\sim 0.2\,\mu A$ in the electron regime at $V_g = +0.9\,V$. The superconducting region in the hole regime is not as wide and shows signs of FP oscillations in I_c. The different magnitudes of I_c for opposite doping regimes are attributed to the presence of *pn*-junctions in the hole regime.[30,234,236]

In the following, the magnetic field dependence of the GJJ is evaluated. Tuned to the electron regime and at high magnetic fields, the resistance across the junction exhibits well pronounced SdH oscillations shown in figure 4.23 a), which is another sign of the high quality of the graphene. Figure 4.23 b) plots the inverse magnetic field dependence of the SdH oscillations, from which a low charge carrier density of $n \approx 2.4 \times 10^{11}\,cm^{-2}$ is deduced.

The superconducting state of the GJJ is extremely sensitive to an external perpendicular magnetic field. Figure 4.23 c) shows the bias current dependence of the differential resistance at $V_g = 1\,V$ under small magnetic fields. The maximum in the critical current I_c at $\boldsymbol{B} = 0\,mT$ (dark red) rapidly vanishes at $\sim 1\,mT$. However, at slightly higher fields a secondary ($\sim 2\,mT$) and a third ($\sim 3.5\,mT$) maximum is observed, which we attribute to signatures of a weak Fraunhofer pattern. Such a Fraunhofer interference pattern is generally expected in GJJs and arises from the magnetic flux induced phase difference across the junction.[30,31,102,104,236,237] Consider-

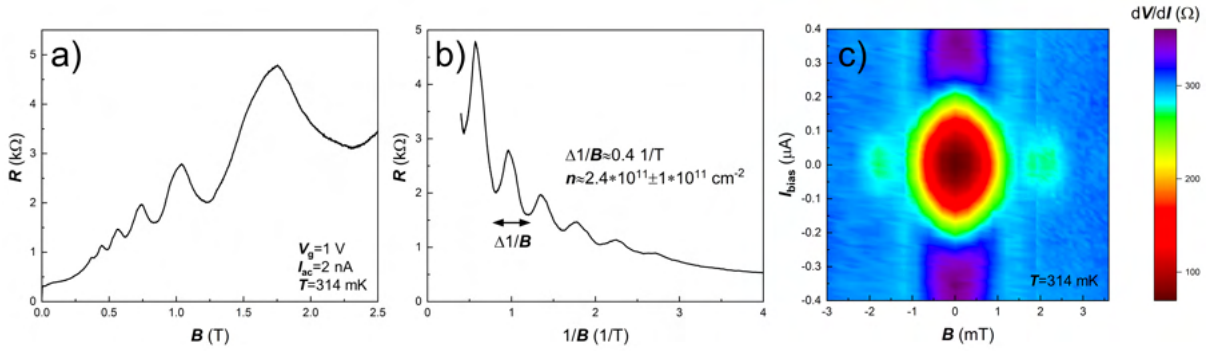

Figure 4.23.: a) The resistance of the GJJ exhibits SdH oscillations at high magnetic fields, while tuned into the electron regime ($V_\mathrm{g} = 1\,\mathrm{V}$). b) A charge carrier density of $n \approx 2.4 \times 10^{11}\,\mathrm{cm}^{-2}$ is determined from the inverse magnetic field dependence of the SdH oscillations. c) At small magnetic fields, signatures of a Fraunhofer pattern are observed.[30,31] The vertical line at $+2\,\mathrm{mT}$ is an artifact resulting from stitching of the measurements.

ing that the first minimum of I_c in figure 4.23 c) at $1.5\,\mathrm{mT}$ corresponds to one flux quantum ϕ_0, the effective area of the junction can be estimated as $A_\mathrm{eff} = \phi_0/\boldsymbol{B} = 1.38\,\mu\mathrm{m}^2$. Although our collaborator could not provide classified information on the geometry of the device, this value is in good agreement with reports by Lee *et al.* on a similar device.[36]

The resonance frequency of the superconducting resonator coupled to the GJJ was studied in a different cryogenic setup. As shown in the appendix (figure A.7), the designated cryogenic setup for the initial electrical characterization could not accommodate the necessary microwave components to perform DC readout of the GJJ under high-frequency radiation.[36] A compact dry cryostat in the group of Prof. Horns with a large sample stage and sufficient space for the high-frequency cables and components was used instead. The cryostat typically operates at 4 K and can go to 120 mK for short periods of time by adiabatic demagnetization. However, for this system, DC lines were not available to perform electrical readout of the GJJ. Hence, only the resonance behavior of the resonator could be studied, as shown in figure 4.24 a). These measurements were carried out in collaboration with Dr. Le Hoang Nguyen and Dr. Marios Maroudas, who are members of the Horns group. The plot shows the quasi-reflectometry measurement (S_{11}) on the resonator of the GJJ bolometer device at microwave frequencies around the expected resonance for various gate voltages at 4 K. At $\sim 8.73\,\mathrm{GHz}$, a significant drop in attenuation is observed for gate voltages close to the previously determined CNP ($\sim 0.3\,\mathrm{V}$). A high-resolution measurement of the region around this peak at 120 mK is shown in figure 4.24 b). This measurement confirms that the resonance frequency of the device is at $\sim 8.73\,\mathrm{GHz}$.

By taking vertical and horizontal line cuts along different gate voltages in figure 4.24 b), the resonance peak can be identified even more clearly, as shown in figure 4.24 c). In contrast to

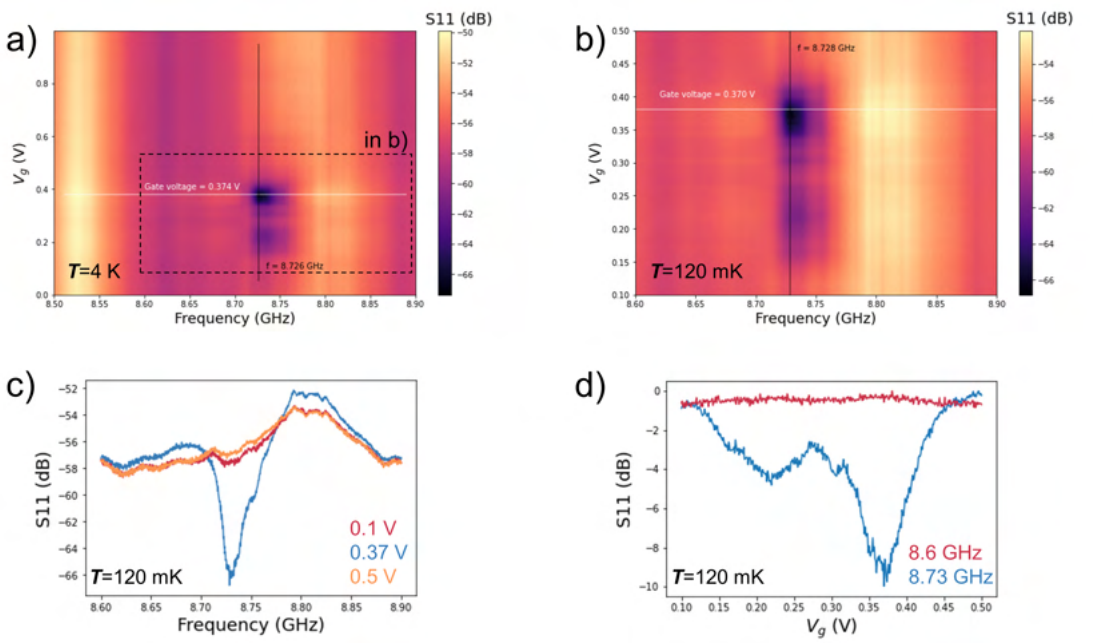

Figure 4.24.: a) Quasi-reflectometry measurement at 4 K for various gate voltages around the expected resonance frequency. S_{11} exhibits a pronounced dip at ~ 8.73 GHz close to the previously determined CNP. b) High-resolution measurement at 120 mK of the parameter space indicated by the dashed rectangle in a). c) Line cuts at different gate voltages confirm the resonance frequency position at ~ 8.73 GHz. d) Compared to 8.6 GHz, the reflected microwave signal exhibits a strong response to the gate voltage at the resonance frequency.

other gate voltages, S_{11} exhibits a peak at ~ 8.73 GHz around $V_g = 0.37$ V. This is illustrated again in figure 4.24 d), which shows line cuts of the gate voltage dependence of S_{11} at two different frequencies. Compared to 8.6 GHz, a clear gate voltage dependency of the reflected signal is observed at the resonance frequency. These measurements show that the charge carrier system of the graphene is tightly connected to the microwave resonator of the device, demonstrating efficient coupling.

The results obtained by our characterization measurements on this GJJ bolometer demonstrate the high quality of the device. For high sensitivity few-photon detection,[36–38,238] observable as supercurrent switching in response to microwave excitation, none of the available cryostats were adequately equipped.

4.3.2. Superconducting Thin Films

Superconducting thin films acting as electrodes that induce superconductivity via the proximity effect (see section 2.2) are the foundation of many novel nanostructured quantum devices such

as graphene Josephson junctions. As discussed in section 3.3.2, these thin films can consist of different superconducting materials and are prepared via sputtering or electron beam evaporation. In this section, the results on superconducting niobium (Nb) and niobium nitride (NbN) samples are presented, which are employed due to their high critical temperature T_c and critical magnetic field B_c compared to superconducting aluminum (Al). Some of our findings were published in Strenzke *et al.* J. Appl. Phys. 136, 205301 (2024)[49] and are included in the following.

RF sputtering and characterization of Nb thin films

GJJs are fabricated with superconducting thin films by nanostructuring processes that typically involve EBL. This fabrication process is normally based on poly(methylmethacrylate) (PMMA) resist, which can be used to pattern the superconducting thin film by material deposition and lift-off. Our Nb and NbN thin films are deposited by radio frequency (RF) sputtering at room temperature (see section 3.3.2 for details). This makes the sputtering process generally compatible with nanolithography techniques, which is in contrast to other deposition methods such as plasma-enhanced atomic layer deposition or CVD. In this thesis, the influence of deposition parameters and nanostructuring methods on the superconducting properties of Nb and NbN thin films were studied.

First, the results on RF sputtered Nb thin films and the superconducting hybrid graphene nanodevices are presented. Figure 4.25 illustrates the sputter deposition of a Nb thin film that is interfaced with graphene in a nanostructuring process involving PMMA resist.[49]

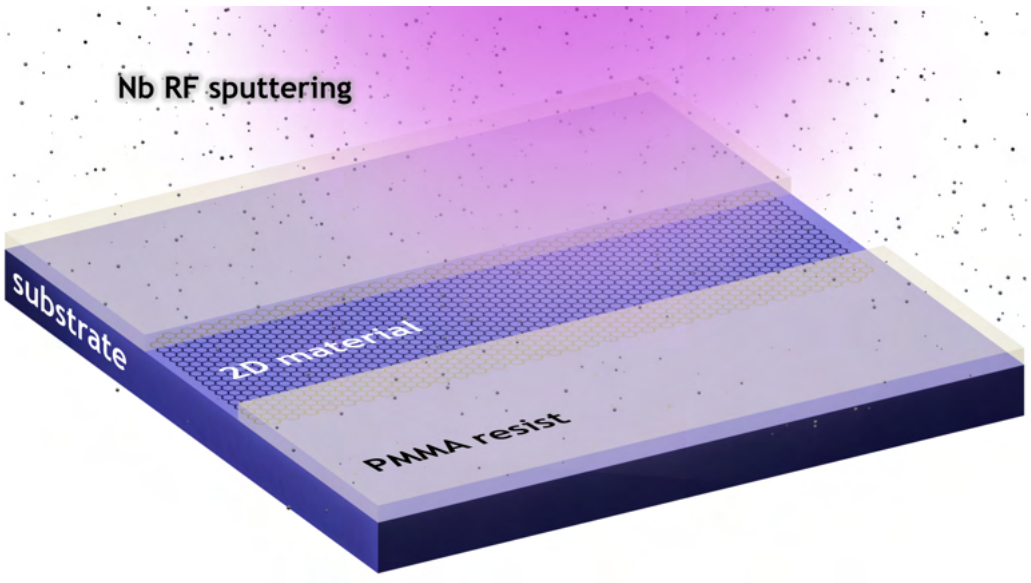

Figure 4.25.: Illustration of RF sputtering of Nb as part of a nanostructuring process that involves PMMA resist to obtain hybrid 2D material nanodevices. Figure adapted from Strenzke *et al.* (2024) under terms of the Creative Commons CC BY license.[49]

As discussed in section 3.4.2, the deposited thin films are electrically characterized in a physical property measurement system (PPMS) from 300 K down to 2 K and up to 9 T using a standard four-terminal measurement scheme that is schematically depicted in the inset in figure 4.26 a). By taking temperature and magnetic field dependent resistance measurements, T_c and B_c are determined, as shown exemplary in figure 4.26 a).[49]

When the thickness of a superconducting film is comparable or less than the coherence length and the superconducting penetration depth, quantum size effects affect the superconducting properties because Cooper pairs cannot form effectively in confined dimensions. The thickness dependence, shown in figure 4.26 b), is a combination of increasing grain sizes that exhibit properties closer to the bulk value[239–242] and of stress and strain effects when niobium thin films are grown on substrates like silicon.[243–245] Most reports on sputtered Nb and NbN films use 200 nm or larger[246,247] to reduce these effects. For our studies, we consider niobium films with thicknesses larger than 60 nm, which is a common thickness for electrical contacts.[36] For the Nb film with the largest thickness, the T_c of 7.6 K is closest to that of single crystal bulk Nb, which has a T_c of 9.25 K.[241,242,248] The deviation from the bulk value could be the result of residual oxygen content in the sputter chamber, which is known to impact the superconducting properties of sputtered Nb films.[49,183]

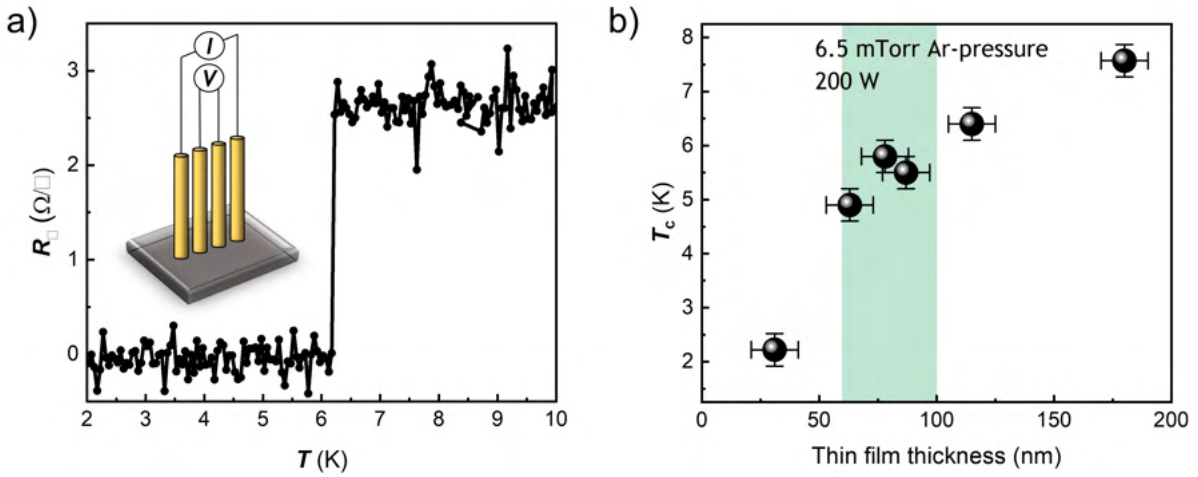

Figure 4.26.: a) Exemplary measurement of the sheet resistance as a function of temperature to determine the critical temperature T_c of a 73 nm thick niobium thin film. The inset in shows a schematic of the four-terminal measurement. b) For fixed sputter parameters (200 W and 6.5 mTorr Ar pressure), the dependence of the T_c of the Nb thin films on the layer thickness is displayed. The green shaded area marks our desired thickness range. Figure adapted from Strenzke *et al.* (2024) under terms of the Creative Commons CC BY license.[49]

For Nb thin films, the two most important growth parameters are the plasma power P and the argon (Ar) pressure. Figure 4.27 a) gives an overview of the power dependence. Here, each

data point represents the best result obtained for a fixed P but within a parameter range for the layer thickness (60 nm to 100 nm) and Ar pressure (3.4 mTorr to 6.6 mTorr). For our system, we observed a complex interdependence of the growth parameters, which requires a readjustment of Ar pressure to obtain optimized Nb films. Lower argon pressures (3.4 mTorr to 4.3 mTorr) are required for a lower power to achieve good Nb thin films. Additionally, the quality and reproducibility of most deposition techniques, including sputter-deposition of superconducting Nb, are also significantly influenced by the chamber's condition and growth history, which will be discussed in detail later.[49]

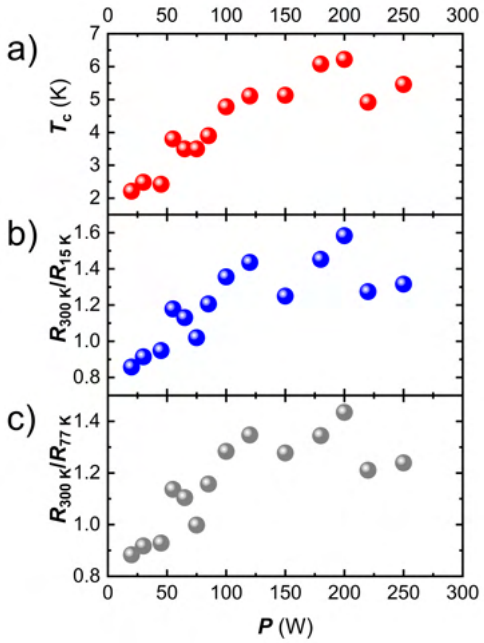

Figure 4.27.: a) Power dependence of a) T_c, b) $\frac{R_{300K}}{R_{15K}}$ and c) $\frac{R_{300K}}{R_{77K}}$ for thin films between 60 nm and 100 nm thickness. Best results were obtained for a power of 200 W (at 6.5 mTorr Ar pressure). Figure adapted from Strenzke *et al.* (2024) under terms of the Creative Commons CC BY license.[49]

The increase of the RF power in figure 4.27 results in a steady rise of the critical temperature, indicating a continuous improvement in film quality. The cleanest Nb thin films and thus highest T_c is achieved at 200 W, followed by a slight decrease at higher powers. The power dependence can be understood via the growth kinetics: at ambient temperature, adatom mobility is rather low and their binding affinity is comparably high, which generally promotes island growth.[249] Increasing the kinetic energy of the sputtered particles leads to more uniform films as it allows for a redistribution of adsorbed atoms, thus effectively reducing the likelihood of island growth. At very high powers, however, detrimental effects such as re-sputtering and amorphization[250,251] begin to deteriorate the quality of the films.[49]

The room temperature resistance $R_{300\mathrm{K}}$ of the sputtered films is dominated by electron-phonon scattering, while the resistance at low temperatures above T_c is dominated by impurity scattering that affect the superconducting properties. The residual resistance ratio (RRR), defined as $\frac{R_{300\mathrm{K}}}{R_{15\mathrm{K}}}$ and shown in figure 4.27 b), is commonly used and provides a standardized method to compare different films.[248,252] While bulk Nb can have a RRR above 2000, Nb films often display a lower RRR < 10.[241,242,248] Figure 4.27 a) demonstrates that RRR shares a similar dependence on power with the T_c, indicating that $\frac{R_{300\mathrm{K}}}{R_{15\mathrm{K}}}$ can indeed serve as a quality figure of merit for the thin superconducting films. However, the experimental determination of this ratio requires a cryogenic system, offering no real advantage over directly determining T_c. While previous studies on the effect of residual oxygen on Nb films observed a clear dependence between T_c and $R_{300\mathrm{K}}$,[183,242] we found that for our study of RF power dependence, $R_{300\mathrm{K}}$ alone is not a reliable quality indicator, which could result from other effects beyond residual oxygen such as grain size. However, its ratio with $R_{77\mathrm{K}}$ is already sufficient to evaluate the superconducting properties, as shown by figure 4.27 c).[252] Hence, in scientific environments where access to liquid helium or cryogenic systems is limited, characterizing the resistance simply in liquid nitrogen at 77 K can already screen suitable thin films. Nevertheless, the following sections will focus on the more commonly used T_c, in particular in the context of nanostructured devices.[49]

Nanostructured graphene devices with superconducting Nb electrodes

With optimized growth parameters, multiple GJJ devices were fabricated with Nb electrodes using RF sputtering (see section 3.3.2). An exemplary GJJ sample is depicted in figure 4.28 a), where an array of different JJ lengths is presented. This particular device represents the typical behavior of most fabricated GJJs based on Nb. The Nb sputter deposition on this sample was carried out with 200 W and 6.5 mTorr Ar pressure that have shown good results ($T_\mathrm{c} > 6\,\mathrm{K}$) for the same film thickness of 80 nm. The sample was cooled down to $\sim 260\,\mathrm{mK}$ in a cryogenic ^{3}He system.

Now the behavior of the Nb-graphene-Nb junction marked by the white box in figure 4.28 a) is addressed. First, the superconducting properties of the Nb electrodes are assessed alone by measuring only the two terminal resistance along the split contact lines, as illustrated in figure 4.28 b). Note that the other side of the junction and all other contacts were left floating to prevent current flow across the GJJ. The electrical properties of the Nb thin film are probed by setting a DC bias current I_bias and monitoring the resulting DC voltage V_film. Since the critical current I_c is significantly larger than $10\,\mu\mathrm{A}$, a perpendicular magnetic field $\boldsymbol{B}$ can be applied to lower I_c. For magnetic field values ranging from $0.9\,\mathrm{T}$ to $1.4\,\mathrm{T}$, current-voltage characteristics are shown in figure 4.28 c). The constant slope results from the background resistance of the two-terminal configuration. However, the Nb film exhibits a critical current I_c that decreases for larger magnetic fields. Additional measurements of the differential resistance $\mathrm{d}V/\mathrm{d}I$ are shown

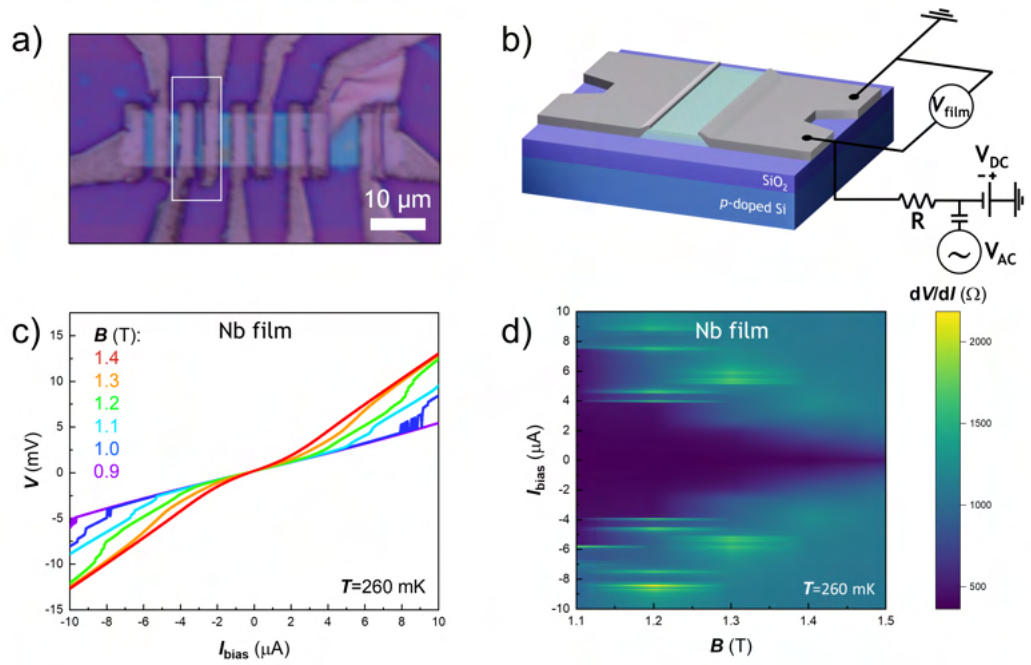

Figure 4.28.: a) Optical image of a nanostructured graphene device with multiple sputtered Nb electrodes to form GJJs of different lengths. b) Schematic circuit that is used to assess the superconducting properties of an individual Nb contact. In this configuration, no current is passed across the graphene junction. c) Current-voltage characteristics of the nanostructured Nb contact at various magnetic fields. d) Differential resistance $\mathrm{d}V/\mathrm{d}I$ as a function of bias current I_{bias} for a similar magnetic field range. The critical magnetic field B_{c} of the Nb contacts appears to be close to $1.5\,\mathrm{T}$. All measurements are performed at 260 mK.

in figure 4.28 d) with I_{c} indicated by the boundaries of the darker region of low resistance. At $\boldsymbol{B}_{\mathrm{c}} \sim 1.5\,\mathrm{T}$ I_{c} becomes vanishingly small. This value is in good agreement to PPMS electrical characterization measurements that were performed on a reference sample, which was deposited in the same sputter run. Note that such reference samples were not coated with PMMA, nor nanostructured in any way. The Nb thin film of the reference sample displayed a $T_{\mathrm{c}} \sim 3.6\,\mathrm{K}$ and a $B_{\mathrm{c}} \sim 1.5\,\mathrm{T}$. This T_{c} is significantly lower than anticipated from previous deposition runs without PMMA-coated samples. Possible reasons for this observation will be discussed later.

The electrical resistance $R_{\mathrm{JJ}} = V_{\mathrm{JJ}}/I$ across the same GJJ was studied in a four-terminal configuration, as shown schematically in figure 4.29 a). $R_{\mathrm{JJ}}(\boldsymbol{B})$ across the junction and the contact resistance $R_{\mathrm{film}}(\boldsymbol{B})$ can be measured simultaneously. Note that R_{film} was measured on a contact that was not connected to the graphene. Figure 4.29 b) shows that the Nb contact (green solid line) indeed has a $B_{\mathrm{c}} \sim 1.5\,\mathrm{T}$ and is superconducting at lower fields. The $\sim 500\,\Omega$ background resistance originate from the two-terminal configuration. However, R_{JJ} that is measured across the junction (black solid line) exhibits no signs of superconductivity. Instead, oscillations are

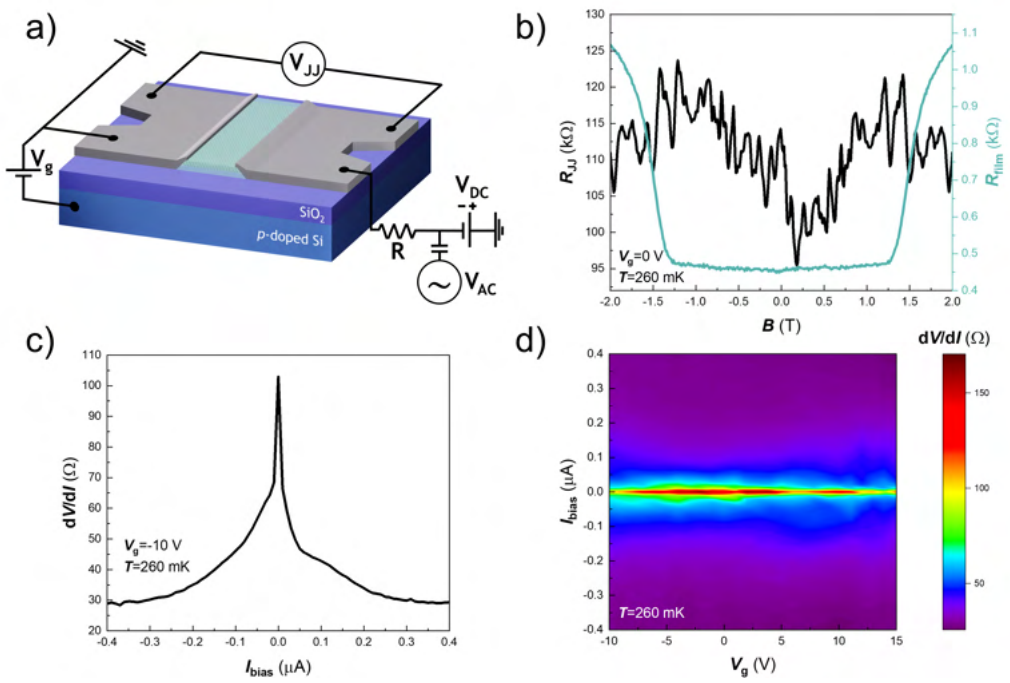

Figure 4.29.: a) Schematic drawing of the four-terminal measurement configuration to R_{JJ} across the Nb-graphene-Nb junction. b) Comparison of R_{JJ} (black) and the Nb contact (two-terminal) resistance R_{film} (green). The contact exhibits a superconducting transition at $\sim 1.5\,\mathrm{T}$ while R_{JJ} is extremely high and displays no signs of superconductivity. c) The differential resistance $\mathrm{d}V/\mathrm{d}I$ across the junction rapidly decreases when a DC current bias is applied. d) Small variations but no qualitative changes are observed in $\mathrm{d}V/\mathrm{d}I$ as a function of V_{g}.

observed which are symmetric in $\boldsymbol{B}$ and could result from universal conductance fluctuations. Additionally, the four-terminal R_{JJ} displays an extremely high resistance of $>100\,\mathrm{k}\Omega$. When a small DC current bias is applied to the sample, the differential resistance decreases to a level of $\sim 30\,\mathrm{k}\Omega$, as shown in figure 4.29 c) and d). This zero-bias peak in $\mathrm{d}V/\mathrm{d}I$ is not expected for a GJJ. It rather reflects the behavior of a normal tunnel junction, which indicates poor contact transparency although the Nb contacts are superconducting.

Unfortunately, a poor contact transparency is observed for most graphene devices with sputtered Nb contacts, despite a fully developed superconductivity in the material itself and $T_{\mathrm{c}} \gg 260\,\mathrm{mK}$. Hence, we suspect the niobium-graphene interface to be the main reason behind the poor transmission across the graphene junction and the absence of a superconducting proximity effect.

Challenges and solutions in RF sputtering of superconducting Nb nanostructures

In order to identify possible reasons for the poor contact performance of the Nb electrodes, the sputter conditions were examined in more detail. With the standard parameters (200 W

RF power and 6.5 mTorr Argon), a critical temperature of approximately 6 K is consistently obtained for large lateral thin films, which are now defined as *pristine*. However, also a significantly lower T_c is encountered for samples that were sputtered with the same parameters as shown in figure 4.30 a). The deterioration of the superconducting properties can be attributed to the lithographic process and the history of the chamber. In figure 4.30, the superconducting properties and the resistive behavior of pristine samples are compared to reference samples.[49]

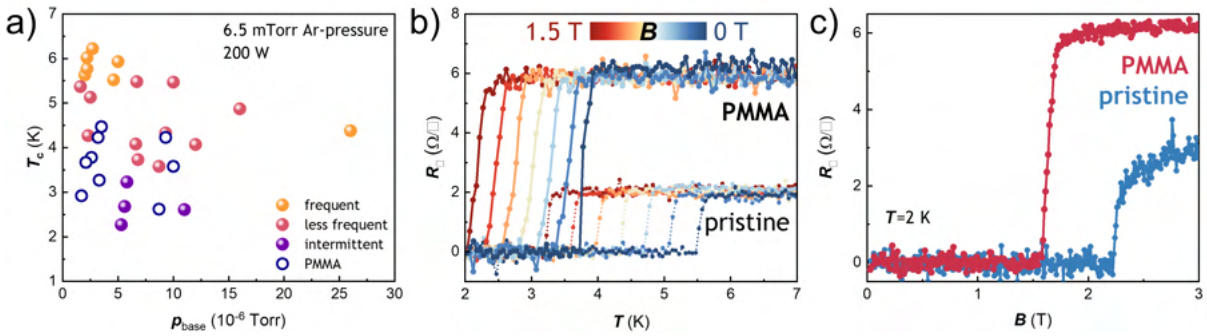

Figure 4.30.: a) Best T_c for the same set of deposition parameters and at lowest base pressures p_{base} for *frequent* sputtering (orange, multiple times per day to daily), *less frequent* sputtering (red, daily to several times per week), *intermittent* sputtering (purple, weekly or less) and reference samples that experienced contamination by PMMA resist (open circles). b) Film resistances as a function of temperature for different magnetic fields from 0 T to 1.5 T for a pristine Nb thin film compared to a film prepared together with PMMA resist-coated substrates. c) Measurement of the upper critical field at 2 K for the samples used in b). Figure adapted from Strenzke *et al.* (2024) under terms of the Creative Commons CC BY license.[49]

The degradation of material quality due to contamination and impurities is a well-known problem in materials science. A significant sensitivity of Nb to impurities[240] from PMMA resist during sputtering is observed that dramatically impacts the critical temperature. The material quality also depends on the history of the chamber and growth frequency. Despite a cleaning and conditioning procedure described in section 3.3.2 prior to deposition to remove oxides and most other contaminants from the target surface, figure 4.30 a) illustrates a clear dependence on the frequency of deposition. Best and most consistent results are generally obtained at frequent depositions. Less frequent and intermittent depositions yield significantly lower critical temperatures. As discussed earlier, the niobium films are also very sensitive to residual oxygen levels in the sputter chamber.[183] We thus suspect that frequent deposition keeps the target conditioned, with minimal oxidation, leading to more consistent results and higher film quality. For less frequent and intermittent depositions, the conducted initial cleaning procedure is not sufficient to yield ideal starting conditions. Our results highlight the importance of a well-conditioned chamber. Conditioning protocols prior to sputter deposition can significantly reduce run-to-run variations.[184,185] Heating of the sample stage, which is often included in such conditioning pro-

tocols,[185] as well as the application of a sample bias voltage to reduce oxygen content in the Nb films[183] is not available in our experiments.[49]

Increasing the growth frequency can indeed enhance and restore the superconducting properties. However, addressing issues associated with lithographic processes, that are required for nanostructured graphene devices for example, are much more challenging. When the results of the pristine sputter depositions are compared to that of PMMA reference samples, we find that those samples always show inferior properties, independent of the growth frequency. Note, that the reference samples, referred to as PMMA, were neither coated with PMMA, nor nanostructured in any way. The PMMA-labeled samples are niobium films on clean silicon substrates that were sputtered together with other PMMA-coated substrates that constitute a contamination source.[49]

In figure 4.30 b) the critical temperatures for a pristine (thin dashed lines) and a PMMA sample (thick solid lines) are determined at different magnetic fields. The two blue traces representing $0\,\mathrm{T}$ show a significant decrease of approximately $30\,\%$ in T_c from $5.5\,\mathrm{K}$ (pristine) to roughly $3.8\,\mathrm{K}$ for PMMA. While the PMMA resist retains its integrity during the sputter deposition and can be easily removed in a lift-off process, outgassing of PMMA or an interaction of Nb species having high kinetic energies in the plasma with the PMMA, leads to an enhanced incorporation of impurities in the superconducting thin film. The impurities not only decrease T_c but also significantly affect the sensitivity to magnetic fields, as shown in figure 4.30 b) and c). At a constant temperature of $2\,\mathrm{K}$, a significantly higher upper critical field is observed for the pristine sample compared to the PMMA sample. The underlying physical details are complex and will not be discussed here. However, the different magnetic field dependencies in figure 4.30 are consistent with previous reports and relate to impurity scattering that affects the Cooper pair formation and the interplay of flux pinning at defects under external magnetic fields.[49,253,254]

To mitigate the degradation of Nb thin film quality, different nanostructuring approaches are evaluated in figure 4.31 a) by comparing the averaged critical temperatures $T_\mathrm{c,avg}$ and film stress, determined from an ensemble of samples. On average, a pronounced drop of almost $40\,\%$ is observed in the $T_\mathrm{c,avg}$ between a pristine sample and sputter processes involving PMMA resist, displayed as blue and red data points, respectively. However, $T_\mathrm{c,avg}$ significantly increases when the PMMA resist is hard-baked (PMMA+HB) previous to the Nb deposition (orange data point). This suggests that resist outgassing is responsible for the degradation as additional baking reduces the amount of solvent residues and hardens the resist. We could not observe any further improvement of the superconducting properties when using alternative EBL resists such as CSAR 62 that are advertised as resilient against higher temperatures and plasma processes.[49]

An alternative nanostructuring method that avoids polymer-based resist and contamination introduced during the sputter deposition process is based on a thick layer of aluminum

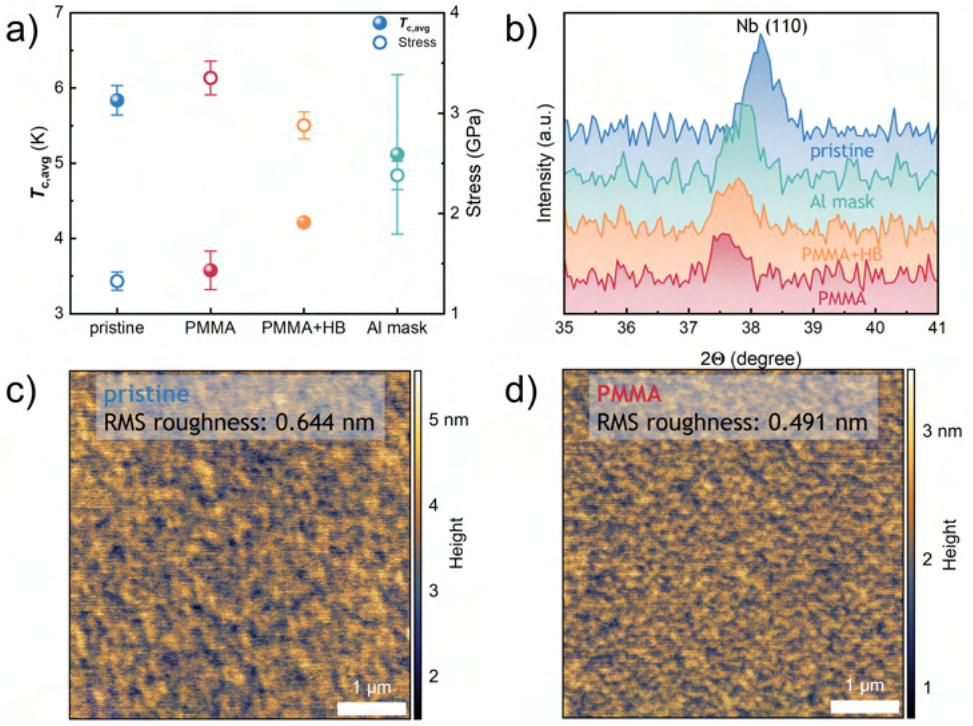

Figure 4.31.: a) Influence of the nanofabrication method on the average critical temperature (closed circles) and the estimated stress from XRD measurements (open circles). b) XRD results of Nb thin films deposited under different conditions. The curves are vertically shifted for clarity. c), d) Topographic $5 \times 5\,\mu m^2$ AFM images of sputtered niobium thin films. c) pristine Nb film with a RMS roughness of 0.644 nm d) PMMA sample with a roughness of 0.491 nm. We interpret the larger surface roughness of the pristine film as a higher level of crystallinity. RMS values for the surface roughness are determined by using the open-source software Gwyddion. Figure adapted from Strenzke *et al.* (2024) under terms of the Creative Commons CC BY license.[49]

(~ 800 nm) as described in section 3.3.2. The resulting critical temperature (green data point) is closer to that of pristine Nb thin films. Hence, Al presents a promising alternative to polymer-based masks to obtain RF-sputtered nanostructures. Due to the novelty and the complex wet etching behavior resulting from natural oxide formation on the Al surface, this method requires further process optimization tailored to the specific feature sizes and application to achieve high-precision lithography results. This was not possible in the time scope of this thesis. However, from first preliminary results on Nb-structures obtained by the unoptimized Al-mask approach, a lateral resolution of < 350 nm is deduced. The edge shape roughness of these structures was twice as rough compared to structures patterned by PMMA resist. The thin film quality can also be assessed through X-ray diffraction (XRD) scans, which are plotted in figure 4.31 b). The continuous decrease of the XRD peak amplitude for the Nb (110) direction from pristine to PMMA suggests a reduction of the film crystallinity. This is accompanied by a shift of the

Sample	$T_{c,avg}$ (K)	d (Å)	σ (GPa)
pristine	5.84 ± 0.2	3.33	1.33
PMMA	3.58 ± 0.26	3.38	3.35
PMMA+HB	4.21 ± 0.02	3.37	2.88
Al-mask	5.12 ± 1.06	3.36	2.38

Table 4.1.: Evaluation of different nanostructuring approaches: Averaged $T_{c,avg}$, estimated lattice constant d and stress σ based on X-ray diffraction patterns of niobium thin films. The error in figure 4.31 a) and table 4.1 represents the range of obtained T_c values. For the Al-mask approach, one of the measured samples exhibited greater divergence, leading to an increased error.

peak towards lower diffraction angles which indicates a change in the lattice constant d. With the calculated lattice constant, it is possible estimate the strain ϵ and stress σ of the niobium thin films by using

$$\epsilon = (d - d_0)/d_0 \tag{4.6}$$

$$\text{and } \sigma = -E\epsilon/2\nu, \tag{4.7}$$

with the lattice constant of stress-free bulk niobium $d_0 \approx 3.3\,\text{Å}$, the Young's modulus $E = 104.9\,\text{GPa}$ and Poisson ratio $\nu = 0.397$ of niobium.[255] From these equations, values for d and σ are estimated and compared with the averaged $T_{c,avg}$ values for the different nanostructuring approaches in table 4.1. We observe that even the pristine thin films with the best superconducting properties exhibit tensile stress. Although the stress in sputtered niobium films can be adjusted by modifying the Ar pressure,[256] our setup does not maintain stable plasma in that Ar pressure range. The decrease in critical temperature for PMMA samples in figure 4.31 a) is in agreement with a significant increase in stress due to a larger lattice constant. This effect is reduced for the PMMA+HB and Al-mask samples. The enhanced tensile stress is a clear indicator of reduced thin film quality, caused by multiple factors, with contamination from PMMA resist as a dominant one. However, a more detailed and precise analysis of the local surface deformation and stress distribution in niobium is complex and also requires chambers with enhanced vacuum conditions and a larger Ar pressure range.

Achieving high-quality superconducting Nb thin films through sputter deposition can be challenging, especially when incorporated into larger nanostructuring schemes for two-dimensional materials. However, our findings demonstrate that advanced growth and characterization facilities are not required to obtain films with good superconducting properties. The provided guidelines are transferable to other superconducting materials and 2D material systems to construct hybrid superconducting devices. Unfortunately, the Al-mask approach was developed towards the end of this thesis and could not be employed to prepare Nb-GJJs due to time constraints.

In addition to pure Nb, NbN thin films were deposited by reactive RF sputtering in a N_2/Ar atmosphere with different gas mixture ratios (see section 3.3.2). These films have a significantly higher T_c compared to pure Nb samples and exhibit very high critical magnetic fields. In fact, the B_c is too high to be probed by the available magnetic fields (max. $10\,T$) in our cryogenic systems. This is in agreement with reported values, where the upper critical field of NbN films is estimated to reach up to $30\,T$.[247] The perpendicular magnetic field dependence of the T_c of an exemplary NbN thin film (150 W, $\sim 20\,\%$ N_2/Ar, 85 nm film thickness) is shown in figure 4.32 a). This sample exhibits a $T_c \approx 12.5\,K$ at $0\,T$, which decreases to $\sim 9.5\,K$ at $8\,T$. Such a strong resilience to perpendicular magnetic fields would allow probing of quantum Hall states with superconducting electrodes.[186]

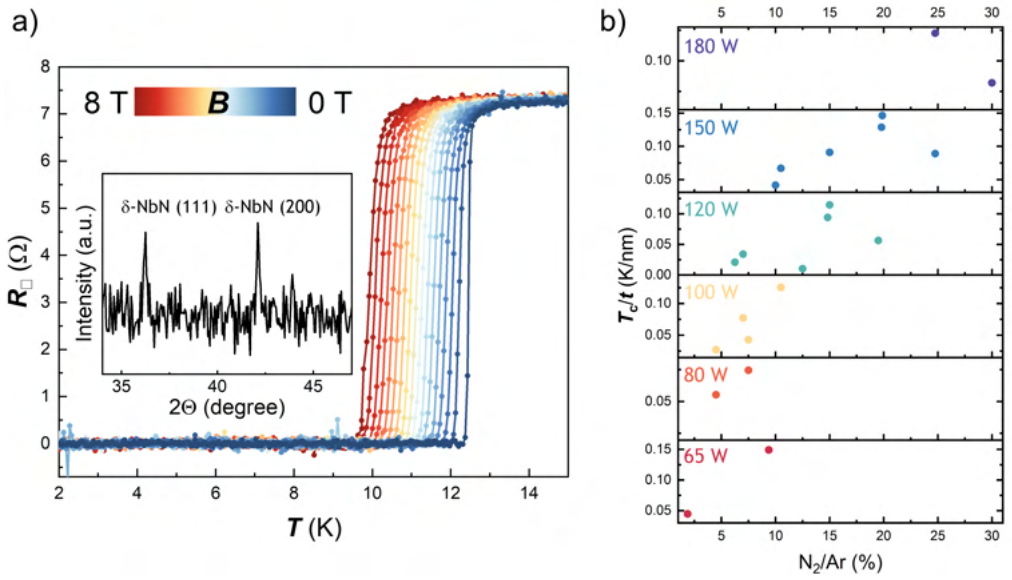

Figure 4.32.: a) The superconducting transition of an exemplary NbN thin film (150 W, $\sim 20\,\%$ N_2/Ar, 85 nm film thickness) decreases from $T_c \approx 12.5\,K$ at $0\,T$ to $\sim 9.5\,K$ at $8\,T$ of the perpendicular external magnetic field. The inset shows the XRD pattern of a different NbN film that exhibits the δ-NbN (111) and (200) peaks. b) Film thickness corrected critical temperature T_c/t as a function of N_2/Ar gas mixture ratio for different values of RF sputter power. The optimal N_2/Ar ratio shifts towards higher ratios with increasing RF power.

An exemplary XRD pattern of a NbN film that exhibits the NbN (111) and (200) peaks that correspond to the superconducting δ-NbN phase is depicted in the inset in figure 4.32 a).[247,257,258] The superconducting properties of our sputtered NbN thin films are very sensitive to the applied RF power and N_2/Ar gas mixture ratio. Their interdependence is shown in figure 4.32 b), which compares the obtained T_c per film thickness t for different growth conditions. Since many different film thicknesses are compared, the value T_c/t is used to normalize the thickness dependent effects. The optimal N_2/Ar ratio shifts with the RF power due to the increasing sputtering rate of

Nb at a fixed N_2 partial pressure. By increasing the sputtering rate of Nb, more of the available nitrogen is incorporated, which can be used to tune the Nb/N_2 ratio and consequently the nitrogen content in the thin film.[259] Further increasing the RF power above a certain threshold leads to the formation of Nb_2N. This Nb_2N phase is non-superconducting and leads to a decrease in critical temperature.[257,258,260,261]

Although NbN films have been prepared with record $T_c \sim 14 - 16\,\mathrm{K}$,[257,258,260,261] our thin films with $T_c \sim 12 - 13\,\mathrm{K}$ are highly competitive and suitable for the use in superconducting circuits in research, considering they were not grown in a high-end deposition system. Furthermore, the detailed investigation of the superconducting properties of NbN thin films on the interdependence of RF power and N_2/Ar ratio presents new insights on the RF sputter process of these films.

The quality of our Nb and NbN thin films is expected to be improved by optimizing the vacuum level, to reduce the amount of residual oxygen[183] and by adding a temperature controlled sample stage that allows either cooling or heating of the samples. Due to the RF sputter deposition at ambient temperatures, a relatively high RF power is required to improve the crystallinity and consequently the superconducting properties of our films.[257,258,261] However, reducing the RF power could be beneficial to obtain a well developed interface to sensitive 2D materials and preserve the integrity of resist.

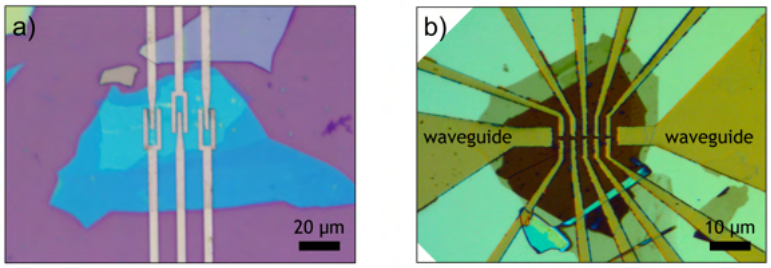

Figure 4.33.: Optical images of two exemplary graphene devices with superconducting NbN electrodes. a) Device with three NbN-graphene SQUID loops. b) Graphene device equipped with five JJs and a resistively-coupled waveguide.

GJJs have also been fabricated with NbN contacts, as shown in figure 4.33. Analogous to GJJs based on Nb (as discussed earlier), the contacts were intransparent for a wide range of sputter parameters. Either the graphene interface suffers from damage induced by a high deposition rate or a lack of adhesion. A reduction of deposition rate did not directly result in major improvements. However, it is possible that our depositions were not performed below a certain threshold rate, necessary for reducing damage to the graphene sheet.

Typically, a thin adhesive layer of titanium (Ti) is utilized to facilitate contact of the superconducting material to the graphene, which massively enhances contact transparency.[186,236,262] Our

simple sputtering setup can not be equipped with a secondary material source such as Ti, which is a major disadvantage compared to most other deposition systems for superconductors. We suspect the missing adhesion Ti-layer to be the key element that puts a stop to the functionality of our Nb and NbN junctions.

4.3.3. Characterization of Graphene Josephson Junctions

Device A

Due to the low contact transparency of our sputter-deposited Nb and NbN graphene junctions, we explored the usage of aluminum-based electrodes. As described in detail in section 3.3.2, a trilayer of Ti/Al/Ti is deposited by PVD. Here, the bottom Ti-layer serves as an adhesion layer while the top Ti-layer protects the Al from oxidation. Device A consists of a few JJs on the same graphene flake, covered by a top hBN, all situated on a silicon wafer with a p-doped global backgate, as shown in the inset in figure 4.34 a). The white box marks the junction which is used in the following measurements in a dilution refrigerator. This junction has a width $W = 5\,\mu\text{m}$ and length $L = 650\,\mu\text{m}$.

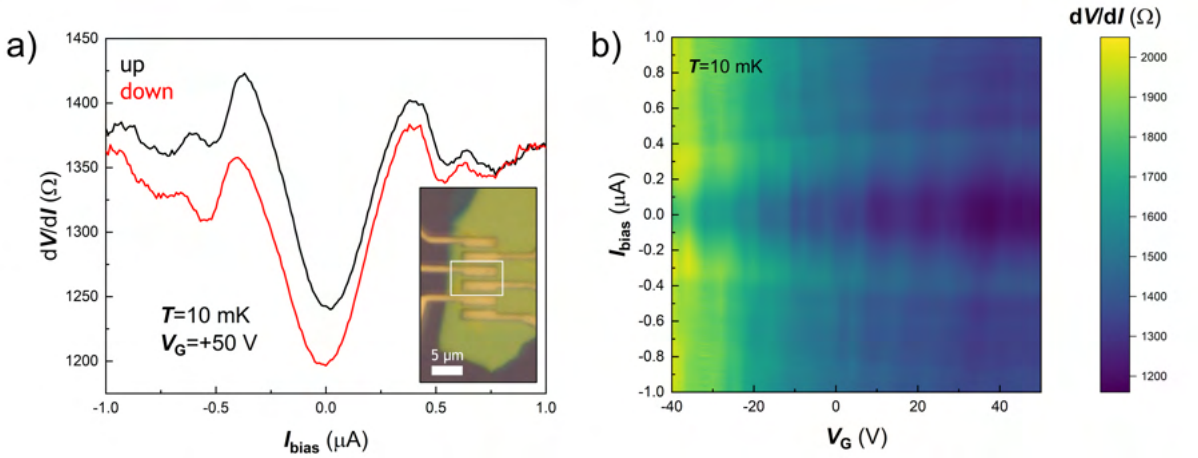

Figure 4.34.: a) Differential resistance $\mathrm{d}V/\mathrm{d}I$ of device A with superconducting aluminum contacts as a function of applied DC bias current I_{bias}. The resistance minimum around zero bias indicates a superconducting state in the junction with a critical current $I_{\text{c}} \sim 0.4\,\mu\text{A}$. The inset shows an optical image of the graphene device with multiple Ti/Al/Ti electrodes with different junction lengths. The white box marks the junction used for the presented measurements. b) Probing the gate voltage dependence reveals a weak tunability of I_{c}. The resistance oscillations probably stem from charge transfer effects from neighboring (floating) junctions.

In four-terminal current-biased measurements shown in figure 4.34 a), a minimum differential resistance is observed around zero bias, indicative of a superconducting state with a critical current of $\sim 0.4\,\mu\text{A}$. The resistance does not drop to zero and instead maintains a value of

1.2 kΩ. We attribute this to imperfections at the graphene-superconductor interface which lead to a reduced contact transparency. Nevertheless, the observed behavior demonstrates a significant enhancement in contact quality compared to the Nb and NbN junctions.

The gate voltage dependence of I_c is studied in figure 4.34 b). Coming from a high positive gate voltage towards negative voltage values, a decrease in I_c is accompanied by an overall increase in resistance. The gate tunability of I_c provides evidence that the supercurrent is carried by the graphene. The gate dependence indicates a position of the CNP close to -40 V, which is a sign of strong n-doping. Since this graphene stack was fabricated without a bottom hBN flake, the graphene is directly in contact with the silicon surface and exposed to impurities, which leads to doping effects. The observed gate voltage dependent oscillations are reproducible but without any apparent periodicity. FP oscillations are unlikely as the graphene is in the electron regime and diffusive transport is expected for this device. We suspect charge transfer effects from the unused (floating) neighboring junctions to result in the observed resistance oscillations. Unfortunately, strong gate leakage at ~ -50 V resulted in lasting changes to the sample properties.

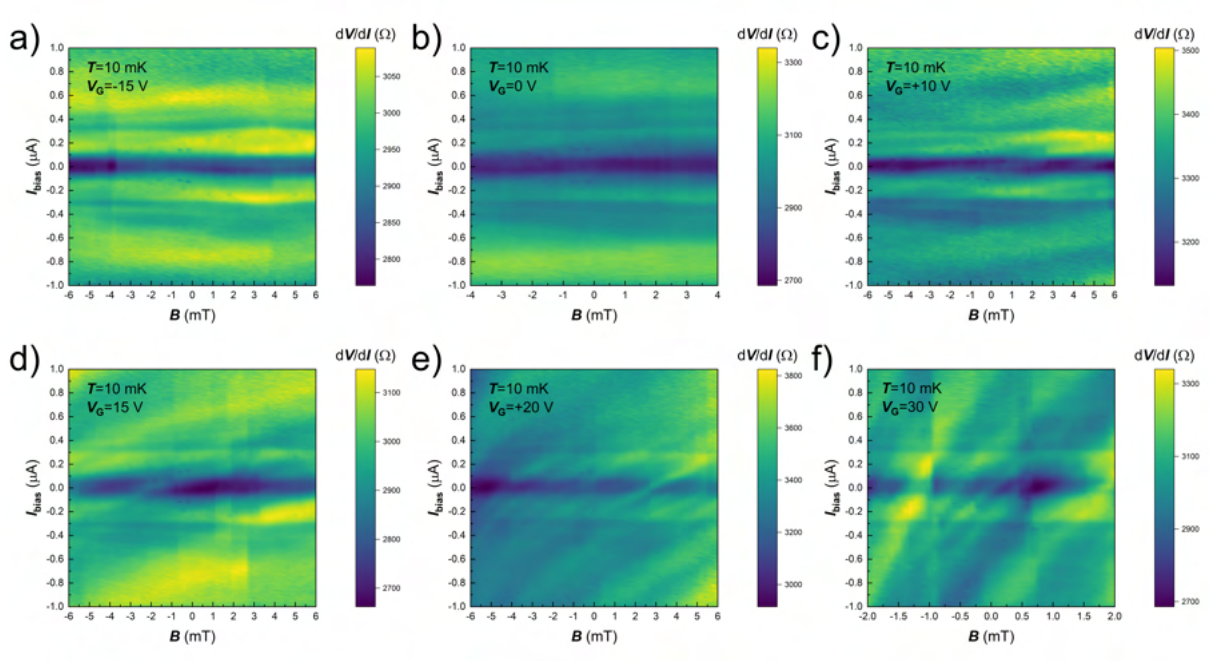

Figure 4.35.: a) to f) Differential resistance of device A at small magnetic fields and different gate voltages. A Fraunhofer pattern is not observed.

In order to probe for a Fraunhofer pattern,[29,30,104] small perpendicular magnetic fields were applied at different backgate voltages, as shown in figure 4.35. Here, the change from low (-15 V) to high ($+30$ V) electron densities is expected to influence the junction behavior. However, in this range of magnetic field, no periodic oscillations of I_c, i.e., Fraunhofer pattern, is

observed. Instead, diagonal features appear more pronounced towards higher electron densities. Since these diagonal lines are also present above I_c, they are attributed to changes in the resistive background which are potentially connected to the gate leakage. The visible abrupt vertical lines in some of the measurements are most likely also caused by the leaking gate. To avoid these artifacts in subsequent measurements, the gate voltage is kept at $0\,\mathrm{V}$ from then on.

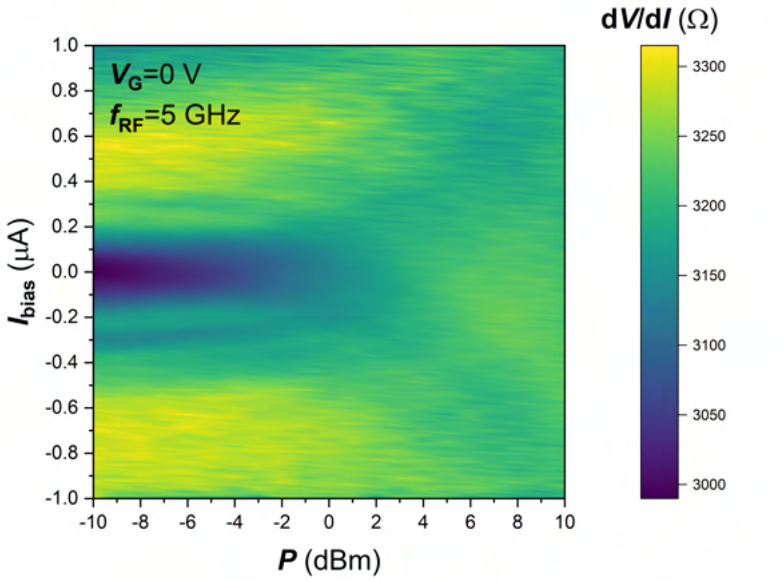

Figure 4.36.: Differential resistance $\mathrm{d}V/\mathrm{d}I$ as a function of bias current I_{bias} and microwave power P at a fixed frequency of $5\,\mathrm{GHz}$ and $0\,\mathrm{V}$ gate voltage.

Figure 4.36 plots the differential resistance $\mathrm{d}V/\mathrm{d}I$ as a function of bias current I_{bias} and microwave power P at a fixed frequency of $5\,\mathrm{GHz}$. Here, the microwave radiation is employed to probe the AC Josephson effect in graphene-based JJs, which typically results in quantized voltages steps also referred to as Shapiro steps.[29,263,264]

The microwave radiation is applied to the sample via a loop antenna near the sample. However, clear signatures of Shapiro steps could neither be observed at $5\,\mathrm{GHz}$, nor at other frequencies, shown in the appendix in figure A.8. The vanishing of the superconducting state at zero bias around $0\,\mathrm{dBm}$ is accompanied by diverging features of lower resistance, which is reminiscent of blurred Shapiro steps reported in literature.[29,263,264] While the junction itself is probably not sufficiently transparent, the increasing microwave power causes a significant rise in sample temperature, preventing the observation of well-developed Shapiro steps.

Device B

Device B was fabricated from separate islands of hBN-encapsulated graphene, thereby avoiding the previously described resistance oscillations during gating for device A. The inset in

figure 4.37 b) depicts an optical image of device B with the measured junction ($W = 4.4\,\mu\text{m}$ and $L = 450\,\mu\text{m}$) highlighted by the white box. The magnetic field dependence of the aluminum contact material for devices A and B is compared in figure 4.37 a) and b).

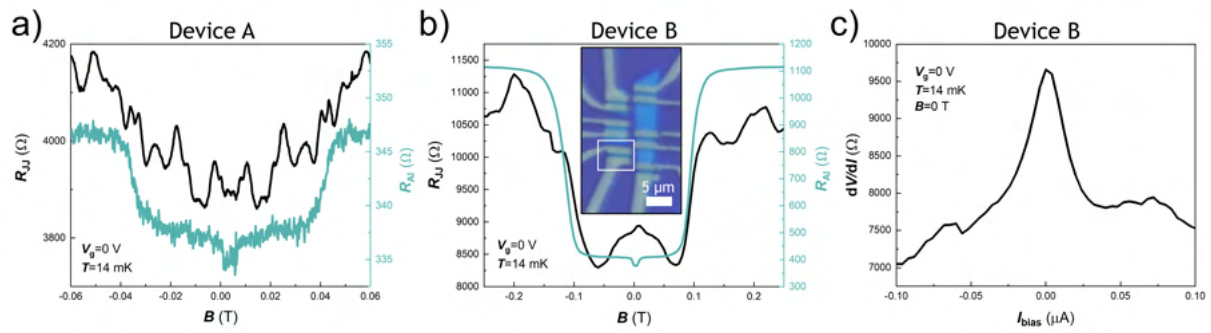

Figure 4.37.: Comparison of the magnetic field response of the resistance across the Al-graphene junction R_{JJ} (black solid line) and the Al contact material (two-terminal) resistance R_{Al} (green solid line) for a) device A and b) device B. The inset in b) shows an optical image of device B, with the junction marked by a white box. c) The current-bias dependence of the junction in device B does not show signs of the proximity effect. Instead, $\mathrm{d}V/\mathrm{d}I$ exhibits a maximum at zero bias, representative of low contact transparency.

Interestingly, for the aluminum contact materials in both devices a double transition is observed in R_{Al} (green solid line) that is extremely pronounced for device B. The magnetic field values for the inner and outer transitions are approximately $\pm 5\,\text{mT}$ and $\pm 40\,\text{mT}$ ($\pm 10\,\text{mT}$ and $\pm 100\,\text{mT}$) for device A (device B). The critical magnetic field for aluminum is typically found at $\sim 10\,\text{mT}$.[102] However, much larger critical magnetic fields have been found for granular aluminum thin films that are partially oxidized by depositing aluminum in very diluted oxygen atmosphere.[265–268] In the used PVD system, a pressure of $\sim 10^{-7}\,\text{mbar}$ could lead to similar partial oxidation effects that increase the effective B_{c} of our aluminum thin films, depending on the deposition conditions. This explains the variations in B_{c} between device A and B and the two different transitions, corresponding to pure aluminum (inner transition) and partially oxidized aluminum (outer transition). Although the electrodes in both devices consist of a Ti/Al/Ti trilayer, contributions from potentially superconducting titanium are improbable since aluminum will be the dominant layer due to the ~ 10 times larger film thickness.

Also, the behavior of the resistance of the junction R_{JJ} (black solid line) is qualitatively different. Both devices exhibit pronounced oscillations in a magnetic field, however, around $\boldsymbol{B} \approx 0\,\text{T}$, where pure Al is expected to be superconducting, R_{JJ} of device A has a small minimum and R_{JJ} of device B a small peak. In addition, the bias-current dependence of the differential resistance in device B, shown in figure 4.37 c), does not show the proximity effect, despite a $200\,\text{nm}$ shorter junction length compared to device A. Instead, $\mathrm{d}V/\mathrm{d}I$ exhibits a maximum at zero bias,

representative of low contact transparency. Although this is in contrast to the behavior of device A, it is in agreement to the pronounced outer magnetic field transition of the Al-film in device B, which is attributed to a higher degree of partial oxidation. Thus, inferior deposition conditions, i.e., higher oxygen content, are most likely responsible for reduced contact junction transparency in device B.

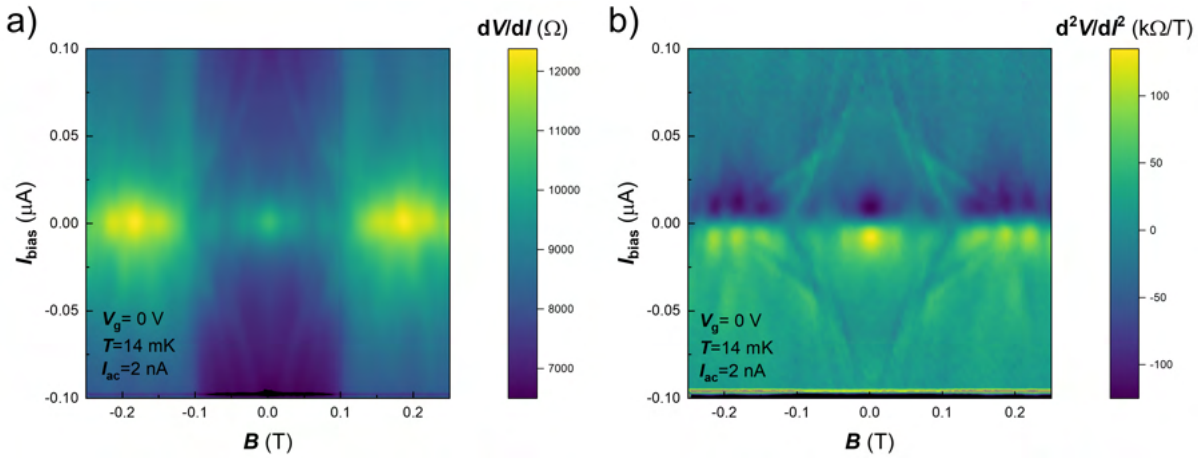

Figure 4.38.: a) Detailed measurement of $\mathrm{d}V/\mathrm{d}I$ of device B as a function of magnetic field and bias current at 14 mK. The outer superconducting transition of the Al-film is observed at ± 0.1 T. b) $\mathrm{d}^2V/\mathrm{d}I^2$ is obtained by taking the derivative of the data in a), which resolves diamond structures that are suppressed at larger magnetic fields.

The dependence of $\mathrm{d}V/\mathrm{d}I$ on magnetic field and bias current are assessed for device B, as shown in figure 4.38 a). The outer transition of the Al electrodes at ± 0.1 T is visible as an overall increase of the resistance. At lower magnetic fields however, fine structures can be identified. The calculated derivative of this measurement is presented in figure 4.38 b), which eliminates the large resistance variations due to the superconducting transition of the electrodes and resolves the fine structures more clearly.

Two interleaving diamond-shaped structures are observed that depend on I_{bias} and $\boldsymbol{B}$. These structures are suppressed at larger magnetic fields and vanish around the outer B_{c} of the Al. While one diamond-feature closes at ± 0.1 T, the closing of the second diamond-feature can be extrapolated to approximately ± 0.2 T. The diamonds cross at ± 0.8 T and diverge towards large bias currents around $\boldsymbol{B} \approx 0$ T.

The diamond-structures appear to be related to the junction's superconducting state, which is surprising given the expected low transparency of the contacts and the bias current dependence at zero magnetic field. Before discussing possible origins of the diamond-features, their response to different gate voltages and temperatures is assessed.

In figure 4.39 a) the junction resistance R_{JJ} is plotted as a function of backgate voltage V_{g}, with the large peak at ~ -18 V representing the CNP. The CNP is also clearly visible in the

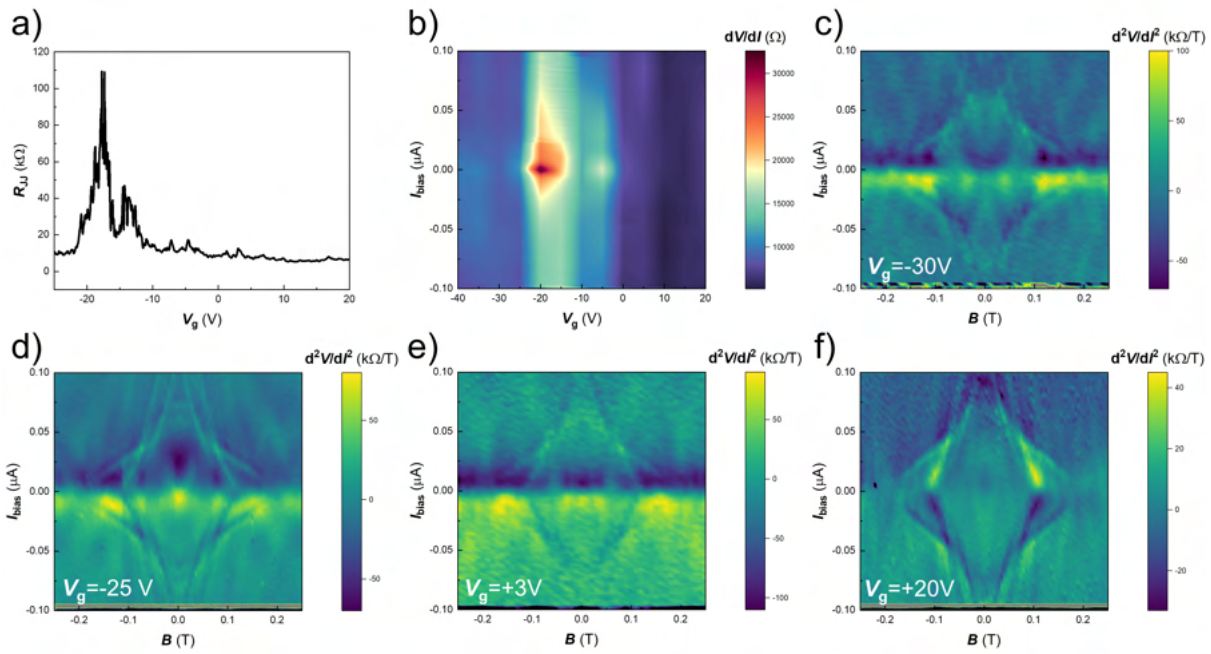

Figure 4.39.: a) Junction resistance R_{JJ} of device B as a function of backgate voltage V_{g}. The CNP is located at ~ -18 V. b) Gate voltage and bias current dependence of the differential resistance. The resistance peak at zero bias persists over the entire range of gate voltages. c) - f) Evolution of the diamond-shaped features at c) -30 V, d) -25 V, e) $+3$ V and f) $+20$ V. All measurements were performed at 14 mK.

differential resistance under current bias shown in figure 4.39 b). However, a resistance peak at zero bias appears over the entire range of carrier density.

Also, the diamond-shaped features are consistently and reproducibly observed for various gate voltages in the electron and hole regime, as shown in figures 4.39 c) to f). Strikingly, the position and shape of the diamonds in $\boldsymbol{B}$ and I_{bias} remains unaffected by the gate voltage. A significant gate voltage dependence is only observed for the resistance inside the diamonds, that can be attributed to the conductivity of the graphene. This is in agreement with a measurement directly at the CNP, shown in the appendix in figure A.9, where the diamond-features can not be resolved due to the large resistance of the graphene.

The temperature-dependence of this phenomenon was studied at various temperatures ranging from 14 mK to 470 mK. Results at four exemplary temperatures are presented in figure 4.40, which compares the measured $\mathrm{d}V/\mathrm{d}I$ with the derived $\mathrm{d}^2V/\mathrm{d}I^2$. A significant decrease of B_{c} of the Al with increasing temperature is observed, which is analyzed quantitatively in the appendix (see figure A.10). From our analysis, we estimate the T_{c} of the Al electrodes to range between 550 mK and 650 mK. The induced superconducting gap can be inferred from these values via $\Delta_{\mathrm{ind}} = 1.76\, k_{\mathrm{B}} T_{\mathrm{c}} = 83\,\mu\mathrm{eV}$ and $97\,\mu\mathrm{eV}$, respectively, which is much smaller than $\Delta \approx 180\,\mu\mathrm{eV}$ in bulk Al.[102,269,270] As the superconducting magnetic field range narrows upon increasing the

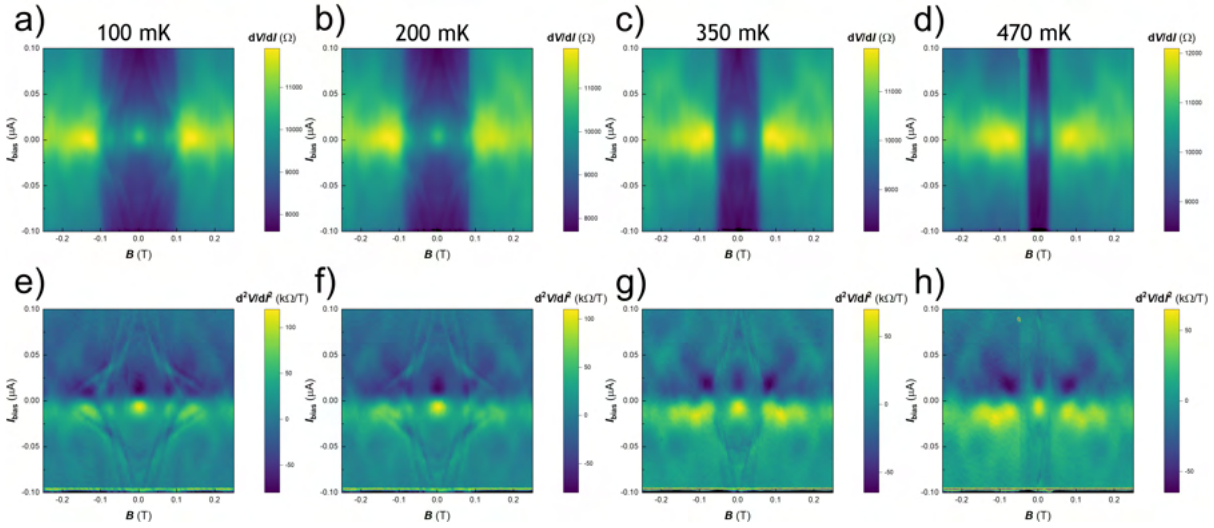

Figure 4.40.: Magnetic field and bias current dependence of the measured $\mathrm{d}V/\mathrm{d}I$ a) to d) and the derived $\mathrm{d}^2V/\mathrm{d}I^2$ e) to h) for varios temperatures. All measurements are performed at $V_\mathrm{g} = -25\,\mathrm{V}$. The B_c of the Al electrodes decreases with increasing temperature, which is analyzed in more detail in A.10.

temperature, the diamond-shaped features are squeezed together.

Measurements at larger bias currents, shown in the appendix in figure A.11, were performed to follow the evolution of the diamonds. However, the signal intensity of the features vanishes in the increasing noise towards higher bias. Furthermore, reducing the AC current modulation to $0.4\,\mathrm{nA}$, also shown in figure A.11, does not yield sharper features. An open terminated coaxial cable in close proximity to the sample was utilized to apply microwave radiation to device B. However, measurements at different gate voltages and frequencies, shown in the appendix in figure A.12, did not reveal any additional insights on the origin of the diamond-features.

In summary, the observed diamond-shaped resistance features are based on transport through graphene that is tightly connected to superconductivity of the Al electrodes but in first approximation independent of the applied gate voltage. Given the high resistance of $\sim 10\,\mathrm{k\Omega}$ and the absence of a Fraunhofer pattern or zero resistance around zero bias current, the aluminum-graphene junction transparency is low. In addition to the generally large resistance, the CNP position at $-18\,\mathrm{V}$ is a sign of significant n-doping, which probably has contributions from the edge contact fabrication and other impurities. Hence, we do not expect charge carrier transport to be ballistic in this device. For diffusive transport, the coherence length ξ in GJJs is calculated by including the mean free path l_mfp, which we estimate to be around $100\,\mathrm{nm}$. Considering the superconducting gap of aluminum to be $\Delta \approx 180\,\mu\mathrm{eV}$, we find ξ to be comparable to the junction length, i.e., $\xi \approx L \approx 450\,\mu\mathrm{m}$. The smaller induced superconducting gap value of $\Delta_\mathrm{ind} = 83\,\mu\mathrm{eV}$ from above results in an even larger value for ξ. Since ξ is in the order of the junction length, coherent superconducting transport is generally possible.

As mentioned before, the observed diamond-features are not related to a Fraunhofer pattern, which is also expected at lower magnetic field values.[29,30] Sufficiently strong Landau quantization is expected to develop at much larger magnetic fields and signatures of SdH or quantum Hall effects are not observed, possibly due to disorder in the sample. Another effect that is closely connected to the disorder in graphene is weak localization (WL).[190] An increase in resistance at $\boldsymbol{B} = 0\,\mathrm{T}$ as a result of WL has been observed before in GJJs with Ti/Al electrodes.[29] However, figure 4.37 b) shows an WL-atypical behavior of the resistance. The observed resistance peaks at various magnetic field values rather depend on I_{bias}. Nevertheless, it is possible that the observed resistance features are related to diffusive scattering mechanisms, including contributions from WL.

A previous study on other graphene junctions with imperfect contacts reported a conductance peak at zero bias.[271] This effect was explained by reflectionless tunneling in the junction, that is promoted by diffusive transport.[271] The transmission of a tunnel barrier between a superconductor and a normal conductor is enhanced due to diffusive scattering on impurities in the normal conductor.[272–274] Although this effect should be observed as a *dip* (not a peak) in resistance at zero bias, the general scattering mechanism could boost superconducting transport in our device. The same report attributed high resistance peaks to self-induced Shapiro steps.[271] We can not fully exclude such effects, however, this seems very unlikely given the observed junction behavior and the sample enclosure, which is not likely to support standing waves.

As explained in section 2.2, multiple Andreev reflections (MARs) can occur in a GJJ resulting in a series of peaks and dips in the resistance at source-drain bias voltages of $V = 2\Delta/en$ with $n = 1, 2, 3...$,[112,113,275] depending on the transparency of the junction.[269] Exact determination of the energy scales requires a voltage-bias measurement technique, which could not be performed due to the large resistance of the GJJ. However, the appearance of MARs is unlikely due to their high sensitivity to the contact transparency, which is low for device B.

Our observations are most consistent with Tomasch and McMillan-Rowell oscillations.[276–279] Although these two phenomena are rarely investigated in graphene-based systems, a recent study by Huang *et al.* discovered very similar magnetic field dependent diamond-features in Al-proximitized graphene devices.[280] Tomasch oscillations arise in SNS JJs from quasiparticle interference inside the superconductor, in particular, when the electron- and hole-like quasiparticles are strongly confined and forced to interfere with their Andreev-reflected counterpart from the NS interface.[281] This interference effect results in periodic oscillations that occur at bias voltages given by

$$V_m = \pm\sqrt{\Delta^2 + \left(\frac{mhv_{\mathrm{F}}^{\mathrm{S}}}{2d_{\mathrm{S}}}\right)^2}, \tag{4.8}$$

with integer m, the superconductor Fermi velocity $v_{\mathrm{F}}^{\mathrm{S}}$ and the superconductor thickness d_{S}.

Conversely, McMillan-Rowell oscillations also result from quasiparticle interference, but in the normal region of the SNS junction, i.e., the graphene in this case. Analogous to Tomasch oscillations, Andreev-reflected quasiparticles from the NS interface interfere with their counterpart. In a normal material, however, an electron and hole can not interfere directly and the reflected quasiparticle has to undergo another Andreev reflection first at the opposite NS interface before interfering.[281] As a consequence, this interference process requires phase coherence between the reflection events. McMillan-Rowell resonances occur at bias voltages of

$$V_m = V_0 + \frac{mhv_{\mathrm{F}}^{\mathrm{N}}}{4L_{\mathrm{N}}}, \tag{4.9}$$

with integer m and the Fermi velocity $v_{\mathrm{F}}^{\mathrm{N}}$ and length L_{N} of the normal region. Unfortunately, for device B, we can not extract the energetic spacing of the diamonds and thus it is not possible to determine the exact effect with certainty. However, based on their appearance and compared to previous studies,[280] the observed diamond-features are most likely due to Tomasch and McMillan-Rowell oscillations. In device B, these effects occur on an uncommonly large magnetic field scale, in contrast to other studies that do not observe this double transition of the Al electrodes.

Device C

The superconducting electrodes to separate hBN-encapsulated graphene islands of device C consist again of a Ti/Al/Ti trilayer. However, the Ti-adhesion layer is slightly thicker (8 nm instead of 6 nm for device B) to better understand the influence of the interface. Due to fabrication on a high-res Si substrate, no p-Si backgate is available. An optical image in the inset of figure 4.41 d) shows device C, which exhibits three independent functional junctions, labeled by JJ1 to JJ3. The fourth junction is not operational, probably due to misalignment to the graphene flake (marked by the white dashed lines). The three operational junctions are fabricated with different lengths L and varying widths W due to the shape of the graphene flake. Finite regions of pure hBN without encapsulated graphene exist in between the electrodes, which do not contribute to transport and can be neglected. The geometrical parameters are $L = 350\,\mathrm{nm}$, $W = 4.2\,\mu\mathrm{m}$ for JJ1, $L = 400\,\mathrm{nm}$, $W = 7\,\mu\mathrm{m}$ for JJ2 and $L = 450\,\mathrm{nm}$, $W = 4.5\,\mu\mathrm{m}$ for JJ3.

The response of the three junctions to a bias-current, large magnetic fields and electric field is shown in figure 4.41. The differential resistance $\mathrm{d}V/\mathrm{d}I$ was characterized in detail for JJ1 to JJ3 for bias currents up to $1\,\mu\mathrm{A}$, as depicted in figures 4.41 a) to c). All three operational junctions exhibit very similar behavior and show signs of the proximity effect, as signaled by the resistance response around zero bias. The $\mathrm{d}V/\mathrm{d}I$ does not approach zero but the overall resistance is in the order of $\sim 1\,\mathrm{k}\Omega$ and thus much lower compared to device B.

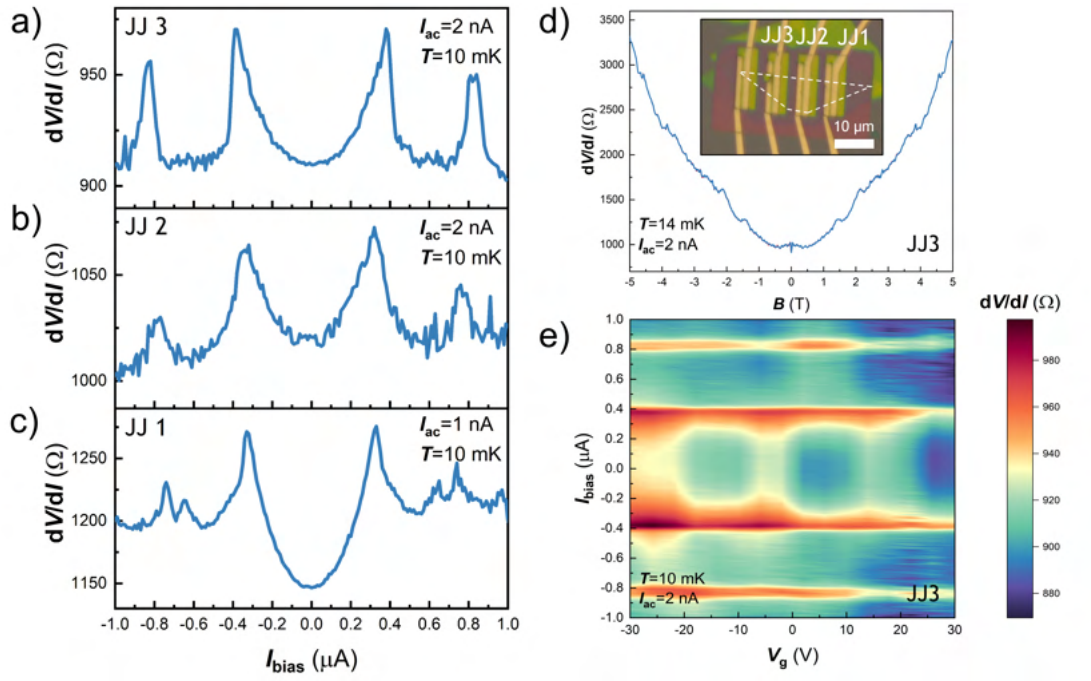

Figure 4.41.: Differential resistance $\mathrm{d}V/\mathrm{d}I$ as a function of bias current for a) JJ3, b) JJ2 and c) JJ1 of device C. All three operational junctions exhibit signs of the proximity effect. d) Response of the resistance in JJ3 to large magnetic fields up to $5\,\mathrm{T}$. The critical magnetic field of the junction is observed at small fields, before a continuous rise of the magnetoresistance is accompanied by small oscillations. e) Dependence of the observed peaks in JJ3 to the gate voltage (applied via the metallization layer of the chip carrier).

The resistance peaks at approximately $\pm 0.4\,\mu\mathrm{A}$ signal the critical current of the junctions I_c. Typically, the transparency of GJJs can be examined by calculating $I_\mathrm{c}R_\mathrm{N}$, with the normal state resistance of the junction R_N.[31,187,282,283] However, while the respective values of $I_\mathrm{c} = 0.33\,\mu\mathrm{A}$, $0.35\,\mu\mathrm{A}$ and $0.38\,\mu\mathrm{A}$ for JJ1, JJ2 and JJ3 are comparable to other Al-graphene junctions,[187] their R_N is far higher. Even for larger bias currents, as presented in figure A.13 in the appendix, the resistance does not decrease significantly. Note that no additional peaks or other features are present at such large bias currents. The large values of $R_\mathrm{N} = 1210\,\Omega$, $1010\,\Omega$ and $910\,\Omega$ at $I_\mathrm{bias} = 1\,\mu\mathrm{A}$ for JJ1, JJ2 and JJ3, respectively, result in large $I_\mathrm{c}R_\mathrm{N} > 300\,\mu\mathrm{V}$. This ratio can be put into perspective by normalization to the bulk superconducting gap of Al $\Delta \approx 180\,\mu\mathrm{eV}$.[102,269] This yields $eI_\mathrm{c}R_\mathrm{N}/\Delta \approx 2.2, 2$ and 1.9 for JJ1, JJ2 and JJ3, which is 5 to 10 times higher than the values reported for other GJJs.[31,187,282,283] We attribute this anomaly to the unusually high R_N of our junctions, which most likely results from poor transparency that complicates a direct comparison of $I_\mathrm{c}R_\mathrm{N}$ to literature values.

The response of JJ3 from device C to large magnetic fields is shown in figure 4.41 d), which represents the behavior of the other two junctions as well. After exceeding the B_c of Al at very

small magnetic fields, the resistance is almost featureless and increases approximately parabolic with magnetic field. This behavior indicates diffusive transport due to disorder.

Although device C has no backgate (such as p-Si) an electric field/voltage was applied via the metallization layer of the chip carrier, as shown in figure 4.41 e). Fluctuations of the resistance are visible but due to the small capacitance no significant gate voltage dependence could be induced.

The coherence length ξ can be estimated for our junctions under the assumption of diffusive transport by $\xi = \sqrt{\hbar D/\Delta}$, with the diffusion constant $D = v_\mathrm{F} l_\mathrm{mfp}/2$.[111] Since it is not possible to effectively tune the charge carrier density in device C, we can not accurately determine l_mfp and thus assume typical values between $10\,\mathrm{nm}$ and $100\,\mathrm{nm}$, resulting in $\xi \approx 130\,\mathrm{nm}$ and $430\,\mathrm{nm}$, respectively. Thus, as explained in section 2.2, we estimate our junctions to be in the diffusive, "dirty" and short to intermediate regime, due to the long coherence length of Al.

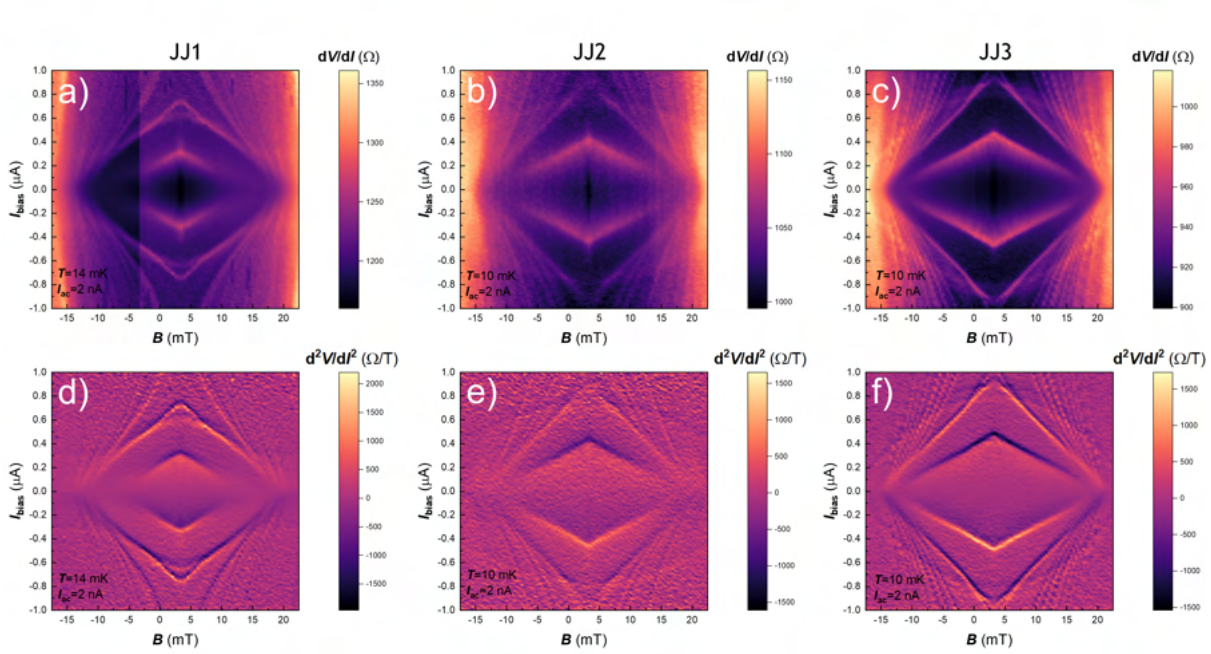

Figure 4.42.: Magnetic field and bias current dependence of the measured $\mathrm{d}V/\mathrm{d}I$ a) to c) and the derived $\mathrm{d}^2V/\mathrm{d}I^2$ d) to f) for the three operational junctions in device C.

Compared to device B, the Al-film of the electrodes in device C only shows one superconducting transition under a perpendicular magnetic field at around $\pm 20\,\mathrm{mT}$. Hence, we focus on this range for detailed measurements of the bias current dependence. Figure 4.42 compares these measurements on JJ1, JJ2 and JJ3. Their individual behaviors are strikingly similar. Again, diamond-shaped resistance features can be observed. We find that the zero of our magnetic field power supply is offset by $+3.3\,\mathrm{mT}$, which is not corrected in our data. JJ1 exhibits resistance instabilities that result in artifacts such as regions with different contrast in figure

4.41 a). In the center of the inner diamond in JJ1, multiple periodic lobes of low resistance are visible, reminiscent of a Fraunhofer pattern. This observation would indicate coherent superconducting transport across the junction. Considering that the first superconducting lobe ends at $\sim 1\,\mathrm{mT}$ away from the "real" zero and corresponds to one flux quantum ϕ_0, the effective area of the junction can be estimated as $A_{\mathrm{eff}} = \phi_0/\boldsymbol{B} \approx 2\,\mu\mathrm{m}^2$. This is in good agreement with the geometrical size of the junction $A_{\mathrm{geo}} \approx 1.5\,\mu\mathrm{m}^2$, considering possible flux focusing effects of the superconducting electrodes. However, an additional measurement of this region with higher resolution does not confirm the Fraunhofer pattern, as shown in the appendix in figure A.13. It remains unclear whether the observed pattern originates from flux quantization or from artifacts due to the magnetic field resolution of the original measurement.

For all junctions, two pronounced diamond-shaped resistance features can be identified particularly well in the derived $\mathrm{d}^2V/\mathrm{d}I^2$. In addition, a broad oval structure is visible in the background as well as diverging fringes that evolve towards larger I_{bias}.

JJ3 exhibits the most pronounced resistance variations and will be discussed in detail. The different features observed in the $\mathrm{d}^2V/\mathrm{d}I^2$ map of JJ3, shown separately in figure 4.43 a), are illustrated by a schematic color-coded contour in figure 4.43 b).

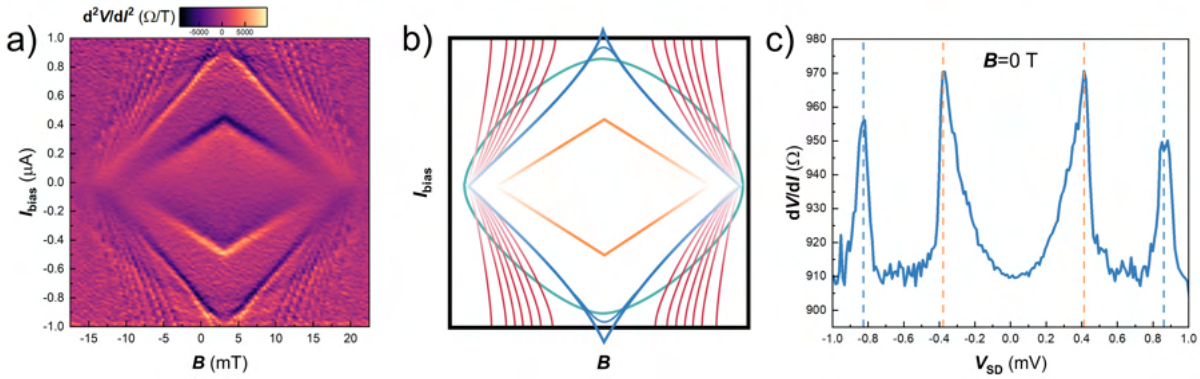

Figure 4.43.: Exemplary results obtained on JJ3 of device C in a) the derived $\mathrm{d}^2V/\mathrm{d}I^2$ map. b) Qualitative color-coded contour of the different features. c) Differential resistance $\mathrm{d}V/\mathrm{d}I$ of JJ3 as a function of DC voltage V_{SD} across the junction at $\boldsymbol{B} = 0\,\mathrm{T}$. The dashed lines indicate the peak positions of the inner (orange) and the outer (blue) diamond.

Despite some qualitative differences, the observed diamond-shaped resistance behavior is reminiscent of those effects that were observed in device B. Hence, we consider Tomasch and McMillan-Rowell oscillations in our interpretation.

The *oval-shaped structure* in the background (green oval in figure 4.43 b)) can be attributed to the magnetic field dependence of superconducting gap Δ. A similar effect has been observed in Al-based semiconductor nanowire JJs and is expected from theory following[284]

$$\Delta(B) = \Delta\sqrt{1 - \left(\frac{B}{B_\mathrm{c}}\right)^2}. \tag{4.10}$$

Two pronounced *diamond-shaped features* (colored in orange and blue) appear as peaks in $\mathrm{d}V/\mathrm{d}I$ as a function of DC source-drain voltage V_SD. This DC voltage was measured across the junction allowing us to extract the involved energies.

According to MAR, peaks are expected for $V = 2\Delta_\mathrm{ind}/en$ with $n = 1, 2...$ corresponding to the number of Andreev reflections. If the inner peak (orange) at around $\pm 400\,\mu\mathrm{V}$ is interpreted as the first order MAR or as the critical current I_c, the calculated proximity-induced gap of $\Delta_\mathrm{ind} \approx 200\,\mu\mathrm{eV}$ would be in good agreement with expected values for Al of $100-200\,\mu\mathrm{eV}$.[102, 104] However, the outer peak at approximately $\pm 800\,\mu\mathrm{V}$ appears above the superconducting gap and can not be attributed to MARs. The inferred superconducting gap with $\Delta_\mathrm{ind} \approx 400\,\mu\mathrm{eV}$ would be twice as high as reported for bulk Al[102, 104] whereas other Al-devices typically exhibit lower Δ_ind than the bulk gap Δ.[187, 269, 270] To evaluate the distinct features in more detail, measurements were performed at various temperatures.

Figure 4.44 compares the temperature-dependence of JJ3 to that of the Al-film in the electrodes. A significant decrease of the critical magnetic field B_c of the Al-film is observed when the temperature is increased from 10 mK in figure 4.44 d) to 345 mK in figure 4.44 e). The diamond structures and fringes in the $\mathrm{d}^2V/\mathrm{d}I^2$ map in figure 4.44 a) vanish exactly at the B_c of the Al-film at 10 mK, only the oval background structure persists up to slightly higher fields. A comparison of the $\mathrm{d}^2V/\mathrm{d}I^2$ maps at 10 mK and 345 mK with the resistance response of the Al-film demonstrates that the different features originate from proximity-induced superconductivity. Similar to the temperature dependence in device B, the features in device C are squeezed into a smaller magnetic field range as the temperature increases. Figure 4.44 b) shows that both peaks in $\mathrm{d}V/\mathrm{d}I$ at $\boldsymbol{B} = 0\,\mathrm{T}$ move towards lower bias currents for increasing temperatures, reminiscent of the temperature dependence of the superconducting gap Δ. A quantitative analysis of this temperature dependence is given in figure 4.45.

The temperature evolution of both peaks is fitted with the BCS relation for the temperature dependence of the superconducting gap[102, 270, 285]

$$\Delta(T) = \frac{2\Delta_0}{n}\tanh\left(1.74\sqrt{\frac{T}{T_\mathrm{c}} - 1}\right), \tag{4.11}$$

with Δ_0 the superconducting gap at $T = 0\,\mathrm{K}$ and a prefactor that is modified to account for possible MAR processes. The inner peak is well described by a fit (orange solid line) that yields $T_\mathrm{c} = 424\,\mathrm{mK}$ and $\Delta_0 = 185\,\mu\mathrm{eV}$, which is in good agreement with the expected value for Al. Strikingly, the outer peak vanishes at a higher temperature, with the fit (blue solid line) yielding

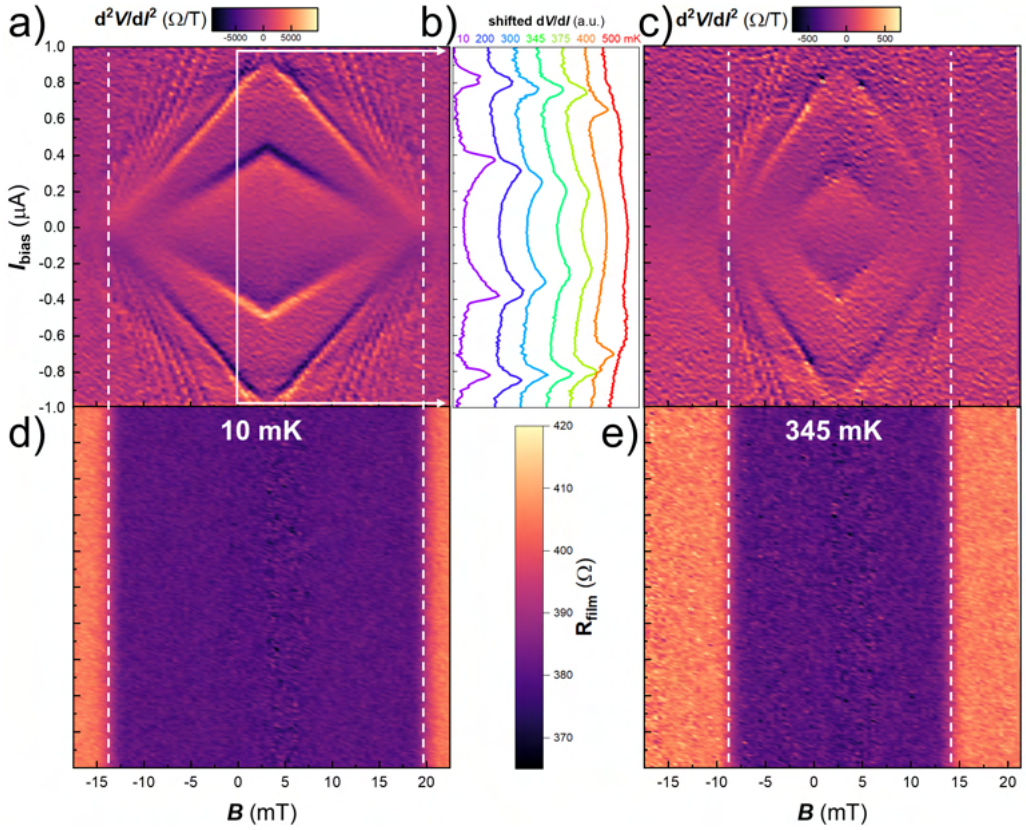

Figure 4.44.: a) Derived $\mathrm{d}^2V/\mathrm{d}I^2$ map of JJ3 at 10 mK. b) Evolution of the peaks in $\mathrm{d}V/\mathrm{d}I$ at $\boldsymbol{B} = 0$ T, indicated by the line cut in a), for increasing temperatures ranging from 10 (purple) to 500 mK (red). c) Derived $\mathrm{d}^2V/\mathrm{d}I^2$ map of JJ3 at 345 mK. d) Resistance data acquired on the Al-film at the non-operational junction show the critical magnetic field B_c of the electrodes at 10 mK and e) 345 mK.

$T_\mathrm{c} = 594$ mK and $\Delta_0 = 428$ μeV. Note that the large Δ_0 does not match values expected for Ti or Al. Typically, various peaks that originate from superconductivity such as MARs converge on the same T_c value.[270,285] While we acknowledge that more data points may infer T_c and Δ_0 of the peaks more reliably, this unusual behavior is supported by our results obtained by power dependent microwave measurements shown in figure A.15 in the appendix.

The temperature evolution of the outer peak (blue data) can be interpreted in the context of McMillan-Rowell oscillations. As explained for device B, resistance oscillations can arise due to Andreev-reflected quasiparticle interference in the normal conductor in a SNS junction.[278,279,281] Although we expect them to follow the temperature dependence of the superconducting gap, a slightly increased T_c could result from their origin in the normal conductor of a SNS junction. As McMillan-Rowell oscillations require two Andreev reflections (or more) to occur, it could explain the large $\Delta_0 = 428$ μeV of the outer peak, which is approximately twice the size of the inner peak or 4Δ of Al.

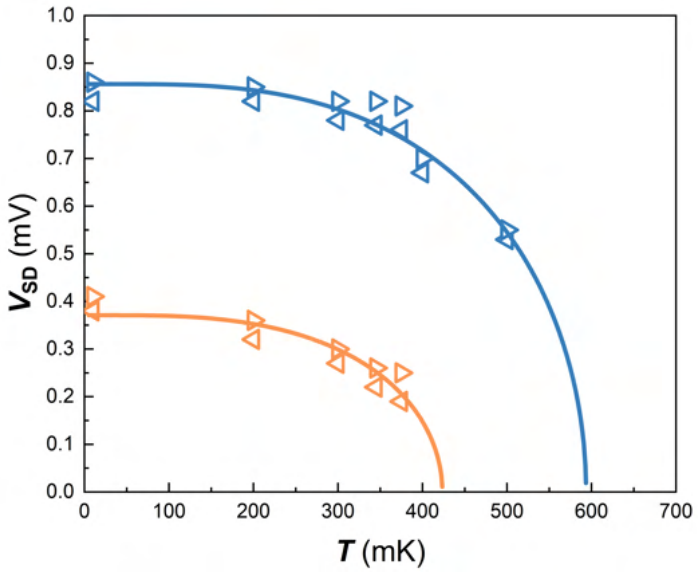

Figure 4.45.: Analysis of the V_{SD} peak position of the inner (orange triangles) and the outer peak (blue triangles) as a function of temperature, extracted from the measurements shown in figure 4.44 b). The negative and positive V_{SD} values are represented by the left and right pointing direction of the triangles. The data points are fitted using Eq. 4.11.

McMillan-Rowell oscillations occur at bias voltages of

$$V_m = V_0 + \frac{mhv_{\mathrm{F}}^{\mathrm{N}}}{4L_{\mathrm{N}}}, \tag{4.12}$$

with integer m and the Fermi velocity $v_{\mathrm{F}}^{\mathrm{N}}$ and length L_{N} of the normal region.[281] Based on a recent study by Huang *et al.*,[280] it is possible that quasiparticle interference effects in the superconductor of the SNS junctions results in Tomasch oscillations. As explained for device B, these oscillations occur at bias voltages of

$$V_m = \pm\sqrt{\Delta^2 + \left(\frac{mhv_{\mathrm{F}}^{\mathrm{S}}}{2d_{\mathrm{S}}}\right)^2}, \tag{4.13}$$

with integer m, the superconductor Fermi velocity $v_{\mathrm{F}}^{\mathrm{S}}$ and the superconductor thickness d_{S}.[281] We estimate for both McMillan-Rowell and Tomasch oscillations $V_m \sim 2\,\mathrm{mV}$, using 10^6 m/s as Fermi velocity and the given length scales of device C.

For comparison, the periodicity of the oscillations is also assessed towards higher bias (red fringes in figure 4.43 b)). Figure 4.46 a) shows the magnetic field dependence of JJ3 in $\mathrm{d}V/\mathrm{d}I$ as a function of DC bias source-drain voltage V_{SD}. Four exemplary line cuts at various magnetic fields are used to extract the V_{SD} value of the peaks in figure 4.46 b). The voltage difference between the peaks ΔV_{SD} ranges between $0.1\,\mathrm{mV}$ and $0.2\,\mathrm{mV}$.

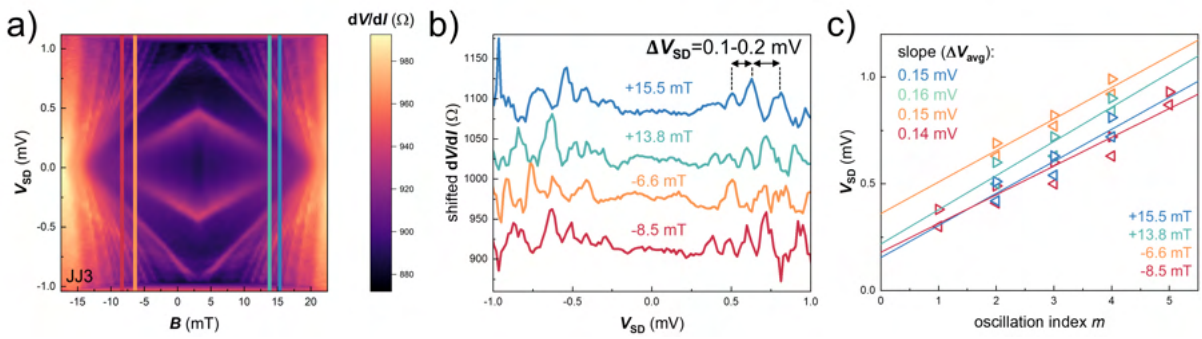

Figure 4.46.: a) Magnetic field dependence of the $\mathrm{d}V/\mathrm{d}I$ of JJ3 as a function of DC bias source-drain voltage V_{SD}. b) Line cuts at four exemplary magnetic fields as indicated by the colored lines are plotted in a). For most magnetic fields only three peaks can be resolved sufficiently to determine the voltage values of the oscillation peaks. c) V_{SD} position of the peaks in a) at negative (positive) values plotted as left pointing (right pointing) triangles as a function of oscillation index m. The linear fit is used to extract the voltage period. Note that only for $-8.5\,\mathrm{mT}$ five oscillation peaks could be resolved sufficiently.

The average voltage difference ΔV_{avg} can be determined from a linear fit to the V_{SD} position of the peaks, as shown in figure 4.46 c). For the four exemplary data sets, the extracted ΔV_{avg} values are in good agreement and range in between $0.14\,\mathrm{mV}$ and $0.16\,\mathrm{mV}$. These value are approximately one order of magnitude smaller than estimated for McMillan-Rowell and Tomasch oscillations. Although the Fermi velocity can be slightly larger than 10^6 m/s in some superconductors, this can not explain the apparent mismatch.

The magnetic field dependence of the oscillation peaks is analyzed in figure A.16 in the appendix. The magnetic field distance between peaks ranges between $1\,\mathrm{mT}$ and $2\,\mathrm{mT}$, which corresponds to $\mu_{\mathrm{B}} B \approx 0.1\,\mu\mathrm{eV}$.

Based on previous reports[280,286] and given that our sample exhibits low contact transparency and diffusive transport, Tomasch and McMillan-Rowell oscillations are a reasonable explanation for the additional outer diamond-feature and the diverging fringes. However, our estimations are one order of magnitude off from the obtained energetic peak spacing. Indeed, the energetic position of the outer peak at 4Δ could also result from two-quasiparticle or multiple Cooper pair tunneling processes.[277,278] However, in the absence of additional energy sources such as microwave radiation, such processes are typically less likely.

In summary, this section provided an overview of the experimental results obtained from three superconducting aluminum-based graphene junction samples. These devices exhibit clear signs of proximity-induced superconductivity, which is attributed to an optimized interface provided by the Ti adhesion layer. This improvement enabled systematic studies of the GJJ devices as a function of bias current, gate voltage, magnetic field, temperature and microwave

radiation. While device A showed signatures of a gate tunable I_c and blurred Shapiro steps, these effects were absent in device B. The magnetic field and bias current dependence of device B exhibited diamond-shaped features on a magnetic field scale larger than that typically expected for superconducting aluminum, whereas Device C exhibited similar effects in three junctions on a smaller magnetic field scale. A detailed analysis suggests that these phenomena most likely originate from above-gap interference effects, such as Tomasch and McMillan-Rowell oscillations.

High-frequency circuits for the integration of graphene Josephson junctions

This section presents a short overview of preliminary results that were obtained on high-frequency circuits, which are designed for the integration of graphene Josephson junctions. The design and fabrication of these circuits is described in detail in section 3.3.1. Here, only the results of unloaded resonators without a GJJ are presented.

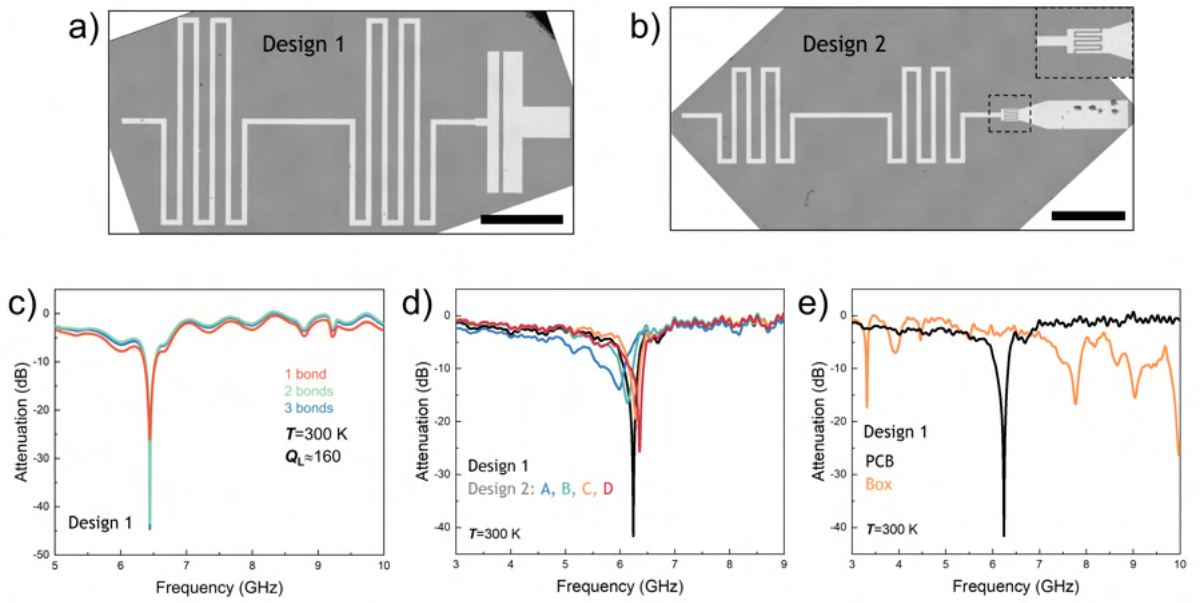

Figure 4.47.: Two designs of superconducting Nb microstrip $\lambda/2$ resonators with a) plate capacitor and b) finger capacitor coupling architecture. c) Reflectometry measurement (S_{11}) of the resonator design 1 for different number of wire bonds. d) Comparison of resonator design 1 (black line) with four different resonators of design 2 (colored lines). e) Comparison of the spectra of the same resonator (design 1) mounted to its initial PCB (black line) and to a different sample box (orange line), used for measurements at low temperatures. All measurements were performed at room temperature.

Figures 4.47 a) and b) show two designs of superconducting Nb microstrip $\lambda/2$ resonators. Reflectometry measurements (S_{11}) at room temperature are possible since the Nb thin films have a resistance of only a few Ω. The influence of the number of wire bonds was studied for

the resonator with design 1, as shown in figure 4.47 c). The amplitude of the resonance peak at ~ 6.5 GHz increases with the number of wire bonds. Hence, three wire bonds were consistently used for all measurements. Since the setups and the design are not optimized for high-frequency measurements and a high quality factor Q_{L}, the resonance peak reaches only $Q_{\mathrm{L}} \sim 160$.

In figure 4.47 d), the resonator design 1 (black line) is compared to four other resonators of design 2 (colored lines). The resonance peak of all resonators aligns around the same value, but is most pronounced for design 1. Hence, the resonator of design 1 was chosen for further measurements at low temperatures and mounted into a (shielded) sample holder box for cryogenic measurements. Figure 4.47 e) compares the spectra of the same resonator in the previous PCB (black line) and in the sample box (orange line). The previously observed peak at ~ 6.3 GHz is absent in the spectrum of the resonator in the sample box, which exhibits more noise and a peak at ~ 8 GHz instead. The setup that is not optimized for high-frequency experiments and variations in the grounding that affect the electromagnetic field distribution and radiation loss can lead to signal degradation and a shift of the resonance frequency.

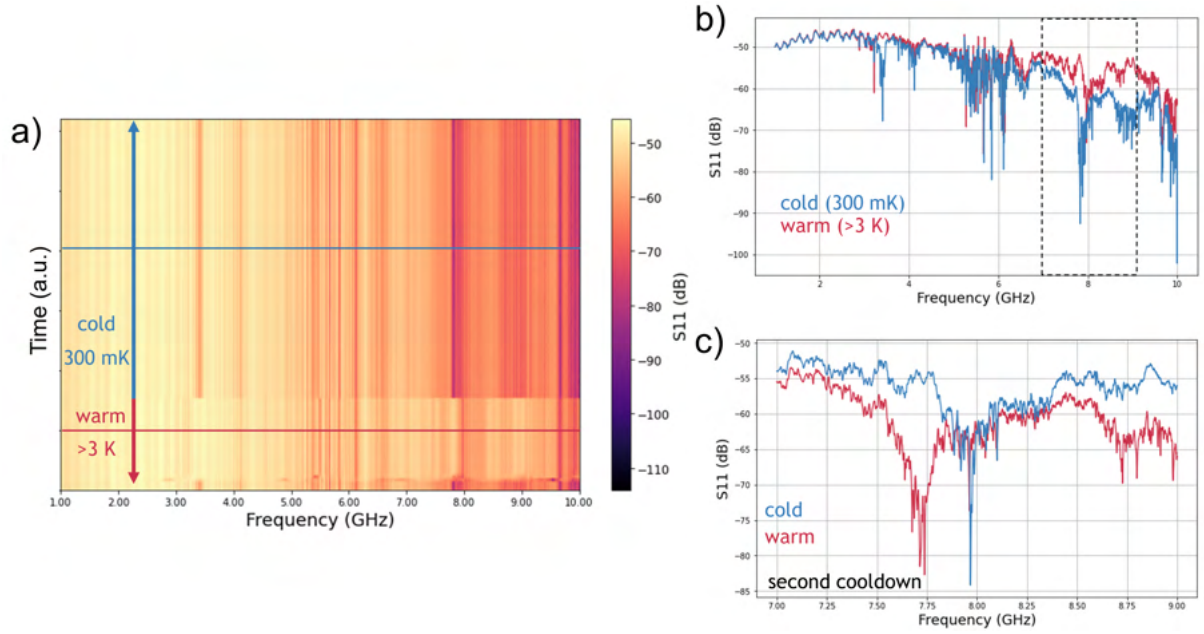

Figure 4.48.: a) Reflectometry spectrum of the resonator with design 1 as a function of time while cooling to mK-temperatures. The moment of transition from the warm state (>3 K) to the cold state (~ 300 mK) of the cryostat is clearly visible. b) Comparison of spectra at warm (red line) and cold (blue line) state, taken at the solid red and blue lines in a). c) Measurements of a second cooldown with higher resolution around the resonance frequency of ~ 8 GHz, as indicated by the black dashed rectangle b). Spectra at warm (red line) and cold (blue line) state are compared.

Measurements at low temperatures were performed in collaboration with Dr. Marios Maroudas in the compact dry cryostat, shown in figure A.7), in the group of Prof. Horns. The cryostat typ-

ically operates at 4 K, but reaches temperatures of a few hundred mK for short periods of time by adiabatic demagnetization. However, the mounted resonator is subjected to strong magnetic fields and elevated temperatures that quench the superconductivity of Nb (here $T_c \sim 3.7$ K) before reaching mK-temperatures. Hence, upon cooling to mK-temperatures a significant change of the resonator spectrum is expected. The spectrum of the resonator from 1 GHz to 10 GHz during the cooldown is shown in figure 4.48 a). When the temperature decreases to approximately 300 mK, the spectrum changes dramatically and a dip in the reflected S_{11} signal appears at ~ 8 GHz, which corresponds to the expected resonance frequency f_0. The change of the spectrum is illustrated by comparing line cuts taken at elevated temperatures (warm, red) and mK-temperatures (cold, blue), as indicated by the solid lines in figure 4.48 a). Both spectra in figure 4.48 b) exhibit similar peaks that are attributed to parasitic resonances, except for the peak at ~ 8 GHz, which is significantly more pronounced in the cold state. Two spectra of a second cooldown with a higher resolution around the resonance frequency are compared in figure 4.48 c). The resonance peak slightly shifts and appears much more narrow upon cooling to ~ 300 mK, which is consistent with a superconducting transition in the resonator that results in an increased kinetic inductance.[287,288]

These preliminary measurements illustrate the behavior of the fabricated superconducting Nb microstrip $\lambda/2$ resonators. The first characterization at room temperature and low temperatures shows promising results. However, for the integration of GJJs into high-frequency circuits, setups and groundings need to be optimized to prevent signal degradation and minimize losses. The results presented in this chapter highlight the significant advances made during this thesis towards combining GJJs and high-frequency circuits. A successful integration of graphene devices into superconducting microwave circuits seems within reach.

4.4. Terahertz Detection in Graphene-based Photodetector Devices

A substantial amount of work in this thesis was invested in the development of THz-detectors, based on asymmetric dual-grating gate graphene terahertz field-effect-transistors (ADGG GTeraFETs). Although this topic was intended as a sideproject, significant advancements and finally successful THz-detection could be achieved. The complex analysis of the observed THz-signal is beyond the scope of this project in this thesis. Thus, this section only summarizes the most important advancements on such GTeraFET devices in our group and presents successful THz-measurements that serve as a proof of concept.

4.4.1. Terahertz Detectors based on Large-Area Graphene

The development of ADGG GTeraFETs in our group started with devices based on large-area CVD graphene, as discussed in section 3.1.3. An exemplary device is shown in figure 4.49 a). In this device, large-area CVD graphene is encapsulated by two hBN flakes. Metallic Cr/Au electrodes serve as source (S) and drain (D) contacts and two interdigitated finger gates (TG_1 and TG_2) form the asymmetric dual-grating gate structure.

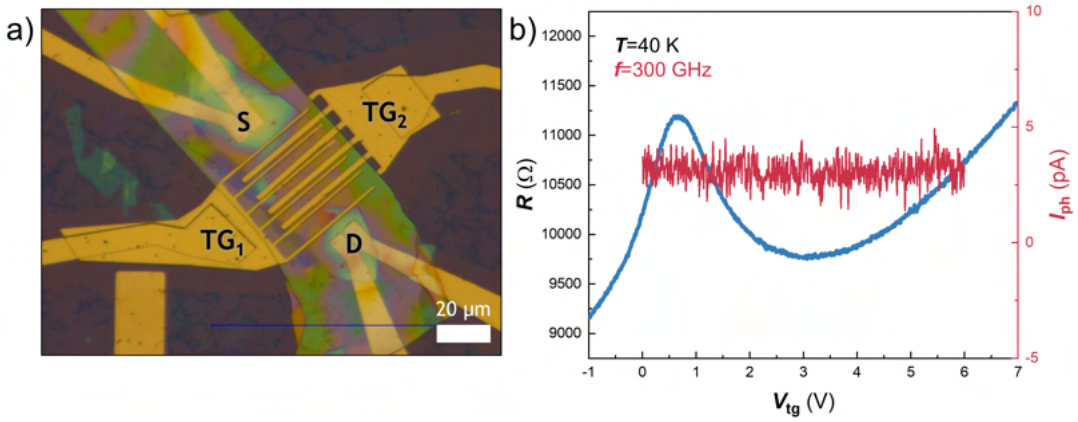

Figure 4.49.: a) Optical image of an ADGG THz detector of the first generation of devices based on CVD graphene encapsulated by hBN flakes. This device is equipped with two source (S) and drain (D) contacts on each side and two interdigitated topgates (TG_1 and TG_2). b) Two-terminal resistance (blue line) and THz-induced photocurrent I_{ph} (red line) of the device in a) at 40 K as a function of topgate voltage.

Since the p-Si backgate was not functional due to a short to one of the contacts, only the topgates could be used to locally tune the charge carrier density of the graphene. Unfortunately, the topgates exhibit a leakage current as well, which limits the voltage range from -1 V to $+7$ V.

Figure 4.49 b) plots the two-terminal resistance (blue line) as a function of top gate voltage V_{tg} at 40 K. The resistance peak at ~ 0.8 V is interpreted as the CNP of the graphene. This signals a very low p-doping level, which is typically much higher for our large-area graphene devices.[19,137] These devices are generally fabricated on silicon substrates and are thus exposed to the environmental conditions such as moisture, which leads to significant p-doping.[16,23] Thus, the low doping level in this device can be attributed to the hBN encapsulation that protects the graphene.

Additionally, figure 4.49 b) shows an exemplary THz-detection measurement of the induced photocurrent I_{ph} (red line) at 40 K and 300 GHz with a power of 5 dBm. Note that these measurements were performed without globally biasing the graphene by a backgate. From previous studies on ADGG GTeraFET devices, we expect a significant change of I_{ph} close to the CNP.[40,124,133] However, only a very small and constant background of ~ 3 pA is observed.

Various attempts to observe a sizable photocurrent in this and similar large-area graphene devices did not succeed. Although there are reports for CVD-graphene-based THz detection,[43,128,289] plasmonic THz-rectification mechanisms depend on the charge carrier mobility μ in the graphene. Hence, we suspect that the device quality was still insufficient to generate a significant photocurrent. Furthermore, the device fabrication with large-area graphene is even more complex and has a lower device yield compared to that of exfoliated graphene devices. All following GTeraFETs were exclusively prepared from exfoliated graphene.

4.4.2. Terahertz Detectors based on Exfoliated Graphene

Detector A

Detector A consists of a hBN encapsulated exfoliated trilayer graphene flake on a silicon substrate with a p-Si backgate and is equipped with two finger gates (TG_1 and TG_2) and two source and drain contacts. The inset in figure 4.50 b) shows an optical image of detector A. The *global* backgate and the two *local* topgates are utilized to tune the charge carrier density. The topgates can either be used simultaneously or independently of each other, as shown in the schematic in figure 4.50 a). For the electrical transport characterization presented in figure 4.50 a small AC bias current of 2 nA is imposed. As explained in section 3.4.1, the photodetection experiments are conducted without using a source-drain bias.

A backgate voltage sweep shown in figure 4.50 b) indicates minuscule doping of the graphene with the CNP located at ~ 0 V. Unfortunately, the backgate voltage V_{bg} is limited to this small range due to an increasing backgate leakage current I_{bg} (orange line).

Both topgates are fully functional without any electrical shorts, allowing to locally tune the charge carrier density as shown in figure 4.50 c). Here, the resistance (blue line) is plotted as a function of topgate voltage V_{tg}, which reveals a (local) CNP at ~ -0.25 V. Note that both

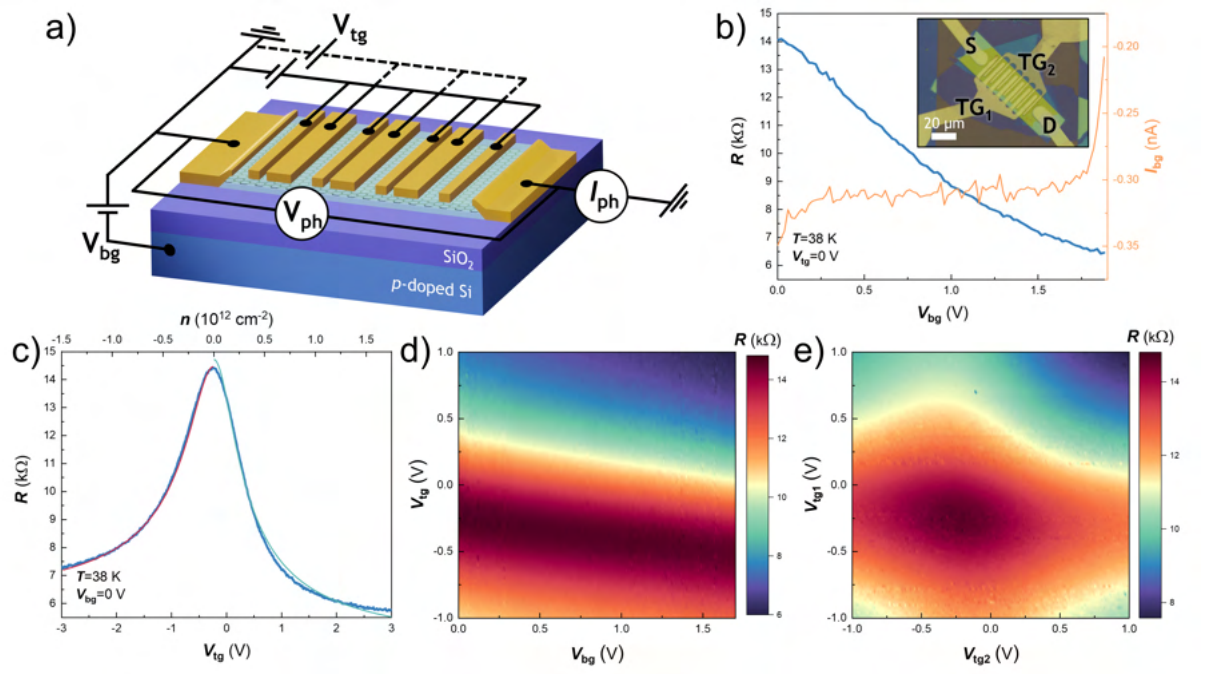

Figure 4.50.: a) Schematic representation of THz-detection measurements with a ADGG GTeraFET. The two topgates are connected either in parallel or independently, as indicated by the dashed lines. b) Two-terminal resistance (blue line) and simultaneously recorded leakage current I_{bg} (orange solid line) as a function of backgate voltage V_{bg} of detector A. The global CNP appears at $\sim 0\,\mathrm{V}$. An optical image of this exfoliated graphene device is depicted in the inset. c) The measurement of the resistance (blue line) as a function of topgate voltage V_{tg} reveals the (local) CNP at $-0.25\,\mathrm{V}$. The two topgates are utilized in parallel here. The resistance is fitted separately with Eq. 4.14 for the electron (green line) and hole (red line) side. d) Map of the resistance as a function of both V_{bg} and V_{tg}. The CNP is shifted by the backgate in respect to the topgate voltage. e) Map of the resistance as a function of the two individual topgate voltages V_{tg1} and V_{tg2}.

topgates are used in parallel in this measurement. The resistance is fitted separately for the electron (green line) and hole (red line) side using

$$R = R_{\mathrm{c}} + R_{\mathrm{ch}} = R_{\mathrm{c}} + \frac{1}{en\mu} \tag{4.14}$$

with the contact resistance R_{c} and the channel resistance of the graphene R_{ch}. This equation combines Eq. 2.7 and Eq. 2.6 to determine the residual charge carrier density n^* and the mobility μ as fit parameters in addition to R_{c}.[57,58,60] The fits yield a combined $n^* \approx 2.4 \times 10^{11}\,\mathrm{cm}^{-2}$, $\mu \approx 2700\,\mathrm{cm}^2/\mathrm{Vs}$ and $R_{\mathrm{c}} \approx 5\,\mathrm{k\Omega}$. Aside from the moderately low mobility, these values match well to our expectations.

In figure 4.50 d), the influence of the global backgate on the effect of the local topgates is

presented. As the graphene channel is n-doped by V_{bg}, the CNP is shifted in respect to V_{tg} which requires higher negative voltages to compensate the influence of the backgate.

The two topgates can be controlled independently, as depicted in figure 4.50 e). This measurement shows the resistance as a function of both topgate voltages V_{tg1} and V_{tg2}. A cross shape is observed with the center at the CNP. This characterization is necessary to identify the ideal resonance conditions for the THz-detection measurements.

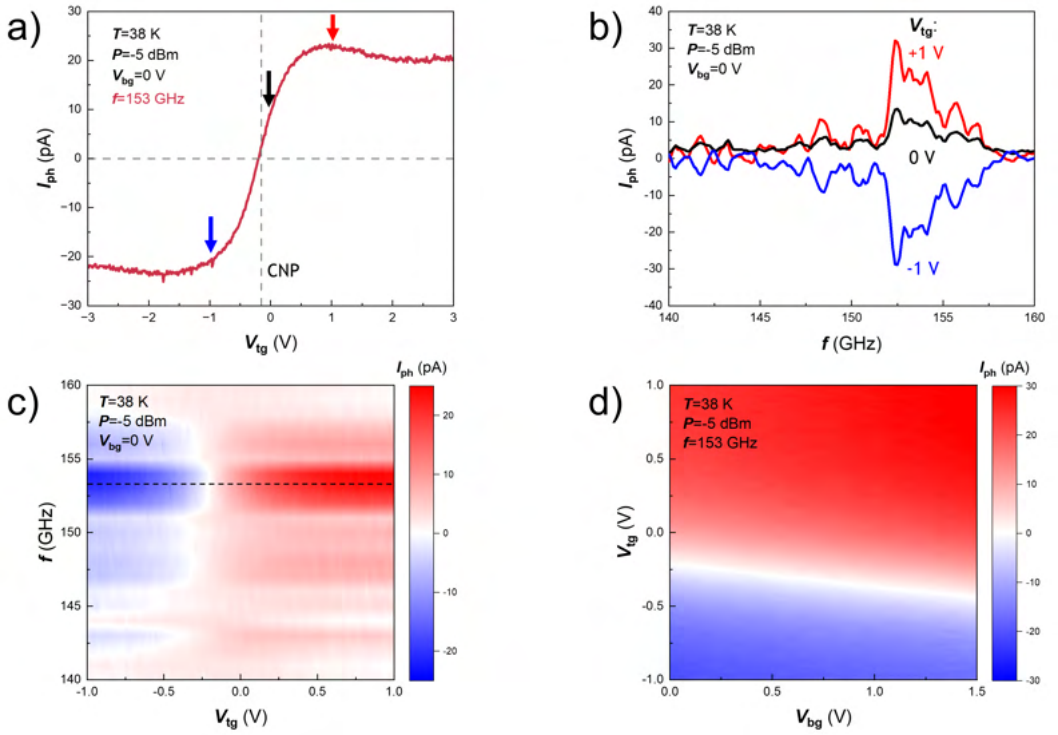

Figure 4.51.: a) Exemplary measurement of the sub-THz radiation-induced photocurrent I_{ph} at 153 GHz and power $P = -5$ dBm as a function of topgate voltage. A photosignal of up to 23 pA is detected. I_{ph} switches sign at the CNP, as the charge carrier type changes. b) Frequency dependence of I_{ph} for three different topgate voltages, as indicated by the arrows in a). A maximum signal is observed around 153 GHz. c) Detailed measurement of I_{ph} as a function of V_{tg} and frequency f. The dashed line indicates the position at 153 GHz of the exemplary measurement in a). d) Analogous to the shift of the CNP, tuning the backgate voltage results in a shift in V_{tg} of the photoresponse. All measurements were performed at 38 K.

An exemplary measurement under sub-THz illumination at ~ 40 K and a frequency of 153 GHz is shown in figure 4.51 a). A clear photoresponse of up to 23 pA of the graphene detector is observed. As expected, I_{ph} switches sign at the CNP when the charge carrier type changes from holes to electrons. For this and the following measurements a nominal power of -5 dBm is set at the frequency generator and source module that emits the radiation. However, the detector is subjected to a significantly lower *effective* power because the beam is not focused

and has to pass through 1 cm of atmosphere and the optical window. By assuming $-5\,\mathrm{dBm}$, we overestimate the incident power at the detector, which results in a general underestimation of the sensitivity of our detectors.

The photoresponse curve is point symmetric and does not decay to zero at higher gate voltages, as observed in other studies.[40,124] Instead, I_{ph} saturates at a constant level of $\sim \pm 20\,\mathrm{pA}$. In order to evaluate its frequency-dependence, measurements were performed at three constant topgate voltages (as indicated by the arrows in figure 4.51 a)). The resulting I_{ph} exhibits a maximum around $\sim 153\,\mathrm{GHz}$, as shown in figure 4.51 b). Several other peaks with lower amplitude are present across the entire frequency range from $140\,\mathrm{GHz}$ to $160\,\mathrm{GHz}$. The polarity of the peaks switches when the charge carrier type is changed by the topgate voltage. A detailed measurement of I_{ph} a function of frequency and V_{tg} is shown in figure 4.51 c). We interpret the most pronounced signal around $\sim 153\,\mathrm{GHz}$ as a signature of resonant (plasmonic) photocurrent excitation. The dashed line indicates the position of the measurement depicted in figure 4.51 a). The response of I_{ph} at $153\,\mathrm{GHz}$ to a change of the global charge carrier density is presented in figure 4.51 d). Analogous to the shift of the CNP in the transport measurement in figure 4.50 d), the sign change of I_{ph} is shifted by V_{bg} towards higher negative topgate voltage. This is evidence that the signal originates from rectification mechanisms in the graphene layer.[39,40,124,130]

As explained in section 2.3.2, multiple different THz-rectification mechanisms can coexist in ADGG GTeraFETs that could explain the obtained photoresponse. Before giving a brief interpretation of the observed THz-signal and an estimation of the achieved sensitivity, the results of a second device (detector B) will be presented.

Detector B

Detector B consists of a hBN encapsulated exfoliated few-layer graphene flake (four to five layers). An optical image of detector B is presented in the inset of figure 4.52 a), showing the electric contacts and the two separate topgates TG_1 and TG_2. In contrast to detector A, the p-Si backgate of detector B is fully functional and allows to tune the global charge carrier density across a wide range, as depicted in figure 4.52 a). At 38 K, the global CNP is located at $-0.8\,\mathrm{V}$, indicating a very low doping level. The topgate sweeps in figure exhibit a local CNP at $V_{\mathrm{tg}} = -0.08\,\mathrm{V}$ at $V_{\mathrm{bg}} = 0\,\mathrm{V}$, that can be shifted by the applied backgate voltage. By fitting the resistance around the CNP as a function of V_{tg}, a combined charge carrier mobility μ of $14100\,\mathrm{cm^2/Vs}$ (μ_{e} of $10800\,\mathrm{cm^2/Vs}$, μ_{h} of $17400\,\mathrm{cm^2/Vs}$) with a very low residual charge carrier density $n^* \approx 4.5 \times 10^{10}\,\mathrm{cm^{-2}}$ is determined, which signals a clean graphene device with good electronic quality. The contact resistance is extracted as $R_{\mathrm{c}} \approx 8.8\,\mathrm{k\Omega}$ for the hole and $R_{\mathrm{c}} \approx 0.7\,\mathrm{k\Omega}$ for the electron side. This pronounced asymmetry is attributed to n-doping near the 1D-contacts which increases the resistance for hole carriers.[39,130] The fits to the resistance are shown in figure A.17 in the appendix.

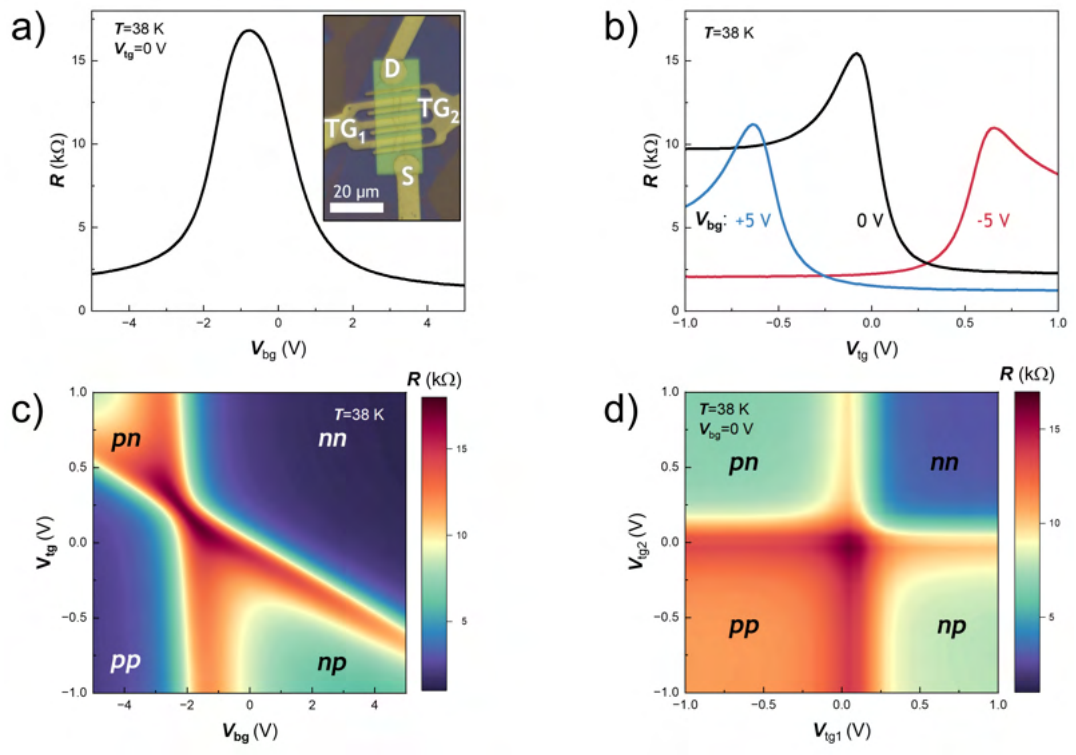

Figure 4.52.: a) The backgate sweep of detector B reveals at global CNP at $V_{\mathrm{bg}} = -0.8\,\mathrm{V}$. The inset shows an optical image of detector B. b) Dependence of the two-terminal resistance on the topgate voltage V_{tg} for three different backgate voltages. c) Resistance as a function of V_{bg} and V_{tg}. Four different regions pn, nn, pp and np can be identified, that correspond to the charge carrier type induced by the backgate and topgates, respectively. d) Advanced tunability of the resistance when the two topgates are controlled independently. Four regions are observed that correspond to the formation of pn-junctions in the graphene. All measurements were performed at 38 K.

A detailed map of the backgate and topgate dependence of the two-terminal resistance is depicted in figure 4.52 c). The global CNP branches out into two arms, reflecting the density shifts induced by V_{tg} and V_{bg}. Tuning the global backgate and the local topgates induces multiple pn-junctions in the graphene channel. Four characteristic regions pn, nn, pp and np can be identified that are labeled according to the doping of the global and the local gates, respectively.[290] Here, the regions with equal carrier type doping nn and pp display a reduced resistance compared to pn and np regions. At a constant backgate voltage, the two topgates can be used separately to enable advanced control of the formation of pn-junctions in the graphene channel, as shown in figure 4.52 d). Similar to detector A, a cross-shaped resistance feature is observed that separates the four pn, nn, pp and np regions, labeled according to the tuning of V_{tg1} and V_{tg2}, respectively. The contrasting resistance levels between the pp and nn region are explained by the overall global n-doping at $V_{\mathrm{bg}} = 0\,\mathrm{V}$, which leads to a reduced resistance for

the nn region and, vice versa, an increased resistance for the pp region. This transport characterization demonstrates the tunability of the device and illustrates the interplay between the different gates and the formation of pn-junctions.

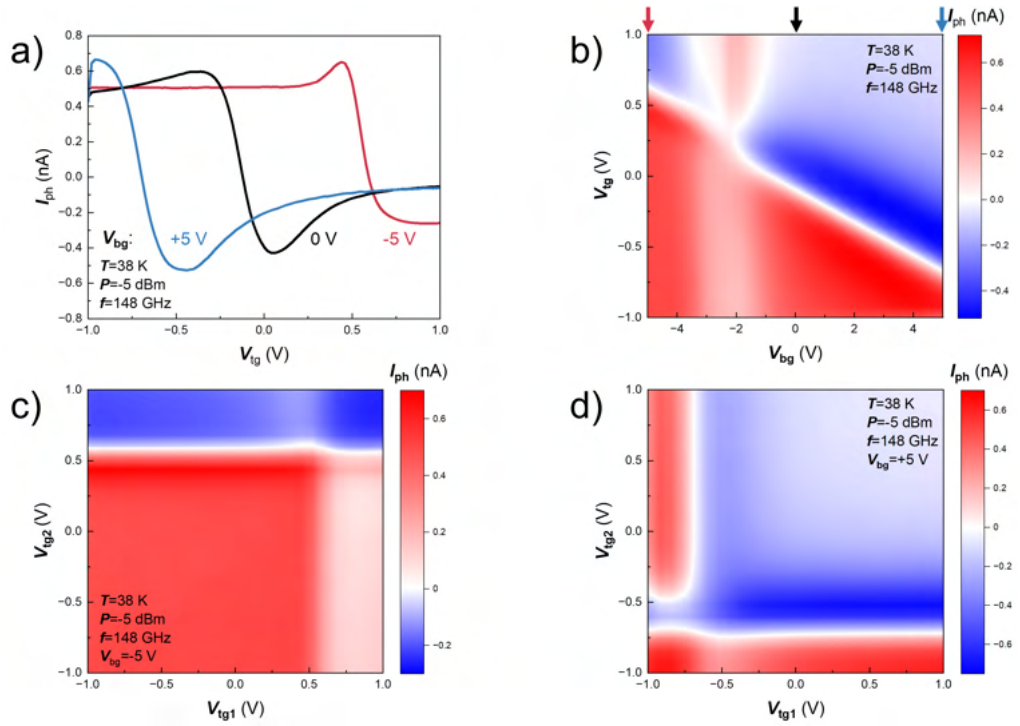

Figure 4.53.: a) I_{ph} as a function of topgate voltage for three different global doping conditions at $148\,\mathrm{GHz}$ and a nominal power of $-5\,\mathrm{dBm}$. b) I_{ph} as a function of V_{bg} and V_{tg}. The colored arrows indicate the position of the single sweeps depicted in a). The photoresponse resembles the four different doping regions identified in the transport characterization. The maximum signal is detected at the transition from the np to the nn region. c) Photoresponse when both topgate voltages V_{tg1} and V_{tg2} are tuned independently at $V_{\mathrm{bg}} = -5\,\mathrm{V}$ and d) $V_{\mathrm{bg}} = +5\,\mathrm{V}$. All measurements were performed at 38 K.

Under constant illumination of 148 GHz and a nominal power of $-5\,\mathrm{dBm}$, the topgate voltage dependency is shown for three different global doping conditions in figure 4.53 a). At $V_{\mathrm{bg}} = 0\,\mathrm{V}$, the photocurrent exhibits an abrupt sign change at the (local) CNP of $V_{\mathrm{tg}} = -0.08\,\mathrm{V}$, similar to previous reports and to the behavior of detector A.[39–41] This sign change can be tuned by the global backgate voltage. A maximum signal of $I_{\mathrm{ph}} = 0.68\,\mathrm{nA}$ is observed when the device operates close to the local CNP. The photoresponse is mapped as a function of V_{bg} and V_{tg}, as shown in figure 4.53 b). The arrows at the upper boundary box indicate the positions of the single measurements depicted in figure 4.53 a). The measurement reflects the transport behavior observed in figure 4.52 c). However, instead of a four-fold pattern, a five- or six-fold pattern can be identified, which has been reported by other studies.[41,128] A strong photoresponse is

observed at the boundaries between the four pn, nn, pp and np regions identified in figure 4.52 d). The strongest response is detected at the transition from the np to the nn regime which corresponds to the measurement at $+5\,\mathrm{V}$ (blue line) in figure 4.53 a). The rectified THz signal is generally maximized by tuning the global charge carrier density completely into either the electron or hole regime and then performing a topgate sweep across the CNP.

Figures 4.53 c) and d) illustrate the response of I_{ph} when both topgates are tuned separately at extreme global p- and n-doping, respectively. The largest signal is detected at the transition between doping regimes. As V_{bg} is tuned from $-5\,\mathrm{V}$ to $+5\,\mathrm{V}$, the photoresponse is almost completely inverted. Meanwhile, I_{ph} reaches its maximum in figure 4.53 c) as np transitions to nn under global n-doping. This translates to maximum sensitivity when the majority of the graphene is electron-doped and only a small fraction is hole-doped.

The photoresponse observed in these detector architectures is often discussed in terms of a mixture of different underlying mechanisms. As presented in chapter 2.3.2, the metallic asymmetric dual-grating gates are fundamental for the THz rectification process. They act as both a grating coupler to conserve momentum and as additional gates that generate an asymmetric charge carrier density distribution along the graphene channel that enhances rectification effects. Two plasmonic THz rectification effects are typically present in ADGG GTeraFETs: the plasmonic drag effect and the electron-hole ratchet effect.[291] The plasmonic drag effect originates from the interaction of THz-induced plasmonic oscillations and charge carriers and is dominant for the photoresponse in a nn^{+} modulated system. However, it acts only a small length scale and is very sensitive to the carrier mobility. Hence, we expect the electron-hole ratchet effect to be dominant for our device due to the rather long graphene channel and the moderate mobility. In addition, the observed photoresponse reaches its maximum when discrete pn-junctions are formed in the graphene channel. This is in good agreement with the electron-hole ratchet effect, which is proportional to the density and mobility of each carrier type and results in a net drift of electrons *or* holes in one direction.

The majority of experimental reports on THz detection in graphene address resistive self mixing (RSM) and the photo-thermoelectric (PTE) effect as dominating contribution to I_{ph}. Based on the theoretical framework by Dyakonov and Shur,[122] RSM occurs due to nonlinear self-gating effects in the ADGG GTeraFET induced by the THz electric field.[41,128] Our measurements here were carried out in the low sub-THz and overdamped plasma wave regime, given the scattering time $\tau \sim 150\,\mathrm{fs}$ for $150\,\mathrm{GHz}$ as the incident frequency ω, resulting in the quality factor $Q = \omega\tau \ll 1$. The theoretically expected photovoltage V_{ph} is related to the photocurrent I_{ph} via the Drude model and is given by[129,292]

$$V_{\mathrm{ph}} = RI_{\mathrm{ph}} = -\frac{1}{\sigma}\left(\frac{d\sigma}{dV_{\mathrm{tg}}}\right), \tag{4.15}$$

with the two-terminal conductance σ. Our observed response of I_{ph} to the applied topgate voltage in figure 4.53 a) is generally in good agreement with the RSM model and previous reports.[39,128] A telltale sign is the increasing signal upon approaching the CNP before changing its sign and approaching zero towards high positive topgate voltages.

However, also the PTE effect contributes significantly to the overall photoresponse.[128] The PTE effect arises from the local heating of charge carriers by the incident radiation, which are only very weakly thermally coupled to the crystal lattice in graphene.[53,54] Consequently, the thermal diffusion process of hot carriers to the cold metallic contacts generates in a measurable photovoltage. This photoresponse is sensitive to the charge carrier type and density. Thus, in graphene with pn-junctions, the PTE effect can result in a photovoltage V_{PTE} that is given by[290]

$$V_{\text{PTE}} = \Delta T(S_2 - S_1), \tag{4.16}$$

and depends on the temperature difference ΔT and the Seebeck coefficients S_1 and S_2 of the gated and ungated regions of graphene, respectively. According to the Mott formula, the Seebeck coefficient can be calculated by[290,293]

$$S(V_{\text{tg}}) = -\frac{\pi^2 k_{\text{b}} T}{3e} \frac{\partial ln(\sigma(V_{\text{tg}}))}{\partial V_{\text{tg}}} \frac{\partial V_{\text{tg}}}{\partial E_{\text{F}}}. \tag{4.17}$$

A quantitative analysis of the detected photoresponse by fitting the data with a model that combines contributions from RSM and the PTE effect is complex and beyond the intended scope of this chapter and will be left for future studies. However, we can interpret the contribution of the PTE effect to the rectified I_{ph} qualitatively, e.g., by studying the saturating current towards large topgate voltages. For a globally p-doped graphene channel ($V_{\text{bg}} = -5\,\text{V}$), a PTE contribution occurs at pn-junctions (formed at the boundary between the p-doped graphene and the n-doped contact regions), yielding a finite I_{ph} that does not approach zero.[39] When the graphene channel is strongly n-doped ($V_{\text{bg}} = +5\,\text{V}$), these pn-junctions are absent and the current approaches zero. However, when V_{tg} induces locally p-doped regions in the otherwise completely $n-$doped graphene channel, the doping profile is abrupt and well defined, resulting in a maximized photoresponse.

Although the obtained photoresponse is generally composed of a mixture of different mechanisms, in particular of RSM and PTE effect contributions, we expect a different temperature and frequency dependence for both effects. The RSM contribution increases with lower temperatures and is expected to be sensitive to the incident frequency.[39,128] The PTE effect depends mostly on the radiation-induced temperature difference ΔT, which can be high even for elevated temperatures.[40,41,128,290] Additionally, the PTE effect occurs on a broadband frequency scale and is mostly sensitive to the incident radiation power instead of frequency.

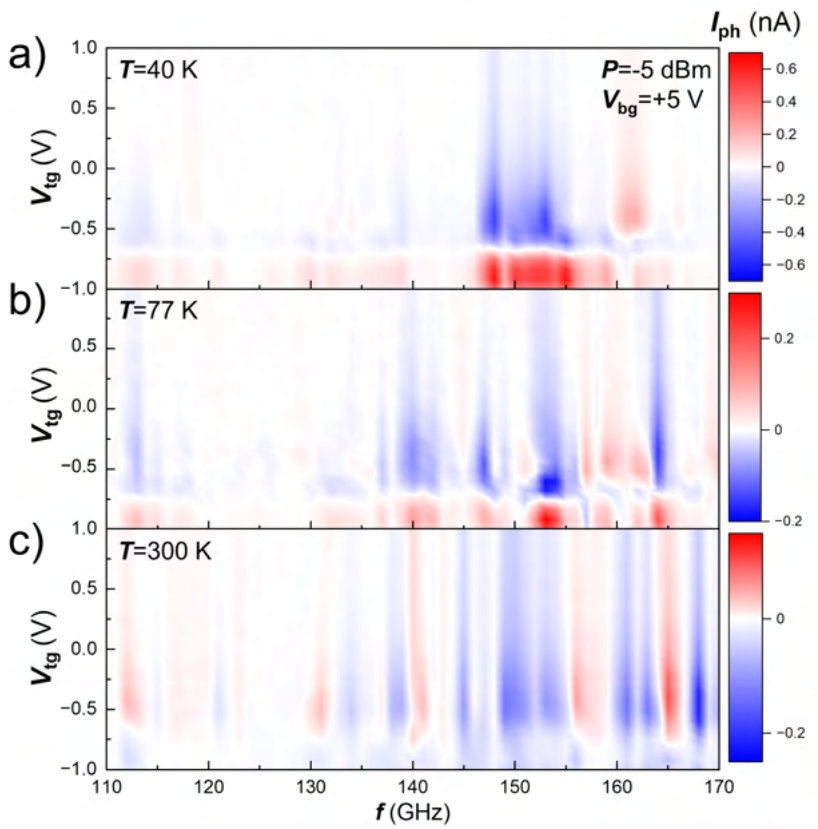

Figure 4.54.: Measured photocurrent I_{ph} at detector B as a function of frequency and topgate voltage for a) 40 K, b) 77 K and c) 300 K. At 40 K, the maximum photoresponse is confined to a range of 152 ± 5 GHz, which is weakened and broadened as the temperature is increased. All measurements were performed at $V_{\mathrm{bg}} = +5$ V and a nominal power of -5 dBm.

Hence, frequency and temperature dependent measurements were carried out, as shown in figure 4.54. At $V_{\mathrm{bg}} = +5$ V, a nominal power of -5 dBm and a temperature of ~ 40 K, the photocurrent shown in figure 4.54 a) exhibits a strong signal as a function of V_{tg} around 150 GHz. This maximum photoresponse is confined to a range of ± 5 GHz. When the temperature is increased to 77 K, as shown in figure 4.54 b), the signal intensity decreases and the range of frequencies with a stronger photoresponse is broadened to ± 15 GHz. The measurement depicted in 4.54 c) was performed at room temperature and shows an even smaller maximum I_{ph}. Moreover, the maximum photoresponse which was previously confined to a small frequency range is now washed out over a wide spectrum. We interpret the observed temperature and frequency dependency of the photoresponse to the presence of a RSM-dominated regime around 150 GHz at low temperatures. As the temperature approaches 300 K, the RSM contribution vanishes, resulting in a significant decrease in I_{ph}, while the PTE effect persists on a broad frequency range.

The performance of our ADGG GTeraFETs can be evaluated by calculating the current re-

Device	μ (cm^2/Vs)	R_{ch} (Ω)	S (pA)	R_I (mA/W)	NEP (pW/Hz$^{1/2}$)
Detector A	2700	3500	23	0.495 [312]	1564 [2.5]
Detector B	14100	1100	655	46 [29100]	30 [0.05]

Table 4.2.: Overview of relevant figures of merit to evaluate the detector performance. The values are calculated for two possible output power scenarios (0.316 mW and [0.5 µW]), the low power case is given in brackets.

sponsivity R_I and the noise-equivalent power (NEP) of the individual detectors. Although optimizing the detector performance was not the primary focus of this project, the relevant figures of merits can be useful to compare our devices to other detectors and technologies.[40,41,128] As presented in section 2.3.2, the current responsivity can be determined from the maximum measured THz-signal S by[40]

$$R_I = \frac{\pi}{\sqrt{2}} \frac{S}{P} \frac{S_{\text{T}}}{S_{\text{D}}}, \tag{4.18}$$

with the power of the incident THz radiation P and the coupling efficiency of the THz-radiation $S_{\text{T}}/S_{\text{D}}$ that is given by the spot size S_{T} at the detector area S_{D}. According to the diffraction limit of radiation in the sub-THz-regime, $1\,\text{mm}^2$ is a good approximation for the beam spot size.[294] Note that the actual spot size is much larger since the beam is not focused. Using R_I, the channel resistance R_{ch} determined by Eq. 4.14 and the noise spectral density $N = \sqrt{4k_{\text{B}}TR_{\text{ch}}}$, the NEP of these graphene-based THz detectors can be determined with[40]

$$\text{NEP} = \frac{N}{R_I R_{\text{ch}}} = \frac{\sqrt{4k_{\text{B}}TR_{\text{ch}}}}{R_I R_{\text{ch}}}. \tag{4.19}$$

By performing power sensitive measurements with a pyroelectric detector, we were able to estimate the effective power output of the utilized source module to be only ~ 0.5 µW, which is roughly three orders of magnitude lower than the nominal value of $P = -5$ dBm ≈ 0.316 mW. The power level remained approximately constant over the entire frequency range and a range of values was estimated for the resulting R_I and NEP in table 4.2 by assuming two possible output power scenarios.

Finally, the estimated values for the NEP of detector A and B range between $1564\,\text{pW/Hz}^{1/2}$ and $30\,\text{pW/Hz}^{1/2}$ [$2.5\,\text{pW/Hz}^{1/2}$ and $0.05\,\text{pW/Hz}^{1/2}$], respectively. This sensitivity is similar to reports on comparable ADGG GTeraFETs[40,128,131] and is the first successful step towards tunable ultrahigh sensitivity detectors in the future. However, we acknowledge the room for possible errors in this estimation given the uncertainties about the output power of our THz-source and the current experimental setup. Further detector improvements such as graphite backgates,[40] enhanced radiation-coupling via bowtie-antennas[133] or tunable acoustic-grating couplers[135] seem feasible.

5. Summary and Outlook

In this thesis various complex graphene devices were engineered by combining vdW materials, microwave circuits, and metallic or superconducting electrodes in different configurations. These hybrid architectures provide a versatile platform to investigate charge carrier transport in graphene under electromagnetic radiation ranging from the radio-frequency to the terahertz domain.

Technological challenges and solutions encountered during the fabrication of these hybrid circuits were presented in chapter 3. Details on the processing of vdW materials, superconducting nanostructures and, in particular, electrical contacts emphasize the advancements in device fabrication. A description of the design and patterning of microwave circuits is included as well as an overview of different measurement procedures.

In an effort to maximize the hyperfine interaction between electron spins and nuclear spins, isotopically enriched ^{13}C graphene was investigated by low temperature magnetotransport, ESR and NMR experiments, as shown in chapter 4.1. While the absence of clear nuclear magnetic resonances confirms the weak character the hyperfine interaction in graphene, the data analysis reveals signatures of nuclear effects acting on the electron spin dynamics. Additionally, unexpected resistance anomalies at low magnetic fields were observed for polycrystalline MBE-grown and exfoliated ^{13}C few-layer graphene and are attributed to nuclear spin ordering effects. Our findings consistently point towards dynamic nuclear polarization processes that generate a nuclear magnetic field in the order of $\sim 20\,\mathrm{mT}$.[19,50]

Microwave spectroscopy was addressed in chapter 4.2 with hybrid circuits which integrate graphene with metallic contacts into high-frequency waveguides to enhance the coupling efficiency. Fabricating devices with large-area graphene coupled to CPWs without electrical shorts was a technological challenge. The transition to high-quality exfoliated graphene heterostructures addressed fundamental fabrication issues and enabled the study of devices with varying transmission line coupling techniques. However, the absence of resonances in our ESR measurements indicates that the mechanism required for efficient ESR might be missing in pristine graphene compared to the previously studied large-area graphene. Solving this puzzle might reveal new insights to the fundamental physics of graphene.

Graphene-based JJs have been investigated in chapter 4.3. First, the low-temperature characterization of a GJJ bolometer from an external collaborator[36] revealed Fabry-Pérot oscilla-

tions emerging from ballistic transport across the junction. SdH oscillations and signatures of a Fraunhofer pattern were observed by applying a magnetic field. The resonance frequency of the device could be determined at $\sim 8.73\,\mathrm{GHz}$, however, it was not possible to combine high-frequency and DC measurements in the scope of this thesis due to space limitations of the cryogenic setups. Our findings are the first step towards the exploration of dark matter axions with novel vdW-based devices in this group.

The in-house fabrication of Nb and NbN GJJs, faced challenges associated with the RF sputter deposition process of superconducting thin films.[49] Although technological solutions were identified and high-quality Nb and NbN thin films with excellent critical temperatures were achieved, obtaining GJJs with sufficiently high contact transparency remains an unsolved issue. Superconducting Ti/Al/Ti-electrodes, on the other hand, displayed significantly improved junction properties. The characterization of three aluminum graphene junctions showed proximity-induced superconductivity and diamond-shaped interference features under magnetic fields that can be attributed to Tomasch and McMillan-Rowell oscillations. Interestingly, these diamond-features appear on two different energy scales for two of the devices, which may correspond to the purity of the superconducting electrodes and requires further investigation. Although, it was not possible to combine functional GJJs and superconducting resonators in the scope of this thesis, the characterization of superconducting microstrip resonators at mK-temperatures shows that the integration of graphene devices into superconducting microwave circuits is feasible and in reach. Improvements to the existing PVD depositions chambers, e.g., optimization of the vacuum conditions, are expected to enhance the contact transparency of graphene junctions significantly for the next generation of devices.

Experimental results of sub-THz detectors based on large-area and exfoliated graphene and equipped with asymmetric dual-grating gates were presented in section 4.4. After different doping regimes have been identified by transport measurements, the photoresponse of these GTeraFETs was evaluated as a function of doping, frequency and temperature. The strongest signal was detected at the transition from the np to the nn doping regime in the graphene channel. While the contribution of resistive self mixing to the rectified photocurrent seems to vanish with increasing temperature, the photo-thermoelectric effect appears to persist up to room temperature.[41,128] The sensitivity of our graphene-based sub-THz detectors is competitive with other reports and was estimated to be in the range of $\sim 10^{-12}\,\mathrm{W/Hz^{1/2}}$.[40,124]

The experimental results in this thesis were enabled by major advances in device processing technology, such as the reliable fabrication of high-quality graphene heterostructures. The established fabrication processes of graphene devices, superconducting thin films and microwave circuits represent the foundation for GJJs, superconducting resonators and THz detectors, as illustrated in the diagram in figure 5.1. This thesis has demonstrated the potential for hybridizing

these versatile fields for the exploration of physical phenomena and applications. For example, GJJs coupled to superconducting microwave resonators can act as single-photon detectors (SPDs) and Josephson parametric amplifiers (JPAs) operating at the quantum noise limit.[33–36]

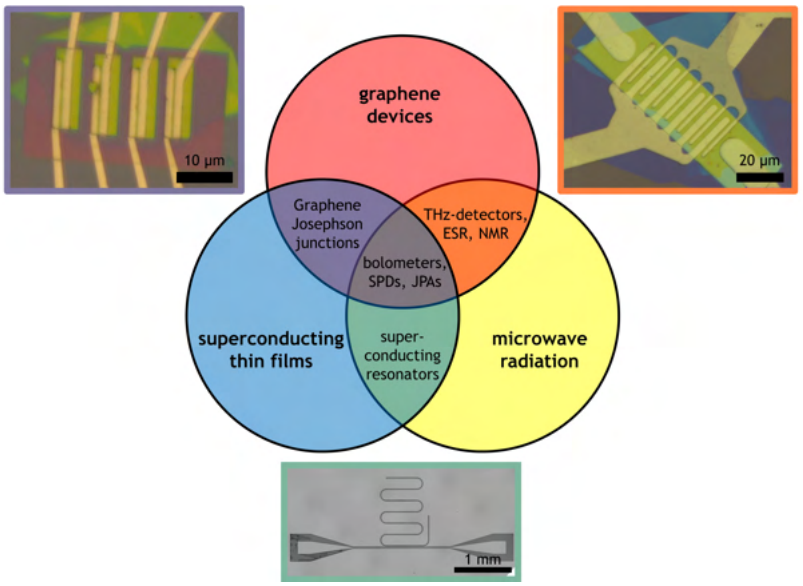

Figure 5.1.: Schematic diagram illustrating the interconnections between the various fields of research on graphene devices, superconducting thin films and microwave radiation. The optical images show aluminum GJJs (left), a graphene-based THz detector (right) and a superconducting microwave resonator (bottom) from this thesis.

With these fundamental tools at hand, the fabrication and study of even more complex systems such as twisted bilayer graphene (TBG) are possible. Preliminary tests on the (AFM-tip) cutting and stacking of graphene layers show promising results. The combination of the rich phase diagram of 2D TBG with conventional 3D superconductors could shed light on its moiré physics.[295] Recent reports investigated the thermal properties of MATBG and demonstrated single-photon detection in the infrared,[119,120] hence, it would be interesting to study its sensitivity to microwave photons with the technologies developed in this thesis.

Reliable heterostructure fabrication can now be utilized to incorporate also other vdW materials, such as WSe_2, which has been reported to stabilize superconducting phases in TBG and *untwisted* Bernal bilayer graphene.[296–298] The gate tunable phases in these systems revealed insulating and superconducting phases that are stabilized by the sizeable spin-orbit coupling of WSe_2. A recent theoretical studies predicts that gate-defined Josephson junctions in Bernal bilayer graphene/WSe_2 structures, prepared similar to those in MATBG,[92–94] could form Majorana zero-energy modes and thus topologically protected JJs.[299] If such gate-defined JJs in Bernal bilayer graphene/WSe_2 can be realized, microwave spectroscopy would be the key to study the junction properties.

The role of nuclear effects in superconducting graphene devices is an unexplored aspect that may influence quasiparticle dynamics, pairing or decoherence and warrants experimental investigation. The nuclear magnetic field B_{N} depends on the nuclear spin polarization and is estimated to be in the range of several milliteslas, based on the results obtained on ^{13}C graphene in this thesis. Depending on the size of B_{N}, superconducting transport across a junction could be significantly affected or even quenched. Hence, in a ^{13}C graphene JJ, the hyperfine interaction may be used to control the superconducting state. Additionally, the preparation of ^{13}C MATBG would be interesting since the larger nuclear mass of ^{13}C modifies the electron-phonon interaction, potentially influencing the superconducting states in the system.

There exists an even wider spectrum of experimental possibilities when incorporating strain that can induce pseudomagnetic fields.[300] Theoretical predictions discuss a substantial influence of these pseudomagnetic fields on Josephson currents in graphene.[111,301,302] One elegant way to induce dynamic and periodic strain in graphene is via SAWs.[137,138] Device prototypes of SAWs coupled to GJJs (as shown in chapter 3.3.2, figure 3.27) suffered from poor contact transparency and require further optimization.

To conclude, the nanoscale engineering of hybrid architectures in this thesis enables the investigation of hyperfine, quantum interference, superconducting and photosensing phenomena in graphene by electromagnetic radiation across the microwave spectrum. Specifically tailored superconducting nanostructures, microwave circuits or asymmetric metallic gratings can access various physical regimes. When this versatile technological toolbox is applied to novel 2D material heterostructures, a plethora of fascinating phenomena become experimentally accessible.

A. Appendix

A.1. Fabrication Details

Edge contact fabrication

The fabrication of edge contacts to graphene devices is based on a RIE etching process, immediately followed by metal deposition. The RIE plasma etching recipe uses a combination of O_2/CHF_3 in a 1:10 ratio to etch exfoliated hBN-graphene heterostructures. The process is conducted at 3 Pa, 0 °C, 60 W RF power, 4 sccm O_2 and 40 sccm CHF_3, resulting in a etching rate of $\sim$ 30 nm/min. The edge profile of an etched hBN flake was measured by AFM, as depicted in figure A.1.

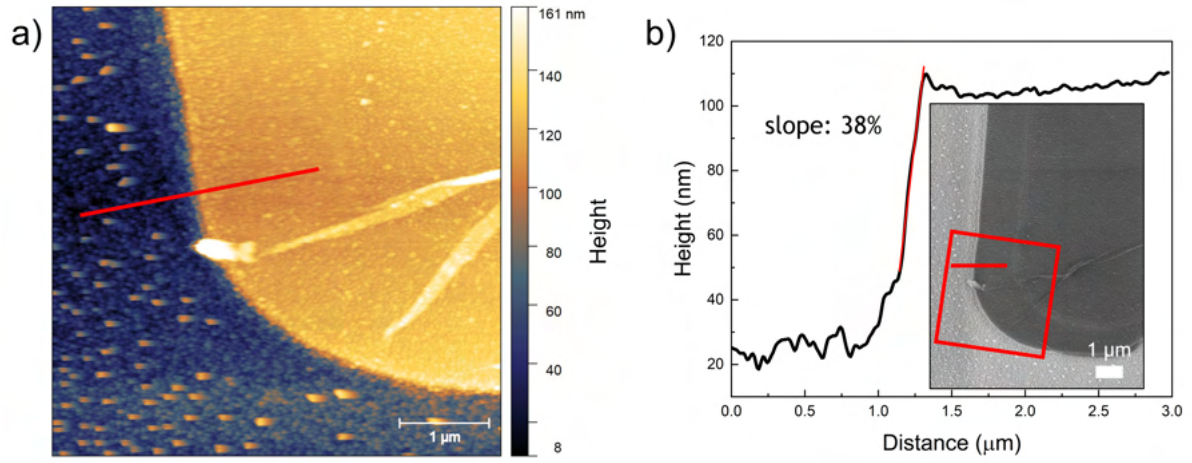

Figure A.1.: a) Atomic force microscope (AFM) image of a etched hBN flake. The red line indicates the position of the extracted profile. b) Height profile extracted along the red line in a). The slope extracted from a linear fit to the edge profile corresponds to a value of 38 %. The inset shows a scanning electron microscopy (SEM) image of the same structure, where the AFM measurements are indicated by the red shapes.

The etch profile (figure A.1 b)), extracted from the red line in figure A.1 a), shows a slope of 38 %. This is close to the reported value by Wang *et al.*[66] and confirms that the etching recipe works as intended.

A.2. Extended Data

Resistance anomalies in ^{13}C graphene at low magnetic fields

The resistance anomalies observed in MBE-grown ^{13}C few-layer graphene samples are microwave frequency independent as shown in figure A.2 a). The magnetic field position of both steps does not shift with frequency. The different appearance for different frequencies is related to varying effective power levels due to frequency-dependent attenuation in the setup.

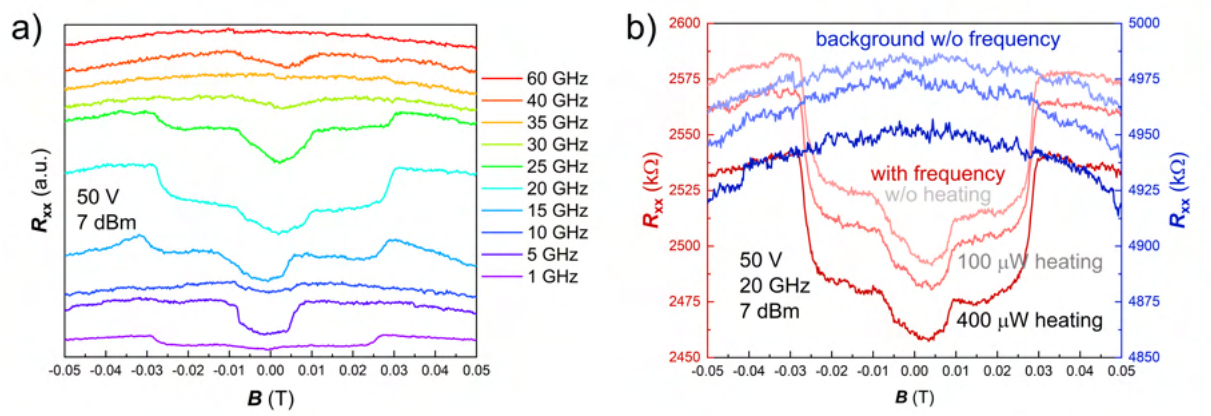

Figure A.2.: a) The magnetic field position of the two steps around 0 T in MBE-grown ^{13}C few-layer graphene appear only under microwave illumination but are frequency independent. b) Comparison of measurements with microwave radiation (red) and without (blue) for different heating powers (lighter to darker colors). The two step features neither appear for higher temperatures in the measurement without microwaves, nor disappear in the measurements with microwave radiation.

To exclude simple heating effect as the origin of the effect, figure A.2 b) compares measurements with microwave radiation (red) and without (blue) for different heater powers. A heating power of 100 µW and 400 µW corresponds to a measured temperature T_{sens} of 93 mK and 190 mK, respectively. The measurements without radiation show reduced resistance at higher heating power and higher temperature, but step-like features are not observed. Measurements under microwave radiation exhibit both steps even for increasing temperatures. Even if the temperature is increased to $\approx$ 500 mK (2000 µW heating power), the resistance still does not show any steps around zero field.

The measured sensor temperature T_{sens} is compared to the effective electron temperature T_{e} and the sample resistance R_{xx} as a function of the applied microwave power in figure A.3. Here, the microwave power is plotted in units of dBm in figure A.3 a) and in units of milliwatt (mW) in figure A.3 b). We use the results from previous temperature-dependent heated measurements to reference sample resistance and T_{e}.

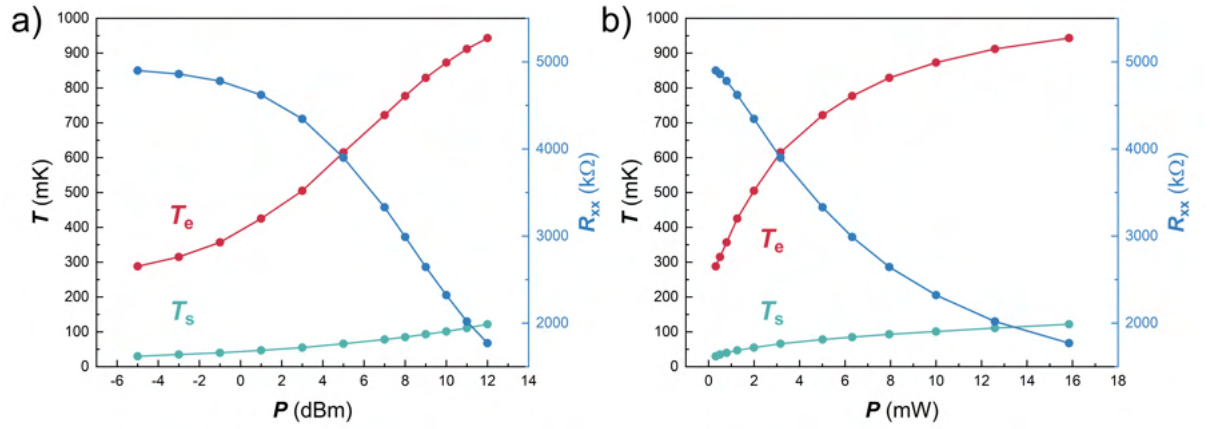

Figure A.3.: The measured sensor temperature T_{sens} is compared to the effective electron temperature T_{e} and the sample resistance R_{xx} as a function of the applied microwave power in units of a) dBm and b) milliwatt (mW).

Microwave circuits with exfoliated graphene

In section 4.2.2, electron spin resonance experiments on exfoliated graphene heterostructures using high-frequency waveguides are presented. Since a significant ESR can not be detected in resistively-detected measurements by sweeping the magnetic field under constant microwave irradiation, different approaches were used. The measurements presented here exemplary show frequency-swept ESR measurements conducted on the sample shown in figure 4.18 a). Figures A.4 a) and b) show the resistance under microwave radiation in a range between a) $13.5\,\mathrm{GHz}$ to $15\,\mathrm{GHz}$ and b) $22\,\mathrm{GHz}$ to $25.5\,\mathrm{GHz}$ at constant magnetic field values of $0.5\,\mathrm{T}$, $0.51\,\mathrm{T}$ and $0.9\,\mathrm{T}$, as indicated by the colors.

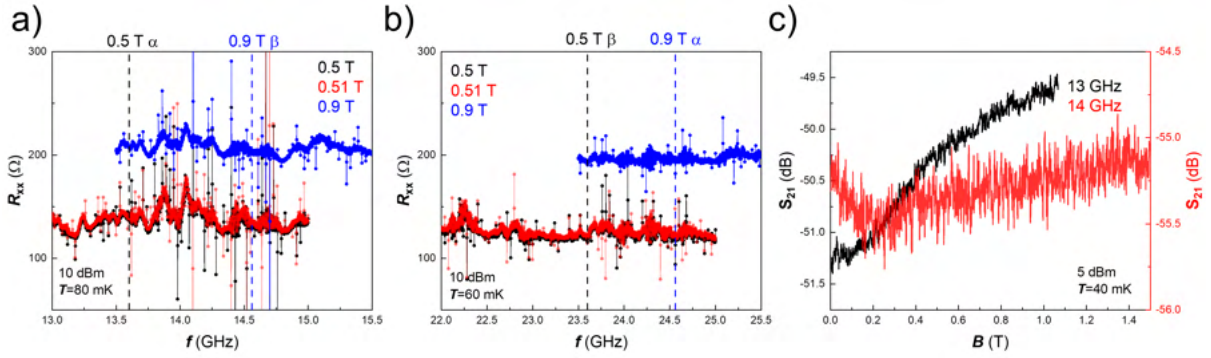

Figure A.4.: The measured sensor temperature T_{sens} is compared to the effective electron temperature T_{e} and the sample resistance R_{xx} as a function of the applied microwave power in units of a) dBm and b) milliwatt (mW).

These frequency-swept measurements exhibit significantly more noise compared to standard ESR measurements, which are based on magnetic field sweeps. Additionally, the radiation induced heating depends on the frequency-dependent attenuation of the high-frequency coaxial

lines of the setup. The effective power and consequently also the sample temperature changes as the frequency is varied. This is reflected by the resistance oscillations shown in figure A.4 a) and b). The dashed lines indicate the expected resonance frequencies for the α and β resonances at different magnetic fields. While the measurements at $0.5\,\mathrm{T}$ and $0.51\,\mathrm{T}$ overlap, the resistance is increased for $0.9\,\mathrm{T}$ due to the expected increase in magnetoresistance. However, no resonances can be identified for these measurements.

Similar to other microwave circuits equipped with graphene, transmission-based ESR measurements were also performed for this sample. Two exemplary measurements are shown in figure A.4 c). The microwave transmission S_{21} exhibits a magnetic field dependence with a minimum that shifts in position, depending on the applied frequency. It is unclear if this signal corresponds to resonance effects in the graphene or is the results from artifacts in the experimental setup.

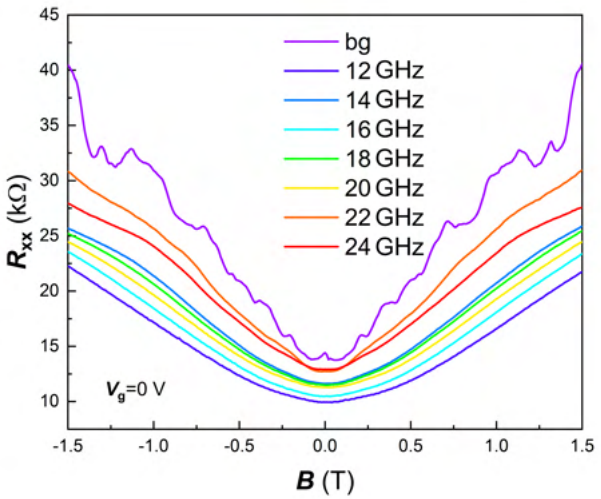

Figure A.5.: Resistively-detected ESR measurements of an exfoliated ^{13}C graphene device at $10\,\mathrm{dBm}$ power and various constant microwave frequencies.

Figure A.5 shows results of electron spin resonance experiments with microwave radiation coupled via a waveguide to an exfoliated ^{13}C few-layer graphene device. Compared to the background measurement (purple line), a significant decrease of the resistance is observed when various microwave frequencies are applied. This is attributed to radiation-induced heating effects. However, resonant features are absent in these measurements.

Graphene-based Josephson junction microwave bolometer

The electrical transport of a graphene-based JJ bolometer[36] was characterized at low temperatures. Figure A.6 a) shows a gate sweep, with the CNP of the graphene located at $\sim 0.2\,\mathrm{V}$.

Separate fits to the resistance around the CNP for the electron and hole regime according to Eq. 4.14 can be used to extract relevant parameters such as the contact resistance R_c, the residual charge carrier density n^* and the mobility μ. Note that a gate dielectric of 40 nm Al_2O_3 was assumed. However, the fits do not match the resistance curve well. Hence, R_c and n^* can not be determined accurately. The mobility μ is approximately in the order of 10^5 cm^2/Vs.

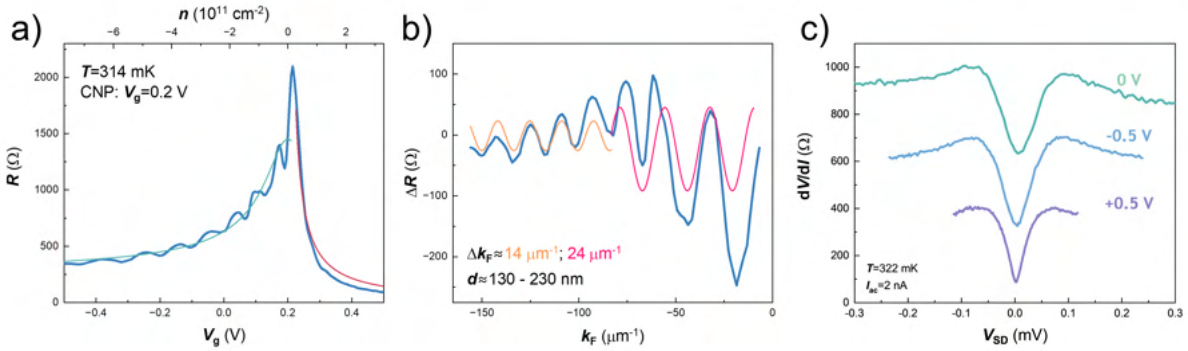

Figure A.6.: a) Resistance (blue line) as a function of gate voltage V_g, i.e., density, at 314 mK. The fits to the resistance in the electron (green line) and hole regime (red line) did not converge with high accuracy, but yield a mobility of $\mu \approx 10^5$ cm^2/Vs. b) After subtracting a slowly varying background from the resistance in a), the Fabry-Pérot (FP) oscillation period Δk_F yields an effective junction length $d = 130-230$ nm. c) Differential resistance $\mathrm{d}V/\mathrm{d}I$ of the GJJ as a function of DC source-drain voltage V_{SD} for three different gate voltages.

Fabry-Pérot (FP) resistance oscillations in the hole regime are analyzed by subtracting a slowly varying background and extracting the Fabry-Pérot oscillation period Δk_F, which yields an effective junction length in the range of $d = 130 - 230$ nm, as explained in the main text. It is unclear whether the two different FP oscillation periods (orange and pink sine functions) in figure A.6 b) result from inhomogeneity in the sample.

The differential resistance of the GJJ is plotted as a function of DC source-drain voltage V_{SD} in figure A.6 c) for three different gate voltages. The junction transitions at $\sim \pm 80\,\mu$V to the normal state. This value corresponds to an induced superconducting gap of $\Delta_{ind} \approx 80\,\mu$eV. This value is much lower than expected for common superconductors such as Al or Nb and indicates a thermally induced reduction of the superconducting gap.

The cryogenic ^{3}He setup that was used to perform low temperature characterization measurements was initially planned to accommodate all necessary microwave components to reproduce microwave photon detection experiments.[36] A schematic diagram of the required connections and components at different temperature stages of the cryostat is given in figure A.7 a). Lines in black are DC lines for the readout of the GJJ, the blue line is the DC line for electrostatic gate control and the red lines can be used to apply high-frequency signals to the GJJ bolometer device via a directional coupler. Note that all lines are high-frequency coaxial lines, even the

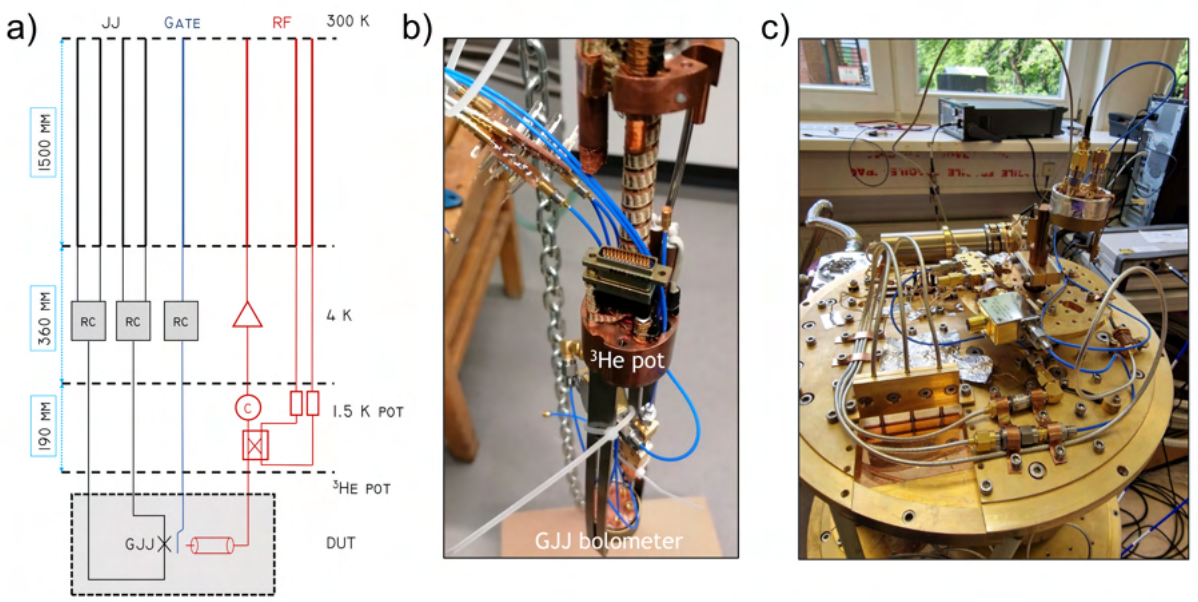

Figure A.7.: a) Schematic diagram of the intended cryogenic ^{3}He setup including all lines and components at different temperature stages for DC and high-frequency characterization of the GJJ bolometer. b) Image of the ^{3}He insert that exemplifies the limited space available. c) Cryogenic setup at the group of Prof. Horns. This setup had enough space to accommodate all high-frequency components and was used to determine the resonance frequency of the GJJ bolometer device.

DC lines, which results in better shielding.

However, during the installation of the components, we faced multiple challenges and issues which could not be resolved completely. For instance, the ^{3}He insert of the intended cryostat has only very limited space, as shown in figure A.7 b). Not all components could fit into the space without causing a big thermal short to the insert shielding or between the 1.5 K pot and the ^{3}He pot. This would elevate the sample temperature from 300 mK to 1.5 K and higher, reducing the sensitivity of the device. Hence, only DC lines with RC-filters could be installed for transport characterization experiments, without the high-frequency components.

In order to assess the resonance frequency of the GJJ bolometer at low temperatures, the device was installed in a cryogenic setup of the Horns group, which has much more space to accommodate all necessary cables and components, as shown in figure A.7 c). This cryostat operates at 4 K and can go to 120 mK for short periods of time by adiabatic demagnetization. Unfortunately, this setup could not be equipped to perform simultaneous DC readout of the GJJ and only high-frequency measurements were carried out.

Characterization of graphene Josephson junctions

Device A

Microwave power dependent measurements were repeated at different frequencies to probe the AC Josephson effect in the first GJJ with superconducting aluminum electrodes (device A). The differential resistance $\mathrm{d}V/\mathrm{d}I$ as a function of bias current I_{bias} and microwave power P is shown for different fixed microwave frequencies in figure A.8.

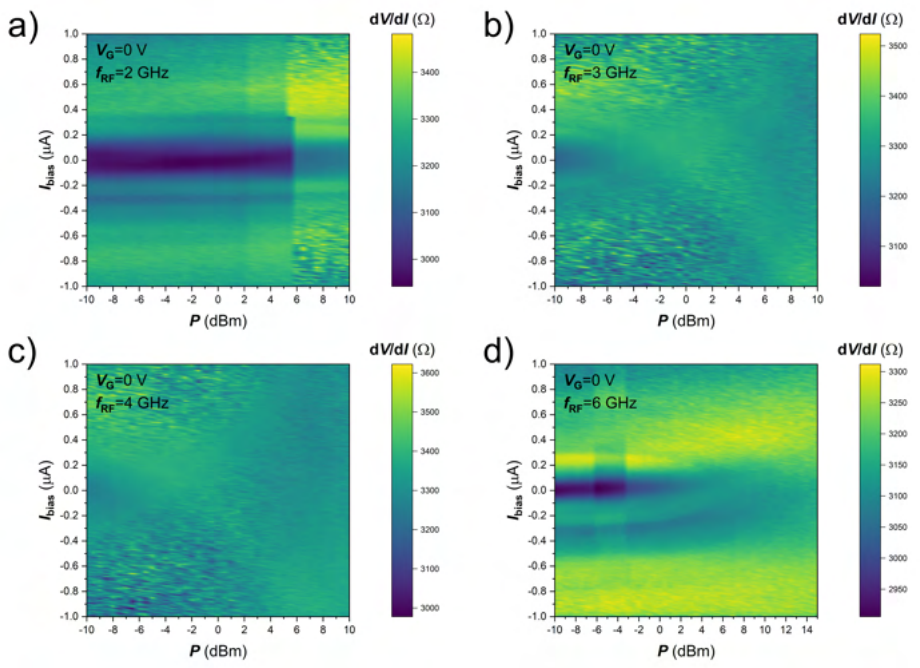

Figure A.8.: Differential resistance $\mathrm{d}V/\mathrm{d}I$ of device A as a function of bias current I_{bias} and microwave power P at $0\,\mathrm{V}$ gate voltage and a fixed frequency of a) $2\,\mathrm{GHz}$, b) $3\,\mathrm{GHz}$, c) $4\,\mathrm{GHz}$ and d) $6\,\mathrm{GHz}$. Vertical lines are artifacts that stem from resistance jumps due to the leaking backgate.

These measurements are impacted by the leaking backgate, which causes jumps in the resistance and adds a parasitic conduction channel. For the measurements in figure A.8 b) and c), the behavior of the junction is almost completely obscured by these artifacts. Still, the diverging features observed in figure 4.36 in the main text are faintly visible. This is not the case for the measurement at $2\,\mathrm{GHz}$ in figure A.8 a), where the behavior of the junction is mostly unaffected by the applied microwave power. In contrast, the measurement at $6\,\mathrm{GHz}$ exhibits a superconducting state that vanishes at $\sim 2\,\mathrm{dBm}$ power and additionally signs of diverging features towards higher microwave power. However, in none of the measurements well pronounced Shapiro steps could be observed, which is attributed mostly to insufficient junction transparency.

Device B

The dependence of $\mathrm{d}V/\mathrm{d}I$ on magnetic field and bias current of the second graphene device with superconducting aluminum electrodes (device B) was evaluated at different gate voltages. Figure A.9 a) plots the measured $\mathrm{d}V/\mathrm{d}I$ at the CNP ($\sim -18\,\mathrm{V}$); the calculated $\mathrm{d}^2V/\mathrm{d}I^2$ is depicted figure A.9 b). The resistance at the CNP is approximately 10 to 20 times higher, which results in an extremely sharp resistance peak at zero bias that dominates the overall signal. The diamond features can therefore not be resolved and are even absent in $\mathrm{d}^2V/\mathrm{d}I^2$ in figure A.9 b). Note that the diamond-features are observed for all other gate voltages.

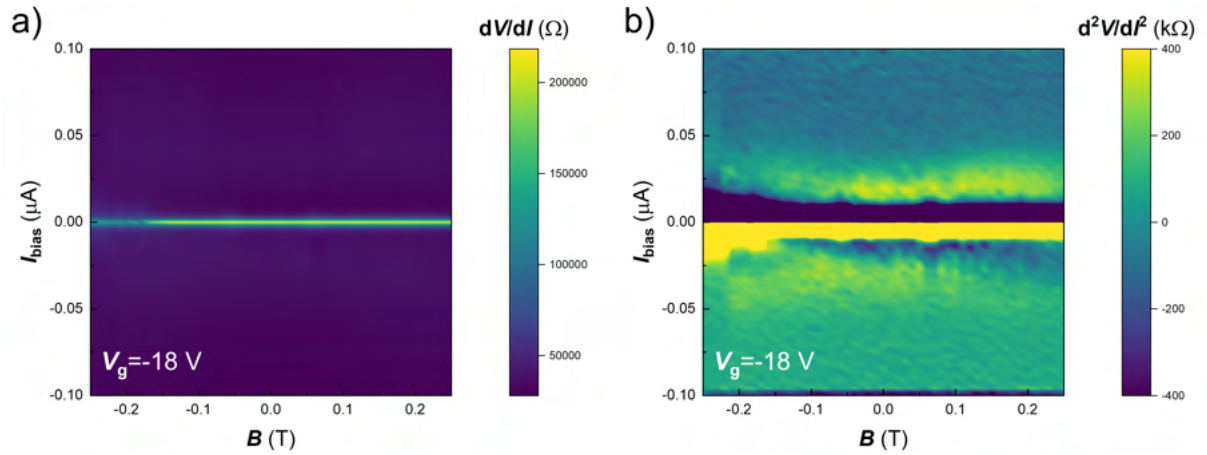

Figure A.9.: a) Measured $\mathrm{d}V/\mathrm{d}I$ and b) derived $\mathrm{d}^2V/\mathrm{d}I^2$ of device B as a function of magnetic field and bias current at the CNP ($\sim -18\,\mathrm{V}$) and 14 mK.

Measurements at various temperatures reveal a decreasing critical magnetic field B_c of the Al-film upon increasing temperature. Figure A.10 plots the extracted B_c values as a function of temperature. The temperature dependence of B_c can be fitted using Eq. 2.17.[102] The resulting fit is shown as the red solid line in figure A.10 and yields a critical temperature $T_\mathrm{c} = 547\,\mathrm{mK}$. Although the temperature dependence is expected to be parabolic,[102] the decrease in B_c can also be approximated by a simple linear fit (blue solid line). A linear decrease of B_c has been observed in previous reports on granular aluminum.[265–267] This extrapolation yields a slightly higher $T_\mathrm{c} \approx 640\,\mathrm{mK}$. Following BCS theory, the size of the induced superconducting gap can be inferred from these values via $\Delta = 1.76 k_\mathrm{B} T_\mathrm{c} = 83$ and $97\,\mu\mathrm{eV}$, respectively, which is much smaller than bulk Al.[269,270]

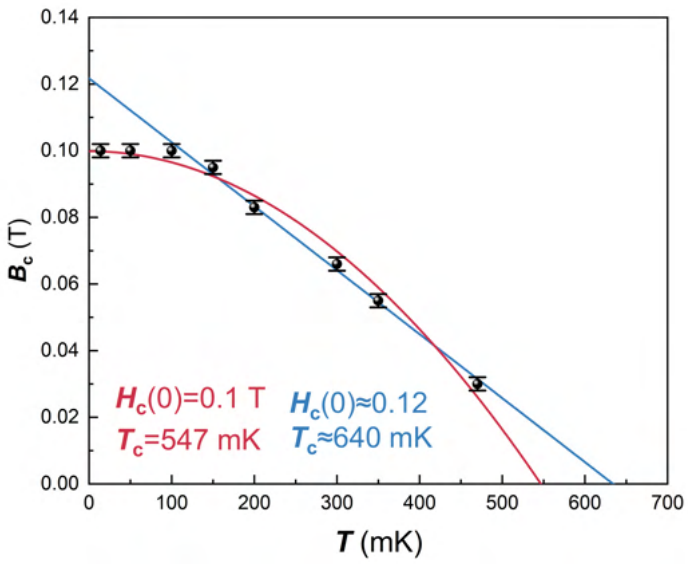

Figure A.10.: Temperature dependence of the critical magnetic field B_c of the Al-film extracted from the measurements shown in figure 4.40. The data can be fitted with Eq. 2.17 (red solid line) with $R^2 = 0.984$, yielding a $T_c = 547\,\text{mK}$. The decrease in B_c can also be approximated by a simple linear fit (blue solid line) with $R^2 = 0.995$, yielding a slightly higher $T_c \approx 640\,\text{mK}$.

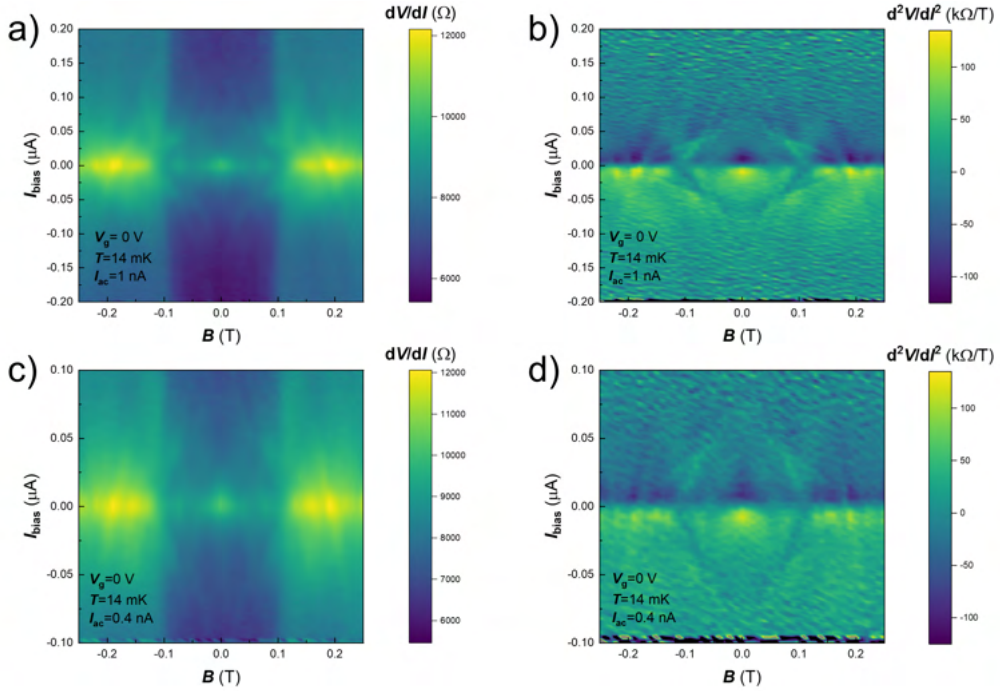

Figure A.11.: a) Measured $\mathrm{d}V/\mathrm{d}I$ and b) derived $\mathrm{d}^2V/\mathrm{d}I^2$ of device B as a function of magnetic field and higher bias current. c) Measured $\mathrm{d}V/\mathrm{d}I$ and d) derived $\mathrm{d}^2V/\mathrm{d}I^2$ with reduced AC current amplitude of $0.4\,\text{nA}$.

In order to resolve the evolution of the diverging diamond-features, a higher bias current was applied to the aluminum-graphene junction, as shown in figures A.11 a) and b). However, the signal vanishes in the resistive background as the noise increases drastically at values above $|0.1|\,\mu$A. Further evaluation of the signal by decreasing the AC current amplitude to $0.4\,$nA could not resolve the diamonds more clearly, as shown in figure A.11 c) and d). Instead, the signal-to-noise ratio worsens.

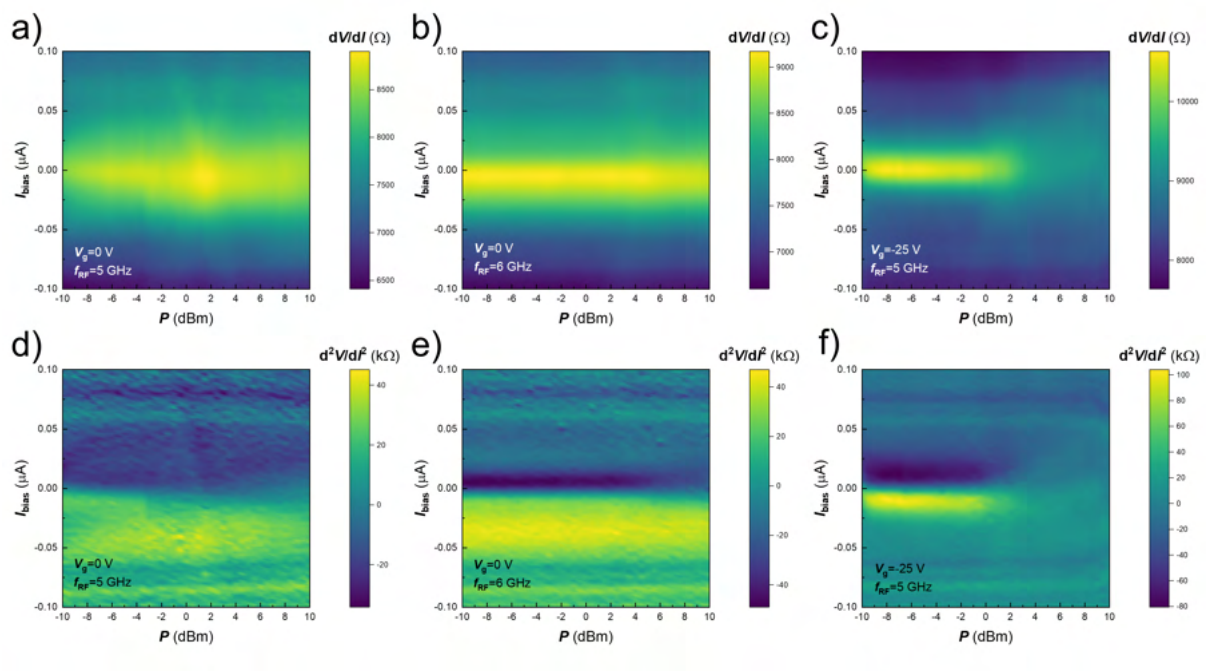

Figure A.12.: Measured $\mathrm{d}V/\mathrm{d}I$ and derived $\mathrm{d}^2V/\mathrm{d}I^2$ as a function of bias current I_{bias} and microwave power P at a), d) $0\,$V and $5\,$GHz, b), e) $0\,$V and $6\,$GHz and c), f) at $-25\,$V and $5\,$GHz. All measurements were performed at mK-temperatures.

Microwave power dependent measurements were performed via an open coaxial cable in close proximity to device B. However, this approach is very inefficient and results in lower effective power at the sample position. Measurements at different microwave frequencies and two different gate voltages are presented in figure A.12.

The increasing microwave power has no immediate effect on the observed features, probably due to insufficient coupling. Apart from the resistance maximum at zero bias current, two resistance maxima are observed $\pm 0.7\,\mu$A which are potentially connected to the previously observed diamond-features. Interestingly, a faint X-shaped features can be observed in the measurements at 5 GHz at around $2\,$dBm for both gate voltages. Such a crossing is not expected and should be studied in more detail in future studies.

Device C

Figure A.13 a) shows the differential resistance of JJ3 towards high bias currents up to $\pm 5\,\mu$A. Aside from the previously observed peaks, only increasing noise and no other resistance effects can be identified.

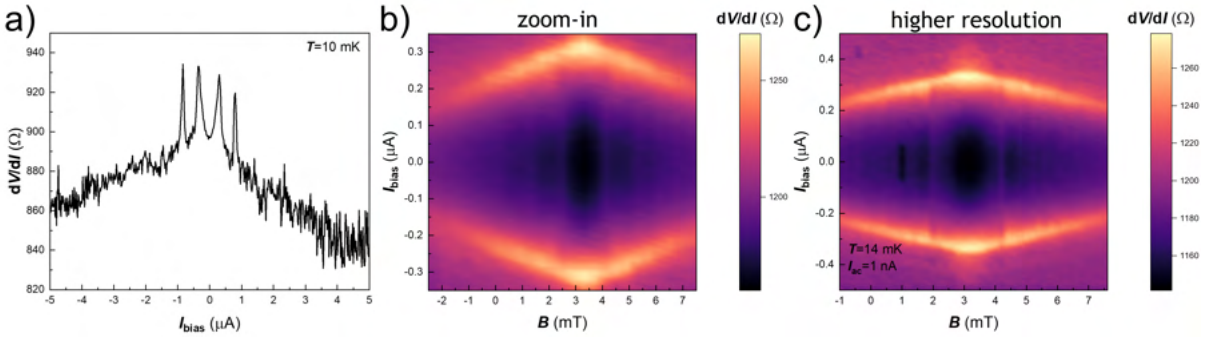

Figure A.13.: a) The differential resistance of JJ3 does not show any additional effects at high bias currents. b) Zoom-in on the original data from JJ1 in figure 4.42 a) showing of the low-field region in the $\mathrm{d}V/\mathrm{d}I$ map. The oscillations of the superconducting region inside this inner diamond-structure are reminiscent of a Fraunhofer pattern. c) Measurement of this region with higher resolution does not confirm the Fraunhofer pattern and is affected by artifacts that probably result from the resolution limit of the power supply.

Inside the first diamond-shaped structure of JJ1 in device C, a pattern can be observed that is reminiscent of a Fraunhofer pattern. Figure A.13 b) shows a magnified view of this region from the measurement depicted in figure 4.42 a) in the main text. Another measurement of this region with higher resolution is shown in figure A.13 c). However, this measurement is obscured by artifacts and does not confirm the Fraunhofer pattern, most likely to resolution limits of our magnetic field power supply. Additional with another power supply, such as a high-precision current source, could not be performed in the available time. Thus, it remains unclear if the observed oscillations of the superconducting state in JJ1 originate from flux quantization.

The DC source-drain voltage V_{SD} across the junctions in device C was measured simultaneously with the AC voltage. A representative measurement of V_{SD} as a function of bias current in JJ3 is depicted in figure A.14 a). The calculated differential resistance $\mathrm{d}V_{\mathrm{SD}}/\mathrm{d}I$ is in agreement with the differential resistance $\mathrm{d}V/\mathrm{d}I$ *measured* via lock-in detection, but exhibits significantly higher noise. Due to a large background resistance, V_{SD} does not show the zero-voltage state plateau expected for a JJ. Nevertheless, we observe the same resistance features in the magnetic field and bias current dependence for the calculated $\mathrm{d}V_{\mathrm{SD}}/\mathrm{d}I$, shown in figure A.14 b), compared to the measurements of $\mathrm{d}V/\mathrm{d}I$ shown in the main text. Note, that voltage-biased measurements could not be performed with sufficient signal-to-noise ratio. The V_{SD} voltage-

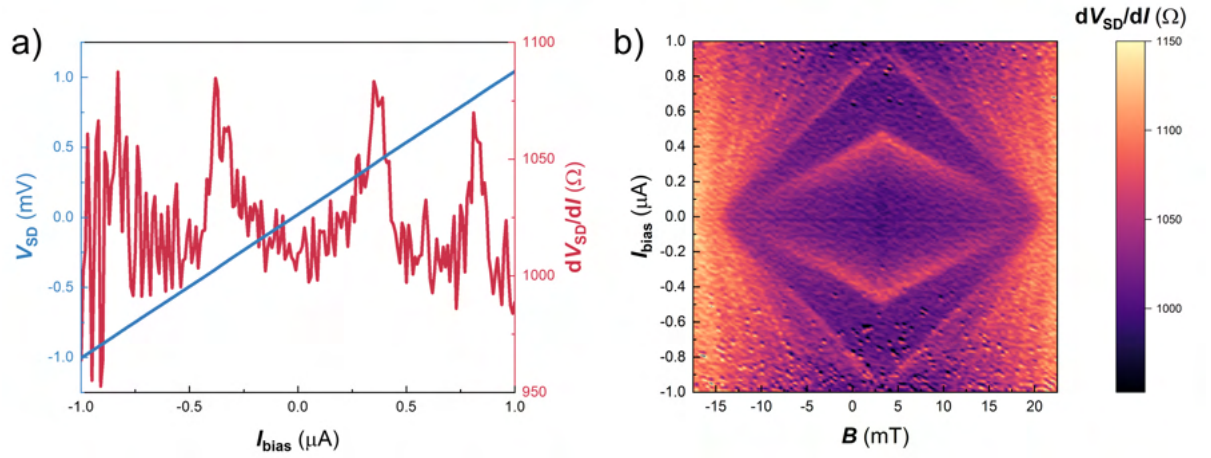

Figure A.14.: a) Exemplary measurement of the DC source-drain voltage V_{SD} (blue solid line) across the junctions in device C on JJ3 as a function of bias current. The derived $\mathrm{d}V_{\mathrm{SD}}/\mathrm{d}I$ is in agreement with the $\mathrm{d}V/\mathrm{d}I$ measured via lock-in detection. b) Magnetic field dependence of the $\mathrm{d}V_{\mathrm{SD}}/\mathrm{d}I$ as a function of bias current.

values of device C allow to extract the involved energies.

Microwave power dependent measurements were performed with the end of an open coaxial cable placed exactly above device C. As discussed above, this approach is inefficient and only a fraction of the electromagnetic radiation is actually coupled to the sample. Hence, it comes to no surprise that the measurements on JJ3 of device C at different microwave frequencies, shown in figure A.15, do not exhibit the expected Shapiro steps. Instead, the response in $\mathrm{d}V/\mathrm{d}I$ is purely due to microwave-induced heating effects.

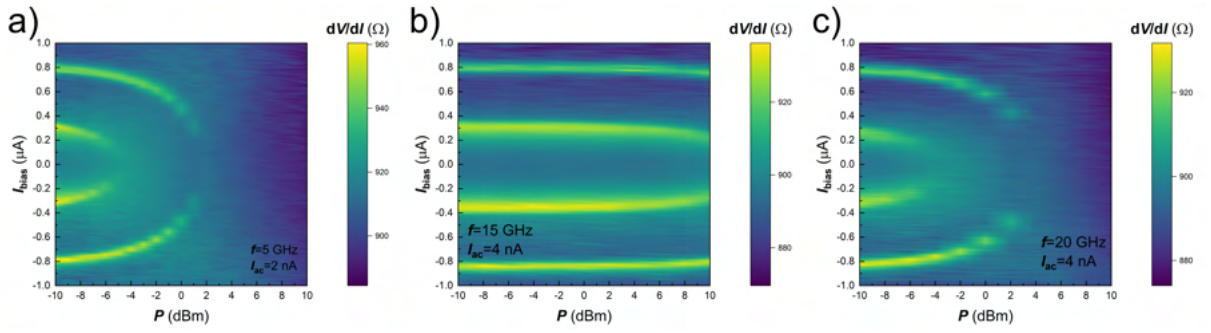

Figure A.15.: Differential resistance $\mathrm{d}V/\mathrm{d}I$ on JJ3 of device C as a function of bias current I_{bias} and microwave power P at a constant frequency of a) $5\,\mathrm{GHz}$, b) $15\,\mathrm{GHz}$ and c) $20\,\mathrm{GHz}$. Due to inefficient coupling of the electromagnetic radiation, only microwave-induced heating effects are observed. All measurements were performed at mK-temperatures.

These power dependent measurements are therefore mostly probing the temperature dependence of the junction and present a valuable addition to the measurements shown in figure 4.44

in the main text. We suspect high attenuation of the setup to reduce the effective power at 15 GHz, which leads to less heating and thus to no significant change in figure A.15 b). However, the peaks in $\mathrm{d}V/\mathrm{d}I$ in figure A.15 a) and c) follow the temperature-dependent closing of the superconducting gap Δ.[102,269,270,284] The inner peak disappears first at approximately -4 dBm, before the outer peak vanishes at around 2 dBm. This observation is in agreement with the discussion in the main text regarding the temperature dependence of the effects. The visible spots in the evolution of the outer peak before it vanishes are not microwave-induced periodic replicas of resistance features.[303,304] Rather, they are artifacts which have the same energetic distance for 5 GHz and 20 GHz and occur due to the power step-size resolution in our measurements.

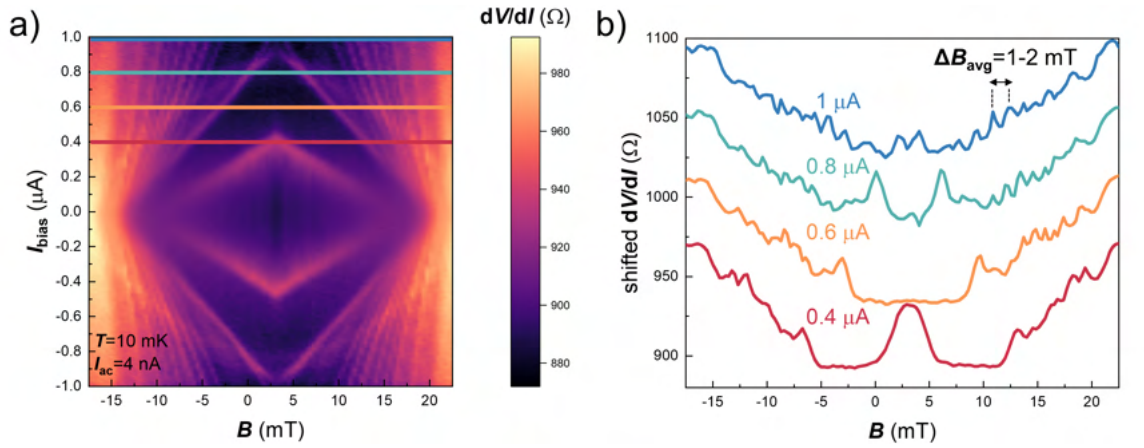

Figure A.16.: a) Magnetic field dependence of the $\mathrm{d}V/\mathrm{d}I$ of JJ3 as a function of bias current. b) Line cuts at four exemplary bias currents as indicated by the colored lines are plotted in a). The average magnetic field distance between peaks ΔB_{avg} ranges between 1 and 2 mT.

In order to evaluate possible explanations for the observed phenomena in device C, the oscillation period in magnetic field is assessed in figure A.16. Figure A.16 a) depicts the differential resistance map of JJ3 as a function of magnetic field and bias current.

Line cuts at multiple different bias currents are plotted in figure A.16 b). In addition to pronounced peaks of the inner and outer diamond-features, several peaks of the diverging fringes are observed which exhibit an average magnetic field spacing ΔB_{avg} of 1 to 2 mT. This magnetic field value corresponds to $\mu_{\mathrm{B}} B \approx 0.1\,\mu$eV, which is much smaller than the energy spacing in bias voltage, discussed in the main text.

Terahertz detectors based on exfoliated graphene

Detector B

Transport measurements at 38 K are employed to characterize detector B. The two-terminal resistance is measured as a function of backgate voltage V_{bg} and topgate voltage V_{tg}, as shown in figure A.17. Separate fits to the resistance around the CNP for the electron and hole regime according to Eq. 4.14 can be used to extract relevant parameters such as the contact resistance R_{c}, the residual charge carrier density n^* and the mobility μ.

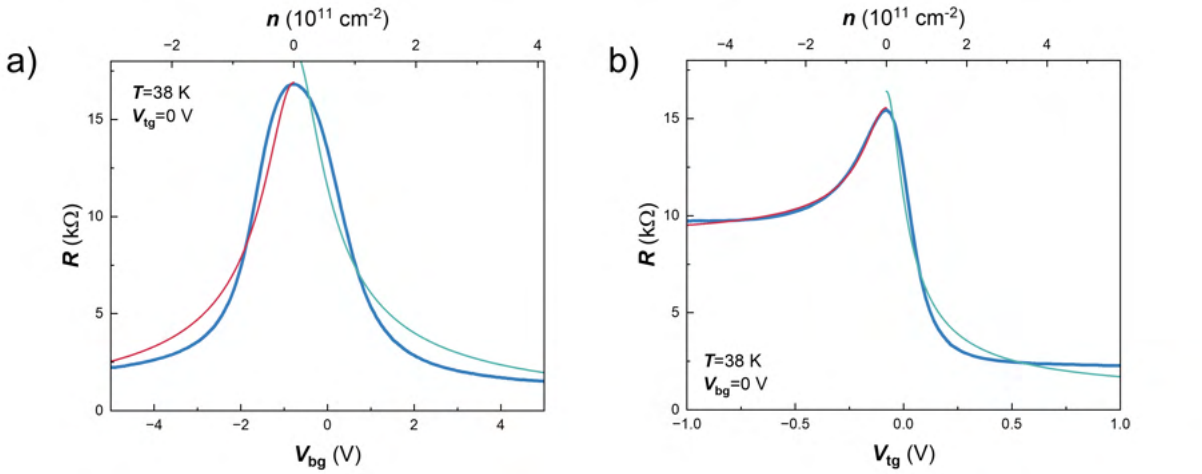

Figure A.17.: a) Two-terminal resistance of detector B (blue line) as a function of backgate voltage V_{bg} at 38 K. The fits to the resistance did not converge with high accuracy. b) Resistance as a function of topgate voltage V_{tg} at 38 K.

The fits to the backgate sweep in figure A.17 did not converge with high accuracy, but yielded a combined $n^* \approx 4.5 \times 10^{10}\,\mathrm{cm}^{-2}$ and $\mu \approx 8000\,\mathrm{cm}^2/\mathrm{Vs}$. However, the fit results exhibit a physically not meaningful vanishing contact resistance. Hence, the results of the fits to the topgate sweep are used for the analysis, which yield a combined $n^* \approx 4.5 \times 10^{10}\,\mathrm{cm}^{-2}$, $\mu \approx 14100\,\mathrm{cm}^2/\mathrm{Vs}$ and $R_{\mathrm{c}} \approx 4.8\,\mathrm{k}\Omega$. Note, that due to n-doped contact regions the contact resistance appears to be asymmetric for electron and hole charge carriers, with $R_{\mathrm{c,\,e}} \approx 0.7\,\mathrm{k}\Omega$ and $R_{\mathrm{c,\,h}} \approx 8.8\,\mathrm{k}\Omega$, respectively.

Bibliography

[1] K. S. Novoselov, A. K. Geim, S. V. Morozov, D. Jiang, Y. Zhang, S. V. Dubonos, I. V. Grigorieva, and A. A. Firsov, "Electric Field Effect in Atomically Thin Carbon Films," *Science*, vol. 306, no. 5696, pp. 666–669, 2004.

[2] K. S. Novoselov, A. K. Geim, S. V. Morozov, D. Jiang, M. I. Katsnelson, I. V. Grigorieva, S. V. Dubonos, and A. A. Firsov, "Two-dimensional gas of massless Dirac fermions in graphene," *Nature*, vol. 438, no. 7065, pp. 197–200, 2005.

[3] A. K. Geim and I. V. Grigorieva, "Van der Waals heterostructures," *Nature*, vol. 499, no. 7459, pp. 419–425, 2013.

[4] K. S. Novoselov, A. Mishchenko, A. Carvalho, and A. H. Castro Neto, "2D materials and van der Waals heterostructures," *Science*, vol. 353, no. 6298, p. aac9439, 2016.

[5] P. Ajayan, P. Kim, and K. Banerjee, "Two-dimensional van der Waals materials," *Physics Today*, vol. 69, no. 9, pp. 38–44, 2016.

[6] A. Castellanos-Gomez, X. Duan, Z. Fei, H. R. Gutierrez, Y. Huang, X. Huang, J. Quereda, Q. Qian, E. Sutter, and P. Sutter, "Van der Waals heterostructures," *Nat. Rev. Methods Primers*, vol. 2, no. 1, p. 58, 2022.

[7] R. R. Nair, P. Blake, A. N. Grigorenko, K. S. Novoselov, T. J. Booth, T. Stauber, N. M. R. Peres, and A. K. Geim, "Fine structure constant defines visual transparency of graphene," *Science*, vol. 320, no. 5881, pp. 1308–1308, 2008.

[8] K. F. Mak, M. Y. Sfeir, Y. Wu, C. H. Lui, J. A. Misewich, and T. F. Heinz, "Measurement of the Optical Conductivity of Graphene," *Phys. Rev. Lett.*, vol. 101, p. 196405, 2008.

[9] C. H. Lui, K. F. Mak, J. Shan, and T. F. Heinz, "Ultrafast Photoluminescence from Graphene," *Phys. Rev. Lett.*, vol. 105, p. 127404, 2010.

[10] K. F. Mak, L. Ju, F. Wang, and T. F. Heinz, "Optical spectroscopy of graphene: From the far infrared to the ultraviolet," *Solid State Commun.*, vol. 152, no. 15, pp. 1341–1349, 2012.

[11] A. K. Geim and K. S. Novoselov, "The rise of graphene," *Nat. Mat.*, vol. 6, pp. 183–191, 2007.

[12] A. H. Castro Neto, F. Guinea, N. M. R. Peres, K. S. Novoselov, and A. K. Geim, "The electronic properties of graphene," *Rev. Mod. Phys.*, vol. 81, pp. 109–162, 2009.

[13] V. P. Gusynin, S. G. Sharapov, and J. P. Carbotte, "Unusual Microwave Response of Dirac Quasiparticles in Graphene," *Phys. Rev. Lett.*, vol. 96, p. 256802, 2006.

[14] K. F. Mak, J. Shan, and T. F. Heinz, "Seeing Many-Body Effects in Single- and Few-Layer Graphene: Observation of Two-Dimensional Saddle-Point Excitons," *Phys. Rev. Lett.*, vol. 106, p. 046401, 2011.

[15] R. G. Mani, J. Hankinson, C. Berger, and W. A. De Heer, "Observation of resistively detected hole spin resonance and zero-field pseudo-spin splitting in epitaxial graphene," *Nat. Comm.*, vol. 3, no. 1, p. 996, 2012.

[16] T. J. Lyon, J. Sichau, A. Dorn, A. Centeno, A. Pesquera, A. Zurutuza, and R. H. Blick, "Probing Electron Spin Resonance in Monolayer Graphene," *Phys. Rev. Lett.*, vol. 119, p. 066802, 2017.

[17] J. Sichau, M. Prada, T. Anlauf, T. J. Lyon, B. Bosnjak, L. Tiemann, and R. H. Blick, "Resonance Microwave Measurements of an Intrinsic Spin-Orbit Coupling Gap in Graphene: A Possible Indication of a Topological State," *Phys. Rev. Lett.*, vol. 122, p. 046403, 2019.

[18] U. R. Singh, M. Prada, V. Strenzke, B. Bosnjak, T. Schmirander, L. Tiemann, and R. H. Blick, "Sublattice symmetry breaking and ultralow energy excitations in graphene-on-hBN heterostructures," *Phys. Rev. B*, vol. 102, p. 245134, 2020.

[19] V. Strenzke, J. M. Meyer, I. Grandt-Ionita, M. Prada, H.-S. Kim, M. Heilmann, J. M. J. Lopes, L. Tiemann, and R. H. Blick, "Nuclear-induced dephasing and signatures of hyperfine effects in isotopically purified ^{13}C graphene," *Phys. Rev. B*, vol. 105, p. 144303, 2022.

[20] C. P. Slichter, *Principles of magnetic resonance*, vol. 3rd edition. Springer Berlin, Heidelberg, 1990.

[21] C. L. Kane and E. J. Mele, "Quantum Spin Hall Effect in Graphene," *Phys. Rev. Lett.*, vol. 95, p. 226801, 2005.

[22] N. Petrone, C. R. Dean, I. Meric, A. M. van der Zande, P. Y. Huang, L. Wang, D. Muller, K. L. Shepard, and J. Hone, "Chemical Vapor Deposition-Derived Graphene with Electrical Performance of Exfoliated Graphene," *Nano Letters*, vol. 12, no. 6, pp. 2751–2756, 2012.

[23] T. J. Lyon, J. Sichau, A. Dorn, A. Zurutuza, A. Pesquera, A. Centeno, and R. H. Blick, "Upscaling high-quality CVD graphene devices to 100 micron-scale and beyond," *Appl. Phys. Lett.*, vol. 110, no. 11, p. 113502, 2017.

[24] Y. Cao, V. Fatemi, S. Fang, K. Watanabe, T. Taniguchi, E. Kaxiras, and P. Jarillo-Herrero, "Unconventional superconductivity in magic-angle graphene superlattices," *Nature*, vol. 556, pp. 40–53, 2018.

[25] Y. Cao, V. Fatemi, A. Demir, S. Fang, S. L. Tomarken, J. Y. Luo, J. D. Sanchez-Yamagishi, K. Watanabe, T. Taniguchi, E. Kaxiras, R. C. Ashoori, and P. Jarillo-Herrero, "Correlated insulator behaviour at half-filling in magic-angle graphene superlattices," *Nature*, vol. 556, pp. 80–84, 2018.

[26] B. A. Bernevig and D. K. Efetov, "Twisted bilayer graphene's gallery of phases," *Physics Today*, vol. 77, no. 4, pp. 38–44, 2024.

[27] M. Tanaka, J. Wang, T. H. Dinh, D. Rodan-Legrain, S. Zaman, M. Hays, A. Almanakly, B. Kannan, D. K. Kim, B. M. Niedzielski, K. Serniak, M. E. Schwartz, K. Watanabe, T. Taniguchi, T. P. Orlando, S. Gustavsson, J. A. Grover, P. Jarillo-Herrero, and W. D. Oliver, "Superfluid stiffness of magic-angle twisted bilayer graphene," *Nature*, vol. 638, no. 8049, pp. 99–105, 2025.

[28] A. Banerjee, Z. Hao, M. Kreidel, P. Ledwith, I. Phinney, J. M. Park, A. Zimmerman, M. E. Wesson, K. Watanabe, T. Taniguchi, R. M. Westervelt, A. Yacoby, P. Jarillo-Herrero, P. A. Volkov, A. Vishwanath, K. C. Fong, and P. Kim, "Superfluid stiffness of twisted trilayer graphene superconductors," *Nature*, vol. 638, no. 8049, pp. 93–98, 2025.

[29] H. B. Heersche, P. Jarillo-Herrero, J. B. Oostinga, L. M. K. Vandersypen, and A. F. Morpurgo, "Bipolar supercurrent in graphene," *Nature*, vol. 446, no. 7131, pp. 56–59, 2007.

[30] V. E. Calado, S. Goswami, G. Nanda, M. Diez, A. R. Akhmerov, K. Watanabe, T. Taniguchi, T. M. Klapwijk, and L. M. K. Vandersypen, "Ballistic josephson junctions in edge-contacted graphene," *Nat. Nano.*, vol. 10, no. 9, pp. 761–764, 2015.

[31] I. V. Borzenets, F. Amet, C. T. Ke, A. W. Draelos, M. T. Wei, A. Seredinski, K. Watanabe, T. Taniguchi, Y. Bomze, M. Yamamoto, S. Tarucha, and G. Finkelstein, "Ballistic Graphene Josephson Junctions from the Short to the Long Junction Regimes," *Phys. Rev. Lett.*, vol. 117, p. 237002, 2016.

[32] J. I. J. Wang, D. Rodan-Legrain, L. Bretheau, D. L. Campbell, B. Kannan, D. Kim, M. Kjaergaard, P. Krantz, G. O. Samach, F. Yan, J. L. Yoder, K. Watanabe, T. Taniguchi, T. P. Orlando, S. Gustavsson, P. Jarillo-Herrero, and W. D. Oliver, "Coherent control of a hybrid superconducting circuit made with graphene-based van der Waals heterostructures," *Nat. Nano.*, vol. 14, no. 2, pp. 120–125, 2019.

[33] G. Butseraen, A. Ranadive, N. Aparicio, K. Rafsanjani Amin, A. Juyal, M. Esposito, K. Watanabe, T. Taniguchi, N. Roch, F. Lefloch, and J. Renard, "A gate-tunable graphene Josephson parametric amplifier," *Nat. Nano.*, vol. 17, no. 11, pp. 1153–1158, 2022.

[34] J. Sarkar, K. V. Salunkhe, S. Mandal, S. Ghatak, A. H. Marchawala, I. Das, K. Watanabe, T. Taniguchi, R. Vijay, and M. M. Deshmukh, "Quantum-noise-limited microwave amplification using a graphene Josephson junction," *Nat. Nano.*, vol. 17, no. 11, pp. 1147–1152, 2022.

[35] R. Kokkoniemi, J.-P. Girard, D. Hazra, A. Laitinen, J. Govenius, R. E. Lake, I. Sallinen, V. Vesterinen, M. Partanen, J. Y. Tan, K. W. Chan, K. Y. Tan, P. Hakonen, and M. Möttönen, "Bolometer operating at the threshold for circuit quantum electrodynamics," *Nature*, vol. 586, pp. 47–51, 2020.

[36] G. H. Lee, D. K. Efetov, W. Jung, L. Ranzani, E. D. Walsh, T. A. Ohki, T. Taniguchi, K. Watanabe, P. Kim, D. Englund, and K. C. Fong, "Graphene-based Josephson junction microwave bolometer," *Nature*, vol. 586, pp. 42–46, 2020.

[37] E. D. Walsh, W. Jung, G.-H. Lee, D. K. Efetov, B.-I. Wu, K.-F. Huang, T. A. Ohki, T. Taniguchi, K. Watanabe, P. Kim, D. Englund, and K. C. Fong, "Josephson junction infrared single-photon detector," *Science*, vol. 372, no. 6540, pp. 409–412, 2021.

[38] B. Huang, E. G. Arnault, W. Jung, C. Fried, J. B. Russell, K. Watanabe, T. Taniguchi, E. A. Henriksen, D. Englund, G. H. Lee, and K. C. Fong, "Graphene calorimetric single-photon detector," *arXiv*, no. 2410.22433, 2024.

[39] D. A. Bandurin, D. Svintsov, I. Gayduchenko, S. G. Xu, A. Principi, M. Moskotin, I. Tretyakov, D. Yagodkin, S. Zhukov, T. Taniguchi, K. Watanabe, I. V. Grigorieva, M. Polini, G. N. Goltsman, A. K. Geim, and G. Fedorov, "Resonant terahertz detection using graphene plasmons," *Nat. Comm.*, vol. 9, no. 1, p. 5392, 2018.

[40] J. A. Delgado-Notario, W. Knap, V. Clericò, J. Salvador-Sánchez, J. Calvo-Gallego, T. Taniguchi, K. Watanabe, T. Otsuji, V. V. Popov, D. V. Fateev, E. Diez, J. E. Velázquez-Pérez, and Y. M. Meziani, "Enhanced terahertz detection of multigate graphene nanostructures," *Nanophotonics*, vol. 11, no. 3, pp. 519–529, 2022.

[41] E. Titova, D. Mylnikov, M. Kashchenko, I. Safonov, S. Zhukov, K. Dzhikirba, K. S. Novoselov, D. A. Bandurin, G. Alymov, and D. Svintsov, "Ultralow-noise Terahertz Detection by p–n Junctions in Gapped Bilayer Graphene," *ACS Nano*, vol. 17, no. 9, pp. 8223–8232, 2023.

[42] M. Romagnoli, V. Sorianello, M. Midrio, F. H. L. Koppens, C. Huyghebaert, D. Neumaier, P. Galli, W. Templ, A. D'Errico, and A. C. Ferrari, "Graphene-based integrated photonics for next-generation datacom and telecom," *Nat. Rev. Mat.*, vol. 3, no. 10, pp. 392–414, 2018.

[43] S. M. Koepfli, M. Baumann, Y. Koyaz, R. Gadola, A. Güngör, K. Keller, Y. Horst, S. Nashashibi, R. Schwanninger, M. Doderer, , E. Passerini, Y. Fedoryshyn, and J. Leuthold, "Metamaterial graphene photodetector with bandwidth exceeding 500 gigahertz," *Science*, vol. 380, no. 6650, pp. 1169–1174, 2023.

[44] P. W. Graham, I. G. Irastorza, S. K. Lamoreaux, A. Lindner, and K. A. van Bibber, "Experimental searches for the axion and axion-like particles," *Annu. Rev. Nucl. Part. Sci.*, vol. 65, no. 1, pp. 485–514, 2015.

[45] A. V. Dixit, S. Chakram, K. He, A. Agrawal, R. K. Naik, D. I. Schuster, and A. Chou, "Searching for Dark Matter with a Superconducting Qubit," *Phys. Rev. Lett.*, vol. 126, p. 141302, 2021.

[46] B. E. Kane, "A silicon-based nuclear spin quantum computer," *Nature*, vol. 393, no. 6681, pp. 133–137, 1998.

[47] D. D. Awschalom, D. Loss, and N. Samarth, *Semiconductor Spintronics and Quantum Computation*. Springer Berlin, Heidelberg, 2002.

[48] B. Trauzettel, D. V. Bulaev, D. Loss, and G. Burkard, "Spin qubits in graphene quantum dots," *Nat. Phys.*, vol. 3, no. 3, pp. 192–196, 2007.

[49] V. Strenzke, A. Weber, P. Heydolph, I. Moch, I. González Díaz-Palacio, W. Hillert, R. Zierold, L. Tiemann, and R. H. Blick, "Challenges and solutions in RF sputtering of superconducting Nb for nanostructuring processes," *J. Appl. Phys.*, vol. 136, no. 20, p. 205301, 2024.

[50] V. Strenzke, M. Prada, J. M. J. Lopes, L. Tiemann, and R. H. Blick, "The quest for harnessing nuclear effects in graphene-based devices," *Applied Physics Reviews*, vol. 11, no. 1, p. 011312, 2024.

[51] P. R. Wallace, "The Band Theory of Graphite," *Phys. Rev.*, vol. 71, pp. 622–634, 1947.

[52] T. Wehling, A. Black-Schaffer, and A. Balatsky, "Dirac materials," *Adv. Phys.*, vol. 63, no. 1, pp. 1–76, 2014.

[53] K. C. Fong and K. C. Schwab, "Ultrasensitive and Wide-Bandwidth Thermal Measurements of Graphene at Low Temperatures," *Phys. Rev. X*, vol. 2, p. 031006, 2012.

[54] J. C. W. Song and L. S. Levitov, "Energy flows in graphene: hot carrier dynamics and cooling," *J. Phys.: Condens. Matter*, vol. 27, no. 16, p. 164201, 2015.

[55] C. B. McKitterick, D. E. Prober, and B. S. Karasik, "Performance of graphene thermal photon detectors," *J. Appl. Phys.*, vol. 113, no. 4, p. 044512, 2013.

[56] J. H. Gosling, O. Makarovsky, F. Wang, N. D. Cottam, M. T. Greenaway, A. Patanè, R. D. Wildman, C. J. Tuck, L. Turyanska, and T. M. Fromhold, "Universal mobility characteristics of graphene originating from charge scattering by ionised impurities," *Commun. Phys.*, vol. 4, no. 1, p. 30, 2021.

[57] S. Kim, J. Nah, I. Jo, D. Shahrjerdi, L. Colombo, Z. Yao, E. Tutuc, and S. K. Banerjee, "Realization of a high mobility dual-gated graphene field-effect transistor with Al_2O_3 dielectric," *Appl. Phys. Lett.*, vol. 94, no. 6, p. 062107, 2009.

[58] L. Gammelgaard, J. M. Caridad, A. Cagliani, D. M. A. Mackenzie, D. H. Petersen, T. J. Booth, and P. Bøggild, "Graphene transport properties upon exposure to PMMA processing and heat treatments," *2D Materials*, vol. 1, no. 3, p. 035005, 2014.

[59] J. Crossno, J. K. Shi, K. Wang, X. Liu, A. Harzheim, A. Lucas, S. Sachdev, P. Kim, T. Taniguchi, K. Watanabe, T. A. Ohki, and K. C. Fong, "Observation of the Dirac fluid and the breakdown of the Wiedemann-Franz law in graphene," *Science*, vol. 351, no. 6277, pp. 1058–1061, 2016.

[60] S. Adam, E. H. Hwang, V. M. Galitski, and S. Das Sarma, "A self-consistent theory for graphene transport," *Proc. Natl. Acad. Sci.*, vol. 104, no. 47, pp. 18392–18397, 2007.

[61] J. Martin, N. Akerman, G. Ulbricht, T. Lohmann, J. H. Smet, K. von Klitzing, and A. Yacoby, "Observation of electron–hole puddles in graphene using a scanning single-electron transistor," *Nat. Phys.*, vol. 4, no. 2, pp. 144–148, 2008.

[62] J.-H. Chen, C. Jang, S. Xiao, M. Ishigami, and M. S. Fuhrer, "Intrinsic and extrinsic performance limits of graphene devices on SiO_2," *Nat. Nano.*, vol. 3, no. 4, pp. 206–209, 2008.

[63] C. R. Dean, A. F. Young, I. Meric, C. Lee, L. Wang, S. Sorgenfrei, K. Watanabe, T. Taniguchi, P. Kim, K. L. Shepard, and J. Hone, "Boron nitride substrates for high-quality graphene electronics," *Nat. Nano.*, vol. 5, no. 10, pp. 722–726, 2010.

[64] A. S. Mayorov, R. V. Gorbachev, S. V. Morozov, L. Britnell, R. Jalil, L. A. Ponomarenko, P. Blake, K. S. Novoselov, K. Watanabe, T. Taniguchi, and A. K. Geim, "Micrometer-scale ballistic transport in encapsulated graphene at room temperature," *Nano Lett.*, vol. 11, no. 6, pp. 2396–2399, 2011.

[65] T. Taychatanapat, K. Watanabe, T. Taniguchi, and P. Jarillo-Herrero, "Electrically tunable transverse magnetic focusing in graphene," *Nat. Phys.*, vol. 9, no. 4, pp. 225–229, 2013.

[66] L. Wang, I. Meric, P. Y. Huang, Q. Gao, Y. Gao, H. Tran, T. Taniguchi, K. Watanabe, L. M. Campos, D. A. Muller, J. Guo, J. Hone, K. L. Shepard, and C. R. Dean, "One-dimensional electrical contact to a two-dimensional material," *Science*, vol. 342, no. 6158, pp. 614–617, 2013.

[67] N. Xin, J. Lourembam, P. Kumaravadivel, A. E. Kazantsev, Z. Wu, C. Mullan, J. Barrier, A. A. Geim, I. V. Grigorieva, A. Mishchenko, A. Principi, V. I. Fal´ko, L. A. Ponomarenko, A. K. Geim, and A. I. Berdyugin, "Giant magnetoresistance of Dirac plasma in high-mobility graphene," *Nature*, vol. 616, no. 7956, pp. 270–274, 2023.

[68] K. Watanabe, T. Taniguchi, and H. Kanda, "Direct-bandgap properties and evidence for ultraviolet lasing of hexagonal boron nitride single crystal," *Nat. Mat.*, vol. 3, no. 6, pp. 404–409, 2009.

[69] Y. Liu, S. Bhowmick, and B. I. Yakobson, "BN White Graphene with "Colorful" Edges: The Energies and Morphology," *Nano Lett.*, vol. 11, no. 8, pp. 3113–3116, 2011.

[70] M. Yankowitz, Q. Ma, P. Jarillo-Herrero, and B. J. LeRoy, "van der Waals heterostructures combining graphene and hexagonal boron nitride," *Nat. Rev. Phys.*, vol. 1, no. 2, pp. 112–125, 2019.

[71] Y. Liu, N. O. Weiss, X. Duan, H.-C. Cheng, Y. Huang, and X. Duan, "Van der Waals heterostructures and devices," *Nat. Rev. Mat.*, vol. 1, no. 9, pp. 1–17, 2016.

[72] A. F. Young, C. R. Dean, I. Meric, S. Sorgenfrei, H. Ren, K. Watanabe, T. Taniguchi, J. Hone, K. L. Shepard, and P. Kim, "Electronic compressibility of layer-polarized bilayer graphene," *Phys. Rev. B*, vol. 85, p. 235458, 2012.

[73] A. A. Zibrov, C. Kometter, H. Zhou, E. M. Spanton, T. Taniguchi, K. Watanabe, M. P. Zaletel, and A. F. Young, "Tunable interacting composite fermion phases in a half-filled bilayer-graphene Landau level," *Nature*, vol. 549, no. 7672, pp. 360–364, 2017.

[74] C. R. Dean, A. F. Young, P. Cadden-Zimansky, L. Wang, H. Ren, K. Watanabe, T. Taniguchi, P. Kim, J. Hone, and K. Shepard, "Multicomponent fractional quantum Hall effect in graphene," *Nature Physics*, vol. 7, no. 9, pp. 693–696, 2011.

[75] D. Sander, S. O. Valenzuela, D. Makarov, C. H. Marrows, E. E. Fullerton, P. Fischer, J. McCord, P. Vavassori, S. Mangin, P. Pirro, B. Hillebrands, A. D. Kent, T. Jungwirth, O. Gutfleisch, C. G. Kim, and A. Berger, "The 2017 Magnetism Roadmap," *J. Phys. D: Appl. Phys.*, vol. 50, no. 36, p. 363001, 2017.

[76] S. Manzeli, D. Ovchinnikov, D. Pasquier, O. V. Yazyev, and A. Kis, "2D transition metal dichalcogenides," *Nat. Rev. Mat.*, vol. 2, no. 8, pp. 1–15, 2017.

[77] J. Cai, E. Anderson, C. Wang, X. Zhang, X. Liu, W. Holtzmann, Y. Zhang, F. Fan, T. Taniguchi, K. Watanabe, Y. Ran, T. Cao, L. Fu, D. Xiao, W. Yao, and X. Xu, "Signatures of fractional quantum anomalous Hall states in twisted $MoTe_2$," *Nature*, vol. 622, no. 7981, pp. 63–68, 2023.

[78] Y. Zeng, Z. Xia, K. Kang, J. Zhu, P. Knüppel, C. Vaswani, K. Watanabe, T. Taniguchi, K. F. Mak, and J. Shan, "Thermodynamic evidence of fractional Chern insulator in moiré $MoTe_2$," *Nature*, vol. 622, no. 7981, pp. 69–73, 2023.

[79] S. Carr, D. Massatt, S. Fang, P. Cazeaux, M. Luskin, and E. Kaxiras, "Twistronics: Manipulating the electronic properties of two-dimensional layered structures through their twist angle," *Phys. Rev. B*, vol. 95, p. 075420, 2017.

[80] Y. Zhang, T.-T. Tang, C. Girit, Z. Hao, M. C. Martin, A. Zettl, M. F. Crommie, Y. R. Shen, and F. Wang, "Direct observation of a widely tunable bandgap in bilayer graphene," *Nature*, vol. 459, no. 7248, pp. 820–823, 2009.

[81] M. J. Ruckriegel, L. M. Gächter, D. Kealhofer, M. Bahrami Panah, C. Tong, C. Adam, M. Masseroni, H. Duprez, R. Garreis, K. Watanabe, T. Taniguchi, A. Wallraff, T. Ihn, K. Ensslin, and W. W. Huang, "Electric Dipole Coupling of a Bilayer Graphene Quantum Dot to a High-Impedance Microwave Resonator," *Nano Letters*, vol. 24, no. 24, pp. 7508–7514, 2024.

[82] J. M. B. Lopes dos Santos, N. M. R. Peres, and A. H. Castro Neto, "Graphene bilayer with a twist: Electronic structure," *Phys. Rev. Lett.*, vol. 99, p. 256802, 2007.

[83] J. M. B. Lopes dos Santos, N. M. R. Peres, and A. H. Castro Neto, "Continuum model of the twisted graphene bilayer," *Phys. Rev. B*, vol. 86, p. 155449, 2012.

[84] R. Bistritzer and A. H. MacDonald, "Moiré bands in twisted double-layer graphene," *Proc. Natl. Acad. Sci.*, vol. 108, no. 30, pp. 12233–12237, 2011.

[85] Y. Cao, J. Y. Luo, V. Fatemi, S. Fang, J. D. Sanchez-Yamagishi, K. Watanabe, T. Taniguchi, E. Kaxiras, and P. Jarillo-Herrero, "Superlattice-Induced Insulating States and Valley-Protected Orbits in Twisted Bilayer Graphene," *Phys. Rev. Lett.*, vol. 117, p. 116804, 2016.

[86] Y. Xie, A. T. Pierce, J. M. Park, D. E. Parker, E. Khalaf, P. Ledwith, Y. Cao, S. H. Lee, S. Chen, P. R. Forrester, K. Watanabe, T. Taniguchi, A. Vishwanath, P. Jarillo-Herrero, and A. Yacoby, "Fractional Chern insulators in magic-angle twisted bilayer graphene," *Nature*, vol. 600, pp. 439–443, 2021.

[87] X. Lu, P. Stepanov, W. Yang, M. Xie, M. A. Aamir, C. Das, I.and Urgell, K. Watanabe, T. Taniguchi, G. Zhang, A. Bachtold, A. H. MacDonald, and D. K. Efetov, "Superconductors, orbital magnets and correlated states in magic-angle bilayer graphene," *Nature*, vol. 574, pp. 653–657, 2019.

[88] A. Jaoui, I. Das, G. Di Battista, J. Díez-Mérida, X. Lu, K. Watanabe, T. Taniguchi, H. Ishizuka, L. Levitov, and D. K. Efetov, "Quantum critical behaviour in magic-angle twisted bilayer graphene," *Nat. Phys.*, vol. 18, pp. 633–638, 2022.

[89] M. Serlin, C. L. Tschirhart, H. Polshyn, Y. Y. Zhang, J. Zhu, K. Watanabe, T. Taniguchi, L. Balents, and A. F. Young, "Intrinsic quantized anomalous Hall effect in a moiré heterostructure," *Science*, vol. 367, no. 6480, pp. 900–903, 2020.

[90] U. Zondiner, D. Rozen, A.Rodan-Legrain, Y. Cao, R. Queiroz, T. Taniguchi, K. Watanabe, Y. Oreg, F. von Oppen, A. Stern, E. Berg, P. Jarillo-Herrero, and S. Ilani, "Cascade of phase transitions and Dirac revivals in magic-angle graphene," *Nature*, vol. 582, pp. 203–208, 2020.

[91] J. R. Prance and M. Ben Shalom, "Building devices in magic-angle graphene," *Nat. Nano.*, vol. 16, no. 7, pp. 745–746, 2021.

[92] J. Díez-Mérida, A. Díez-Carlón, S. Y. Yang, Y.-M. Xie, X.-J. Gao, J. Senior, K. Watanabe, T. Taniguchi, X. Lu, A. P. Higginbotham, K. T. Law, and D. K. Efetov, "Symmetry-broken Josephson junctions and superconducting diodes in magic-angle twisted bilayer graphene," *Nat. Comm.*, vol. 14, no. 1, p. 2396, 2023.

[93] D. Rodan-Legrain, Y. Cao, J. M. Park, S. C. de la Barrera, M. T. Randeria, K. Watanabe, T. Taniguchi, and P. Jarillo-Herrero, "Highly tunable junctions and non-local Josephson effect in magic-angle graphene tunnelling devices," *Nat. Nano.*, vol. 16, no. 7, pp. 769–775, 2021.

[94] F. K. de Vries, E. Portolés, G. Zheng, T. Taniguchi, K. Watanabe, T. Ihn, K. Ensslin, and P. Rickhaus, "Gate-defined Josephson junctions in magic-angle twisted bilayer graphene," *Nat. Nano.*, vol. 16, no. 7, pp. 760–763, 2021.

[95] E. Portolés, S. Iwakiri, G. Zheng, P. Rickhaus, T. Taniguchi, K. Watanabe, T. Ihn, K. Ensslin, and F. K. de Vries, "A tunable monolithic SQUID in twisted bilayer graphene," *Nat. Nano.*, vol. 17, no. 11, pp. 1159–1164, 2022.

[96] H. Zhou, L. Holleis, Y. Saito, L. Cohen, W. Huynh, C. L. Patterson, F. Yang, T. Taniguchi, K. Watanabe, and A. F. Young, "Isospin magnetism and spin-polarized superconductivity in Bernal bilayer graphene," *Science*, vol. 375, no. 6582, pp. 774–778, 2022.

[97] S. C. de la Barrera, S. Aronson, Z. Zheng, K. Watanabe, T. Taniguchi, Q. Ma, P. Jarillo-Herrero, and R. Ashoori, "Cascade of isospin phase transitions in Bernal-stacked bilayer graphene at zero magnetic field," *Nature Physics*, vol. 18, no. 7, pp. 771–775, 2022.

[98] A. M. Seiler, F. R. Geisenhof, F. Winterer, K. Watanabe, T. Taniguchi, T. Xu, F. Zhang, and R. T. Weitz, "Quantum cascade of correlated phases in trigonally warped bilayer graphene," *Nature*, vol. 608, no. 7922, pp. 298–302, 2022.

[99] H. Zhou, T. Xie, T. Taniguchi, K. Watanabe, and A. F. Young, "Superconductivity in rhombohedral trilayer graphene," *Nature*, vol. 598, no. 7881, pp. 434–438, 2021.

[100] H. K. Onnes, "The resistance of pure mercury at helium temperatures," *Commun. Phys. Lab. Univ. Leiden*, vol. 12, no. 120, 1911.

[101] W. Meissner and R. Ochsenfeld, "Ein neuer Effekt bei Eintritt der Supraleitfähigkeit," *Naturwissenschaften*, vol. 21, no. 44, pp. 787–788, 1933.

[102] M. Tinkham, *Introduction to superconductivity*, vol. 2nd edition. McGraw Hill New York, 1996.

[103] F. London and H. London, "The electromagnetic equations of the supraconductor," *Proc. Roy. Soc.*, vol. 149, no. 866, pp. 71–88, 1935.

[104] R. Gross and A. Marx, *Festkörperphysik*. Oldenbourg Wissenschaftsverlag München, 2012.

[105] J. Bardeen, L. N. Cooper, and J. R. Schrieffer, "Theory of Superconductivity," *Phys. Rev.*, vol. 108, pp. 1175–1204, 1957.

[106] L. N. Cooper, "Bound Electron Pairs in a Degenerate Fermi Gas," *Phys. Rev.*, vol. 104, pp. 1189–1190, 1956.

[107] M. R. Norman, "The Challenge of Unconventional Superconductivity," *Science*, vol. 332, no. 6026, pp. 196–200, 2011.

[108] J. G. Bednorz and K. A. Müller, "Possible high T_c superconductivity in the Ba-La-Cu-O system," *Z. Phys. B*, vol. 64, no. 2, pp. 189–193, 1986.

[109] D. J. Scalapino, "A common thread: The pairing interaction for unconventional superconductors," *Rev. Mod. Phys.*, vol. 84, pp. 1383–1417, 2012.

[110] B. D. Josephson, "Possible new effects in superconductive tunnelling," *Phys. Lett.*, vol. 1, no. 7, pp. 251–253, 1962.

[111] G. H. Lee and H. J. Lee, "Proximity coupling in superconductor-graphene heterostructures," *Rep. Prog. Phys.*, vol. 81, no. 5, p. 056502, 2018.

[112] A. F. Andreev, "The thermal conductivity of the intermadiate state in superconductors," *Soviet Physics JETP*, vol. 6, no. 20, pp. 1228–1232, 1964.

[113] G. E. Blonder, M. Tinkham, and T. M. Klapwijk, "Transition from metallic to tunneling regimes in superconducting microconstrictions: Excess current, charge imbalance, and supercurrent conversion," *Phys. Rev. B*, vol. 25, pp. 4515–4532, 1982.

[114] B. Cabrera, R. M. Clarke, P. Colling, A. J. Miller, S. Nam, and R. W. Romani, "Detection of single infrared, optical, and ultraviolet photons using superconducting transition edge sensors," *Appl. Phys. Lett.*, vol. 73, pp. 735–737, 1998.

[115] K. Irwin and G. Hilton, *Cryogenic Particle Detection: Transition-Edge Sensors*. Springer Berlin Heidelberg, 2005.

[116] I. Charaev, D. A. Bandurin, A. T. Bollinger, I. Y. Phinney, I. Drozdov, M. Colangelo, B. A. Butters, T. Taniguchi, K. Watanabe, X. He, O. Medeiros, I. Božović, P. Jarillo-Herrero, and K. K. Berggren, "Single-photon detection using high-temperature superconductors," *Nat. Nano.*, vol. 18, no. 4, pp. 343–349, 2023.

[117] A. F. Morpurgo, T. M. Klapwijk, and B. J. van Wees, "Hot electron tunable supercurrent," *Applied Physics Letters*, vol. 72, no. 8, pp. 966–968, 1998.

[118] S. Tirelli, A. M. Savin, C. P. Garcia, J. P. Pekola, F. Beltram, and F. Giazotto, "Manipulation and Generation of Supercurrent in Out-of-Equilibrium Josephson Tunnel Nanojunctions," *Phys. Rev. Lett.*, vol. 101, p. 077004, 2008.

[119] G. Di Battista, P. Seifert, K. Watanabe, T. Taniguchi, K. C. Fong, A. Principi, and D. K. Efetov, "Revealing the Thermal Properties of Superconducting Magic-Angle Twisted Bilayer Graphene," *Nano Letters*, vol. 22, no. 16, pp. 6465–6470, 2022.

[120] G. Di Battista, K. C. Fong, A. Díez-Carlón, K. Watanabe, T. Taniguchi, and D. K. Efetov, "Infrared single-photon detection with superconducting magic-angle twisted bilayer graphene," *Science Advances*, vol. 10, no. 38, p. eadp3725, 2024.

[121] K. Inomata, Z. Lin, K. Koshino, W. D. Oliver, J.-S. Tsai, T. Yamamoto, and Y. Nakamura, "Single microwave-photon detector using an artificial Λ-type three-level system," *Nat. Comm.*, vol. 7, no. 1, p. 12303, 2016.

[122] M. Dyakonov and M. Shur, "Detection, mixing, and frequency multiplication of terahertz radiation by two-dimensional electronic fluid," *IEEE Trans. on Electron Devices*, vol. 43, no. 3, pp. 380–387, 1996.

[123] V. V. Popov, D. V. Fateev, T. Otsuji, Y. M. Meziani, D. Coquillat, and W. Knap, "Plasmonic terahertz detection by a double-grating-gate field-effect transistor structure with an asymmetric unit cell," *Appl. Phys. Lett.*, vol. 99, no. 24, p. 243504, 2011.

[124] J. A. Delgado-Notario, V. Clericò, E. Diez, J. E. Velázquez-Pérez, T. Taniguchi, K. Watanabe, T. Otsuji, and Y. M. Meziani, "Asymmetric dual-grating gates graphene FET for detection of terahertz radiations," *APL Photonics*, vol. 5, no. 6, p. 066102, 2020.

[125] P. A. D. Gonçalves and N. M. R. Peres, *An Introduction to Graphene Plasmonics*. World Scientific Publishing, 2016.

[126] S. Castilla, B. Terrés, M. Autore, L. Viti, J. Li, A. Y. Nikitin, I. Vangelidis, K. Watanabe, T. Taniguchi, E. Lidorikis, M. S. Vitiello, R. Hillenbrand, K.-J. Tielrooij, and F. H. Koppens, "Fast and Sensitive Terahertz Detection Using an Antenna-Integrated Graphene pn Junction," *Nano Lett.*, vol. 19, no. 5, pp. 2765–2773, 2019.

[127] L. Viti, A. R. Cadore, X. Yang, A. Vorobiev, J. E. Muench, K. Watanabe, T. Taniguchi, J. Stake, A. C. Ferrari, and M. S. Vitiello, "Thermoelectric graphene photodetectors with sub-nanosecond response times at terahertz frequencies," *Nanophotonics*, vol. 10, no. 1, pp. 89–98, 2021.

[128] F. Ludwig, A. Generalov, J. Holstein, A. Murros, K. Viisanen, M. Prunnila, and H. G. Roskos, "Terahertz Detection with Graphene FETs: Photothermoelectric and Resistive Self-Mixing Contributions to the Detector Response," *ACS Appl. Electron. Mater.*, vol. 6, no. 4, pp. 2197–2212, 2024.

[129] P. Olbrich, J. Kamann, M. König, J. Munzert, L. Tutsch, J. Eroms, D. Weiss, M. H. Liu, L. E. Golub, E. L. Ivchenko, V. V. Popov, D. V. Fateev, K. V. Mashinsky, F. Fromm, T. Seyller, and S. D. Ganichev, "Terahertz ratchet effects in graphene with a lateral superlattice," *Phys. Rev. B*, vol. 93, p. 075422, 2016.

[130] D. Bandurin, I. Gayduchenko, Y. Cao, M. Moskotin, A. Principi, I. Grigorieva, G. Goltsman, G. Fedorov, and D. Svintsov, "Dual origin of room temperature sub-terahertz photoresponse in graphene field effect transistors," *Appl. Phys. Lett.*, vol. 112, no. 14, 2018.

[131] E. Mönch, S. O. Potashin, K. Lindner, I. Yahniuk, L. E. Golub, V. Y. Kachorovskii, V. V. Bel'kov, R. Huber, K. Watanabe, T. Taniguchi, J. Eroms, D. Weiss, and S. D. Ganichev, "Ratchet effect in spatially modulated bilayer graphene: Signature of hydrodynamic transport," *Phys. Rev. B*, vol. 105, p. 045404, 2022.

[132] I. M. Moiseenko, V. V. Popov, and D. V. Fateev, "Amplified propagating plasmon in asymmetrical graphene periodic structure," *Journal Phys. Commun.*, vol. 4, no. 7, p. 071001, 2020.

[133] E. Abidi, A. Khan, J. A. Delgado-Notario, V. Clericó, J. Calvo-Gallego, T. Taniguchi, K. Watanabe, T. Otsuji, J. E. Velázquez, and Y. M. Meziani, "Terahertz Detection by Asymmetric Dual Grating Gate Bilayer Graphene FETs with Integrated Bowtie Antenna," *Nanomaterials*, vol. 14, no. 4, 2024.

[134] J. Schiefele, J. Pedrós, F. Sols, F. Calle, and F. Guinea, "Coupling Light into Graphene Plasmons through Surface Acoustic Waves," *Phys. Rev. Lett.*, vol. 111, p. 237405, 2013.

[135] M. M. Mehrnegar, S. Darbari, H. Ramezani, and K. M. Moravvej-Farshi, "Designing Graphene-Based Multi-Mode Acousto-Plasmonic Devices," *J. Lightwave Technol.*, vol. 37, no. 9, pp. 2126–2132, 2019.

[136] D. Mandal and S. Banerjee, "Surface Acoustic Wave (SAW) Sensors: Physics, Materials, and Applications," *Sensors*, vol. 22, no. 3, 2022.

[137] P. Zhao, C. H. Sharma, R. Liang, C. Glasenapp, L. Mourokh, V. M. Kovalev, P. Huber, M. Prada, L. Tiemann, and R. H. Blick, "Acoustically Induced Giant Synthetic Hall Voltages in Graphene," *Phys. Rev. Lett.*, vol. 128, p. 256601, 2022.

[138] P. Zhao, C. H. Sharma, L. Tiemann, and R. H. Blick, "Surface acoustic wave induced transport and strain phenomena in van der Waals materials," *J. Phys. D: Appl. Phys.*, vol. 57, no. 30, p. 303001, 2024.

[139] C. Bray, K. Maussang, C. Consejo, J. A. Delgado-Notario, S. Krishtopenko, I. Yahniuk, S. Gebert, S. Ruffenach, K. Dinar, E. Moench, J. Eroms, K. Indykiewicz, B. Jouault, J. Torres, Y. M. Meziani, W. Knap, A. Yurgens, S. D. Ganichev, and F. Teppe, "Temperature-dependent zero-field splittings in graphene," *Phys. Rev. B*, vol. 106, p. 245141, 2022.

[140] E. Morissette, J.-X. Lin, D. Sun, L. Zhang, S. Liu, D. Rhodes, K. Watanabe, T. Taniguchi, J. Hone, J. Pollanen, M. S. Scheurer, M. Lilly, A. Mounce, and J. I. Li, "Dirac revivals drive a resonance response in twisted bilayer graphene," *Nat. Phys.*, vol. 19, no. 8, pp. 1156–1162, 2023.

[141] L. Tiemann, M. Prada, V. Strenzke, and R. H. Blick, "Comment on "Electron spin resonance and collective excitations in magic-angle twisted bilayer graphene"," *arXiv*, no. 2206.14628, 2022.

[142] H. O. H. Churchill, A. J. Bestwick, J. W. Harlow, F. Kuemmeth, D. Marcos, C. H. Stwertka, S. K. Watson, and C. M. Marcus, "Electron–nuclear interaction in ^{13}C nanotube double quantum dots," *Nat. Phys.*, vol. 5, no. 5, pp. 321–326, 2009.

[143] M. Wojtaszek, I. J. Vera-Marun, E. Whiteway, M. Hilke, and B. J. van Wees, "Absence of hyperfine effects in ^{13}C-graphene spin-valve devices," *Phys. Rev. B*, vol. 89, p. 035417, 2014.

[144] S. Iwakiri, J. Miller, F. Lang, J. Prettenthaler, T. Taniguchi, K. Watanabe, S. S. Lee, P. Becker, D. Günther, T. Ihn, and K. Ensslin, "High-mobility transport in isotopically enriched ^{12}C and ^{13}C exfoliated graphene," *Phys. Rev. Res.*, vol. 5, p. 043212, 2023.

[145] V. Strenzke, *Electron spin - nuclear spin interactions and coupling in ^{13}C graphene*, vol. Master's thesis. Universität Hamburg, Germany, 2021.

[146] D. M. Pozar, *Microwave engineering: theory and techniques*, vol. 4th edition. John wiley & sons, 2012.

[147] C. Wen, "Coplanar Waveguide: A Surface Strip Transmission Line Suitable for Nonreciprocal Gyromagnetic Device Applications," *IEEE Trans. Microwave Theory Techn.*, vol. 17, no. 12, pp. 1087–1090, 1969.

[148] R. E. Collin, *Foundations for Microwave Engineering*, vol. 2nd edition. McGraw-Hill, 2012.

[149] R. Garg, I. Bahl, and M. Bozzi, *Microstrip Lines and Slotlines*, vol. 3rd edition. Artech House, 2013.

[150] R. N. Simons, *Coplanar Waveguide Circuits, Components, and Systems*, vol. 1st edition. John wiley & sons, 2001.

[151] K. Watanabe, K. Yoshida, and T. A. Kohjiro, "Kinetic Inductance of Superconducting Coplanar Waveguides," *Jpn. J. Appl. Phys.*, vol. 33, no. 10R, p. 5708, 1994.

[152] S. Hähnle, N. v. Marrewijk, A. Endo, K. Karatsu, D. J. Thoen, V. Murugesan, and J. J. A. Baselmans, "Suppression of radiation loss in high kinetic inductance superconducting co-planar waveguides," *Appl. Phys. Lett.*, vol. 116, no. 18, p. 182601, 2020.

[153] M. Göppl, A. Fragner, M. Baur, R. Bianchetti, S. Filipp, J. M. Fink, P. J. Leek, G. Puebla, L. Steffen, and A. Wallraff, "Coplanar waveguide resonators for circuit quantum electrodynamics," *J. Appl. Phys.*, vol. 104, no. 11, p. 113904, 2008.

[154] P. K. Day, H. G. LeDuc, B. A. Mazin, A. Vayonakis, and J. Zmuidzinas, "A broadband superconducting detector suitable for use in large arrays," *Nature*, vol. 425, no. 6960, pp. 817–821, 2003.

[155] N. G. Ebensperger, B. Ferdinand, D. Koelle, R. Kleiner, M. Dressel, and M. Scheffler, "Characterizing dielectric properties of ultra-thin films using superconducting coplanar microwave resonators," *Rev. Sci. Instrum.*, vol. 90, no. 11, p. 114701, 2019.

[156] Z. Yan, Y. Zhang, M. Gong, Y. Wu, Y. Zheng, S. Li, C. Wang, F. Liang, J. Lin, Y. Xu, C. Guo, Sun, C. Peng, K. Xia, H. Deng, H. Rong, J. Q. You, F. Nori, H. Fan, X. Zhu, and J. Pan, "Strongly correlated quantum walks with a 12-qubit superconducting processor," *Science*, vol. 364, no. 6442, pp. 753–756, 2019.

[157] M. J. Rahim, T. Lehleiter, D. Bothner, C. Krellner, D. Koelle, R. Kleiner, M. Dressel, and M. Scheffler, "Metallic coplanar resonators optimized for low-temperature measurements," *J. Phys. D: Appl. Phys.*, vol. 49, no. 39, p. 395501, 2016.

[158] D. S. Rausch, M. Thiemann, M. Dressel, D. Bothner, D. Dieter Koelle, R. Kleiner, and M. Scheffler, "Superconducting coplanar microwave resonators with operating frequencies up to 50 GHz," *J. Phys. D: Appl. Phys.*, vol. 51, no. 46, p. 465301, 2018.

[159] A. Antony, M. V. Gustafsson, G. J. Ribeill, M. Ware, A. Rajendran, L. C. G. Govia, T. A. Ohki, T. Taniguchi, K. Watanabe, J. Hone, and K. C. Fong, "Miniaturizing Transmon Qubits Using van der Waals Materials," *Nano Letters*, vol. 21, no. 23, pp. 10122–10126, 2021.

[160] X. Liang, B. A. Sperling, I. Calizo, G. Cheng, C. A. Hacker, Q. Zhang, Y. Obeng, K. Yan, H. Peng, Q. Li, X. Zhu, H. Yuan, A. R. Hight Walker, Z. Liu, L. Peng, and C. A. Richter, "Toward Clean and Crackless Transfer of Graphene," *ACS Nano*, vol. 5, no. 11, pp. 9144–9153, 2011.

[161] A. A. Generalov, M. A. Andersson, X. Yang, A. Vorobiev, and J. Stake, "A 400-GHz Graphene FET Detector," *IEEE Trans. Terahertz Sci. Technol.*, vol. 7, no. 5, pp. 614–616, 2017.

[162] A. A. Generalov, K. L. Viisanen, J. Senior, B. R. Ferreira, J. Ma, M. Möttönen, M. Prunnila, and H. Bohuslavskyi, "Wafer-scale CMOS-compatible graphene Josephson field-effect transistors," *Appl. Phys. Lett.*, vol. 125, no. 1, p. 012602, 2024.

[163] P. Blake, E. W. Hill, A. H. Castro Neto, K. S. Novoselov, D. Jiang, R. Yang, T. J. Booth, and A. K. Geim, "Making graphene visible," *Appl. Phys. Lett.*, vol. 91, no. 6, p. 063124, 2007.

[164] Y. Huang, E. Sutter, N. N. Shi, J. Zheng, T. Yang, D. Englund, H.-J. Gao, and P. Sutter, "Reliable Exfoliation of Large-Area High-Quality Flakes of Graphene and Other Two-Dimensional Materials," *ACS Nano*, vol. 9, no. 11, pp. 10612–10620, 2015.

[165] S. Puebla, H. Li, H. Zhang, and A. Castellanos-Gomez, "Apparent Colors of 2D Materials," *Adv. Photonics Res.*, vol. 3, no. 4, p. 2100221, 2022.

[166] A. C. Ferrari, J. C. Meyer, V. Scardaci, C. Casiraghi, M. Lazzeri, F. Mauri, S. Piscanec, D. Jiang, K. S. Novoselov, S. Roth, and A. K. Geim, "Raman Spectrum of Graphene and Graphene Layers," *Phys. Rev. Lett.*, vol. 97, p. 187401, 2006.

[167] Y. Hao, Y. Wang, L. Wang, Z. Ni, Z. Wang, R. Wang, C. K. Koo, Z. Shen, and J. T. L. Thong, "Probing Layer Number and Stacking Order of Few-Layer Graphene by Raman Spectroscopy," *Small*, vol. 6, no. 2, pp. 195–200, 2010.

[168] D. Graf, F. Molitor, K. Ensslin, C. Stampfer, A. Jungen, C. Hierold, and L. Wirtz, "Spatially resolved Raman spectroscopy of single-and few-layer graphene," *Nano letters*, vol. 7, no. 2, pp. 238–242, 2007.

[169] J. F. Rodriguez-Nieva, R. Saito, S. D. Costa, and M. S. Dresselhaus, "Effect of ^{13}C isotope doping on the optical phonon modes in graphene: Localization and Raman spectroscopy," *Phys. Rev. B*, vol. 85, p. 245406, 2012.

[170] E. del Corro, M. Kalbac, C. Fantini, O. Frank, and M. A. Pimenta, "Isotopic ^{13}C/^{12}C effect on the resonant Raman spectrum of twisted bilayer graphene," *Phys. Rev. B*, vol. 88, p. 155436, 2013.

[171] P. J. Zomer, M. H. D. Guimarães, J. C. Brant, N. Tombros, and B. J. van Wees, "Fast pick up technique for high quality heterostructures of bilayer graphene and hexagonal boron nitride," *Appl. Phys. Lett.*, vol. 105, no. 1, p. 013101, 2014.

[172] K. Kim, M. Yankowitz, B. Fallahazad, S. Kang, H. C. P. Movva, S. Huang, S. Larentis, C. M. Corbet, T. Taniguchi, K. Watanabe, S. K. Banerjee, B. J. LeRoy, and E. Tutuc, "van der Waals Heterostructures with High Accuracy Rotational Alignment," *Nano Letters*, vol. 16, no. 3, pp. 1989–1995, 2016.

[173] F. Pizzocchero, L. Gammelgaard, B. S. Jessen, J. M. Caridad, L. Wang, J. Hone, P. Bøggild, and T. J. Booth, "The hot pick-up technique for batch assembly of van der Waals heterostructures," *Nat. Comm.*, vol. 7, no. 1, p. 11894, 2016.

[174] J. Díez-Mérida, I. Das, G. Di Battista, A. Díez-Carlón, M. Lee, L. Zeng, K. Watanabe, T. Taniguchi, E. Olsson, and D. K. Efetov, "High-yield fabrication of bubble-free magic-angle twisted bilayer graphene devices with high twist-angle homogeneity," *Newton*, vol. 1, no. 100007, 2024.

[175] Y. Matsuda, W. Deng, and W. A. Goddard III, "Contact resistance for end-contacted metal-graphene and metal-nanotube interfaces from quantum mechanics," *J. Phys. Chem. C*, vol. 114, no. 41, pp. 17845–17850, 2010.

[176] M. S. Choi, N. Ali, T. D. Ngo, H. Choi, B. Oh, H. Yang, and W. J. Yoo, "Recent Progress in 1D Contacts for 2D-Material-Based Devices," *Adv. Mater.*, vol. 34, no. 39, p. 2202408, 2022.

[177] E. Y. Andrei, G. Deville, D. C. Glattli, F. I. B. Williams, E. Paris, and B. Etienne, "Observation of a Magnetically Induced Wigner Solid," *Phys. Rev. Lett.*, vol. 60, pp. 2765–2768, 1988.

[178] H. Zhu, G. Sambandamurthy, Y. P. Chen, P. Jiang, L. W. Engel, D. C. Tsui, L. N. Pfeiffer, and K. W. West, "Pinning-Mode Resonance of a Skyrme Crystal near Landau-Level Filling Factor $\nu = 1$," *Phys. Rev. Lett.*, vol. 104, p. 226801, 2010.

[179] S. Dietrich, A. Akbari-Sharbaf, J. H. Edgar, A. Roubos, M. Freeman, and L. W. Engel, "Hall signal-dominated microwave transmission through graphene-loaded waveguides," *arXiv*, no. 2410.18271, 2024.

[180] I. González Díaz-Palacio, M. Wenskat, G. K. Deyu, W. Hillert, R. H. Blick, and R. Zierold, "Thermal annealing of superconducting niobium titanium nitride thin films deposited by plasma-enhanced atomic layer deposition," *J. Appl. Phys.*, vol. 134, no. 3, p. 035301, 2023.

[181] A. Bruno, G. de Lange, S. Asaad, K. L. van der Enden, N. K. Langford, and L. DiCarlo, "Reducing intrinsic loss in superconducting resonators by surface treatment and deep etching of silicon substrates," *Appl. Phys. Lett.*, vol. 106, no. 18, 2015.

[182] I. Besedin and A. P. Menushenkov, "Quality factor of a transmission line coupled coplanar waveguide resonator," *EPJ Quantum Technol.*, vol. 5, no. 1, pp. 1–16, 2018.

[183] M. Manzo-Perez, M. Jamalzadeh, Z. Huang, X. Tong, K. Kisslinger, D. Nykypanchuk, and D. Shahrjerdi, "Effects of residual oxygen on superconducting niobium films," *Appl. Phys. Lett.*, vol. 125, no. 11, p. 112602, 2024.

[184] J. Sosniak and J. Hull, G. W., "Superconductivity of Niobium Thin Films Deposited by dc Diode Sputtering," *J. Appl. Phys.*, vol. 38, no. 11, pp. 4390–4392, 1967.

[185] A. Anferov, K.-H. Lee, F. Zhao, J. Simon, and D. I. Schuster, "Improved coherence in optically defined niobium trilayer-junction qubits," *Phys. Rev. Appl.*, vol. 21, p. 024047, 2024.

[186] P. Rickhaus, M. Weiss, L. Marot, and C. Schönenberger, "Quantum Hall Effect in Graphene with Superconducting Electrodes," *Nano Letters*, vol. 12, no. 4, pp. 1942–1945, 2012.

[187] Z. Huang, N. Lotfizadeh, B. H. Elfeky, K. Kisslinger, E. Cuniberto, P. Yu, M. Hatefipour, T. Taniguchi, K. Watanabe, J. Shabani, and D. Shahrjerdi, "The study of contact properties in edge-contacted graphene–aluminum Josephson junctions," *Appl. Phys. Lett.*, vol. 121, no. 24, p. 243503, 2022.

[188] Z. Cao, F. Lin, G. Gong, H. Chen, and J. Martin, "Low Schottky barrier contacts to 2H-MoS_2 by Sn electrodes," *Appl. Phys. Lett.*, vol. 116, no. 2, 2020.

[189] B.-K. Kim, T.-H. Kim, D.-H. Choi, H. Kim, K. Watanabe, T. Taniguchi, H. Rho, J.-J. Kim, Y.-H. Kim, and M.-H. Bae, "Origins of genuine Ohmic van der Waals contact between indium and MoS2," *npj 2D Mater. Appl.*, vol. 5, no. 1, p. 9, 2021.

[190] E. McCann, K. Kechedzhi, V. I. Fala'Ko, H. Suzuura, T. Ando, and B. L. Altshuler, "Weak-localization magnetoresistance and valley symmetry in graphene," *Phys. Rev. Lett.*, vol. 97, no. 14, pp. 14–17, 2006.

[191] M. Hilke, M. Massicotte, E. Whiteway, and V. Yu, "Weak localization in graphene: theory, simulations, and experiments," *Sci. World J.*, vol. 2014, no. 1, p. 737296, 2014.

[192] A. Pályi and G. Burkard, "Hyperfine-induced valley mixing and the spin-valley blockade in carbon-based quantum dots," *Phys. Rev. B*, vol. 80, p. 201404, 2009.

[193] D. Paget, G. Lampel, B. Sapoval, and V. I. Safarov, "Low field electron-nuclear spin coupling in gallium arsenide under optical pumping conditions," *Phys. Rev. B*, vol. 15, pp. 5780–5796, 1977.

[194] D. Paget, "Optical detection of NMR in high-purity GaAs under optical pumping: Efficient spin-exchange averaging between electronic states," *Phys. Rev. B*, vol. 24, pp. 3776–3793, 1981.

[195] S. Lara-Avila, A. Tzalenchuk, S. Kubatkin, R. Yakimova, T. J. B. M. Janssen, K. Cedergren, T. Bergsten, and V. Fal'ko, "Disordered Fermi Liquid in Epitaxial Graphene from Quantum Transport Measurements," *Phys. Rev. Lett.*, vol. 107, p. 166602, 2011.

[196] M. Long, Y. Gong, X. Wei, C. Zhu, J. Xu, P. Liu, Y. Guo, W. Li, G. Liu, and L. Liu, "Electron-electron interaction, weak localization and spin valve effect in vertical-transport graphene devices," *Appl. Phys. Lett.*, vol. 104, no. 15, p. 153114, 2014.

[197] R. Muñoz and C. Gómez-Aleixandre, "Review of CVD Synthesis of Graphene," *Chemical Vapor Deposition*, vol. 19, no. 10-11-12, pp. 297–322, 2013.

[198] Y. Zhang, L. Zhang, and C. Zhou, "Review of Chemical Vapor Deposition of Graphene and Related Applications," *Acc. Chem. Res.*, vol. 46, no. 10, pp. 2329–2339, 2013.

[199] A. A. Kozikov, D. W. Horsell, E. McCann, and V. I. Fal'ko, "Evidence for spin memory in the electron phase coherence in graphene," *Phys. Rev. B*, vol. 86, p. 045436, 2012.

[200] K. Hsieh, V. Kochat, T. Biswas, C. S. Tiwary, A. Mishra, G. Ramalingam, A. Jayaraman, K. Chattopadhyay, S. Raghavan, M. Jain, and A. Ghosh, "Spontaneous Time-Reversal Symmetry Breaking at Individual Grain Boundaries in Graphene," *Phys. Rev. Lett.*, vol. 126, p. 206803, 2021.

[201] D. Huertas-Hernando, F. Guinea, and A. Brataas, "Spin-orbit coupling in curved graphene, fullerenes, nanotubes, and nanotube caps," *Phys. Rev. B*, vol. 74, p. 155426, 2006.

[202] F. Kuemmeth, S. Ilani, D. C. Ralph, and P. L. McEuen, "Coupling of spin and orbital motion of electrons in carbon nanotubes," *Nature*, vol. 452, p. 448–452, 2008.

[203] C. H. Pennington and V. A. Stenger, "Nuclear magnetic resonance of C_{60} and fulleride superconductors," *Rev. Mod. Phys.*, vol. 68, pp. 855–910, 1996.

[204] O. V. Yazyev, "Hyperfine Interactions in Graphene and Related Carbon Nanostructures," *Nano Letters*, vol. 8, no. 4, pp. 1011–1015, 2008.

[205] J. Fischer, B. Trauzettel, and D. Loss, "Hyperfine interaction and electron-spin decoherence in graphene and carbon nanotube quantum dots," *Phys. Rev. B*, vol. 80, no. 15, 2009.

[206] G. Csiszár and A. Pályi, "Orbital hyperfine interaction and qubit dephasing in carbon nanotube quantum dots," *Phys. Rev. B*, vol. 90, no. 24, 2014.

[207] T. Pei, A. Pályi, M. Mergenthaler, N. Ares, A. Mavalankar, J. H. Warner, G. A. D. Briggs, and E. A. Laird, "Hyperfine and Spin-Orbit Coupling Effects on Decay of Spin-Valley States in a Carbon Nanotube," *Phys. Rev. Lett.*, vol. 118, no. 17, p. 177701, 2017.

[208] A. Berg, M. Dobers, R. R. Gerhardts, and K. v. Klitzing, "Magnetoquantum oscillations of the nuclear-spin-lattice relaxation near a two-dimensional electron gas," *Phys. Rev. Lett.*, vol. 64, pp. 2563–2566, 1990.

[209] S. Kronmüller, W. Dietsche, J. Weis, K. von Klitzing, W. Wegscheider, and M. Bichler, "New Resistance Maxima in the Fractional Quantum Hall Effect Regime," *Phys. Rev. Lett.*, vol. 81, pp. 2526–2529, 1998.

[210] A. V. Shchepetilnikov, D. D. Frolov, Y. A. Nefyodov, I. V. Kukushkin, D. S. Smirnov, L. Tiemann, C. Reichl, W. Dietsche, and W. Wegscheider, "Nuclear magnetic resonance and nuclear spin relaxation in AlAs quantum well probed by ESR," *Phys. Rev. B*, vol. 94, p. 241302(R), 2016.

[211] M. Kindermann and P. N. First, "Local sublattice-symmetry breaking in rotationally faulted multilayer graphene," *Phys. Rev. B*, vol. 83, p. 045425, 2011.

[212] T. Anlauf, M. Prada, S. Freercks, B. Bosnjak, R. Frömter, J. Sichau, H. P. Oepen, L. Tiemann, and R. H. Blick, "Polarization amplification by spin-doping in nanomagnetic/graphene hybrid systems," *Phys. Rev. Materials*, vol. 5, p. 034006, 2021.

[213] M. Prada, L. Tiemann, J. Sichau, and R. H. Blick, "Dirac imprints on the g-factor anisotropy in graphene," *Phys. Rev. B*, vol. 104, p. 075401, 2021.

[214] B. Dóra and F. Simon, "Hyperfine interaction in graphene: The relevance for spintronics," *Phys. Status Solidi B*, vol. 247, no. 11-12, pp. 2935–2940, 2010.

[215] K. Dinar, J. Delgado-Notario, C. Bray, K. Maussang, E. Perez-Martin, B. Benhamou-Bui, C. Consejo, S. Ruffenach, S. S. Krishtopenko, L. Bonnet, M. Paillet, J. Torres, Y. M. Meziani, I. Rozhansky, B. Jouault, S. Nanot, and F. Teppe, "Spin-dependent photovoltage in graphene/MoS_2-based field-effect transistors," *arXiv*, no. 2411.16328, 2024.

[216] S. A. Studenikin, M. Potemski, A. Sachrajda, M. Hilke, L. N. Pfeiffer, and K. W. West, "Microwave-induced resistance oscillations on a high-mobility two-dimensional electron gas: Exact waveform, absorption/reflection and temperature damping," *Phys. Rev. B*, vol. 71, p. 245313, 2005.

[217] R. G. Mani, A. Kriisa, and R. Munasinghe, "Radiation-induced magnetoresistance oscillations in monolayer and bilayer graphene," *Sci. Rep.*, vol. 9, no. 1, p. 7278, 2019.

[218] Y. A. Bychkov and G. Martinez, "Magnetoplasmon excitations in graphene for filling factors $\nu 6$," *Phys. Rev. B*, vol. 77, p. 125417, 2008.

[219] A. Iyengar, J. Wang, H. A. Fertig, and L. Brey, "Excitations from filled Landau levels in graphene," *Phys. Rev. B*, vol. 75, p. 125430, 2007.

[220] D. v. Krosigk, *Spin interaction in isotopically enriched ^{13}C graphene heterostructures*, vol. Bachelor's thesis. Universität Hamburg, Germany, 2024.

[221] G. Gervais, H. L. Stormer, D. C. Tsui, P. L. Kuhns, W. G. Moulton, A. P. Reyes, L. N. Pfeiffer, K. W. Baldwin, and K. W. West, "Evidence for Skyrmion Crystallization from NMR Relaxation Experiments," *Phys. Rev. Lett.*, vol. 94, p. 196803, 2005.

[222] J. Korringa, "Nuclear magnetic relaxation and resonnance line shift in metals," *Physica*, vol. 16, no. 7-8, pp. 601–610, 1950.

[223] K. von Klitzing, "The quantized Hall effect," *Rev. Mod. Phys.*, vol. 58, pp. 519–531, 1986.

[224] M. Yankowitz, J. Xue, D. Cormode, J. D. Sanchez-Yamagishi, K. Watanabe, T. Taniguchi, P. Jarillo-Herrero, P. Jacquod, and B. J. LeRoy, "Emergence of superlattice Dirac points in graphene on hexagonal boron nitride," *Nat. Phys.*, vol. 8, no. 5, pp. 382–386, 2012.

[225] B. Hunt, J. D. Sanchez-Yamagishi, A. F. Young, M. Yankowitz, B. J. LeRoy, K. Watanabe, T. Taniguchi, P. Moon, M. Koshino, P. Jarillo-Herrero, and R. C. Ashoori, "Massive Dirac fermions and Hofstadter butterfly in a van der Waals heterostructure," *Science*, vol. 340, no. 6139, pp. 1427–1430, 2013.

[226] C. R. Dean, L. Wang, P. Maher, C. Forsythe, F. Ghahari, Y. Gao, J. Katoch, M. Ishigami, P. Moon, M. Koshino, T. Taniguchi, K. Watanabe, K. L. Shepard, J. Hone, and P. Kim, "Hofstadter's butterfly and the fractal quantum Hall effect in moiré superlattices," *Nature*, vol. 497, no. 7451, pp. 598–602, 2013.

[227] R. Krishna Kumar, X. Chen, G. H. Auton, A. Mishchenko, D. A. Bandurin, S. V. Morozov, Y. Cao, E. Khestanova, M. Ben Shalom, A. V. Kretinin, K. S. Novoselov, L. Eaves, I. V. Grigorieva, L. A. Ponomarenko, V. I. Fal'Ko, and A. K. Geim, "High-temperature quantum oscillations caused by recurring Bloch states in graphene superlattices," *Science*, vol. 357, no. 6347, pp. 181–184, 2017.

[228] R. Huber, M.-N. Steffen, M. Drienovsky, A. Sandner, K. Watanabe, T. Taniguchi, D. Pfannkuche, D. Weiss, and J. Eroms, "Band conductivity oscillations in a gate-tunable graphene superlattice," *Nat. Commun.*, vol. 13, no. 1, p. 2856, 2022.

[229] M. B. Lundeberg, R. Yang, J. Renard, and J. A. Folk, "Defect-Mediated Spin Relaxation and Dephasing in Graphene," *Phys. Rev. Lett.*, vol. 110, p. 156601, 2013.

[230] K. Hashimoto, K. Muraki, T. Saku, and Y. Hirayama, "Electrically Controlled Nuclear Spin Polarization and Relaxation by Quantum-Hall States," *Phys. Rev. Lett.*, vol. 88, p. 176601, 2002.

[231] N. P. Wilson, K. Lee, J. Cenker, K. Xie, A. H. Dismukes, E. J. Telford, J. Fonseca, S. Sivakumar, C. Dean, T. Cao, X. Roy, X. Xu, and X. Zhu, "Interlayer electronic coupling on demand in a 2D magnetic semiconductor," *Nat. Mater.*, vol. 20, no. 12, pp. 1657–1662, 2021.

[232] M. Sherafati and S. Satpathy, "RKKY interaction in graphene from the lattice Green's function," *Phys. Rev. B*, vol. 83, p. 165425, 2011.

[233] E. Kogan, "RKKY interaction in graphene," *Phys. Rev. B*, vol. 84, p. 115119, 2011.

[234] M. T. Allen, O. Shtanko, I. C. Fulga, J. I.-J. Wang, D. Nurgaliev, K. Watanabe, T. Taniguchi, A. R. Akhmerov, P. Jarillo-Herrero, L. S. Levitov, and A. Yacoby, "Observation of Electron Coherence and Fabry–Perot Standing Waves at a Graphene Edge," *Nano Lett.*, vol. 17, no. 12, pp. 7380–7386, 2017.

[235] F. E. Schmidt, M. D. Jenkins, K. Watanabe, T. Taniguchi, and G. A. Steele, "A ballistic graphene superconducting microwave circuit," *Nat. Commun.*, vol. 9, no. 1, p. 4069, 2018.

[236] M. Ben Shalom, M. J. Zhu, V. I. Fal'Ko, A. Mishchenko, A. V. Kretinin, K. S. Novoselov, C. R. Woods, K. Watanabe, T. Taniguchi, A. K. Geim, and J. R. Prance, "Quantum oscillations of the critical current and high-field superconducting proximity in ballistic graphene," *Nat. Phys.*, vol. 12, no. 4, pp. 318–322, 2016.

[237] G. Nanda, J. L. Aguilera-Servin, P. Rakyta, A. Kormányos, R. Kleiner, D. Koelle, K. Watanabe, T. Taniguchi, L. M. K. Vandersypen, and S. Goswami, "Current-phase relation of ballistic graphene Josephson junctions," *Nano Lett.*, vol. 17, no. 6, pp. 3396–3401, 2017.

[238] A. Wallraff, A. Lukashenko, C. Coqui, A. Kemp, T. Duty, and A. V. Ustinov, "Switching current measurements of large area Josephson tunnel junctions," *Rev. Sci. Instrum.*, vol. 74, no. 8, pp. 3740–3748, 2003.

[239] G. von Minnigerode, "Der Einfluß von Gitterfehlern auf die Übergangstemperaturen verschiedener Supraleiter," *Z. Physik*, vol. 154, no. 4, pp. 442–459, 1959.

[240] W. DeSorbo, "Effect of Dissolved Gases on Some Superconducting Properties of Niobium," *Phys. Rev.*, vol. 132, pp. 107–121, 1963.

[241] D. K. Finnemore, T. F. Stromberg, and C. A. Swenson, "Superconducting Properties of High-Purity Niobium," *Phys. Rev.*, vol. 149, pp. 231–243, 1966.

[242] Y. Asada and H. Nosé, "Superconductivity of Niobium Films," *J. Phys. Soc. Jpn.*, vol. 26, no. 2, pp. 347–354, 1969.

[243] B. Okolo, P. Lamparter, U. Welzel, and E. J. Mittemeijer, "Stress, texture, and microstructure in niobium thin films sputter deposited onto amorphous substrates," *J. Appl. Phys.*, vol. 95, no. 2, pp. 466–476, 2004.

[244] C. Clavero, D. B. Beringer, W. M. Roach, J. R. Skuza, K. C. Wong, A. D. Batchelor, C. E. Reece, and R. A. Lukaszew, "Strain Effects on the Crystal Growth and Superconducting Properties of Epitaxial Niobium Ultrathin Films," *Cryst. Growth Des.*, vol. 12, no. 5, pp. 2588–2593, 2012.

[245] C. Todt, S. Telkamp, F. Krizek, C. Reichl, M. Gabureac, R. Schott, E. Cheah, P. Zeng, T. Weber, A. Müller, C. Vockenhuber, M. B. Panah, and W. Wegscheider, "Development of Nb-GaAs based superconductor-semiconductor hybrid platform by combining in situ dc magnetron sputtering and molecular beam epitaxy," *Phys. Rev. Mater.*, vol. 7, p. 076201, 2023.

[246] C. Wu, "Intrinsic stress of magnetron-sputtered niobium films," *Thin Solid Films*, vol. 64, no. 1, pp. 103–110, 1979.

[247] R. Jha and V. P. S. Awana, "Control of sputtering parameters for deposition of NbN thick films," *Nov. Supercond. Mater.*, vol. 1, pp. 7–12, 2013.

[248] G. W. Webb, "Low-Temperature Electrical Resistivity of Pure Niobium," *Phys. Rev.*, vol. 181, pp. 1127–1135, 1969.

[249] K.-H. Müller, "Ion-beam-induced epitaxial vapor-phase growth: A molecular-dynamics study," *Phys. Rev. B*, vol. 35, pp. 7906–7913, 1987.

[250] O. Auciello and R. Kelly, *Ion bombardment modification of surfaces*, vol. 1st edition. Elsevier Science Publishers, 1984.

[251] D. Brice, J. Y. Tsao, and S. T. Picraux, "Partitioning of ion-induced surface and bulk displacements," *Nucl. Inst. Methods Phys. Res. B*, vol. 44, pp. 68–78, 1989.

[252] R. Frerichs and C. J. Kircher, "Properties of Superconducting Niobium Films Made by Asymmetric ac Sputtering," *J. Appl. Phys.*, vol. 34, no. 12, pp. 3541–3543, 1963.

[253] U. Welp, Z. L. Xiao, J. S. Jiang, V. K. Vlasko-Vlasov, S. D. Bader, G. W. Crabtree, J. Liang, H. Chik, and J. M. Xu, "Superconducting transition and vortex pinning in Nb films patterned with nanoscale hole arrays," *Phys. Rev. B*, vol. 66, p. 212507, 2002.

[254] U. Welp, Z. L. Xiao, V. Novosad, and V. K. Vlasko-Vlasov, "Commensurability and strong vortex pinning in nanopatterned Nb films," *Phys. Rev. B*, vol. 71, p. 014505, 2005.

[255] J. Emsley, *The Elements*, vol. 1st edition. Oxford University Press, 1998.

[256] H. Gao, S. Wang, D. Xu, X. Wang, Q. Zhong, Y. Zhong, J. Li, and W. Cao, "Study of DC Magnetron Sputtered Nb Films," *Crystals*, vol. 12, p. 1, 2022.

[257] D. D. Bacon, A. T. English, S. Nakahara, F. G. Peters, H. Schreiber, W. R. Sinclair, and R. B. van Dover, "Properties of NbN thin films deposited on ambient temperature substrates," *J. Appl. Phys.*, vol. 54, no. 11, pp. 6509–6516, 1983.

[258] S. Thakoor, J. L. Lamb, A. P. Thakoor, and S. K. Khanna, "High Tc superconducting NbN films deposited at room temperature," *J. Appl. Phys.*, vol. 58, no. 12, pp. 4643–4648, 1985.

[259] D. Henrich, S. Dörner, M. Hofherr, K. Il'in, A. Semenov, E. Heintze, M. Scheffler, M. Dressel, and M. Siegel, "Broadening of hot-spot response spectrum of superconducting NbN nanowire single-photon detector with reduced nitrogen content," *J. Appl. Phys.*, vol. 112, no. 7, p. 074511, 2012.

[260] S. P. Chockalingam, M. Chand, J. Jesudasan, V. Tripathi, and P. Raychaudhuri, "Superconducting properties and Hall effect of epitaxial NbN thin films," *Phys. Rev. B*, vol. 77, p. 214503, 2008.

[261] Z. Wang, A. Kawakami, Y. Uzawa, and B. Komiyama, "Superconducting properties and crystal structures of single-crystal niobium nitride thin films deposited at ambient substrate temperature," *J. Appl. Phys.*, vol. 79, no. 10, pp. 7837–7842, 1996.

[262] J. Wang, L. Bretheau, D. Rodan-Legrain, R. Pisoni, K. Watanabe, T. Taniguchi, and P. Jarillo-Herrero, "Tunneling spectroscopy of graphene nanodevices coupled to large-gap superconductors," *Phys. Rev. B*, vol. 98, p. 121411, 2018.

[263] K. Komatsu, C. Li, S. Autier-Laurent, H. Bouchiat, and S. Guéron, "Superconducting proximity effect in long superconductor/graphene/superconductor junctions: From specular Andreev reflection at zero field to the quantum Hall regime," *Phys. Rev. B*, vol. 86, p. 115412, 2012.

[264] T. F. Q. Larson, L. Zhao, E. G. Arnault, M.-T. Wei, A. Seredinski, H. Li, K. Watanabe, T. Taniguchi, F. Amet, and G. Finkelstein, "Zero crossing steps and anomalous shapiro maps in graphene josephson junctions," *Nano Lett.*, vol. 20, no. 10, pp. 6998–7003, 2020.

[265] B. Abeles, R. W. Cohen, and G. W. Cullen, "Enhancement of Superconductivity in Metal Films," *Phys. Rev. Lett.*, vol. 17, pp. 632–634, 1966.

[266] R. W. Cohen and B. Abeles, "Superconductivity in Granular Aluminum Films," *Phys. Rev.*, vol. 168, pp. 444–450, 1968.

[267] G. Deutscher and S. A. Dodds, "Critical-field anisotropy and fluctuation conductivity in granular aluminum films," *Phys. Rev. B*, vol. 16, pp. 3936–3942, 1977.

[268] N. Maleeva, L. Grünhaupt, T. Klein, F. Levy-Bertrand, O. Dupre, M. Calvo, F. Valenti, P. Winkel, F. Friedrich, W. Wernsdorfer, A. V. Ustinov, H. Rotzinger, A. Monfardini, M. V. Fistul, and I. M. Pop, "Circuit quantum electrodynamics of granular aluminum resonators," *Nat. Comm.*, vol. 9, no. 1, p. 3889, 2018.

[269] M. Kjaergaard, H. J. Suominen, M. P. Nowak, A. R. Akhmerov, J. Shabani, C. J. Palmstrøm, F. Nichele, and C. M. Marcus, "Transparent Semiconductor-Superconductor Interface and Induced Gap in an Epitaxial Heterostructure Josephson Junction," *Phys. Rev. Appl.*, vol. 7, p. 034029, 2017.

[270] E. Cheah, D. Z. Haxell, R. Schott, P. Zeng, E. Paysen, S. C. ten Kate, M. Coraiola, M. Landstetter, A. B. Zadeh, A. Trampert, M. Sousa, H. Riel, F. Nichele, W. Wegscheider, and F. Krizek, "Control over epitaxy and the role of the InAs/Al interface in hybrid two-dimensional electron gas systems," *Phys. Rev. Mater.*, vol. 7, p. 073403, 2023.

[271] M. Popinciuc, V. E. Calado, X. L. Liu, A. R. Akhmerov, T. M. Klapwijk, and L. M. K. Vandersypen, "Zero-bias conductance peak and Josephson effect in graphene-NbTiN junctions," *Phys. Rev. B*, vol. 85, p. 205404, 2012.

[272] B. J. van Wees, P. de Vries, P. Magnée, and T. M. Klapwijk, "Excess conductance of superconductor-semiconductor interfaces due to phase conjugation between electrons and holes," *Phys. Rev. Lett.*, vol. 69, pp. 510–513, 1992.

[273] I. K. Marmorkos, C. W. J. Beenakker, and R. A. Jalabert, "Three signatures of phase-coherent Andreev reflection," *Phys. Rev. B*, vol. 48, pp. 2811–2814, 1993.

[274] F. Giazotto, P. Pingue, F. Beltram, M. Lazzarino, D. Orani, S. Rubini, and A. Franciosi, "Resonant Transport in Nb /GaAs /AlGaAs Heterostructures: Realization of the de Gennes–Saint-James Model," *Phys. Rev. Lett.*, vol. 87, p. 216808, 2001.

[275] M. Octavio, M. Tinkham, G. E. Blonder, and T. M. Klapwijk, "Subharmonic energy-gap structure in superconducting constrictions," *Phys. Rev. B*, vol. 27, pp. 6739–6746, 1983.

[276] W. J. Tomasch, "Geometrical Resonance and Boundary Effects in Tunneling from Superconducting In," *Phys. Rev. Lett.*, vol. 16, pp. 16–19, 1966.

[277] W. L. McMillan and P. W. Anderson, "Theory of Geometrical Resonances in the Tunneling Characteristics of Thick Films of Superconductors," *Phys. Rev. Lett.*, vol. 16, pp. 85–87, 1966.

[278] J. M. Rowell and W. L. McMillan, "Electron Interference in a Normal Metal Induced by Superconducting Contacts," *Phys. Rev. Lett.*, vol. 16, pp. 453–456, 1966.

[279] J. M. Rowell, "Tunneling Observation of Bound States in a Normal Metal—Superconductor Sandwich," *Phys. Rev. Lett.*, vol. 30, pp. 167–170, 1973.

[280] K.-F. Huang, Ö. Gül, T. Taniguchi, K. Watanabe, and P. Kim, "Andreev reflection between aluminum and graphene across van der Waals barriers," *Low Temp. Phys.*, vol. 49, no. 6, pp. 662–669, 2023.

[281] C. Visani, Z. Sefrioui, J. Tornos, C. Leon, J. Briatico, M. Bibes, A. Barthélémy, J. Santamaría, and J. E. Villegas, "Equal-spin Andreev reflection and long-range coherent transport in high-temperature superconductor/half-metallic ferromagnet junctions," *Nat. Phys.*, vol. 8, no. 7, pp. 539–543, 2012.

[282] C. T. Ke, I. V. Borzenets, A. W. Draelos, F. Amet, Y. Bomze, G. Jones, M. Craciun, S. Russo, M. Yamamoto, S. Tarucha, and G. Finkelstein, "Critical Current Scaling in Long Diffusive Graphene-Based Josephson Junctions," *Nano Letters*, vol. 16, no. 8, pp. 4788–4791, 2016.

[283] C. Li, S. Guéron, A. Chepelianskii, and H. Bouchiat, "Full range of proximity effect probed with superconductor/graphene/superconductor junctions," *Phys. Rev. B*, vol. 94, p. 115405, 2016.

[284] H. A. Nilsson, P. Samuelsson, P. Caroff, and H. Q. Xu, "Supercurrent and Multiple Andreev Reflections in an InSb Nanowire Josephson Junction," *Nano Letters*, vol. 12, no. 1, pp. 228–233, 2012.

[285] J. Ridderbos, M. Brauns, A. Li, E. P. A. M. Bakkers, A. Brinkman, W. G. van der Wiel, and F. A. Zwanenburg, "Multiple Andreev reflections and Shapiro steps in a Ge-Si nanowire Josephson junction," *Phys. Rev. Mater.*, vol. 3, p. 084803, 2019.

[286] O. Nesher and G. Koren, "Measurements of Δ and v_F from Andreev reflections and McMillan-Rowell oscillations in edge junctions of $YBa_2Cu_3O_{6.6}/YBa_2Cu_{2.55}Fe_{0.45}O_y/YBa_2Cu_3O_{6.6}$," *Phys. Rev. B*, vol. 60, pp. 9287–9290, 1999.

[287] K. Inomata, T. Yamamoto, M. Watanabe, K. Matsuba, and J.-S. Tsai, "Film-thickness dependence of 10 GHz Nb coplanar-waveguide resonators," *J. Vac. Sci. Technol. B*, vol. 27, no. 5, pp. 2286–2291, 2009.

[288] Y.-C. Chang, B. Karimi, J. Senior, A. Ronzani, J. T. Peltonen, H.-S. Goan, C.-D. Chen, and J. P. Pekola, "Utilization of the superconducting transition for characterizing low-quality-factor superconducting resonators," *Appl. Phys. Lett.*, vol. 115, no. 2, p. 022601, 2019.

[289] A. Zak, M. A. Andersson, M. Bauer, J. Matukas, A. Lisauskas, H. G. Roskos, and J. Stake, "Antenna-integrated 0.6 THz FET direct detectors based on CVD graphene," *Nano letters*, vol. 14, no. 10, pp. 5834–5838, 2014.

[290] N. M. Gabor, J. C. W. Song, Q. Ma, N. L. Nair, T. Taychatanapat, K. Watanabe, T. Taniguchi, L. S. Levitov, and P. Jarillo-Herrero, "Hot carrier–assisted intrinsic photoresponse in graphene," *Science*, vol. 334, no. 6056, pp. 648–652, 2011.

[291] D. V. Fateev, K. V. Mashinsky, and V. V. Popov, "Terahertz plasmonic rectification in a spatially periodic graphene," *Appl. Phys. Lett.*, vol. 110, no. 6, p. 061106, 2017.

[292] L. Vicarelli, M. S. Vitiello, D. Coquillat, A. Lombardo, A. C. Ferrari, W. Knap, M. Polini, V. Pellegrini, and A. Tredicucci, "Graphene field-effect transistors as room-temperature terahertz detectors," *Nature Mater.*, vol. 11, no. 10, pp. 865–871, 2012.

[293] N. W. Ashcroft and N. D. Mermin, *Solid State Physics*, vol. 1st edition. Thomson Learning Inc. London, 1976.

[294] A. M. Potts, A. K. Nayak, M. Nagel, K. Kaj, B. Stamenic, D. D. John, R. D. Averitt, and A. F. Young, "On-chip time-domain terahertz spectroscopy of superconducting films below the diffraction limit," *Nano Lett.*, vol. 23, no. 9, pp. 3835–3841, 2023.

[295] M. R. Sinko, S. C. de la Barrera, O. Lanes, K. Watanabe, T. Taniguchi, S. Tan, D. Pekker, M. Hatridge, and B. M. Hunt, "Superconducting contact and quantum interference between two-dimensional van der Waals and three-dimensional conventional superconductors," *Phys. Rev. Mater.*, vol. 5, p. 014001, 2021.

[296] H. S. Arora, R. Polski, Y. Zhang, A. Thomson, Y. Choi, H. Kim, Z. Lin, I. Z. Wilson, X. Xu, J.-H. Chu, K. Watanabe, T. Taniguchi, J. Alicea, and S. Nadj-Perge, "Superconductivity in metallic twisted bilayer graphene stabilized by WSe_2," *Nature*, vol. 583, no. 7816, pp. 379–384, 2020.

[297] Y. Zhang, R. Polski, A. Thomson, E. Lantagne-Hurtubise, C. Lewandowski, H. Zhou, K. Watanabe, T. Taniguchi, J. Alicea, and S. Nadj-Perge, "Enhanced superconductivity in spin–orbit proximitized bilayer graphene," *Nature*, vol. 613, no. 7943, pp. 268–273, 2023.

[298] L. Holleis, C. L. Patterson, Y. Zhang, Y. Vituri, H. M. Yoo, H. Zhou, T. Taniguchi, K. Watanabe, E. Berg, S. Nadj-Perge, and A. F. Young, "Nematicity and orbital depairing in superconducting Bernal bilayer graphene," *Nat. Phys.*, pp. 1–7, 2025.

[299] Y.-M. Xie, E. Lantagne-Hurtubise, A. F. Young, S. Nadj-Perge, and J. Alicea, "Gate-Defined Topological Josephson Junctions in Bernal Bilayer Graphene," *Phys. Rev. Lett.*, vol. 131, p. 146601, 2023.

[300] N. Levy, S. A. Burke, K. L. Meaker, M. Panlasigui, A. Zettl, F. Guinea, A. H. Castro-Neto, and M. F. Crommie, "Strain-induced pseudo–magnetic fields greater than 300 tesla in graphene nanobubbles," *Science*, vol. 329, no. 5991, pp. 544–547, 2010.

[301] M. Alidoust and J. Linder, "Tunable supercurrent at the charge neutrality point via strained graphene junctions," *Phys. Rev. B*, vol. 84, p. 035407, 2011.

[302] L. Covaci and F. M. Peeters, "Superconducting proximity effect in graphene under inhomogeneous strain," *Phys. Rev. B*, vol. 84, p. 241401, 2011.

[303] S. Park, W. Lee, S. Jang, Y.-B. Choi, J. Park, W. Jung, K. Watanabe, T. Taniguchi, G. Y. Cho, and G.-H. Lee, "Steady Floquet–Andreev states in graphene Josephson junctions," *Nature*, vol. 603, no. 7901, pp. 421–426, 2022.

[304] D. Z. Haxell, M. Coraiola, D. Sabonis, M. Hinderling, S. C. Ten Kate, E. Cheah, F. Krizek, R. Schott, W. Wegscheider, W. Belzig, J. C. Cuevas, and F. Nichele, "Microwave-induced conductance replicas in hybrid Josephson junctions without Floquet—Andreev states," *Nat. Comm.*, vol. 14, no. 1, p. 6798, 2023.

Publications

- V. Strenzke, A. Weber, P. Heydolph, I. Moch, I. González Díaz-Palacio, W. Hillert, R. Zierold, L. Tiemann, and R. H. Blick, Challenges and solutions in RF sputtering of superconducting Nb for nanostructuring processes, Journal of Applied Physics 136, 205301 (2024).
- V. Strenzke, M. Prada, J. M. J. Lopes, L. Tiemann, R. H. Blick, The quest for harnessing nuclear effects in graphene-based devices, Applied Physics Review 11, 011312 (2024).
- V. Strenzke, J. M. Meyer, I. Grandt-Ionita, M. Prada, H.-S. Kim, M. Heilmann, J. M. J. Lopes, L. Tiemann, and R. H. Blick, Nuclear-induced dephasing and signatures of hyperfine effects in isotopically purified ^{13}C graphene, Physical Review B 105, 144303 (2022).

Conference Contributions

- V. Strenzke, C. Elsässer, I. Grandt-Ionita, J. Stelzner, L. Tiemann, and R. H. Blick, Sensitive Microwave Spectroscopy of van der Waals Materials with Coplanar Waveguides, MRS Fall Meeting (2023).
- V. Strenzke, C. Elsässer, I. Grandt-Ionita, J. Stelzner, K. Murat, L. Tiemann, R. H. Blick, Coplanar waveguides for sensitive microwave spectroscopy in two-dimensional materials, EP2DS-25 (2023).
- V. Strenzke, J. M. Meyer, I. Grandt-Ionita, M. Prada, H.-S. Kim, M. Heilmann, J. M. J. Lopes, L. Tiemann, and R. H. Blick, Signatures of hyperfine effects in isotopically purified ^{13}C graphene, APS March Meeting (2023).
- V. Strenzke, J. M. Meyer, I. Grandt-Ionita, M. Prada, H.-S. Kim, M. Heilmann, J. M. J. Lopes, L. Tiemann, and R. H. Blick, Nuclear-induced dephasing and signatures of hyperfine effects in isotopically purified ^{13}C graphene, Graphene Week (2022).

Acknowledgments

During my PhD, I have had the honor to interact with many immensely talented and hard-working people. At this point, I would like to express my gratitude to all the people who supported me throughout my time as a PhD student and without whom this thesis would not have been possible.

First, I would like to thank Prof. Robert H. Blick for the opportunity to conduct this exciting dissertation project in his group, for his scientific guidance and constant support, for serving as the first referee of my thesis, and for fostering my academic growth by enabling multiple research stays and conference visits.

I am especially grateful to Dr. Lars Tiemann for his supervision, advice, and expertise throughout my time in this group since I started as a student research assistant in 2019. His invaluable assistance, encouragement, and the freedom he granted me in my research were inspiring and guided me through my PhD journey.

I would like to thank Dr. Robert Zierold for his advice and support in the projects involving superconducting thin films and for joining my thesis committee.

I also want to thank Prof. Dorota Koziej and Prof. Gabriel Bester for being part of my thesis committee.

The achievements presented in this thesis were made possible by the outstanding teamwork of the 2D-transport group, including all past and present members! Thank you Dr. Marta Prada for all the useful theoretical insights and thanks to Dr. Chithra H. Sharma and Dr. Pai Zhao for the great time in the lab and their help on countless experimental aspects. It was a privilege to work together with extremely talented and motivated students, whose projects significantly helped to progress the different fields of my PhD topic. I am especially thankful to Jan Stelzner, Isabell Grandt-Ionita, and Annika Weber for their tremendous efforts in advancing device fabrication and for being indispensable both inside and outside the lab. I am also deeply grateful to Christian, Franziska, Isa, Peer, Kamila, Achim, and Doro for their valuable contributions.

Special thanks to Carina, Isabel, Jun, Jann, Malte, Stefanie and Kristian for the fantastic time we shared together at the CHyN in the office or in the labs, during lunch and at the group events. I would like to thank Bojan, Matthias, and Thomas for their technical support, and Katja for her administrative expertise, as well as for being so approachable and helpful. Additionally, I truly appreciate the entire Blick group for the warm, friendly and collaborative atmosphere that

made the time at work so enjoyable, as well as for all the memorable get-togethers.

I would like to thank Prof. Kin Chun Fong for enlightening conversations and for the opportunity to visit his research group at Raytheon BBN Technologies. In the context of this collaboration, I am also grateful to Dr. Le Hoang Nguyen, Dr. Marios Maroudas, and Prof. Dieter Horns for their help and insights on dark matter axion physics.

Furthermore, I would like to thank Davide Derelli and Sani Harouna-Mayer for support in XRD measurements.

I would also like to thank everyone who took the time to proofread my thesis.

Zu guter Letzt möchte ich mich ganz herzlich bei meinen Freunden und meiner Familie bedanken. Vielen Dank an Silvio für unsere zahlreichen gemeinsamen Abende bei gutem Essen und guten Gesprächen. Danke an meine bois Jonas, Niklas, Lennart und Nathan für immer währende Freundschaft und die unzähligen gemeinsamen Erlebnisse. Allergrößten Dank an meine Eltern Carmen und Stefan für ihren Glauben an mich und für ihre Unterstützung bei allem was ich mache.

Jana – Worte können nicht ausdrücken, wie viel es mir bedeutet Dich in meinem Leben zu haben. Danke, dass Du für mich da bist, dass ich mit Dir über alles reden kann (auch über Nanostrukturierung) und dafür, dass Du so ein einmaliger, toller Mensch und die Liebe meines Lebens bist.

Eidesstattliche Versicherung

Hiermit versichere ich an Eides statt, die vorliegende Dissertationsschrift selbst verfasst und keine anderen als die angegebenen Hilfsmittel und Quellen benutzt zu haben.

Sofern im Zuge der Erstellung der vorliegenden Dissertationsschrift generative Künstliche Intelligenz (gKI) basierte elektronische Hilfsmittel verwendet wurden, versichere ich, dass meine eigene Leistung im Vordergrund stand und dass eine vollständige Dokumentation aller verwendeten Hilfsmittel gemäß der Guten wissenschaftlichen Praxis vorliegt. Ich trage die Verantwortung für eventuell durch die gKI generierte fehlerhafte oder verzerrte Inhalte, fehlerhafte Referenzen, Verstöße gegen das Datenschutz- und Urheberrecht oder Plagiate.

Hamburg, den

Vincent Strenzke